

# ERUPTIVE DYNAMICS AND PETROLOGICAL EVOLUTION OF RECENT VOLCANISM ON THE EL HIERRO ISLAND. IMPLICATIONS FOR VOLCANIC HAZARD ASSESSMENT



**PhD Thesis**

**Stavros Meletlidis Tsiogalos**

**Barcelona 2017**





# **Eruptive dynamics and petrological evolution of recent volcanism on the El Hierro Island. Implications for volcanic hazard assessment**

by

**Stavros Meletlidis Tsiogalos**

A thesis submitted in partial fulfilment

of the requirements for the degree of

Doctor of Philosophy

Programa de Doctorat de "Ciències de la Terra"

Department of Geodynamic and Geophysics

Faculty of Geology

Universidad de Barcelona

Thesis Supervisor:

Prof. Joan Martí Molist

Institute of Earth Sciences Jaume Almera - CSIC

Thesis Tutor:

Prof. Joan Manuel Vilaplana Fernández

Faculty of Geology - UB

June 2017

*On the cover: Monogenetic volcano located in the west sector of El Hierro Island, by the lighthouse of Orchilla. Pahoehoe lava flows originating on the lower flank of the cone, fed by parasitic vents, can be distinguished.*

*Photo: Stavros Meletlidis*



UNIVERSITAT DE  
BARCELONA

**Eruptive dynamics and petrological evolution of recent  
volcanism on the El Hierro Island. Implications for  
volcanic hazard assessment**

Stavros Meletlidis Tsiogalos



*"Ἔν οἶδα ὅτι οὐδέν οἶδα"*

- Socrates (470 - 399 B.C.) -



To Sonia, Paris & Hector,  
because they always understood



## ACKNOWLEDGEMENTS

I would like to thank all the people who have contributed in some way to this thesis, without whose support and encouragement it would not have been possible.

First and foremost, I thank my academic supervisor, Professor Joan Martí Molist, for supporting and guiding me through this journey. During this adventure he contributed to a rewarding PhD experience by giving me intellectual freedom in my work and engaging me in new ideas. Also a big thank you goes to my tutor Professor Joan Manuel Vilaplana Fernández, who had the patience to deal with me all this time and being a good listener and guide.

This thesis would not have been possible without the generous support of the Instituto Geográfico Nacional (I.G.N.), where I work since 2007, which provided me with all the necessary infrastructure and logistical support. Every result achieved in this thesis was accomplished with the help and support of fellow workmates, not only from Tenerife office (Centro Geofísico de Canarias, del I.G.N.) but also from Observatorio Geofísico Central del I.G.N. (Madrid headquarters). Particularly thanks to Alicia Felpeto, Itahiza Dominguez, Pedro Torres, Laura Garcia, Sergio Sainz-Maza Aparicio and Carmen del Fresno Rodríguez-Portugal, for their friendship, support and help. You provided a friendly and cooperative atmosphere at work and also useful feedbacks and insightful comments on my work. I am still missing those endless days in the field or the nights in duty while the eruption.

I was fortunate to have the chance to work under the direction of two exceptional women and scientists, María Jose Blanco (my boss in Tenerife) and Carmen Lopez (my big boss in Madrid). Their effort to understand my spanish-greek-english semi-constructed thoughts and their support to all my crazy ideas were gone beyond this world and to different extents.

Particular thanks to the Italian team: Alessio, Massimo, Antonella and Paola. They have become my personal rescue team when times of storm and uncertainty drew near. I shared great moments with them, field work, lab work, and hours of discussion (thank you Skype!). Many times they were my source of scientific knowledge, and I am grateful for sharing and been taught, tirelessly and with much enthusiasm.

I am also indebted to Professor Michael Fytikas, for introducing me in that "volcanic" world and giving me the possibility to work, learn and love volcanoes. I am very grateful to Dr. George Vougioukalakis who accepted and suffered, years ago, a graduate student as a teammate in his field work all over Greece, and passed me over his knowledge and his enthusiasm in studying the volcanoes. It's a pity that an ocean and a continent lay between us.

I would like to acknowledge friends and family who have supported me during my time here. First and foremost I would like to thank my beloved spouse Sonia for her constant love and unyielding support. I am sure she will never forget these long periods of me away from home, monitoring El Hierro eruption, taking samples, working on monitor network deployment on other islands, congress trips or lab work abroad. Thank you for having faith in my work, standing behind me and sacrificing so many things. Also I would like to thank my two sons, Paris and Hector, they were always there to have my mind occupied (and my body) when too much work was accumulated. However, I have to apologize for the loss of so many moments due to my odd work and I hope that someday Hector could forgive me for abandoning him as a newborn (5 days of life) because of El Hierro eruption; Έκτωρα, το είδες; Τελικά τα καταφέραμε!

To my Mom, Theodora, and my recently passed away Dad, Lazaros, all I have to say is thank you for the effort and support to make me study and also thanks for understanding and suffer these tons of rocks and laundry bags at home, whenever I returned from a field trip.

To my parents-in-law, María and Belio, I want to thank you for being part of this, supporting and helping in every aspect of our family life. Without you, we would not have managed to survive.

Finally, I would like to thank Chris Satow and Maite Martín González, for proof-reading the English manuscript and their constructive comments.

Thanks, you all have my eternal gratitude and love

Stavros

June 2017

# CONTENTS

<b>Abstract</b>	III
<b>1. Introduction</b>	1
1.1. Thesis overview - Canary Islands, magmas and eruptions	1
1.2. Products of a newborn volcano	6
1.3. An explosive felsic eruption on an oceanic island	11
1.4. Clarifying the dubious origin of the xenopumices	15
1.5. Modelling through instrumental data and erupted products	19
1.6. Not a calm basaltic eruption	27
<b>2. Results</b>	35
<b>3. Discussion</b>	51
<b>4. Conclusions</b>	63
<b>5. References</b>	67
<b>6. Annexes</b>	79
6.1. <b>Meletlidis, S.,</b> A. Di Roberto, M. Pompilio, A. Bertagnini, I. Iribarren, A. Felpeto, P. A. Torres, and C. D'Oriano (2012). <i>Xenopumices from the 2011-2012 submarine eruption of El Hierro (Canary Islands, Spain): Constraints on the plumbing system and magma ascent</i> , <i>Geophys. Res. Lett.</i> , doi:10.1029/2012GL052675	
6.2. Pedrazzi, D., Becerril, L., Martí, J., <b>Meletlidis, S.,</b> Galindo, I. (2014). <i>Explosive felsic volcanism on El Hierro (Canary Islands)</i> . <i>Bull of Volcanology</i> , 76:863. doi: 10.1007/s00445-014-0863-1	
6.3. S. Del Moro, A. Di Roberto, <b>S. Meletlidis,</b> M. Pompilio, A. Bertagnini, S. Agostini, F. Ridolfi, A. Renzulli (2015). <i>Xenopumice erupted on 15 October 2011 offshore of El Hierro (Canary Islands): a subvolcanic snapshot of magmatic, hydrothermal and pyrometamorphic processes</i> . <i>Bull of Volcanology</i> , Volume 77:53. doi: 10.1007/s00445-015-0940-0	
6.4. <b>S. Meletlidis,</b> A. Di Roberto, I. Domínguez Cerdeña, M. Pompilio, L. García-Cañada, A. Bertagnini, M. A. Benito-Saz, P. Del Carlo, S. Sainz-Maza Aparicio (2015). <i>New insight into the 2011-2012 unrest and eruption of El Hierro Island (Canary Islands) based on integrated geophysical, geodetical and petrological data</i> . <i>Annals of Geophysics</i> , [S.l.], v. 58, n. 5, p. S0546, doi: 10.4401/ag-6754	
6.5. Di Roberto, A.; Bertagnini, A.; Del Carlo, P.; <b>Meletlidis, S.;</b> Pompilio, M. (2016). <i>The 1909 Chinyero eruption on Tenerife (Canary Islands): insights from historical accounts, and tephrostratigraphic and geochemical data</i> . <i>Bull of Volcanology</i> , 78:88. doi 10.1007/s00445-016-1083-7	



## ABSTRACT

The Canarian archipelago, extends over approximately 500 km in total along the passive continental margin off NW Africa, comprises seven major and four minor islands, and it is part of the so called Macaronesia region, together with the archipelagos of Azores, Madeira, Salvajes and Cape Verde.

Within the oceanic geodynamic context, the Canary archipelago is located on oceanic crust of the big African plate, specifically upon the passive continental margin, with thickness exceeding 20 km. It is a good example of oceanic intraplate alkaline volcanism.

According the radioisotopic data available (Carracedo et al., 1998) the archipelago has been formed during the last 60 Ma and is still volcanically active. Multiple periods of volcanic activity accompanied with extreme range in magma compositions and eruptive styles have been exhibited during the evolution.

A wide variety of models have been proposed for the origin of the Canary Islands, such as, hot spot, decompressing fusion, Atlas generated propagating fracture, or the "block" model based on regional fractures that helped elevate the islands.

Holocene sub-aerial activity has occurred on all islands, except La Gomera, with 18 eruptions in the last 520 years (historic activity) on Tenerife, La Palma, Lanzarote and El Hierro. All these eruptive events consist of monogenetic basaltic eruptions along structures or zones identified as rifts (only the 1798 of Montaña Chahorra in Tenerife, expelled intermediate composition magma and was located at the base of the Teide-Pico Viejo volcanic complex).

Although monogenetic volcanism is the most extended type of volcanic activity on the planet (Walker 2000) and is characterized by a large diversity of eruptive styles and products, it is generally associated to low level volcanic hazard and many times it is underestimated in the hazard assessment.

The main structures generated by these type of eruptions (concentrated as volcanic fields or long rift zones) are cinder cones, formed by the pyroclastic products and lava flows, that can reach several kilometres length. Eventually, can generate phreatomagmatic deposits, when an interaction between magma and water occurs (shallow submarine volcanism or littoral cones).

These eruptions, traditionally, are associated with a single batch and pulse of magma and are greatly influenced by local and regional stress fields. Other parameters that can be important in the evolution

of the activity, as in any other volcanic activity, are magma composition, volume, and rheological contrast beneath the surface.

Recent studies have revealed that, even in a monogenetic eruption, an internal geochemical evolution could be possible, mainly because of the multiple batches involved and the importance of the local stress controls in the migration and finally eruption of magma.

Complexity, derived from these internal and external conditions in combination with the depth where magmas are stored and transported, is reflected in the difficulty to anticipate and forecast these types of eruptions and their evolution, especially, for areas with long quiescent periods and a variety of magmas as in the Canary Islands, where a new volcano could come up in any location.

The reconstruction of the structure, geometry, composition and plumbing system conditions of pre-existed monogenetic eruptions on the Canary Islands along with the data obtained (petrological, seismological, geodetical, etc.) of an eruption in course such as the 2011 El Hierro eruption will help us obtain a significant progress in understanding the processes that take place, improve our knowledge on monogenetic eruptions and as a consequence enhance hazard assessment and reduce the risk to human lives.

# 1. INTRODUCTION

## 1.1 Thesis overview - Canary Islands, magmas and eruptions

A volcanic eruption is a natural phenomenon and such cannot be controlled, but its effects can be mitigated. Volcano activity can threaten or alter human lives and has a direct effect on properties and infrastructure.

Eruption of magma on the surface can be interpreted as the result of complex interactions between many internal and external parameters. Basaltic monogenetic volcanoes can be found in all tectonic settings (Connor and Conway, 2000), have a lifespan of months to years, can appear anytime without a specified pattern and can display different types of eruptions (Valentine and Perry, 2007). They are concentrated in volcanic fields (Valentine and Gregg, 2008; Kereszturi and Németh, 2012) and where the regional or tectonic settings have a major influence, rift zones can be observed, with several cones distributed along fissures oriented along tectonic lines. Cinder and scoria cones, as well as lava flows are the most common volcanic landforms in that type of activity, which can have a very broad variation in eruptive volumes, from few millions of cubic meters to cubic kilometres, although the final volume of magma erupting on the surface is usually a fraction of that which remains at depth.

The Canary Islands, as a volcanic archipelago active during the last 60 Ma, are a typical example of monogenetic basaltic activity concentrated in fields or rifts, displayed in all of their successive stages of evolution. In the last 500 years, this has been the predominant volcanic activity (Figure 1.1) and the most recent eruptions and their precursors have interfered in human activities and provoked losses of lives (Romero, 1991), something that is relevant for the present demographic distribution. As the population of the islands is constantly increasing with concomitant increases in infrastructure dependence, volcanic hazard assessment of such volcanic activity and its mitigation is necessary and it should not be underestimated.

A precise volcanic hazard assessment needs to answer certain questions such as the timing of the next eruption, what kind of volcanic activity will develop and of course where future vent(s) will be located. Almost all of the Canary Islands had volcanic activity during Holocene, with a wide range of products, from basalts to phonolites. As in the rest of world, where most of the efforts in forecasting volcanic eruption had been focused on large stratovolcanoes, a special attention has been paid to the Teide - Pico Viejo volcanic complex in Tenerife, as a result of the recent explosive history (Ablay, 1997; Martí

et al., 2008; García et al, 2014). However, all the historical eruptions throughout the islands (an average of an eruption almost every 30 years) were basaltic monogenetic eruptions, fissure type in many cases (Timanfaya, Lanzarote 1730-1736; Chahorra, Tenerife 1798; Duraznero, La Palma 1949, etc.) commencing with a moderate explosive phase that could include violent phreatomagmatic episodes. The hazard assessment from this type of eruption is mostly lacking. Under these circumstances, studying this type of volcanism is highly recommendable as it is the most recurrent and most probable style.

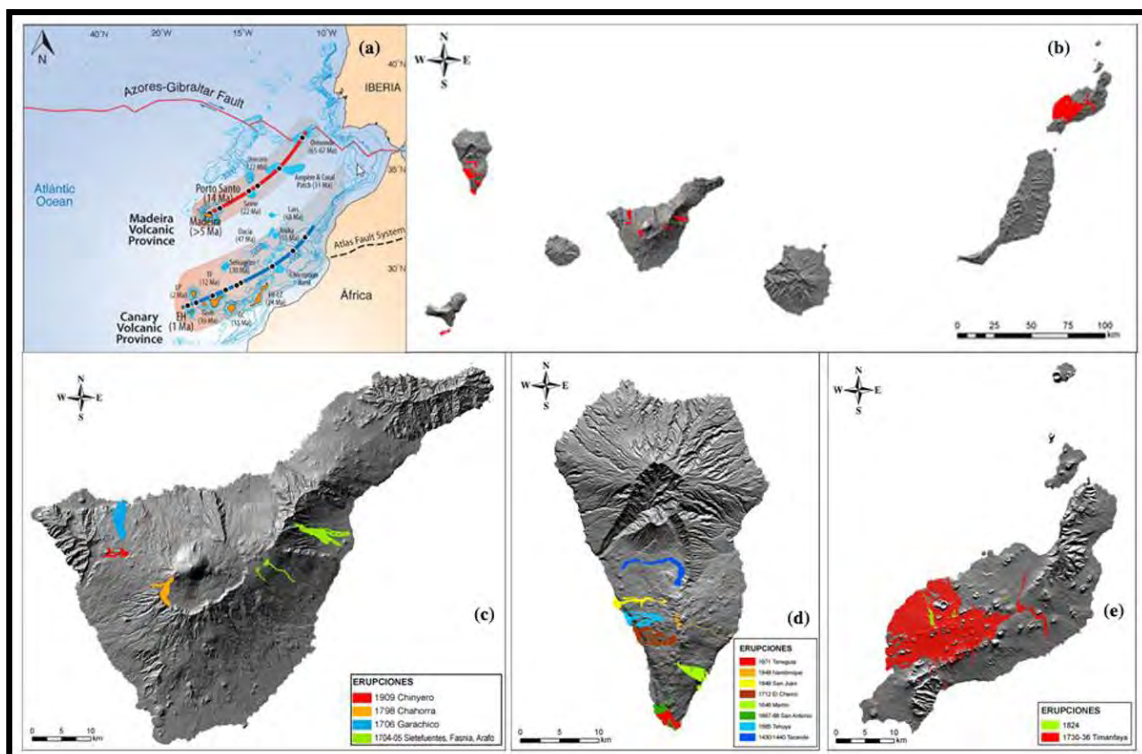


Figure 1.1. (a) The Canary Islands location by the African coast. (b) The historical eruptions on the islands. (c), (d), (e) DEM of the islands with historical eruptions before the 2011 El Hierro eruption.

El Hierro, the youngest island of the archipelago, represents an oceanic island in the early stage of shield development. The comprehensive study of the 2011 submarine eruption and its products in conjunction with that of an explosive felsic eruption in the centre of the island, reveals the complex magmatic processes that could take place even in a monogenetic eruption. For hazard assessment, as the 2011 El Hierro eruption was a submarine one, a similar type but sub-aerial historical eruption was

studied here, the Chinyero basaltic eruption in Tenerife, which shows two important aspects: a) Tenerife is the island where an unrest has been observed on 2004, associated with an intrusion of basaltic magma (Putkin et al., 2014; Cerdeña Dominguez et al., 2011; Martí et al., 2009) and b) it is the most populated island and the one where the historical eruptions mainly have caused lives to be lost and destruction of infrastructure and developed areas (Romero, 1991). The Chinyero eruption was a brief eruption compared to the 2011 one in El Hierro (10 days vs. almost 5 months) but its effects were felt all over the island.

Diverse type of information regarding magma processes and eruption mechanisms, spatial and temporal distribution and hazards of monogenetic volcanism were obtained from petrological data (passed eruptions or contemporary ones) but also from the data that a well-deployed monitor network could register (seismological, geodetical, etc.). Detailed knowledge of these parameters will permit identification of the crucial elements in order to improve a more precise and realistic assessment of potential eruptive hazards.

The aim of the present work is to reveal the conditions within which, the magmatic plumbing systems in monogenetic volcanism function, the way that internal processes are associated with the data collected by a volcano monitoring network, the eruption impact and hazard implications. To achieve the objective of this thesis I adopted an interdisciplinary approach, focused on aspects of monogenetic volcanism such as the relationship between pre-eruptive, syn-eruptive processes along with precursory signals and, magma composition associated - eruptive dynamics. These were realized through both field work and laboratory analyses.

In the frame of my PhD thesis I have been an author or co-author in at least nine scientific papers, of which five of them, will be included in the Appendix and discussed in this academic report, each of them triggering an in-depth study of the monogenetic basaltic volcanism, its processes, evolution and hazard assessment.

The methodology used in this work covered an extended area of modern and physical volcanology, including sampling of fresh volcanic products and also from recent and historical eruptions along with detailed stratigraphic sequences. Furthermore, laboratory analyses were undertaken, including grain size analyses by dry sieving techniques, textural and morphological analyses, petrography, electron microprobe and SEM, isotopic analyses and thermodynamic modelling. In the field of actual monitoring techniques, seismology, geodesy and gravimetry have been integrated with petrological data. Finally, in one of the papers, a detailed review of historical documents, witnesses and scientific reports has been done in order that an accurate reconstruction of the eruption and its dynamics could

be provided. This allows the special benefit of defining the correct hazard assessment and plan risk reduction strategies resulting from this type of volcanic eruption.

The investigation on El Hierro's eruptive dynamics began with the study of the emitted products during the 2011 submarine eruption. There are not many examples of submarine eruptions that have been observed, throughout the globe, with even less where sampling was possible, as their products are buried under subsequent deposits.

El Hierro is located on the southwestern-most edge of the Canary Islands and is the youngest and smallest island of the archipelago. The oldest subaerial rocks are dated at 1.12 Ma (Guillou et al., 1996). The island is the emergent summit of a volcanic shield that rises from a 3800–4000 m depth and grows up to 1500 m a.s.l.. Most of its subaerial part (280 km<sup>2</sup>) is covered by recent cinder cones, lapilli and lava flows. The truncated trihedral shape, revealing three convergent rifts, has been generated by at least three gigantic landslides that formed wide, horseshoe embayments (Masson, 1996; Masson et al., 2002; Gee et al., 2001). The construction of the island can be divided into three main volcanic phases or edifices (Figure 1.2) according the geochronological and paleomagnetic data (Guillou et al., 1996; Pérez-Torrado et al., 2011): 1) Tiñor volcano in the NE of 0.8–1.2 Ma 2) El Golfo edifice in the NW, 130–550 ka and 3) the rift volcanism with simultaneous activity on the three rifts of the island (NE-Rift, NW-Rift and S-Ridge) (Carracedo et al., 2001; Acosta et al., 2003).

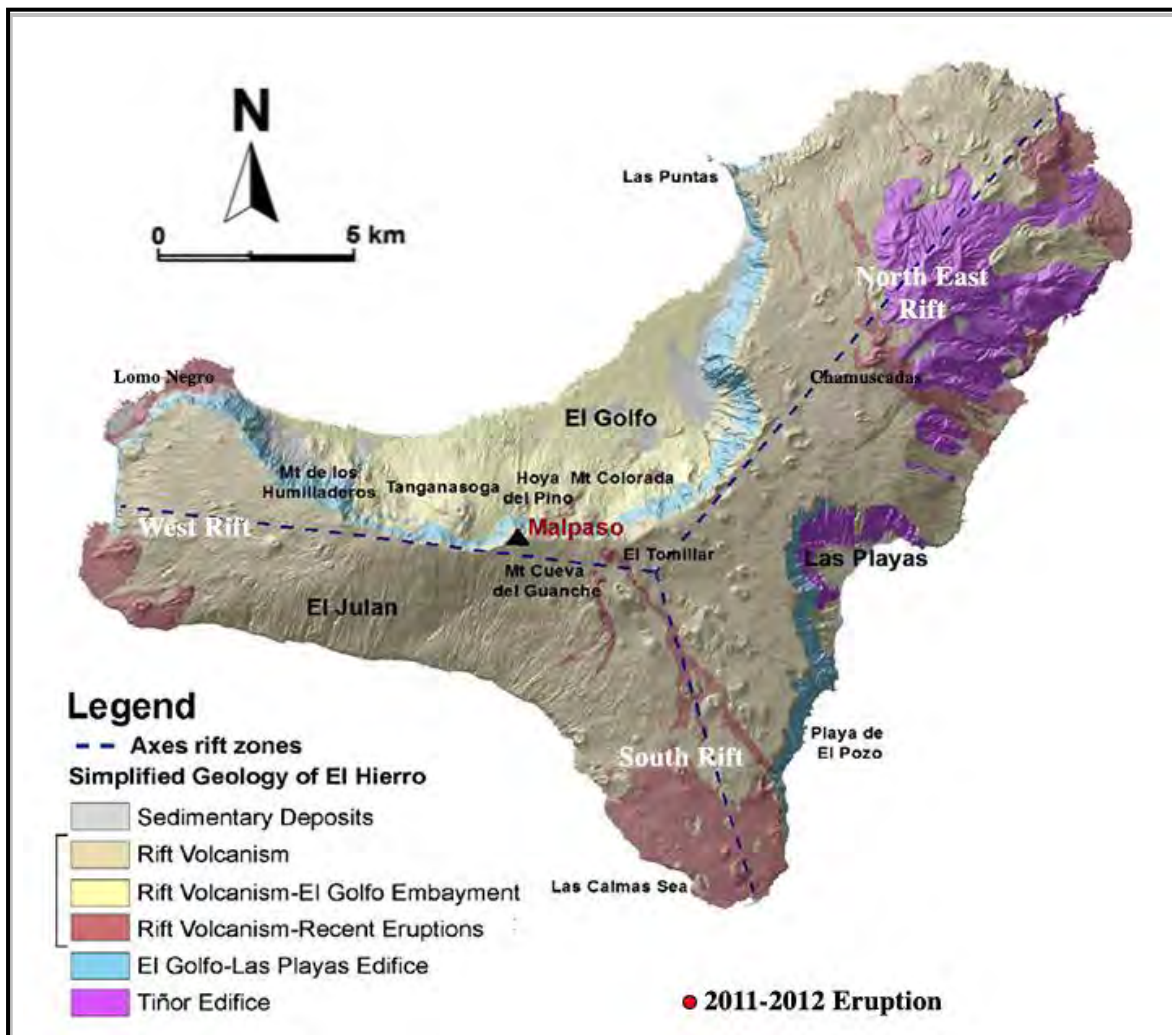


Figure 1.2. Simplified geological map of El Hierro Island with the main volcanic edifices of Tiñor and El Golfo-Las Playas along with the recent Rift Volcanism. Blue dashed lines represent axis rift zones. Red point indicates 2011 eruption vent (after Pedrazzi et al, 2014).

## 1.2 Products of a newborn volcano

The 2011 El Hierro eruption was preceded by 3 months of relatively low energy seismicity, a feature that had been observed in other pre-eruptive phases in Canary Islands such as Teneguía (Albert et al., 2015b; Klügel et al., 1997) accompanied by a surface deformation of at least 5 cm that indicated a magma intrusion (Okada and Yamamamoto, 1991). On 10 October 2011, the onset of volcanic tremor (López et al., 2012), coupled 2 days later with the appearance of a colored water plume in the sea, testified that an eruption had started at about 2.5 km south off the coast of the village of La Restinga from a vent initially located at 365 m depth. On 15 October, during a short but intensive degassing period, bi-colored, spindle-shaped ejecta ranging in size from 5 to 50 cm were observed floating and degassing on the surface. These rare pyroclastic bombs were only observed during the morning of 15 October 2011 (although small fragments <5 cm have been seen since the 12 Oct 2011).

These ejecta resemble a “coconut” and consist of an outer black to greenish, vesicular crust (1–2 cm in thickness with basanite bulk rock composition) and embedded grey to white colored, pumiceous xenoliths (trachytic to alkali rhyolitic bulk rock composition). These initial petrological analyses were accomplished by the Instituto Geográfico Nacional (IGN).

This was not the first time that such a peculiar mixing was observed during an eruption in the Canary Islands, as during a late phase in Teneguía eruption (La Palma Island) of 1971 a similar but not so extended phenomena was reported (Araña and Ibarrola, 1971). However the amount of the ejected material, size, violence and the uncertainty of the depth of the vent, have raised the doubt on the evolution of the eruption and the level of hazards that its products could generate as magma mixing and/or phreatomagmatic explosions could take place.

Concerning magma mixing and/or magma mingling, evidence has been reported in more than one island. In Tenerife, the 1100AD Montaña Reventada eruption, is one of the best known cases of magma mixing, where mafic and phonolitic magmas have erupted simultaneously, or at least in very rapid succession, resulting in a strombolian eruption with important lava flows (Wiesmaier et al., 2011, Albert et al., 2015). Also, petrological studies on the historical fissure eruption of 1949 on La Palma Island (San Juan eruption) reveal mixing of the mafic magma with evolved melts (Klügel et al., 2000) and as mentioned above, similar products have been collected during Teneguía eruption (1971).

Regarding hydrovolcanic processes, where magma and water interaction could lead to powerful explosions, it should be noted that these could occur at volcanoes of all sizes, and the violence would depend on the mixing ratio of water to basaltic melt (Wohletz and Sheridan, 1983). These complex dynamics of magma-water interaction trigger different eruptive phases and variable types of deposits

that represent a serious threat. In Canary Islands, assuming a purely effusive eruptive setting for the majority of monogenetic eruptions could result in considerable underestimation of the associated risks. The rapid evolution and changes within that type of eruption (Clarke et al., 2009; Pedrazzi et al., 2013) are in most cases unpredictable thus the study and analysis of hazard prediction, assessment, mitigation and vulnerability is one of the priorities. Examples of hydrovolcanic activity can be found on all the Canary Islands, and not only as littoral cones or submarine eruptions.

The first paper dealing with the products of the 2011 El Hierro eruption (*"Xenopumices from the 2011–2012 submarine eruption of El Hierro (Canary Islands, Spain): Constraints on the plumbing system and magma ascent, Meletlidis et al., 2012"*) consists of a thorough analysis of textures, petrography and geochemical compositions coupled with thermodynamic modelling. This results, in information about the interaction mechanism between the first rising magma and the crust during the onset of the eruption as well as information on magma storage and plumbing systems beneath El Hierro volcano.

Although initially these products were considered roughly homogenous (Troll et al., 2011) contemplating the two parts (inner light and porous material and outer, black and glassy material), in this work two different inner parts were distinguished (Figure 1.3), something that defines and characterizes the later methodological approach.

Morphological, micro-textural observations, micro-analysis of glass and mineral phases of the external crust and of xenopumices have been performed by means of optical microscope and scanning electron microscopy (SEM). Whole rock chemical composition for major and trace elements was determined from both the external crust and from the grey and white portions forming xenopumices. The concentration of thirty-nine geochemically relevant trace elements, from  ${}^7\text{Li}$  to  ${}^{238}\text{U}$ , was determined in the external crust and in the grey and white portions forming xenopumices using a Laser Ablation Inductively Coupled Plasma Mass Spectrometry (LA-ICP-MS). Vesicularity, bubble number densities and crystal content of selected samples were obtained by image analysis of SEM-backscatter images using ImageJ software.

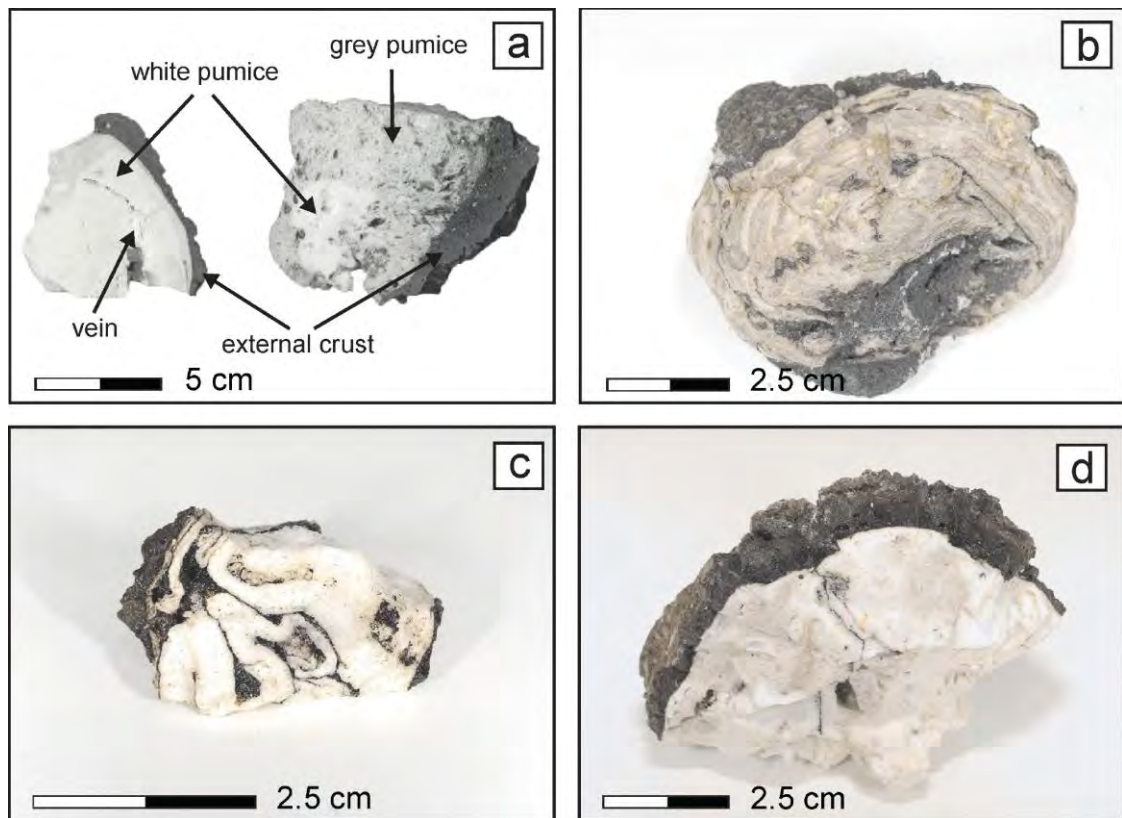


Figure 1.3. Images of products emitted on the morning of 15 October 2011 off El Hierro island coast. (a) Polished slide of grey and white xenopumices showing layering, folding and patchy mingling. (b) Intimate mingling between grey, white xenopumices and external basanite. (c) Folding in white xenopumices and mingling with basanite. (d) Sharp and abrupt contact between external crust and white xenopumice (after Meletlidis et al., 2012)

Such detailed analyses unveil, on one hand, the intimate compositional connection between the two types of the inner material and, on the other hand, the sharp and abrupt contact between external crust and porous material indicating different chemical compositions. Also, a common event of bubble nucleation was inferred by the similarity of vesicles size distribution (Figure 1.4).

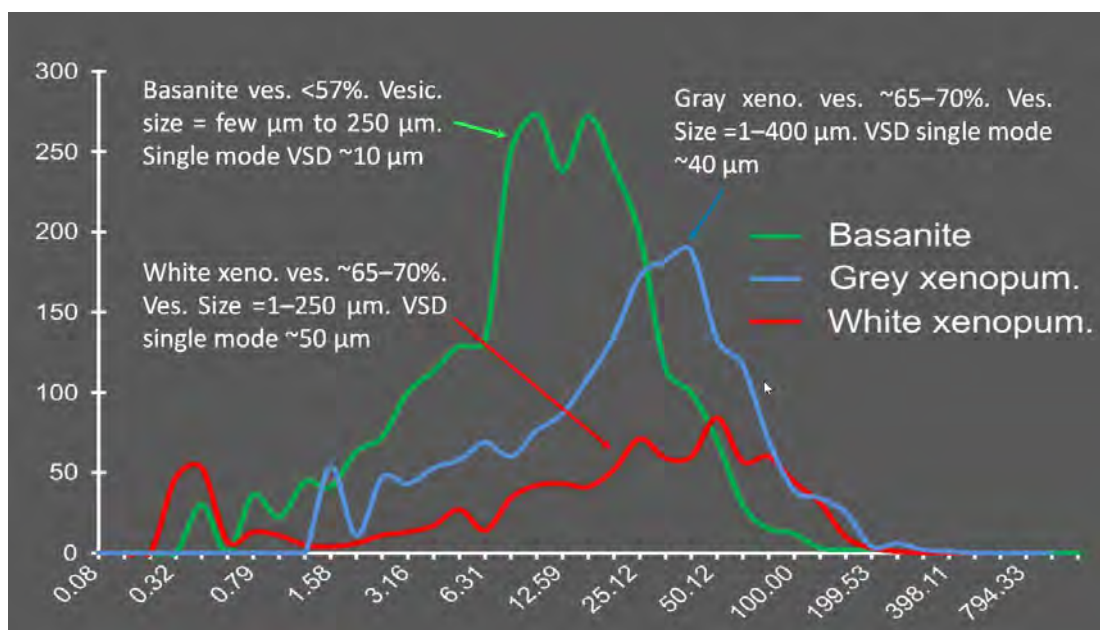


Figure 1.4. Vesicle size distribution. Basanite and xenopumices have an almost concurrent, single event of bubble nucleation and growth.

White xenopumices may have resulted from the total melting of an intensely altered volcanic rock, probably with a pristine trachytic composition, part of which could have undergone hydrothermal alteration processes in low temperature (<250 °C) and in presence of fluids (seawater and magmatic fluids).

As the objective was not only to define the composition of the products, but to characterize and identify internal processes along with transportation and stagnation conditions, the alphaMELTS software package (Ghiorso and Sack, 1995; Smith and Asimow, 2005) was used for the simulation of ascent and differentiation of magma. The software was used for both basanitic and grey xenopumice bulk rock starting compositions.

Paragenesis and mineral abundance observed in the basanite were reproduced through polybaric differentiation from 400 MPa to 30 MPa, from 1190 to 1100 °C of temperature (cooling rate of ~0.33 °C per MPa) and in redox conditions of FMQ -1. The differentiation within a magma reservoir has been reproduced simulating an isobaric cooling (T = 1200 to 1100 °C) at P of 400, 200 and 100 MPa.

Vice-versa crystal content and mineral composition, observed in the grey xenopumice, including the early crystallization of forsteritic olivine (Fo<sub>81</sub> at T = 1035 °C) and late appearance of phlogopite (T =

920 °C), can be modeled through an isobaric ( $P = 100$  MPa) crystallization of a trachytic melt that cools from 1035 to 900 °C under a  $fO_2$  conditions of NNO. On this basis, we consider that the paragenesis observed in investigated mafic and differentiated compositions reflects pre-eruptive equilibrium conditions (Figure 1.5).

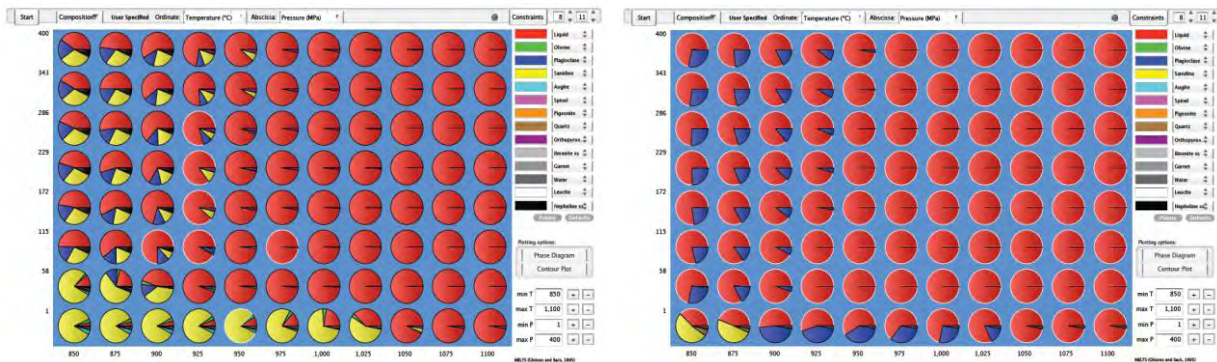


Figure 1.5. Trachyte and Rhyolite phase relationships. Calculated from Phase Plot derived from MELTS algorithm (Ghiorso and Sack, 1995).

In conclusion, all the data extracted from the above techniques, lead to a clear magmatic origin for the three types of products.

These findings confirm the importance of the study of the early products of an eruption since they can contain crucial information on the volcano structure and the mechanism of magma ascent. Regrettably, based only on petrologic data is impossible to constrain the size of the silicic stagnant melt. However, the fact that the emission of these products took place only during the first stage of the eruption suggests that its volume should be rather small compared to that of basanite.

### 1.3. An explosive felsic eruption on an oceanic island

The next paper, "*Explosive felsic volcanism on El Hierro (Canary islands)*", deals with the only recent felsic eruption known on El Hierro Island, which also, had a hydrovolcanic phase. An explosive felsic eruption is not a common feature for an island that, as pointed out previously, is still going through the early stages of its evolution (Carracedo et al., 2001) well marked from the rift volcanism that begun approximately 158 ka ago (Guillou et al., 1996). Understanding the evolution of an eruption, its processes and dynamics, should be seen as key to discussing and enhancing the hazard assessment. Stratigraphy is a critical part of the study, especially in volcanic fields, and provides essential data about the extension of the deposits, eruptive dynamics and deposition mechanisms.

There are few studies about the volcanic activity during Holocene on the island of El Hierro. Most of the eruptions form coastal platforms that are distributed on the extreme ends of the rifts or in the El Golfo depression, sometimes as cinder cones and other times as rootless lavas. The most recent sub-aerial eruption is a basaltic one, Montaña Chamuscada, that has been dated to 2500 +/- 70 years BP (Guillou et al., 1996) and it is located in the northeast sector of the island. As most of the events of that type of activity, that one also was a fissure eruption.

The studied eruption - Malpaso eruption - is situated almost in the centre of the island, on the rim of El Golfo depression, and the distribution of its products indicates that the vent position is now occupied by the Tanganasoga volcano. A relevant trachytic pumice deposit is discussed and detailed stratigraphic, lithological, and sedimentological study had been carried out. Although these deposits have been the target of earlier studies (Pellicer, 1975; Pellicer 1977) and radiometric ages have been achieved, ranging from 8.013 +/- 0.06 ka to 3.95 +/- 0.07 ka (Pellicer, 1975; Pellicer 1977; Pérez Torrado et al., 2011) they have been interpreted as the normal differentiation products of basaltic batches in this type of geodynamic setting (Carracedo et al., 2001).

As mentioned above, due to the 2011 submarine eruption and its emitted products during the open of the conduit, it was likely that a felsic eruption could occur at the early stages. Similarities of the composition of these products with the ones from the Malpaso deposit raise the necessity to carry out this work. So, even though such felsic eruption didn't occur, we could obtain useful data concerning the eruptive dynamics, and hazard assessment could be boosted for a scenario with these characteristics. The evidence that explosive episodes had occurred on the island recently, changes dramatically the perception of the volcanic hazard, not only for the island itself or the extended geography that could be affected, but also for the whole archipelago, as a large central volcanic complex should not be necessary to impose a regional hazard.

In order to trace stratigraphic units that were identified, several techniques were implemented, mainly based on their lithological and granulometrical characteristics. Initially, a detailed study of aerial photos was realized, just to ensure the possible extension of the deposit and identify the points of interest for the stratigraphic sections. A large-scale field map was followed so the broader geological framework would be recognized. At least 150 stratigraphic sections had been measured and sampled with the aim to determine the geometry of the deposit, thickness of the units and obtain clast sizes so isopach and isopleth maps could be drawn; also, volumetric data was obtained.

Morphological, micro-textural observations and microanalysis of juvenile components have been performed by means of optical microscope and scanning electron microscopy (SEM). Furthermore, laboratory analyses were undertaken, including grain size analyses by dry sieving techniques, textural and morphological analyses using ImageJ software.

A sequence of pyroclastic units characterizes the studied deposit, which overlies previous erupted scoria lapilli and lavas, and lies beneath deposits and lava flows emitted by Tanganasoga volcano or nearby vents, extended to nearly 13 km<sup>2</sup> with an estimated volume of 1.8 x 10<sup>6</sup> m<sup>3</sup> (Bonadonna and Costa, 2013). A significant interruption of the volcanic activity is evident, as well-developed paleosols have been developed at the base and top of the sequence.

Four units have been recognized (Figure 1.6), each of them representing a different phase of the eruption. In short, the characteristics of each unit could be summarized as follows:

Unit N1: up to 21 cm thick, it's the base unit, directly placed over the Holocene paleosol (Pellicer, 1975; Pérez Torrado et al., 2011) showing light erosion at its base due to the interaction with the underlying topography. This is mainly composed of thin beds of well-sorted clast-supported grey pumice alternating with matrix-supported fine lapilli/fine ash beds. In this unit two sub-units have been identified (N1a and N1b) having as a main difference the size of the pumices (<1 cm and up to 10 cm respectively) although the further these are observed from the vent less distinction can be established between them. Lithics are present in almost all grain size fractions and the amount of juvenile fragments (pumices and free crystals) ranges between 60-75 wt.%.

Unit N2: is a finer-grained unit than unit N1, with a maximum thickness of 20 cm, made of ~70 wt.% of juvenile fragments. Poorly stratified thin matrix-supported ash beds can be distinguished, intercalated by very thin beds (<5 mm thick) of lapilli-rich poorly vesiculated pumices and identical size lithic clasts. A further discrimination in four sub-levels is possible, using criteria such as ash lamina; notably, nearby the hypothetical emission point.

Unit N3: can be found in the area around Malpaso peak and reaches a maximum thickness of 25 cm, integrated by stratified ash beds, showing, in its lower part, an intercalation with minor fine-grained lapilli. It is significantly different in terms of sorting and overall finer grained samples and lava lithics are also observed. The juvenile content increases upwards with free crystals making up 25 wt.% of this population. As per unit N2, four more sub-levels have been identified, using the lithic percentages and textural aspects, in the proximal outcrops.

Unit N4: a set of laminated ash and lithic-rich lapilli beds compose this unit, with a characteristic grey colour because of the abundance of lithic fragments of old lavas (total values of 55–60 wt.% in almost all of the range in grain sizes have been observed), its thickness can reach approximately 20 cm. Both normal and reverse grading is observed with coarse and fine-grained stratifications.

Texture variation in the juvenile components throughout the units was not accompanied by a compositional variation and we could assign a trachiphonolitic composition to the whole Malpaso member.

The fact that an explosive eruption occurs within an environment in which effusive basaltic activity predominates, shows that the monogenetic basaltic magmatism is capable to develop complex scenarios such as this. Moreover, it raises the question about the likelihood of a large volume intrusion that, due to its differentiation could produce more than one eruptable felsic batch. The uncertainty of the spatial distribution of future vents (Becerril et al., 2013), the moderate occurrence of hydrovolcanic activity (not just littoral cones) on the island (Becerril 2009; Carracedo et al. 2001) and the complex magmatic emplacement beneath the island (Stroncik et al. 2009; Klügel et al. 2000; Meletlidis et al. 2015), lead to a growing need that both long and short-term hazard assessment for any island of the archipelago should take in account both basaltic and felsic eruptions and their associated hazards. Also, a recent study on monogenetic volcanism (Martí et al., 2017) reveals that basaltic ignimbrites can be generated from such activity, increasing further the derived hazards.

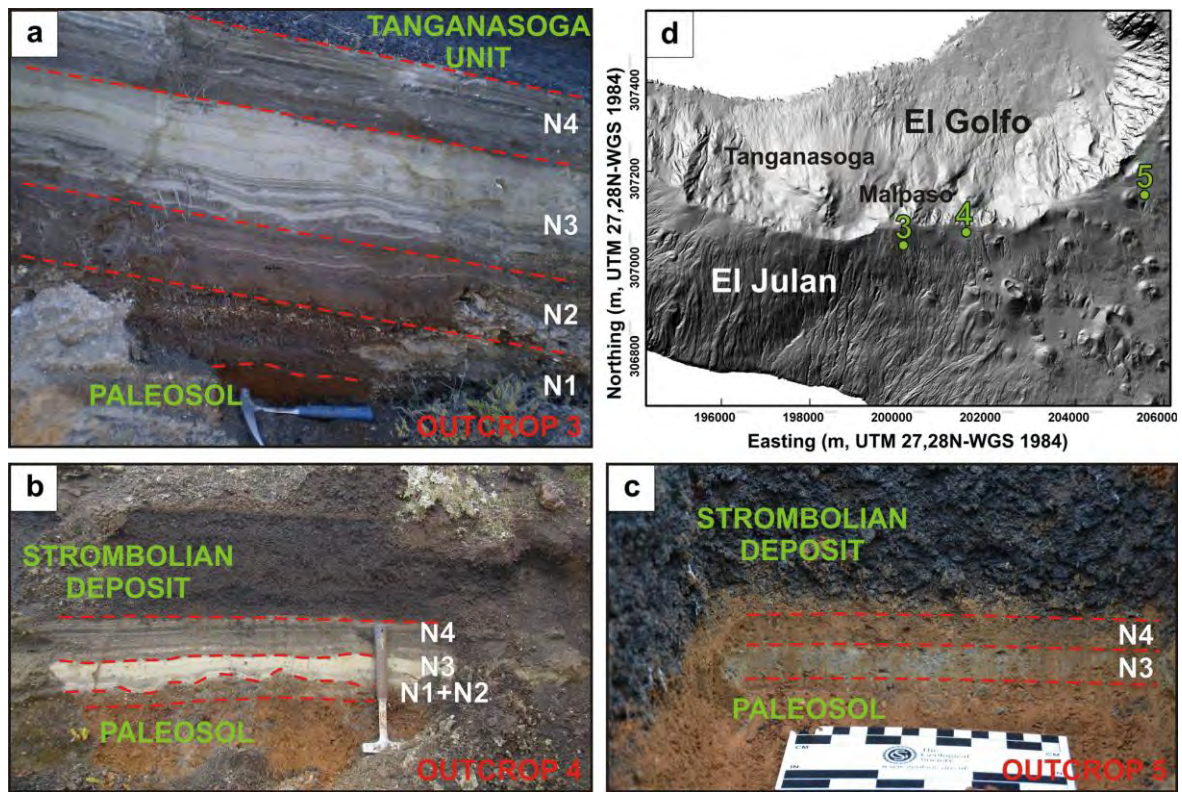


Figure 1.6. Malpaso Member deposits: (a) proximal, (b) medial and (c) distal outcrops. At the right top (d), locations of the photographed outcrops are presented (after Pedrazzi et al., 2014)

#### 1.4. Clarifying the dubious origin of the xenopumices

As the controversy generated on the origin of the xenopumices ejected in the 2011 eruption was still alive while the study on the subaerial trachytic deposit was concluded, the third work, *"Xenopumice erupted on 15 October 2011 offshore of El Hierro (Canary Islands): a subvolcanic snapshot of magmatic, hydrothermal and pyrometamorphic processes"*, was focused on the study of the xenopumices, this time in the context of both the pumice of Malpaso deposit and broader literature dataset of Canary Islands igneous and sedimentary rocks.

A lot of papers have been published, regarding the origin of xenopumices. They were suggested as xenoliths originated from the sedimentary deposits of the pre-island oceanic crust, melted and transported by the ascending basanitic magma (Troll et al., 2012), as products of the interaction between the ascending basanitic magma with a pocket of shallow trachytic magma (Meletlidis et al., 2012), as products of the remobilization of a small, differentiated felsic magma body, slightly contaminated with quartz-rich sediments, by the ascending basanitic magma (Sigmarsson et al., 2013) and finally a sedimentary origin was assigned while acknowledging a hydrothermal contribution (Rodríguez-Losada et al., 2014).

In order to better understand the formation of xenopumice, mineralogical, comprehensive SEM investigation and Sr-Nd-Pb isotope analyses on some samples representative of three different xenopumice facies was carried. This approach facilitates an enhance understanding of the possible magmatic, hydrothermal, and pyrometamorphic processes, which usually operate in the plumbing systems of active volcanoes.

Identifying the source and mechanisms of genesis of this peculiar material is of unquestionable relevance, not only for clarifying magmas internal processes and any transient processes at the magma-wall rock interface, but also in mastering of hazard assessment on volcanic islands.

Briefly, the techniques used to provide new isotopic data, textural, mineral chemistry, and glass analyses, polished thin sections from different parts (in terms of physical features) of eight investigated xenopumice samples and two subaerial Holocene trachyte pumices (Malpaso deposit). Sample texture and major element compositions of glass and mineral phases were investigated by scanning electron microscopy (SEM), whole-rock compositions for major and trace elements were determined and Sr, Nd, and Pb isotope analyses were performed using a multicollector mass-spectrometer.

In the 2011 eruption products, was possible to recognize three main facies: white, vein, and grey, which differ in terms of composition, mineralogy, and texture.

The white parts of the xenopumice are almost completely glassy and highly vesicular (56–70 vol.%). Glass composition is rather heterogeneous, with  $\text{SiO}_2$ ,  $\text{Al}_2\text{O}_3$ ,  $\text{Na}_2\text{O}$ ,  $\text{K}_2\text{O}$  and minor amounts of  $\text{CaO}$ ,  $\text{MgO}$ , and  $\text{FeO}$ . Rare restitic phases are observed, including partially dissolved plagioclase, zircon, biotite, apatite, and quartz which is the most abundant phase (although <1 vol.%). Its crystals, partially melted, are characterized by abundant fluid inclusions.

Vein facies, with size up to 4 mm, found in some of the samples, mainly cutting through the white facies. Their material, milky white colored, show no apparent vesiculation – although elongated trains of vesicles a few microns across, running approximately parallel to the vein edges can found - and consists of microcrystalline zircon (~25 vol.%), quartz (<5 vol.%), REE-oxides (<1 vol.%), and rare rutile.

Considering the grey facies, they can only be identified from the white one, because of small differences in vesicularity (65–70 vol.% for this facies), glass chemistry (lower in  $\text{SiO}_2$ , 56–71 wt.%) and the presence (in the grey facies) of both restitic and newly formed mineral aggregates (Figure 1.7). Seems that the grey facies is volumetrically less abundant relative to the white facies and approximately represents less than 20 vol.% of the xenopumice. They present abundance of partially melted restitic anorthoclase. Anorthoclase fragments generally preserve anorthoclase composition at the core and have sanidine rims . Glass composition close to the fringed rim of the crystals is almost indistinguishable from that of sanidine. Another feature of the grey facies is the presence of mineral aggregates that resemble pseudomorphs after pre-existing minerals.

In the Malpaso pumices, a ~25 vol.% of phenocrysts, in a hyalopilitic groundmass, has been observed. Feldspar is the main phenocryst phase, crystals show zonation, and range in composition from anorthoclase to andesine. Amphibole is the main mafic phase.

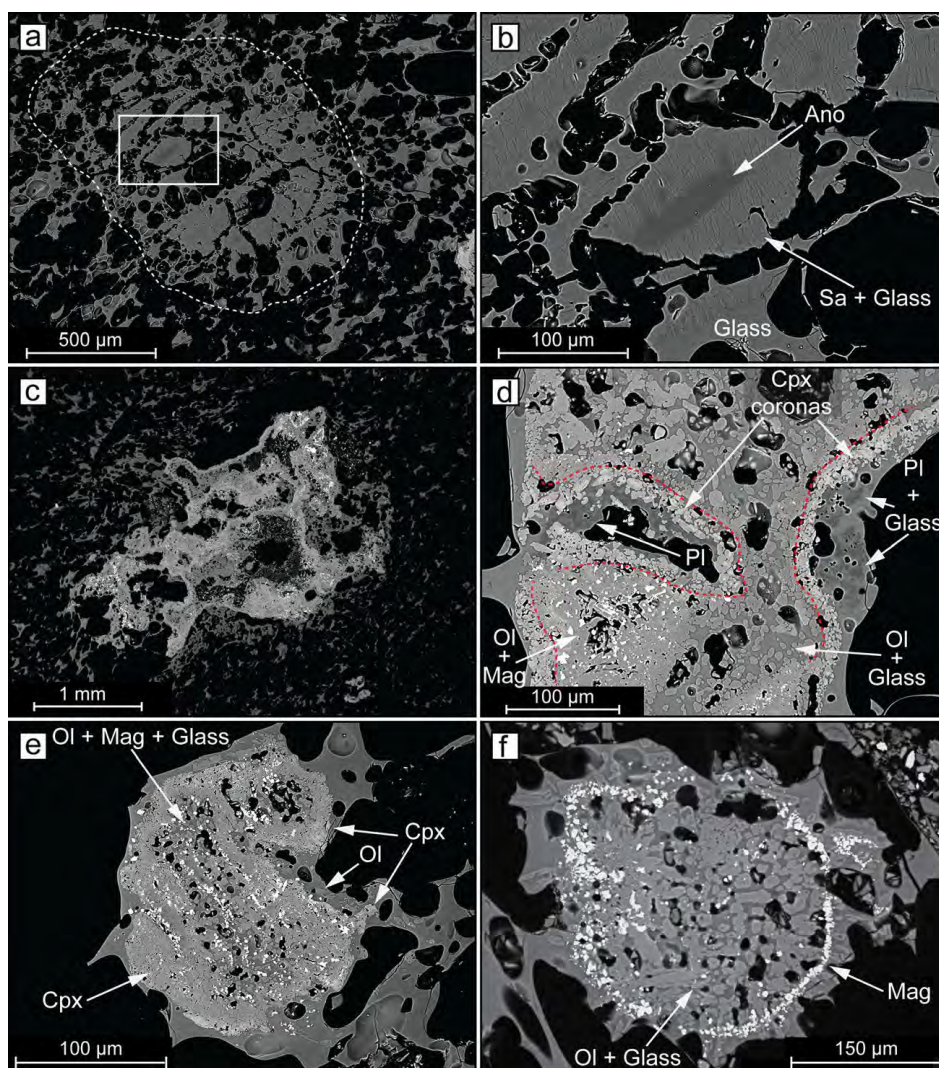


Figure 1.7. SEM-BSE images of the xenopumice grey facies. (a) Broken line contour contains a jigsaw-fit restitic feldspar with the inset. (b) Showing restitic anorthoclase (Ano) composition at the core of a partially melted crystal fragment having sanidine (Sa) composition. (c) Mineral+glass aggregate. (d) Detail of an aggregate showing clinopyroxene (Cpx) coronas formed by zoned crystals, around partially melted plagioclase (Pl) and olivine (Ol) associated with glass and magnetite (Mag). (e) Pseudomorph of olivine+ magnetite+glass surrounded by clinopyroxene after pre-existing primary mafic phase (possibly amphibole or clinopyroxene). (f) Pseudomorph of magnetite+ olivine+glass (possibly after amphibole); (after Del Moro et al., 2015).

Regarding the bulk rock geochemistry, the white facies can be classified as a trachyte ( $\text{SiO}_2=66.3$  wt.%;  $\text{Al}_2\text{O}_3=18.6$  wt.%; alkalis=8.4 wt.%) and the grey facies is less “evolved” than the white facies

(SiO<sub>2</sub>=62.3 wt.%; Al<sub>2</sub>O<sub>3</sub>=16.8 wt.%; alkalis=12.4 wt.%) and closely matches the compositions of the most evolved trachyte rocks and glasses of El Hierro.

Sr isotope ratios of the xenopumices are <sup>87</sup>Sr/<sup>86</sup>Sr ~0.70643 and ~0.71013 for the white and grey facies, respectively. By contrast, <sup>143</sup>Nd/<sup>144</sup>Nd ratios of xenopumice samples appear rather homogeneous. Finally, only <sup>206</sup>Pb/<sup>204</sup>Pb ratio is variable and the other two ratios, <sup>207</sup>Pb/<sup>204</sup>Pb and <sup>208</sup>Pb/<sup>204</sup>Pb, are close to be homogenous, between white and grey facies. Compared with the xenopumice, Holocene trachyte shows a lower <sup>87</sup>Sr/<sup>86</sup>Sr value and a similar <sup>143</sup>Nd/<sup>144</sup>Nd ratio. The <sup>206</sup>Pb/<sup>204</sup>Pb, <sup>207</sup>Pb/<sup>204</sup>Pb and <sup>208</sup>Pb/<sup>204</sup>Pb ratios are slightly lower with respect to xenopumice ratios (Table 1.1).

Radiogenic isotope ratios	El Hierro xenopumices		El Hierro trachyte	
	Literature data	This work		
	Sigmarsson et al. (2013)	White facies	Grey facies	Trac 2
<sup>87</sup> Sr/ <sup>86</sup> Sr		0.706426±6	0.710134±6	0.703029±6
<sup>143</sup> Nd/ <sup>144</sup> Nd	0.512931±8	0.512978±7	0.512905±8	0.512948±8
<sup>206</sup> Pb/ <sup>204</sup> Pb		21.6875±9	20.0511±40	19.4510±40
<sup>207</sup> Pb/ <sup>204</sup> Pb		15.7092±6	15.6778±31	15.5787±10
<sup>208</sup> Pb/ <sup>204</sup> Pb		39.7738±16	39.7877±80	39.0962±31

Table 1.1. Isotope ratio analyses performed on white and grey xenopumice facies and on the El Hierro subaerial trachyte, compared with Nd isotopic ratio of xenopumice analyzed by Sigmarsson et al. (2013). In-run errors are shown for isotope ratio (after Del Moro et al., 2015)

The presence of restitic magmatic phases as well as crystallization of minerals as pseudomorphs after pre-existing mafic phenocrysts, providing evidence of pyrometamorphism induced by the high-T juvenile basanitic magma. These processes are easily recognizable when dealing directly with hydrothermally altered volcanic samples, but they can be very hard to identify when obliterated by pyrometamorphism (Grapes, 2006; Del Moro et al. 2011).

It is evident that a comprehensive study of the products of any eruption can provide us with the hints about the processes taking place beneath the volcanoes. Furthermore, comparing the data obtained through these studies with pre-existing products can also help us understand better the evolution of them, an important aspect to contemplate when hazard assessment is considered.

## 1.5. Modelling through instrumental data and erupted products

The 2011 eruption on El Hierro island was the first to be monitored in the Spanish territory, not only since the very beginning of the seismic unrest but in its whole evolution (López et al., 2012). In many cases, and most of the submarine eruptions around the globe, lack of information is evident, not only about the emitted products but also regarding the geophysical, geodetical and geochemical data. These data are crucial, firstly, for the real time monitoring of the eruptions evolution, as can give us essential information concerning the different eruptive episodes and secondly, can help the decision-making authorities estimate the hazard conditions and provide a real world hazard assessment and an effective crisis management (Fonseca et al., 2003). In recent years, more and more studies have focused on associating the emitted products with instrumental data acquired through the monitoring network, during all the stages of an unrest period or the phases of an eruption, in order to gain details about the inner processes, modelling them and surpassing the uncertainties derived from incomplete scientific knowledge (Surono et al., 2012).

In the case of El Hierro eruption, complete geophysical and geodetical time series were registered, thanks to the IGNs monitor network. This fact allows, a multidisciplinary approach to the eruptions conditions and evolution and permits, a more comprehensive view of the dynamics of magma ascent.

The fourth paper, *"New insight into the 2011-2012 unrest and eruption of El Hierro Island (Canary Islands) based on integrated geophysical, geodetical and petrological data"*, is a result of conjunction of the available petrological data and those registered from the existing monitor network, along with thermodynamically modelling of magma differentiation. It aims to deliver a better understanding of the eruptive sequence, determine any relation between compositional changes and instrumental data registered, establish certain patterns in monogenetic volcanic activity and finally achieve awareness raising in the field of hazard assessment for the Canary Islands and monogenetic activity generally.

In mid-July 2011, anomalous seismicity started to be registered in the existed seismic stations of IGN, with hypocenters preliminarily located in the area of El Golfo and at depths of 8-12 km. In the following two months, the seismic activity suffered minor migration and was accompanied by ground deformation, diffuse emission of CO<sub>2</sub>, anomalous values of the magnetic field and <sup>222</sup>Rn and H<sub>2</sub>S efflux (López et al. 2012; Pérez et al. 2012). In the last days of September seismicity clearly migrated to the south, increasing its magnitude and finally the eruption started on October 10, 2011, about ~2 km from the south coast of the island announced by the appearance of a plume of stained and discoloured water.

During the pre-eruption phase at least 10,000 seismic events were localized and a maximum vertical deformation of up to 6 cm was observed (Figure 1.8). Repeated multibeam surveys revealed that the initial opening occurred in a gully aligned in a NE-SW direction, almost perpendicular to the South Rifts extension and at water depths between ~363 and 89 m, with several vents that functioned simultaneously and a repeated cycle of collapse and subsequent regrowth of the edifice with a total accumulated volume in the order of  $329 \times 10^6$  NDRE  $m^3$  (Rivera et al. 2013).

First massive emission of volcanic materials (Figure 1.9) occurred on October 15, 2011. These products have been studied, as explained above, and a trachytic to rhyolitic composition was determined (Troll et al. 2011; Meletlidis et al. 2012; Sigmarsson et al. 2012; Del Moro et al. 2015).

Since 31st of October and for the next four months, lava balloons (Figure 1.9) were observed while floating and degassing on the sea surface, with sizes between 30 and 200 cm. These products, that have been studied in the actual paper, consisted of an internal gas-filled cavity surrounded by a few centimetres-thick crust of quenched vesicular lava.

Finally, the eruption was officially declared ended on March 5, 2012, with the top of the new submarine cone reaching the depth of 89 m b.s.l. (Rivera et al., 2013).

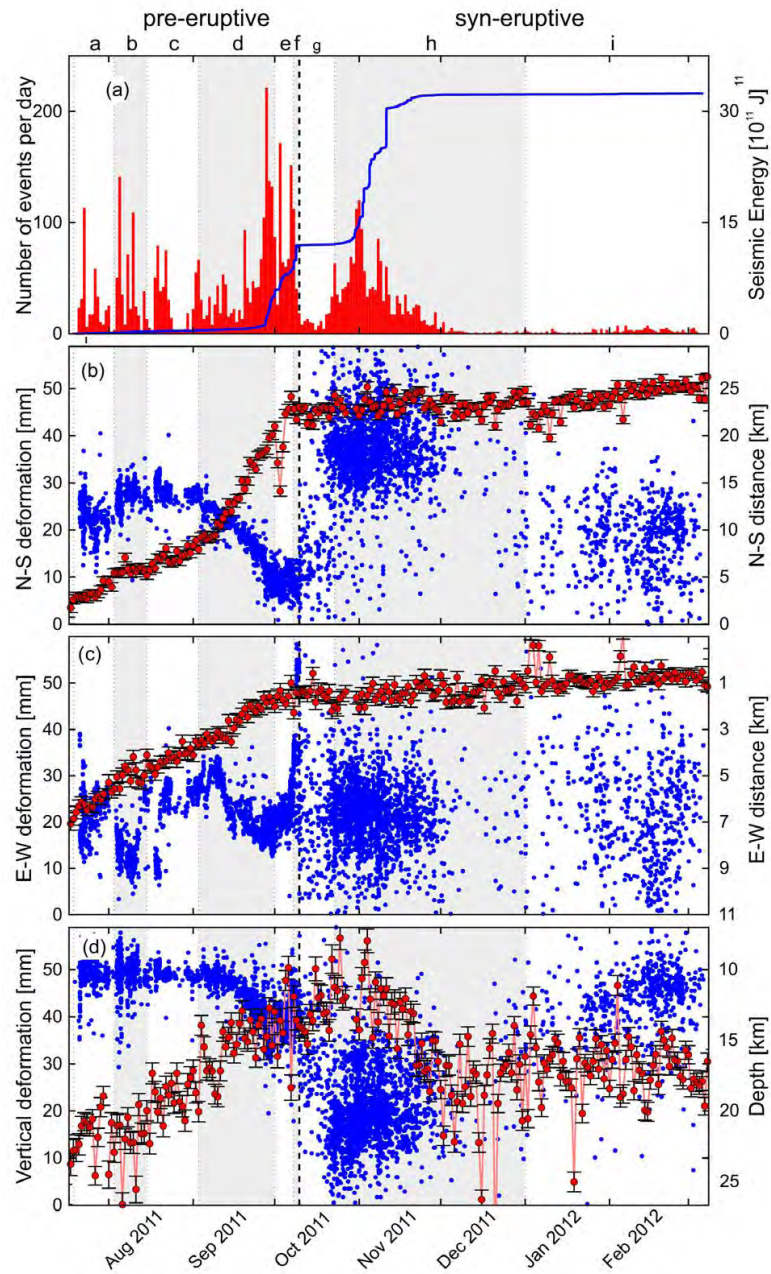


Figure 1.8. (a) Temporal evolution of the daily number of earthquakes with magnitude  $>1.5$  (red histograms) and the accumulated seismic energy curve (blue line). (b-d) Blue dots: temporal evolution of the (b) North-South and (c) East-West distances (km) to the vent and of the (d) depth (km) of the earthquakes after relocation of Domínguez Cerdeña et al. [2014]; red dots (with the axis error) N-S, E-W and vertical components of ground deformation recorded at GPS station FRON (the only station that was active since the very onset of the unrest) during the pre-eruptive and syn-eruptive phases of the 2011-2012 El Hierro eruption. Black dashed line indicates the onset of the eruption. Shaded and white alternating areas indicate the nine phases in which authors divided the pre-eruptive unrest and eruptive activity (after Meletlidis et al., 2015).

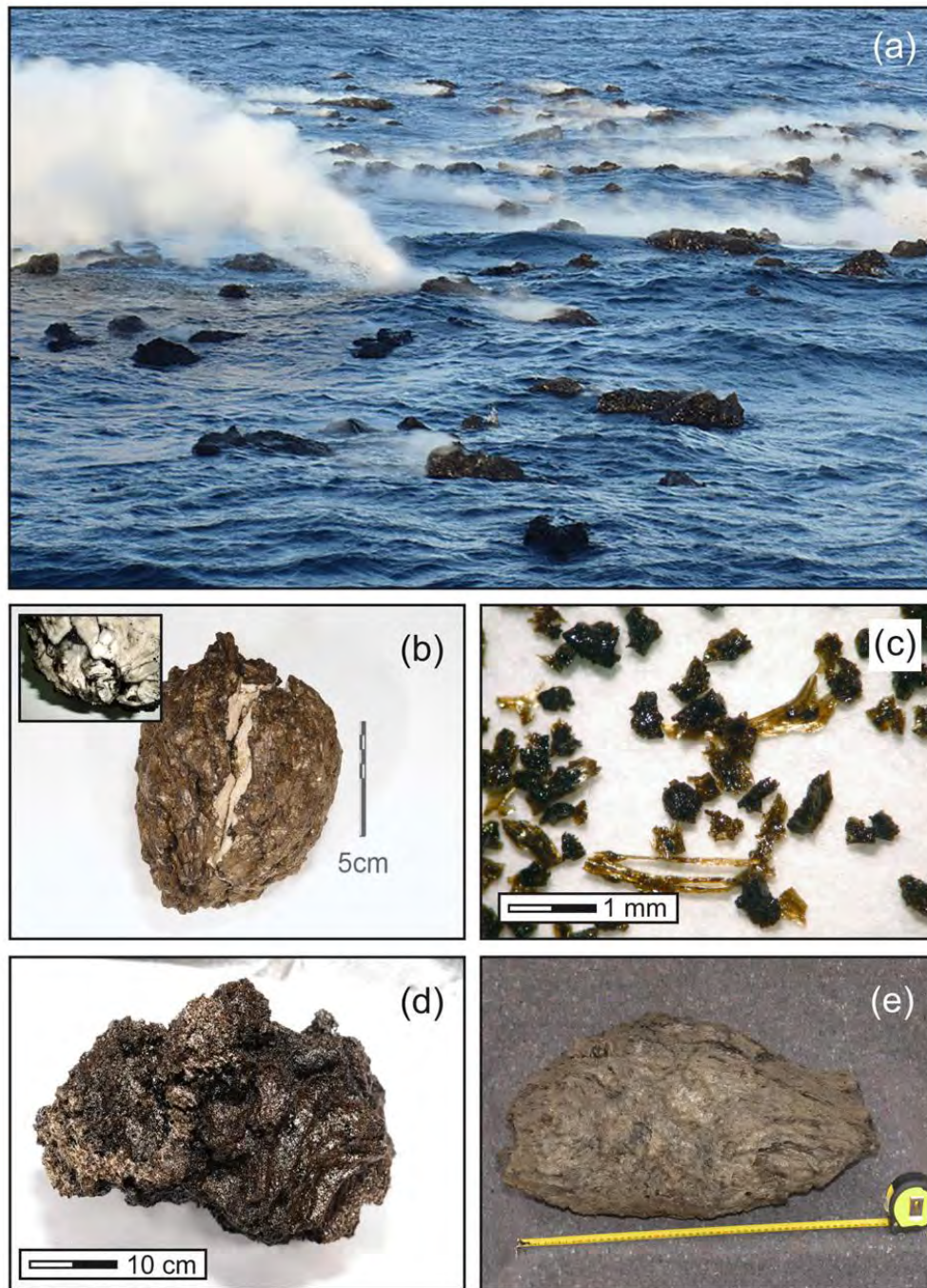


Figure 1.9. Images of volcanic products emitted during the 2011-2012 eruption. (a) Hot scoriaceous blocks and “lava balloons” floating on the sea surface during the eruption. (b) “coconut-like” Bomb consisting of an outer basanite crust embedding a pumiceous xenolith [Troll et al. 2011, Meletlidis et al. 2012, Sigmarsson et al. 2012, Del Moro et al. 2015]. (c) Example of the juvenile ash and fine lapilli sampled in water column on November 5, 2011, and February 12, 2012. (d) Floating lava block erupted during the first days of the eruption. (e) Elliptical-shaped “lava balloon”; (after Meletlidis et al., 2015).

As previously mentioned, in this work, a multidisciplinary approach was performed, and thus, various techniques and methods were applied.

With regard to seismology, in first place, the dataset used in this work includes the 3600 pre-eruptive events with magnitude greater than 1,5 relocated (Domínguez Cerdeña et al., 2014) by means of hypoDD algorithm (Waldhauser and Ellsworth 2000). This method allowed more high-resolution hypocentral relocation and ensured a higher quality of the results in relation to previous published researches. Also the IGN seismic catalogue was used for the activity that took place during the eruption. At least, data of 9 seismological stations were used (Figure 1.10).

Practically, data of 14 GPS stations were used, obtaining daily coordinates through a 30s sampling rate and Bernese software version 5.0 processed (Dach et al., 2007). The ocean-loading model FES2004 was applied and precise satellite orbits from the IGS were also used (Kouba 2009). For the source model, a spherical point source of varying pressure within an elastic, isotropic and homogeneous half-space was applied (Mogi., 1958).

The gravity data, originally recorded at 1Hz sampling rate, was derived from a Micro-g LaCoste gphone that was deployed on the island since August 2011 (Sainz-Maza Aparicio et al., 2014), at the beginning of the crisis in El Golfo area, but due to the seismicity migration it was moved to the centre of the island some days before the onset of the eruption.

The petrological part of the paper comprised a detailed textural, petrographical and geochemical (bulk rock, groundmass glass and mineral phases composition) analysis on 15 samples collected during almost the entire duration of the eruption, comprising 3 floating scoriaceous fragments, 9 lava balloons and 3 samples of ash and lapilli. Textures from thin sections were studied using optical microscope and SEM, also composition of mineral phases. Chemical major element composition of glass was analyzed using microprobe. Along with that, the chemical composition of bulk rocks was determined.

From the instrumental data analysis as a whole, six pre-eruptive and three syn-eruptive phases were distinguished. Most of the time, seismic activity was taking place almost all over the island but, certain patterns were identified. GPS was used not only to characterize the intrusion but also to estimate the volume and emplacement of the intrusion in each of these phases.

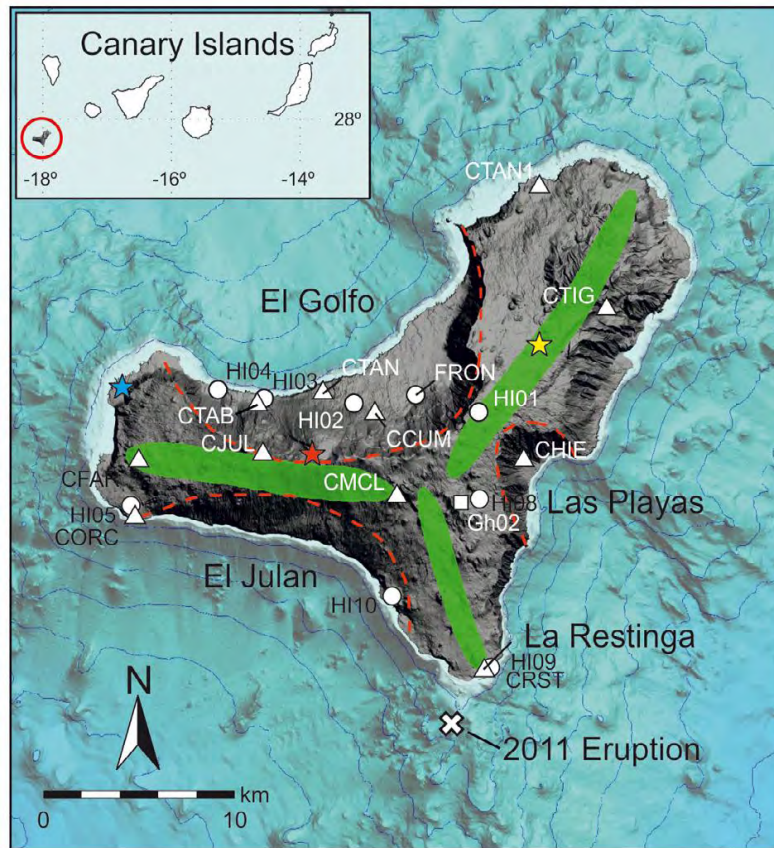


Figure 1.10. Map of El Hierro Island with highlighted the main morphological features. Green shaded zones: rift lines. Red dashed lines: landslides scars. Stars indicate the most recent eruptions on the island; yellow star: Las Chamuscadas, red star: Tanganasoga and blue star: Lomo Negro. White cross: location of the vent of the 2011-2012 eruption. In map are also highlighted the position of instruments of multiparametric monitoring network that was deployed on the island by Instituto Geográfico Nacional: triangles - Seismic stations; circles - permanent GPS stations; squares - permanent gravimetric station (after Meletlidis et al., 2015)

The petrological analysis revealed that all samples are porphyritic rocks, with gradually increase in phenocrystals, reaching from 5% up to 20%, mainly clinopyroxene (most abundant), olivine and spinel. Groundmass shows the same mineral assemblage. All studied samples exhibit a zoned texture, minus the products emitted on October 15, and have a basanite major element bulk rock composition, with SiO<sub>2</sub> ranging between 42.2 and 44.2 wt. % and alkali content ranging between 5.13 and 6.07 wt. %.

Ratios between highly incompatible trace elements (e.g. Rb/Ba, Rb/Th and Rb/La) are quite constant with the exception of the sample of October 15. On the contrary, composition of glass is almost

homogeneous during the entire eruption and its ratio between highly incompatible elements (e.g. Rb/Nb) remains constant (Figure 1.11).

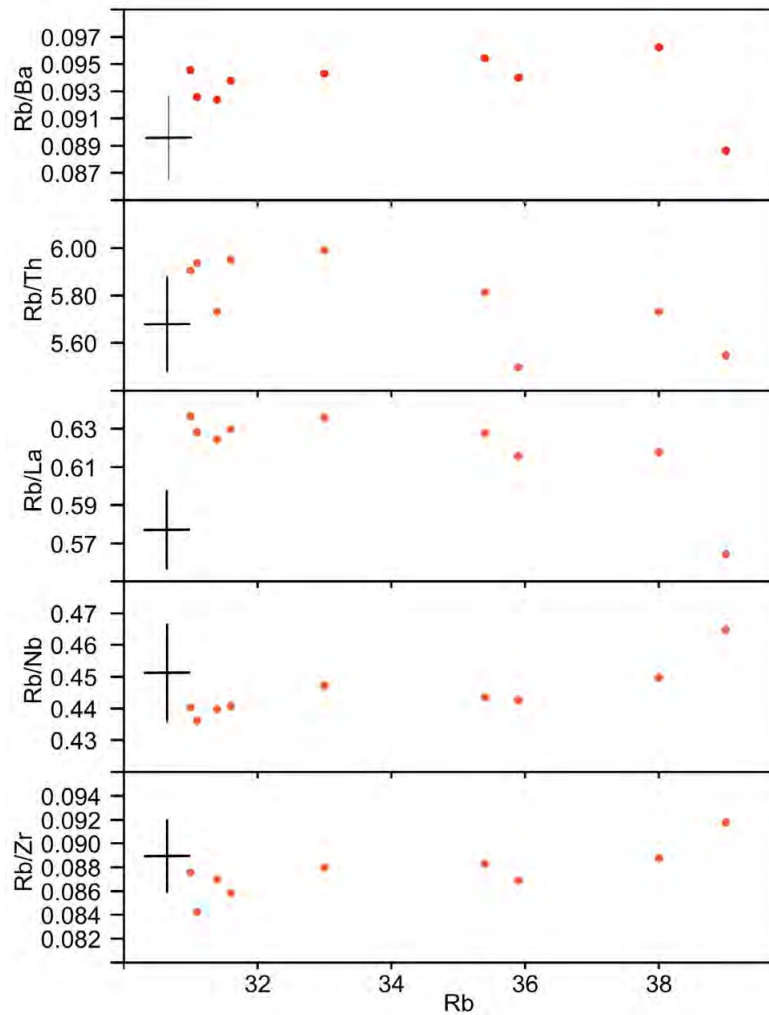


Figure 1.11. Variation diagrams (unit in ppm) for bulk rock Rb/Ba, Rb/Th, Rb/La, Rb/Nb and Rb/Zr ratio versus Rb during the 2011- 12 El Hierro eruption. Error bars (black crosses) represent 1 sigma (after Meletlidis et al., 2015).

Due to variations in bulk rocks composition accompanied by variability in crystal content and significant zoning in crystals (signs of complex magmatic processes), thermodynamic modelling techniques (Ghiorso and Sack, 1995) have been employed. Simulations of cooling and crystallization of mantle derived melts, with a similar composition of the first products, have been implemented for different settings, taking on account the data of the instrumental network. So, cooling and

crystallization of mantle derived melts respectively in a deep magmatic reservoir at mantle pressure of 700 MPa (corresponding to a seismic source at 20-25 km) and in a crustal storage zone at pressure of 350 MPa (corresponding to a seismic source at 8-12 km) were simulated. Also, a final cooling at pressure of 1 MPa corresponding to water column of about 100 m has been also modelled.

The Amoeba routine of AlphaMELTS (Smith and Asimov, 2005) was used to simulate changes in pressure and crystal fractionation processes so an approximation to the liquid line of descent (LLD) of the whole suite from the mantle to the final stages of the ascent, through crustal magma storage, was established.

This multidisciplinary and comprehensive study of both instrumental and petrological data has provided considerable information about the magmatic environments beneath the island, dynamics along the ascent of magma and established the guidelines for the interpretation of any type of data obtained during an eruption as a whole.

## 1.6. Not a calm basaltic eruption

The final paper, "*The 1909 Chinyero eruption on Tenerife (Canary Islands): insights from historical accounts, and tephrostratigraphic and geochemical data*", included in this thesis, deals with the last eruption on Tenerife Island, its evolution and eruptive dynamics, petrological characteristics and most importantly, its reconstruction regarding the impact produced on to the population of the islands.

Although the subject of the present thesis is, "*Eruptive dynamics and petrological evolution of recent volcanism on the El Hierro Island. Implications for volcanic hazard assessment*", the Chinyero eruption (Figure 1.12) has been chosen up for this work because of multiple aspects:

- a) The 2011 eruption was a submarine eruption therefore, a complete sampling of the emitted products was not possible. Most importantly, the sea environment, for an eruption at that depth, acted to slowdown the eruptive dynamics, and the only clues we have are from the texture and composition analysis
- b) The Chinyero eruption, had the same monogenetic basaltic character as the 2011 one, thus inner magmatic processes, eruptive dynamics and deposit mechanisms shows a similarity
- c) The Chinyero eruption is the most recent basaltic one, on the most densely populated island and its study provides crucial information for hazard assessment and help in mitigation of this threat, not only on Tenerife Island but in the entire archipelago, as the basaltic monogenetic volcanism is a common aspect.
- d) During 2004, an unrest took place on the island of Tenerife, associated to a basaltic magma intrusion (Gottsmann et al., 2006; Martí et al., 2009; Cerdeña et al., 2011)
- e) According to the volcanic activity in historical times there is (on average) an eruption every 25-30 years for the Canary archipelago (Sobradelo et al., 2011)
- f) All historic volcanic activity in the islands was basaltic monogenetic type and these eruptions and their accompanying phenomena produced damage to edifices, infrastructure, crops and human beings.

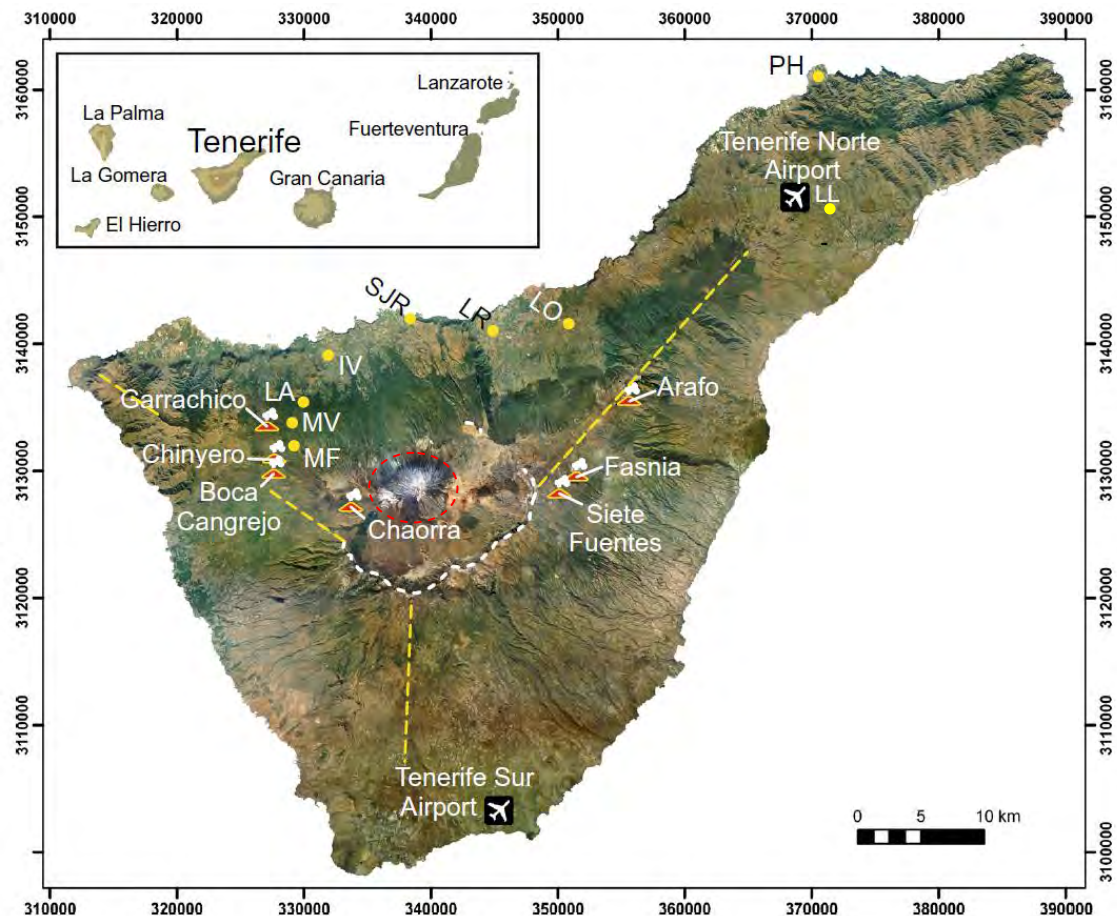


Figure 1.12. Satellite image of Tenerife Island with highlighted main geographic features described in the text. Red volcanoes indicate vents of historical flank eruptions of Boca Cangrejo (1492?), Siete Fuentes (1704), Fasnía (1705), Arafo (1705), Garrachico (1706), Chahorra (1798) and Chinyero (1909). Yellow dots indicate the main localities: IV Icod de los Vinos, LA Las Abiertas, LL La Laguna, LO La Orotava, LR Los Realejos, MF Montaña de la Flores, MV Montaña de Vancheque, SJR San Juan de la Rambla, PH Punta del Hidalgo. White dashed line indicates the rim of Las Cañadas caldera, whereas the yellow line highlights the direction of the three rift zones and the red dashed line enclose the Teide-Pico Viejo complex. Inset: Map of the Canary Islands (after Di Roberto et al., 2016).

For these reasons, it is immediately evident that the Chinyero eruption is maybe the most adequate one to be included in this thesis. Its study helps in a better understanding of the monogenetic volcanism on the islands, and clearly benefits any strategy for an accurate and updated hazard assessment and risk mitigation strategies.

After almost a year of felt seismicity (March 1908 - October 1909), with some of the events perceived on the island of Gran Canaria, ca. 100 km from Tenerife (Perret, 1914; Albert et al., 2016), the

earthquakes became more frequent and intensive in November 1909. Earlier this year, on April 1909, a strong fumarole emission began from the central Teide volcano crater, accompanied by a general increase in ground temperature throughout the cone that melted the snow-cap (Fernandez Navarro, 1911). The eruption began at 2:30 p.m. on 18 November 1909 and ended on 28 November 1909. It was a typical strombolian eruption accompanied by emission of lava, initially from numerous vents aligned along the eruptive fissure but soon it concentrated in two or three vents located close to the crater that remained active until the end of the eruption. The shape of the lava flow field was strongly controlled by ground morphology (total volume of  $11-15 \times 10^6 \text{ m}^3$ ; Carracedo, 2013) and pyroclastic material had been reported not only in the proximities of the vent but also at distances of 52 km on Tenerife Island and 130 km on Gran Canaria Island.

Several techniques were used to study this relatively small eruptive episode. Initially, a detailed study of aerial photos was realized to determine the extension of the pyroclastic deposit, confirm the lava flows extension and identify the points of sampling. During fieldwork, the emitted products in 35 stratigraphic sections (17 samples of pyroclastic fall deposits, 10 lava samples and 6 lava spatter samples) were identified, measured and described.

Grain size and component analyses were carried out on tephra samples in the laboratory and the total grain size distribution of pyroclastic deposits cropping out in proximal areas was estimated using field data and the TOTGS (Biass and Bonadonna, 2014) Matlab® graphical user interface for the code published by Bonadonna and Houghton (2005). Three samples representative of the whole pyroclastic fallout sequence were selected for detailed textural, mineralogical and geochemical analyses through scanning electron microscope (SEM). Bulk rock compositions were determined on ten samples of lava flows and two spatter bombs, also major element analysis and trace element analysis were performed.

One of the most important phases of the present work was the thorough review of the available historical sources (Figure 1.13) and their interpretation from a volcanological perspective. The exhaustive descriptions of the eruption made by Ponte and Cologan (1911) and Fernández Navarro (1911) were of great help, with the last one providing a personal eyewitness account of the eruption starting the early morning of 19 November, among other, including a description of the eruptive phenomena and data on the nature, volume and impact of erupted products, as well as an accurate description of the evolution of the lava flow field. Also, the information that was extracted from dispatches and telegrams sent by/to the local authorities, as well as from reports in newspapers of the time, highly contributed to this research (Tous Meliá, 2011).



*Figure 1.13. Photographs of the 1909 eruption of Chinyero volcano (National Heritage of Spain). Top photo, eruption seen from "El Pino de Chasna". The bottom photo was taken from Montaña Poleos.*

As reported by eyewitnesses, the initial phase of the eruption consisted in an energetic explosion and as per telegrams sent the same night, the eruption must have been relatively violent and intense. A glowing red column of smoke was clearly visible from the nearby islands and up to nine eruptive vents were reported, aligned along a 500 m. fracture. Later, only 3 or 4 of them were still "alive" till the end of the eruption. Just in the second day of the eruption a cone as high as ca. 80 m had already developed.

During the first 3 days almost continuous fire fountaining was observed, feeding the lava flows. From 22 November 1909 (day four of the eruption) to the end of the eruption, the intensity decreased progressively. Vulcanian explosions on the 9th day of the eruption announced the end of it.

Lava flows were extremely fluid, hot and able to flow at a considerable average speed of 21 m/h (ca. 4 km in 8 days) and pyroclastic products in very proximal sites consisted of juvenile vesicular black

lapilli and dense bombs (up to 1 m<sup>3</sup> in volume). At a distance of 11-19 km small volcanic scoriae with the size of a hazelnut (i.e. ca. 15 mm) were driven by light atmospheric currents and fallen almost with the intensity of a regular rain, meanwhile villages located about 25 km or more received fine ashes, a phenomena registered also in Gran Canaria Island (130 km from the vent). The eruptive column could had reached up to 1000 m (Burchard, 1909).

Chinyero scoria cone (80 m high) is covered by a tephra fallout sheet, including, medium to coarse scoriaceous lapilli and bombs, and its topmost part consists of an almost continuous agglutinated spatters. Pyroclastic fallout deposit (Figure 1.14) is well preserved only in very proximal locations  $\leq 1$  km from the vent, and presents a maximum thickness of ca. 130 cm (250 m of the main vent). It is massive, with vague normal grading, and consists of dark, lustrous glassy particles of angular to ragged shape which are vesicular to highly vesicular. Lithic fragments represent less than 1% of the deposit, with the relative proportion of juvenile and lithic components remaining the same throughout the sequence.

The effusive activity formed a compound lava flow field made of blocky aa lava and some hornitos could be found along the main stream flow. In few areas close to the base of the scoria cone where lava ponded, the surfaces of lava flows are shelly or ropy. No evidence for clastogenic or rheomorphic flows has been found.

The bulk rock major element composition is basanitic and homogeneous. Lava and pyroclasts compositions are indistinguishable. Glass compositions are slightly more variable than bulk rock compositions, something compatible with limited fractional crystallization dominated by olivine.

As for the eruption style and dynamics, clues are derived mainly from the texture of the lapilli during the first days (well sorted, moderately to highly vesicular scoriaceous) and ash spatial distribution.

Finally, apart from the descriptions during the eruption that were extracted from the documents, important aspects of the unrest period such as the seismic activity that preceded the eruption of Chinyero or the contemporaneous formation of strong fumarole activity at the base of the Pico Viejo cone, were added in the study.

As revealed by this work, and contrary to previous assumptions, at least during the first 3 days, the eruption was a violent Strombolian eruption. This fact has a major importance, not only for the Tenerife Island but for the all seven islands, as this type of activity, is the most probable in the future years. An eruption of comparable size/intensity in the future, possibly would affect more than an island, causing problems to inhabitants, infrastructures and island's major industry, tourism. During

the 1909 eruption only some thousands of people were impacted and mainly the land grow; nowadays the same area counts more than 215,000 inhabitants, structures such as critical ground transportation systems (highways), hospitals, tourist facilities and areas dedicated to the production of valuable agricultural products (wine) would all be exposed to volcanic ash; both airports on the island are located within 50 km (Olave, 2014).

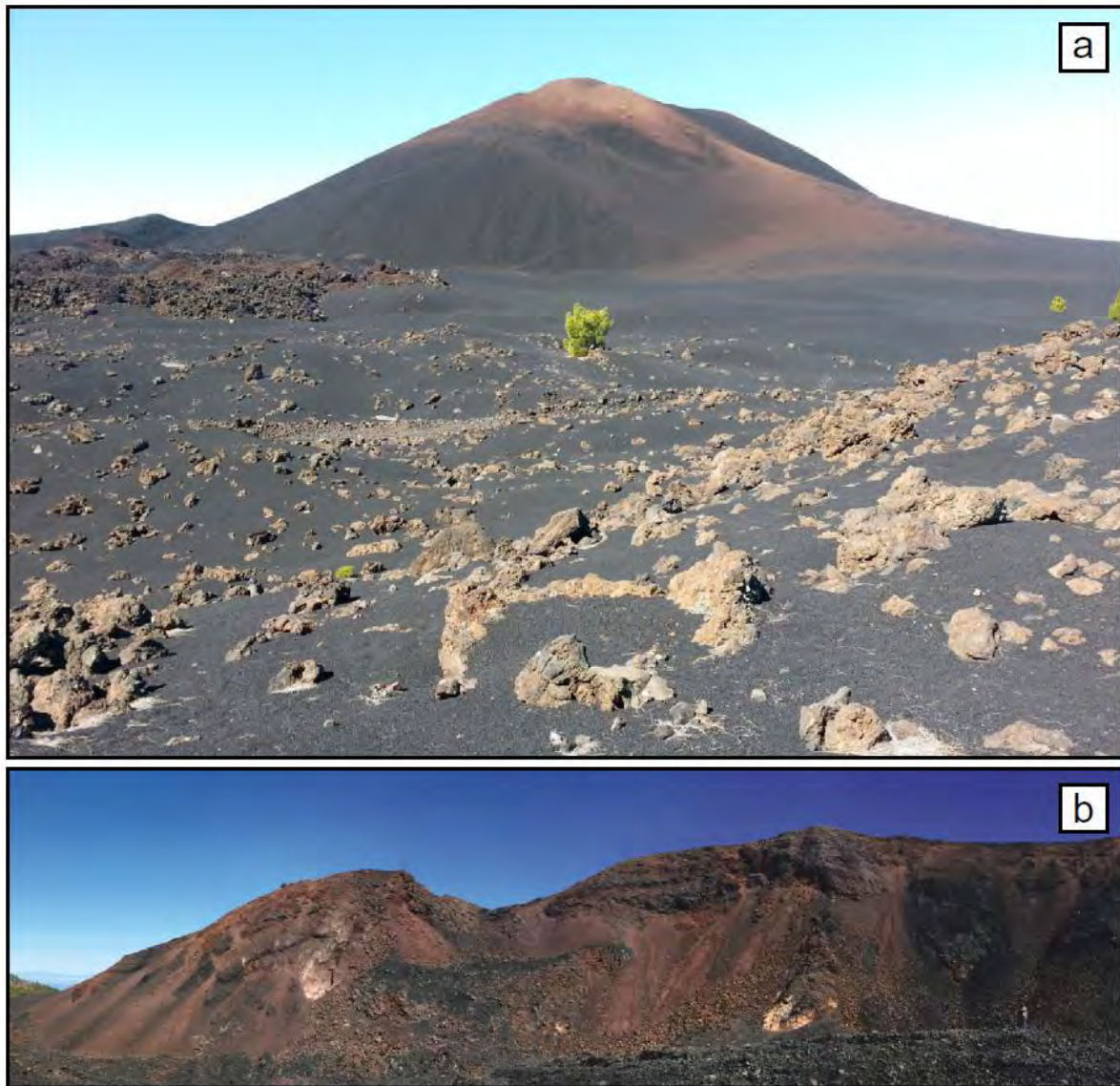


*Figure 1.14. Scoria cone and pyroclastic deposits of the 1909 eruption of Chinyero, Tenerife (a) Panoramic view (from NE) of the Chinyero scoria and pyroclastic deposits emplaced over scoriaceous lava flows from a previous eruption (b) Panoramic view of the breached wall of Chinyero scoria cone showing the internal structure and deposit (after Di Roberto et al., 2016).*

Concluding this introduction, and the short exposition of the papers, it has been demonstrated that a multidisciplinary approach is necessary, not only to achieve a better knowledge concerning the basaltic volcanism in Canary Islands and its deep processes, but also in order to correctly assess hazards, (both long- and short term), and plan risk reduction strategies for the islands. An extra effort is required to evaluate the real intensity and magnitude of past basaltic eruptions and take into account possible scenarios that include fissure eruptions or even magma mixing eruptions.



## 2. RESULTS

Monogenetic basaltic volcanism, because of its small volume and magma type, is often considered as a simple process, where magmas ascend very rapidly from their mantle source. Nonetheless, they often show significant compositional variation within individual eruptions, closely spaced eruptive centres, as well as among eruptions that apparently belong to a homogenous and uniform activity through time. These compositional variations influence the eruption intensity, texture and composition of emitted products, mechanisms of deposition, level of exposure and extension of the affected area. In addition, a water-magma interaction could have almost the same results concerning the evolution of the eruption.

This work, whose results are featured below, argues on the complex processes that can take place before a monogenetic basaltic eruption and their influence on the eruption evolution, reveals their close relationship with the instrumental data achieved by a volcano monitor network and finally emphasizes that a precise hazard assessment could be accomplished only with such a global study.

The principal aim in the first three papers was to characterize the products emitted in the early stage of the 2011 eruption, and to determine through textural, petrological and geochemical analyses, the relation, if any, between these products and pre-existing ones on the island, as well to achieve information about the mechanisms of storage, plumbing and ascent of these magmas. The results, also, were relevant for the hazard assessment in Canary Islands as valuable information regarding eruption types, evolution and mechanism of deposition was acquired, so more than one scenario could be evaluated.

Through these comprehensive analyses (Figure 2.1), and concerning the xenopumices emitted in 2011 El Hierro eruption, two different inner parts were distinguished. For the external crust, composition of basanite was determined - compatible with those of El Hierro volcanics (Carracedo et al., 2001) - while the porous part (hereafter called xenopumices as defined by Troll et al., 2011) fluctuates from trachyte to rhyolite (grey or white respectively).

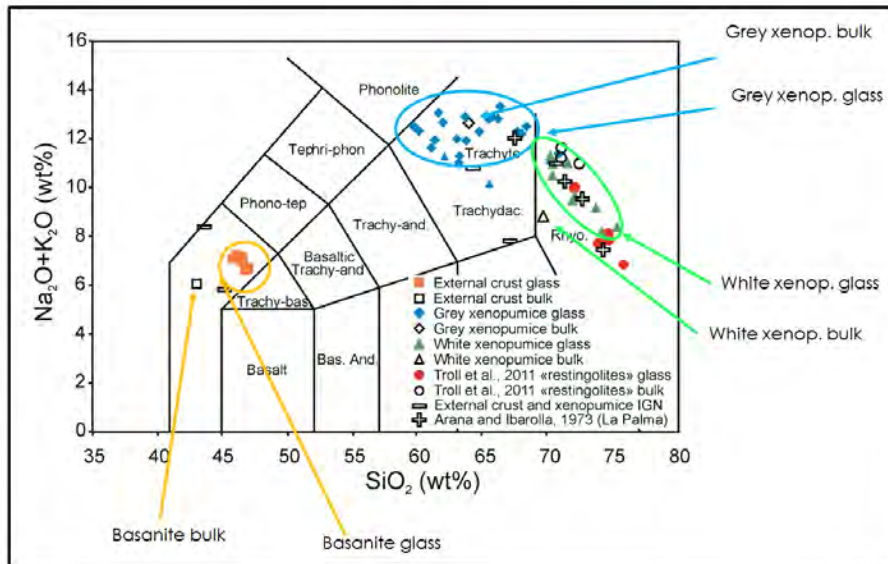


Figure 2.1. Major elements for xenopumices and basanite crust (SEM-EDS for glass and ICP for whole rock analyses).

Also, considering the ratios between highly incompatible elements (e.g., Rb/La, Th/La and Nb/La) in grey xenopumice, we can sustain that they are co-magmatic with both the basanitic carrier magma and the white xenopumice, and similar to the whole differentiation series of El Hierro and thus can be considered products of the same magmatic source (Figure 2.2). The anomalously elevated content of some highly incompatible elements (U, Nb, Zr, Hf, Sm and HRE) observed in white xenopumices demands a complex magmatic differentiation process. This is reinforced by the high values of  $\delta^{18}\text{O}$  that have been found. Finally, the result of this basanite modelling predicts highly crystalline magmas and relative proportions between solid phases (e.g., Ol/Cpx) that are reversed compared to the natural assemblage.

In the case of the deposits nearby Malpaso peak, a succession of pyroclastic units was identified and from the study (“in situ” stratigraphic sections and laboratory analyses) four units have been recognized, that seemed to be in a tight temporal connection and thus to belong to the same eruptive episode. Each one of these units is associated to a different phase of the eruption, and can be interpreted in terms of changing of eruptive dynamics, transport and depositional system. Two of these units were subdivided in sub-units (unit N1 in two sub-units and unit N3 in four sub-units), according to the texture, terms of sorting and lithics (Figure 2.3).

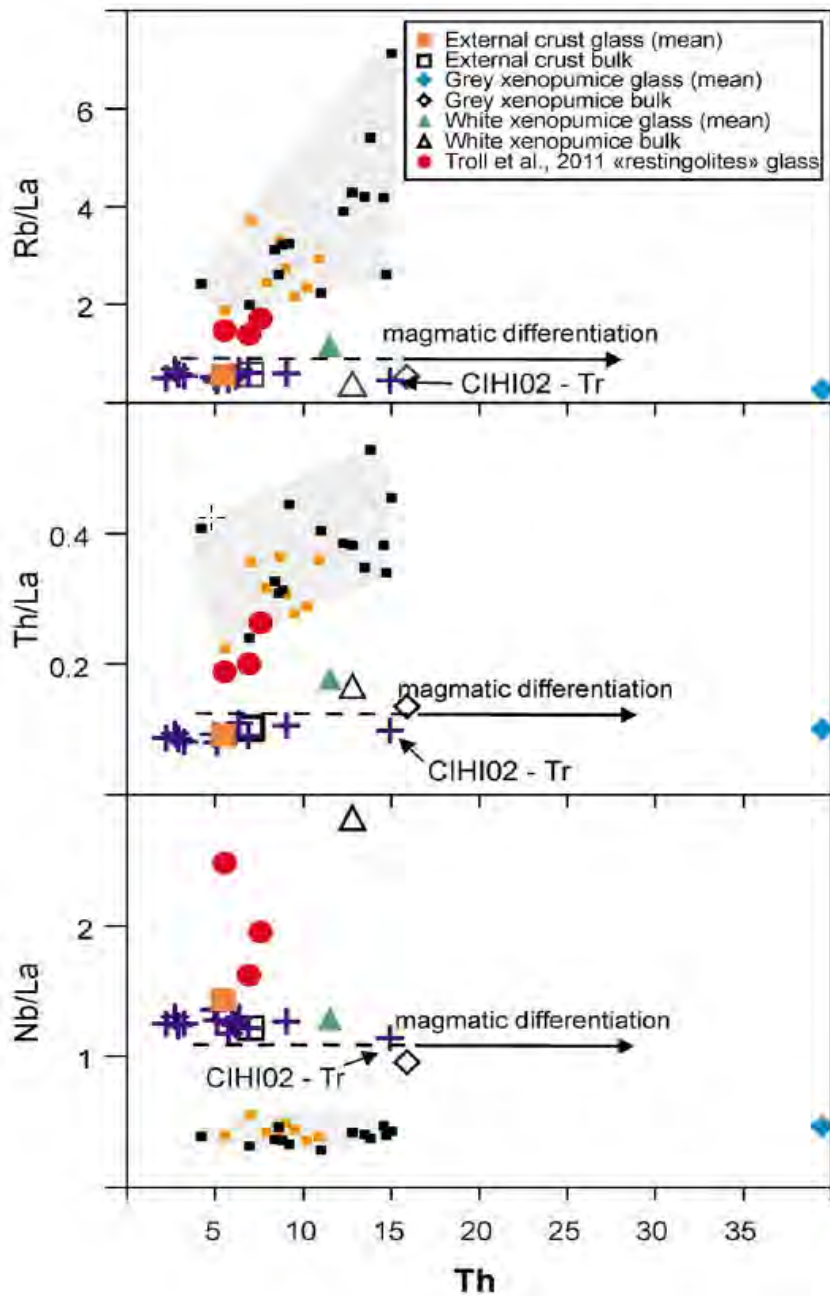


Figure 2.2. Ratios between trace elements ( $Rb/La$ ,  $Th/La$ ,  $Nb/La$ ) differing in their compatibility and affinity for fluids ( $Rb$  for fluid-mobile, and  $Nb$  and  $Th$  for fluid-immobile elements) are plotted against highly incompatible elements ( $Th$ ). The arrows indicate the direction of shifts due to magmatic differentiation from a common parental magma. Grey area represents compositional range of various sediments composites and averages (black full squares) and regional averages of Quaternary Loess (light brown full squares) reported by McLennan [2001]. Trachytic rocks in the El Golfo edifice from Carracedo et al. [2001] (CIHI02 - 176 ka age) are also reported (after Meletlidis et al., 2012).

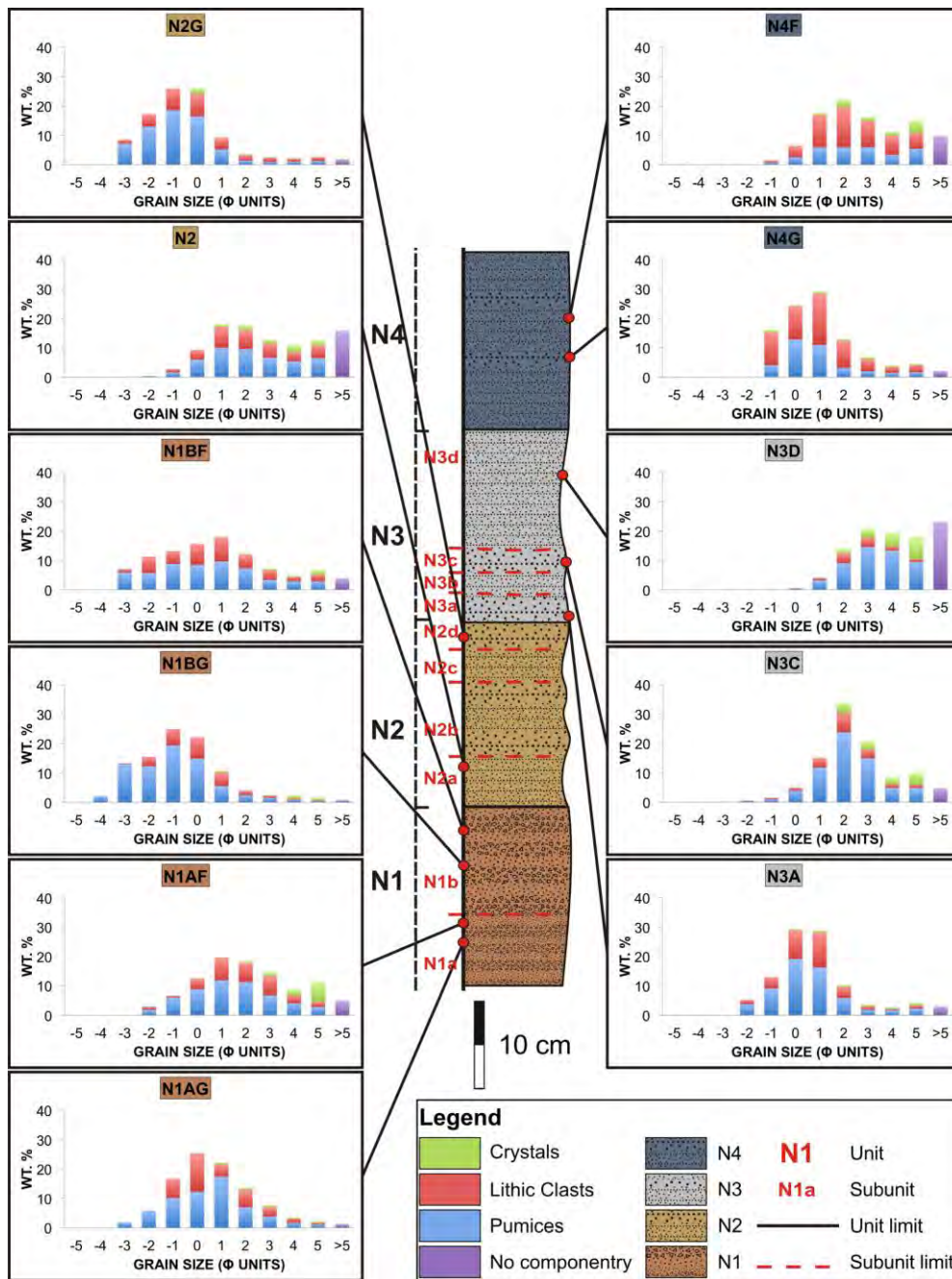
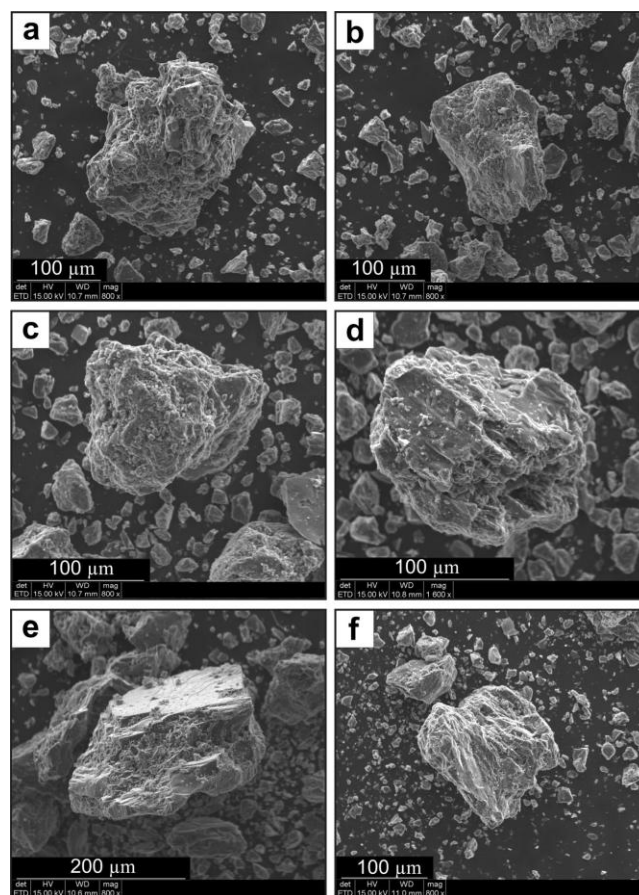


Figure 2.3. Grain-size distribution and modal composition of representative samples from the Malpaso deposit. N1 pumice lapilli layers alternating with poorly stratified ash layers, N2 ash layers with loose pumice-lapilli rich layers, N3 massive poorly stratified ash beds with interbedded lapilli layers, N4 ash and pumice-rich lapilli layers with abundant lava lithic clasts. The different subunits (e.g. N1a) are indicated on the left side of the stratigraphic log. Sample numbers are given at the top of each bar graph (after Pedrazzi et al., 2014).

The morphology and distribution of the deposit, and the sequence and stratigraphic relations between the units and their subunits, are themselves evidences of the style of the eruption. Several pulses of pyroclastic density currents (PDC) have taken place (Branney and Kokelaar, 2002), mainly as base surges, and lack of fall deposits at the base of them, point out that, a column collapse occurred right after the eruption began or the absence of a sustained column.

Through the electron microscope analysis of the juvenile morphology clasts, blocky morphology, poor vesicularity with elongated vesicles and quenching cracks, have been observed, mainly in the N2 to N4 units (Figure 2.4), features that sustain the idea that magma/water interaction was decisive in the dynamics of the eruption, especially in the final phase (Sheridan and Wohletz, 1983; Büttner et al., 1999, Hiroi and Miyamoto, 2016).



*Figure 2.4. Scanning electron microscope (SEM) images of pumice from units 2, 3 and 4. Clasts show little abrasion due to transport. Several examples of the most typical morphological features are shown. (a) & (b) Poorly vesiculated particles from unit N2 with mainly blocky morphologies. (c) & (d) Poorly vesiculated clasts from unit N3 with tiny adhering particles and elongate vesicles. (e) & (f) dense and poorly vesiculated grains with blocky morphology, quenching crack structures and stepped texture (after Pedrazzi et al., 2014).*

This work evidences the importance of an explosive eruption within an environment in which effusive basaltic activity predominates. The associated hazards to that scenario are considerably greater than those associated with a basaltic eruption, the more common type on the island.

With reference to the third paper that completes that first unit, a comparison between the 2011 emitted products and those from Malpaso deposit, was carried on. Apart from the textural and compositional study that results in identifying three different phases concerning the inner part of the xenopumices, Sr-Nd-Pb isotope analyses have been realized in samples of all products.

In particular, according to the bulk rock geochemistry (Figure 5), the white facies can be classified as a trachyte. The grey facies is less “evolved” and closely matches the compositions of the most evolved trachyte rocks and glasses of El Hierro, relationship that is consolidated as seen in the incompatible elements.

In the field of isotopes, Sr isotope ratios of the xenopumice are variable and Nd ratios appear rather homogeneous. Compared with the xenopumice, Holocene trachyte shows a lower  $^{87}\text{Sr}/^{86}\text{Sr}$  value and a similar  $^{143}\text{Nd}/^{144}\text{Nd}$  ratio. The rocks show the same patterns: characterized by positive Th, Zr, and Hf anomalies (very strong for the white facies xenopumice) and Sr, P, and Ti troughs (Figure 2.5). The heterogeneous U contents of the xenopumice samples, ranging from 1.08 ppm (Sigmarsson et al. 2013) to 42.1 ppm (Rodriguez-Losada et al. 2014), is also worth noting.

In agreement with the evidence presented above, it seems that xenopumices formed from the interplay of magmatic, hydrothermal, and pyrometamorphic processes commonly occurring beneath active volcanoes, where hydrothermal fluids are moving along fractures and interact with the surrounding rocks, managing to alter and chemically transform them.

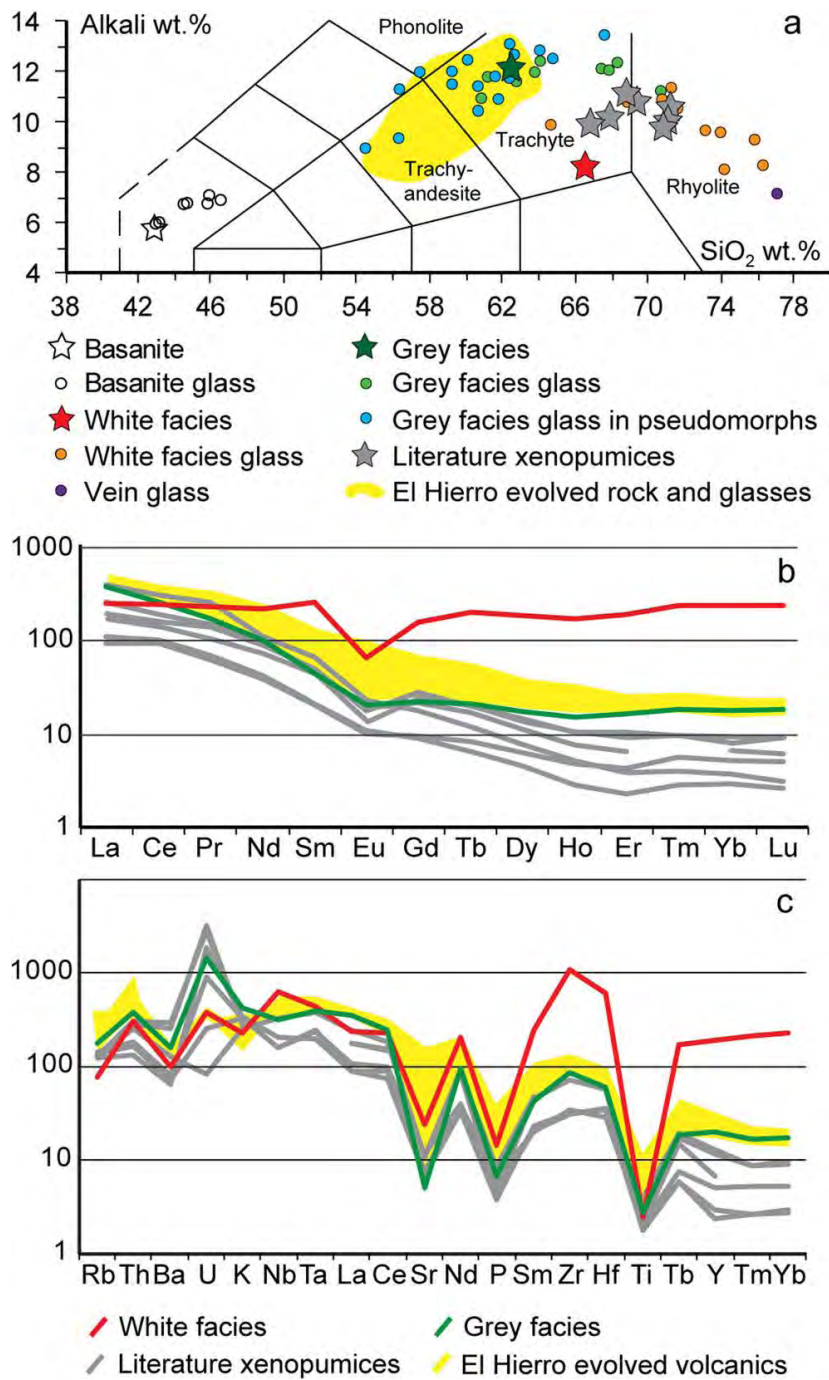


Figure 2.5. (a) TAS diagram showing bulk rock (stars) and glass (circles) compositions of the various studied rocks. (b) REE and (c) incompatible elements spider diagrams comparing white and grey facies compositions with xenopumice data from literature and historical El Hierro evolved volcanic products. El Hierro basanite compositions are from Meletlidis et al. (2012); the trachyandesite-trachyte data (El Hierro evolved rock and glasses) are from Pellicer (1980), Carracedo et al. (2001) and Day et al. (2010) and from this work (after Del Moro et al., 2015).

The petrological data (Figure 2.6) agree with a pre- & syn-eruptive formation of the xenopumice, when El Hierro basanite magma intruded, hydrothermally altered trachyandesite to trachyte rocks and triggered local partial melting. The temperature of the basanitic magma is estimated to have been about 1150-1200 °C (Sigmarsson et al. 2013; Martí et al. 2013), therefore it was hot enough to induce the almost complete dehydration melting of the hydrous and hydroxyl mineral assemblage of the argillic to silicic alteration facies and of anorthoclase. Textural evidence such as jigsaw-fit texture of the crystals is associated to gas expansion related to thermal dissolution of hydrous alteration minerals, whereas the detection of mullite indicates a high temperature conditions and contact metamorphism and pyrometamorphism. The rapid rise of magma engulfed and transformed the original altered rocks, resulting in the eruption of xenopumice at the beginning of the October 2011 event.

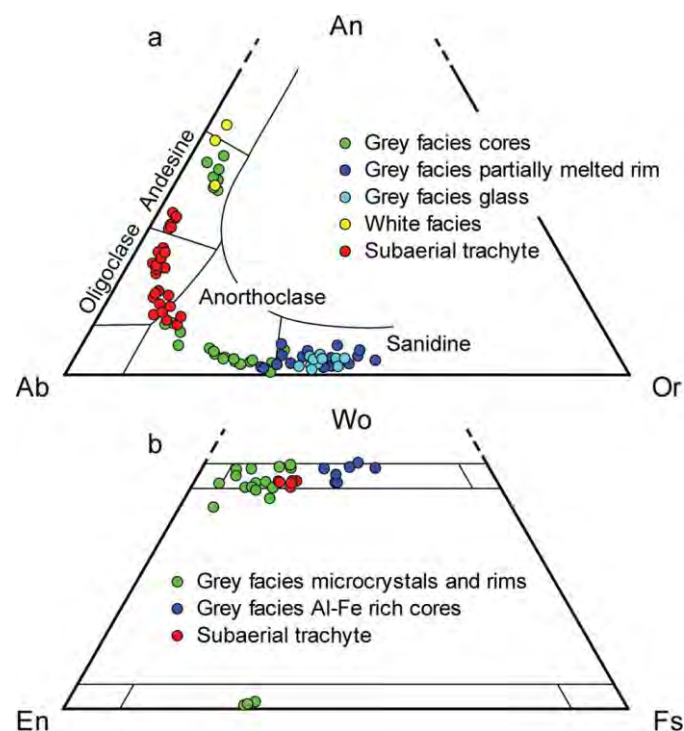


Figure 2.6. (a) Feldspar ternary diagram showing the compositions of restitic and partially melted feldspars in the xenopumice. Grey facies sanidine and glass compositions are representative of the partial melting of anorthoclase. Holocene El Hierro subaerial trachyte feldspars are also plotted. (b) Pyroxene ternary diagram showing the composition of grey facies coronas and microcrystals in the aggregates compared with pyroxene composition of the Holocene El Hierro subaerial trachyte (after Del Moro et al., 2015).

In case of an ongoing eruption, not only the data derived from the samples contribute to understand better the magmatic system and processes that take place; the instrumental data, as shown in the 2011 eruption, can be crucial in that field. In the fourth paper, where these data were pulled together, the results validate the analysis of these data sets as a whole, and reveal the importance of this approach.

Six pre-eruptive (Figure 2.7) and three syn-eruptive phases were distinguished, using the instrumental data.

#### *Pre-eruptive*

*Phase A; July 21, 2011 - August 3, 2011:* repeated, low-energy and intermittent seismic swarms located at depth of 8-14 km beneath the south-central sector of the island. This activity suffered a ~3 km, short-term horizontal migration at depths of 10-12 km and towards the north. The only GPS station available at the moment, FRON, registered a ground deformation vector directed to the NE (López et al., 2012)

*Phase B; August 3, 2011 - August 15, 2011:* intermittent seismicity continued at a depth of 9-10 km. A radial distribution of ground deformation was detected in 4 GPS stations. Calculation of Mogi (1958) source parameters indicated that the deformation centre was located beneath the central part of the island at depth of ~5 km and a preliminary volume was estimated ( $10 \times 10^6 \text{ m}^3$ ).

*Phase C; August 15, 2011 - September 3, 2011:* The earthquakes were clustered mainly at the margins of the area previously affected, located in depths shallower than 12 km. The second highest ( $> 2$ ) b-value (Gutenberg and Richter 1954) for the whole seismic unrest was achieved (Ibáñez et al., 2012; Martí et al., 2013a, 2013b). An increase of volume of the source was calculated ( $30 \times 10^6 \text{ m}^3$ ), and a significant ground deformation was logged, with changes in vector direction

*Phase D; September 3, 2011 - October 1, 2011:* Number and magnitude of seismic events increased and a migration deeper and southern was observed. Strong acceleration in ground deformation with vectors showing a radial pattern registered and a southern and shallower migration of a higher volume ( $160 \times 10^6 \text{ m}^3$ ) deformation centre has been assumed.

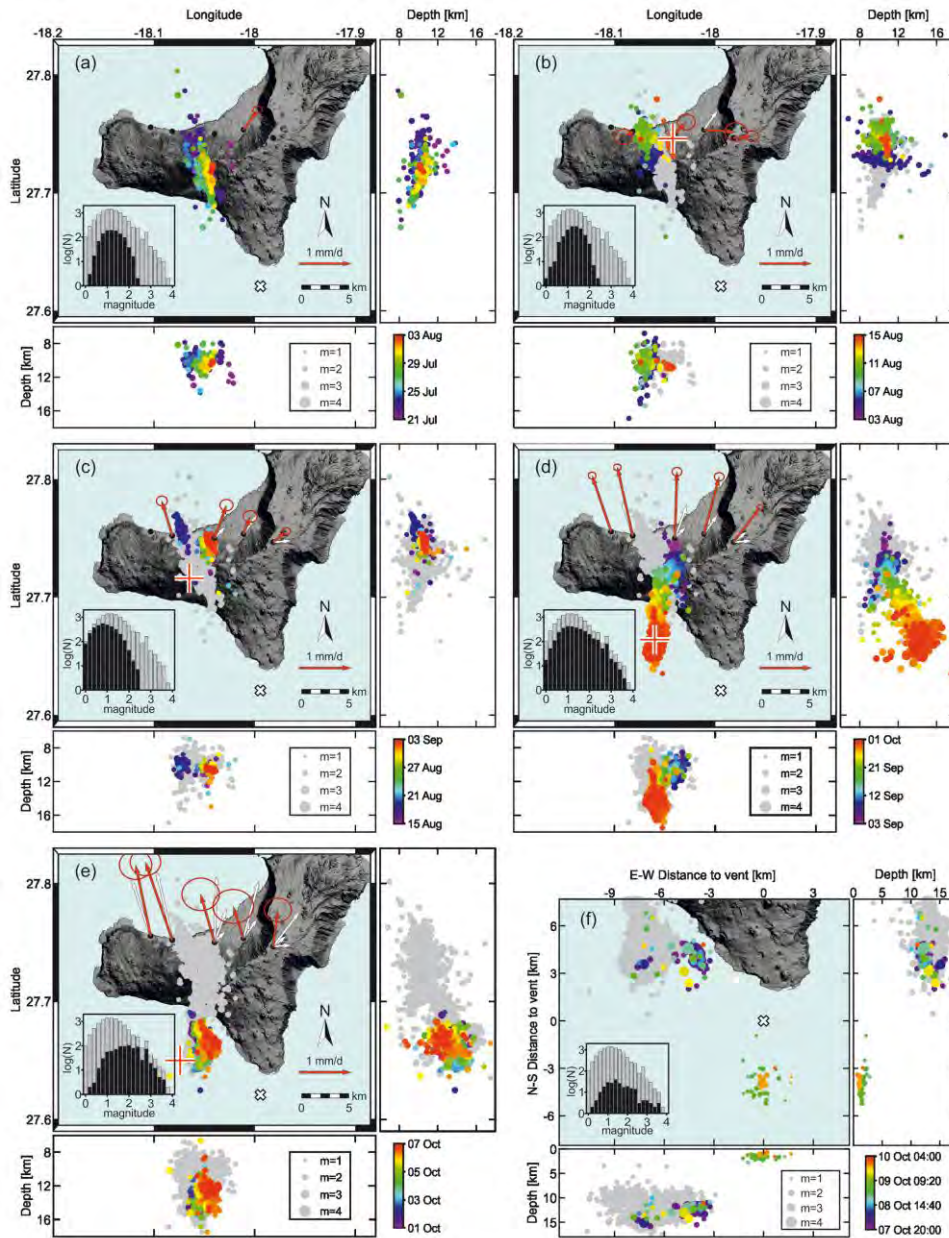


Figure 2.7. Temporal evolution of the latitude, longitude and depth (km) of the earthquakes with magnitude  $>1.5$  (time scale of events is reported in the colour bar and in grey are reported the earthquakes occurred during the previous phases) along with the evolution of the horizontal deformation registered by GPS stations (red arrow for the period in analysis and white arrow for the previous periods) during the pre-eruptive phase of 2011-2012 eruption of El Hierro Island. Red cross indicates the position of the deformation source according to Mogi model and white X marks the vent of 2011-2012 eruption. Inner plots give the histograms of the number of located events (after relocation of Domínguez Cerdeña et al., 2014) versus magnitude for the each phase (black) and for the full period (grey shaded); (after Meletlidis et al., 2015).

*Phase E; October 1, 2011 - October 7, 2011:* During this phase more than 50% of the total seismic energy of the unrest phase was released due to higher magnitudes. Seismicity is located southeast and another change of the direction of deformation vectors, now towards NNW, has been observed. The deformation centre was calculated for depth of ~5 km and with a volume in the order of  $50 \times 10^6 \text{ m}^3$ . At the end of this phase the gravimeter sensors registered tilting of the sensor along with changes in the gravity value of  $3 \mu\text{Gal}$ .

*Phase F; October 7, 2011 - October 10, 2011:* The largest seismic event of the series (ML = 4.3) disrupted a ~12 hours of relative seismic silence and changed drastically the characteristics of the forthcoming activity. Ground deformation suddenly slowed down.

#### *Syn-eruptive activity*

*Phase G; October 10, 2011 - October 23, 2011:* Seismic activity was localized mainly in the south (depths of 10-14 km) but also registered in the north (depth of 20-25 km)

*Phase H; October 23, 2011 - January 1, 2012:* seismicity continued in the central-northern part of the island and in two different depths (15-20 km and 20-25 km), although with common signal characteristics (García et al., 2014). A minor episode, above the background noise level, of gradual ground deflation was registered by GPS network.

*Phase I; January 1, 2012 - March 5, 2012:* The seismic activity was again located in the central-southern part of the island (depths of 10-15 km) and no significant deflation was observed.

In addition, the petrological analysis revealed that compositions found are in accordance with those of products emitted during the Quaternary rift volcanism of El Hierro (Carracedo et al., 2001) and also, trace element bulk rock composition patterns are fully comparable with those of El Hierro volcanics, following a typical OIB trend and the characteristic pattern of the Canary Islands basanites.

Thermodynamic modelling techniques have been applied in conjunction with data such as the relocated depths of hypocentral foci (Domínguez Cerdeña et al., 2014) and the local lithosphere and density structure (Collier and Watts, 2001). A composition similar to that of rocks erupted on October 31, 2011, was chosen, because the compositions of glass and bulk rock almost matched, thus indicating that this sample possibly represents a magmatic liquid.

As a result of the comparisons between liquid line of descent (Figure 2.8), mineral composition calculated by thermodynamic modelling and compositional variations observed in bulk rocks and glasses, it can be pointed out that

- large part of the crystallization (~50%) is controlled by phase equilibria that occur in a storage system located in the mantle or in the crust if oxidizing conditions are considered
- glass composition reflects final precipitation (~5%) during the quenching in the last stage of the ascent
- the vertical extent of the storage system where precipitation of minerals occur, should be limited since the scattering of natural sample composition along isobaric curves is very small
- large part of the cooling (1300-1150 °C) occurs at pressure higher than 350 MPa and the last temperature drop (~30 °C) takes place only during the final stage of the ascent to the surface.

Instrumental data combined with petrological findings and thermodynamic modelling give evidence of a major intrusion beneath the central part of the island and around pre-existing high density magmatic bodies. Seismicity marks the failed attempts of the magma to reach the surface through a low fractured zone located below the central-northern part of the island; finally, magma found its way nearby the El Hierro South Rift. The eruption was fed by the ascent of an important volume of material from the upper mantle that was emplaced near the crust-mantle boundary and progressively tapped during the eruption.

Seismic distribution and ground deformation have been of great assistance in order to define magmas behaviour and provide an input for the thermodynamic modelling. All of this aside, data interrelation was also helpful to keep track of the unrest and the submarine eruption, and as seen in other works (Martí et al., 2013b) this data could be used as an indicator of the forthcoming activity and so, be considered in hazard assessment, almost in a real time response.

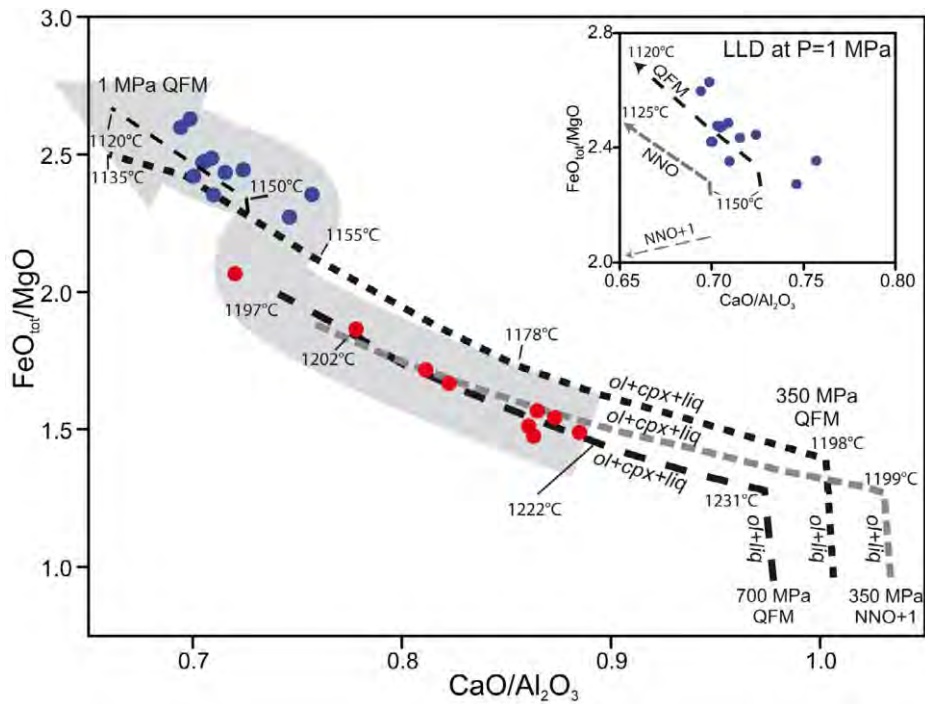


Figure 2.8. Comparison between compositions of bulk rocks (red solid circles), glass (blue solid circles) and liquid lines of descent (LLD) obtained by thermodynamic modelling of cooling (range of temperature are reported) and fractional crystallization at different pressures (700-1 MPa) under distinct oxidation conditions (from QFM to NNO+1). Grey arrow describe possible ascent path of magma that starts to crystallize at 700 MPa (between 1300 and 1200 °C under QFM) or at 350 MPa (between 1199 and 1160 °C under NNO+1), moves at lower pressure and finally quench at temperatures between 1150 °C down to 1120 °C, close to the surface. Inset shows liquid line of descent at P=1 MPa (water depth of 100 m) under different oxidizing conditions and glass compositions measured during the 2011-12 El Hierro eruption (after Meletlidis et al., 2015).

As already mentioned, and argued in the introduction, the 1909 Chinyero eruption (Tenerife Island) was included in this thesis.

From the extensive study of the pyroclastic deposit, a complete characterization of grain size distributions was not possible due to a lack of data across the entire dispersal area, especially in medial and distal sites where the deposits are eroded and strongly reworked, even though the estimated volume of pyroclastic deposits still traceable around the cone is of the order of  $5 \times 10^5 \text{ m}^3$  (calculated from isopach maps using the method described by Pyle, 1989). Due to intense reworking and erosion processes, the order of magnitude of the volume of pyroclastic deposits was estimated by tracing two large isopachs (5 and 0.5 cm) corresponding to the thickness of deposits reported in historical accounts for medial to distal sites, giving an estimated volume of approximately  $1.24 \times 10^7$

m<sup>3</sup>, to which a  $2 \times 10^6$  m<sup>3</sup> volume for the cone was added, thus the minimum volume of pyroclastic deposits emitted during the Chinyero eruption is of the order of  $1.5 \times 10^7$  m<sup>3</sup>.

Concerning the lava flows, the emitted mass results in  $2.6\text{--}3.6 \times 10^{10}$  kg by using as a reference value the 2380 kg/m<sup>3</sup> of Pioli et al. (2008) given for the lavas of Paricutin. The calculated DRE volume is  $9.6\text{--}13.3 \times 10^6$  m<sup>3</sup>.

All studied samples, including pyroclastic fallout deposits and lavas, have basanitic composition (Figure 2.9) with a porphyritic texture <1 to 5 vol.% phenocrysts (up to 2.5 mm in size) of clinopyroxene (diopside field), spinel, rare olivine and plagioclase, presenting a hyalopilitic groundmass.

The thickness and architecture of the pyroclastic sequence, the nature of particles and the dispersal of the products, indicate violent phases of Strombolian eruption (Valentine and Gregg, 2008; Cioni et al. 2010) for the first 3 days of the eruption, with pulsating phases until 21 November. From the initial opening phase, that involved several vents along a fracture, no traces were preserved except the very first point of emission.

The mass discharge rate (MDR) calculated ( $2\text{--}2.6 \times 10^5$  kg/s), assuming a density of ca. 1000 kg/m<sup>3</sup>, is comparable to those calculated for other mid-intensity, violent Strombolian eruptions at Vesuvius and Etna volcanoes (Cioni et al. 2008, 2010). A minimum estimated DRE volume of the eruption ranges between  $14.1$  and  $19.1 \times 10^6$  m<sup>3</sup>, with the effusive activity DRE approximately double that of explosive activity.

Intensity and magnitude of the 1909 Chinyero eruption (Table 2.1) were much greater than previously reported and resulted in the distribution of pyroclastic products very far from the source (lapilli up to 20 km from the vent and of ash 130 km from the vent).

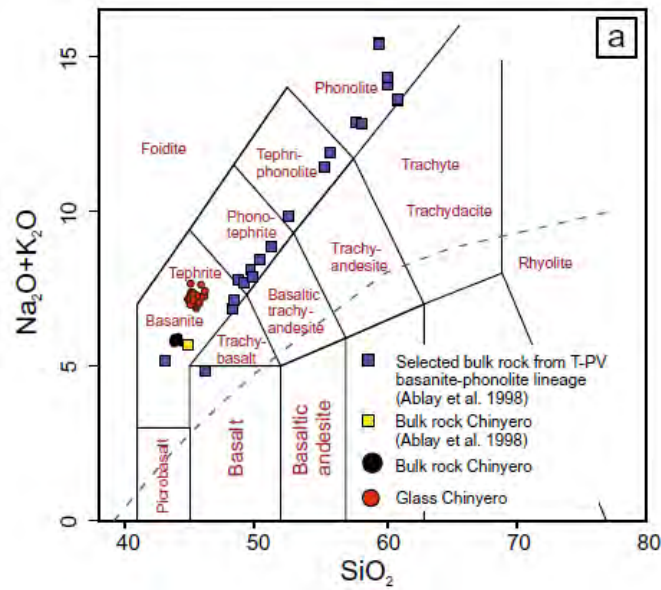


Figure 2.9. Total alkali silica showing composition of bulk rock (black dots) and glass (red dots) of Chinyero samples in comparison with bulk rock composition from the basanite–phonolite series of Teide–Pico Viejo Volcanic Complex, Tenerife (Ablay et al. 1998) ;(after Di Roberto et al., 2016).

Site	Distance (km-vent)	Approximate size of particles (mm)	Thickness	Reference
–	0	–	>300 cm	Fernández Navarro (1911)
Mt. de las Flores	1	50–70	–	Ponte y Cologan (1911)
–	1	<64	Tens of cm	Fernández Navarro (1911)
Las Abiertas	5	10	–	Fernández Navarro (1911)
close Mt. de Vancheque	5	–	Tens of cm	Fernández Navarro (1911)
Icod	9	9–15	Several cm	Newspaper “Arautápala” 20 November 1909
Icod	9	1–1.8	Several cm	Fernández Navarro (1911)
–	11	9–15	–	Newspaper “Arautápala” 20 November 1909
La Rambla	15	–	A few mm	Cabrera Diaz (1911)
Los Realejos	19	9–15]	–	Newspaper “Arautápala” 20 November 1909
La Orotava	25	–	A few mm	Fernández Navarro (1924)
Punta del Hidalgo	52	–	A few mm	Fernández Navarro (1924)
Las Palmas (Gran Canaria)	130	–	–	newspaper “ABC Martes” 23 November 1909

Table 2.1. Approximate size of particles from the fallout and thickness of deposits reported by scientists and witnesses at various distances from the vent during the 1909 eruption (after Di Roberto et al., 2016).



### 3. DISCUSSION

In this chapter the comprised papers will be discussed and an in-depth look of the obtained results will be pursued not only as individual works but also as a whole. The 2011 El Hierro eruption was the framework in order to study the eruptive dynamics for the recent volcanism on the island, the petrology evolution and any implications on volcanic hazard assessment.

As seen in the results chapter, the emitted products during the early stages of the 2011 eruption presented a heterogeneous texture, mineralogy and chemical composition - two inner parts with high SiO<sub>2</sub> concentrations and a common mafic outer part. After identifying the external part, the basanite, as the magma that fed the eruption, and including its data (mineral assemblage and composition) in the thermodynamic modelling, a fast ascent from a reservoir located at 400 MPa (~12–14 km) has been revealed (Figure 3.1), something that is in agreement with the localized seismicity, and hardly indicates any prolonged pre-eruptive stationing in the crust. Comparing the vesicles (size distribution) of the basanite and xenopumices suggests a concurrent, single event of bubble nucleation and growth. Any differences between vesicles size can be ascribed to quenching processes.

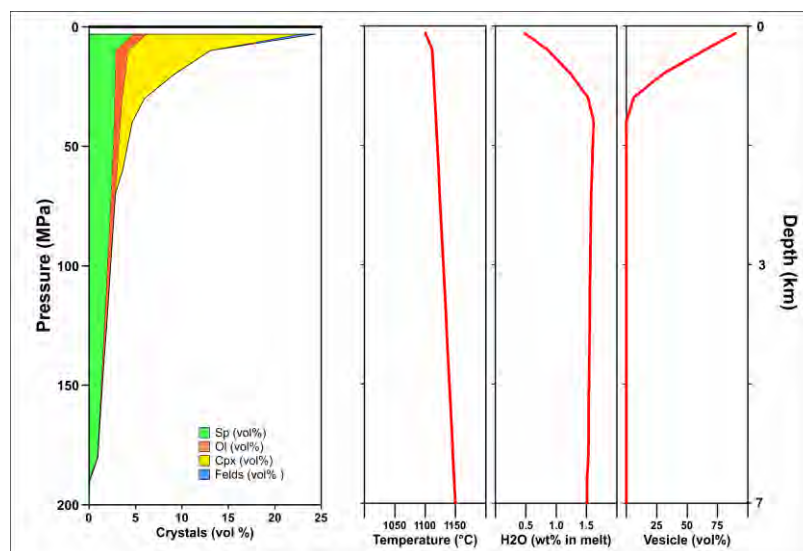


Figure 3.1. Paragenesis and mineral abundance for basanite, reproduced through polybaric differentiation from 400 MPa to 30 MPa, from 1190 to 1100 °C (cooling rate of  $\approx 0.33$  per MPa) and in redox conditions of FMQ -1.

On the other hand, the mineral assemblage and compositions of grey trachytic xenopumices are compatible with those of a magma batch still hot (~900 °C) and differentiating at relative shallow depth (P ~100 MPa ~4 km) probably stored in a small sill within the volcanic edifice that was possibly reheated by the interaction with carrier basanitic magma. The finding of quartz may also be explained by these processes of alteration (Donoghue et al., 2010). High values of  $\delta^{18}\text{O}$  are also strong indicators of this hydrothermal activity (Troll et al., 2011) taking place in presence of sea water.

Reheating and remobilization of a stagnant melt differentiating in the crust is a viable mechanism to explain the origin of the xenopumice. A similar process has been proposed as well by other authors for the products of the same eruption (Sigmarsson et al., 2012).

The detailed stratigraphic and petrological study of the Malpaso deposit evidence its pyroclastic nature, associating it to the last stages of an explosive eruption where water was involved. This trachytic pumice deposit on El Hierro was attributed to different periods of the island evolution and to different types of deposition mechanisms. Even though the erosion has significantly removed part of the deposit, it covers an area of approximately 15 km<sup>2</sup>, almost 5% of the total area of El Hierro, with a volume of the exposed products of about  $1.8 \times 10^6$  m<sup>3</sup>. The distribution of the pumice deposits, variations in lateral grain size and the isopleth map suggest that the position now occupied by Tanganasoga is the most suitable location for the vent of the Malpaso member.

Each of the four units identified in the sequence, points out to a different phase of the eruption and can be interpreted in terms of changing of eruptive dynamics and of the transport and depositional systems.

As per structure, distribution, grain size, gradation and composition these units indicate the following phases and ambients:

N1 : likely to have been formed by deposition from a turbulent and low concentrated unsteady current with direct suspension sedimentation, during a pulsating pyroclastic surge or multiple but discrete closely pyroclastic density current (PDC)-spaced events

N2 : with similar characteristics to those of N1, but due to its structure of thin beds of ash and pumice, we could say that the lapilli-poor material transported by suspension in a dilute turbulent flows, while the lapilli-rich layers represent the base of the flow where traction could be induced

N3 : its laterally continuous stratified thin ash beds with plane-parallel laminations have been interpreted as pyroclastic surge deposits based on plane-parallel and low-angle cross laminations

N4 : based on its characteristic repetitive beds of ash and lithic-rich lapilli thin beds with continuous internal stratification with sharp or diffuse boundaries and inverse grading, could be interpreted as a fallout deposit or as pyroclastic surge and co-surge fallout deposit, and in this case the mechanism of deposition probably was a single low concentration PDC

Overall, the lack of any fall deposits at the base of each unit indicates that most of the studied deposits were formed directly from dilute PDCs radially expanding from the vent during vulcanian-type explosions with no rise of any sustained convective column or due to a progressive feeding of the transporting system by continuous eruption column collapse. Also the sharp contacts with adjacent units demonstrate time-gap between deposition of individual units but not long enough for soil to form, suggesting that the whole Malpaso member corresponds to the products of a single eruptive event with several pulses of PDC generation, something that is also supported from field evidences such as rounding of pumice and lateral changes of texture and thickness on local scale.

Regarding the environment conditions, details like thinly laminated, fine- and coarse-grained beds, grain size (Figure 3.2), internal distribution of the deposits and textural features of the juvenile material, suggest magma/water interaction. Furthermore, units 1 and 2, because of their structure and texture, can be identified with a significant widening of the conduit during the first phases of the eruption. The composition of unit 3 suggests efficient fragmentation of the magma, while unit 4 reflects a renewed efficiency of magma/water interaction with overpressure conditions following the entrance of large quantities of steam in the conduit. In any case, groundwater was most likely, the main source leading to this magma/water interaction.

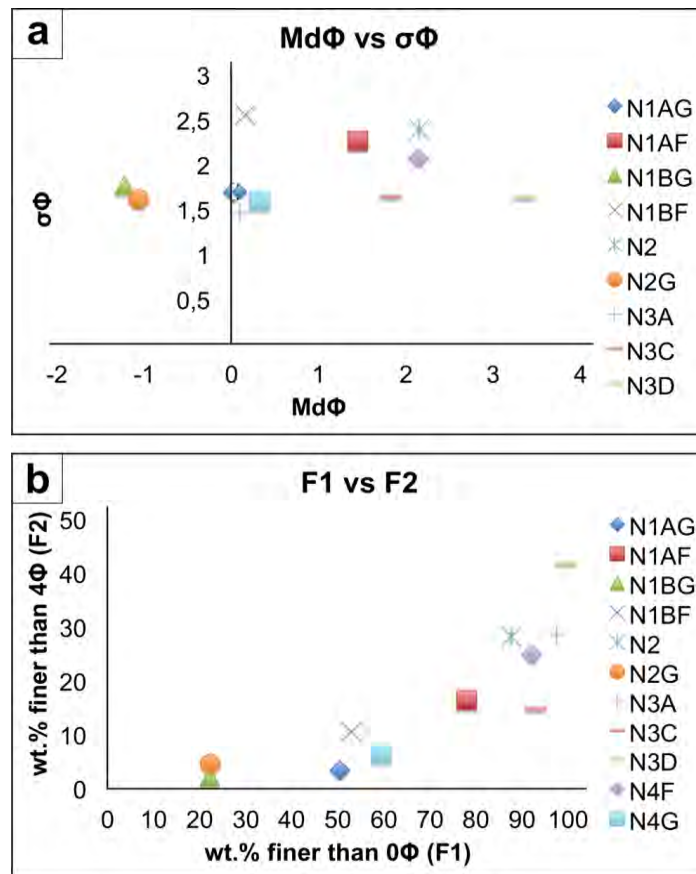


Figure 3.2. (a) Standard deviation versus median diameter. (b) F2 (wt.% <1 mm diameter) versus F1 (wt.% <1/16 mm diameter); (after Pedrazzi et al., 2014).

In order to elucidate the origin of the xenopumice (which is inhomogeneous in texture and geochemistry), characterize and relate it with the volcanic activity on the island, a comparison of bulk rock and glass compositions of El Hierro xenopumice and extrusives has been carried out. In addition, radiogenic isotope compositions of xenopumice samples are compared with: El Hierro and La Palma magmatic extrusive and intrusive rocks, Jurassic oceanic crust beneath Gran Canaria pelagic and terrigenous sediments from Gran Canaria and east Atlantic Ocean.

Clues to the volcanic origin of the xenopumice are preserved in the partially molten feldspars as well as in the remnants of biotite, which are among the phases that better survive hydrothermal alteration. Besides indicating a magmatic origin of the protolith, these restitic phases are compatible with trachyandesite or trachyte mineralogy, matching in composition and mineralogy the subaerial Holocene trachyte (Malpaso deposit).

The role of hydrothermal alteration in transforming an inferred trachytic protolith is supported by the presence of quartz, characterized by argillic and/or silicic alteration and concentric layers of "impurities" (Sigmarsson et al., 2013) and inclusions of Ti- REE phases, evidence that this quartz does not have a sedimentary origin. Also, the heterogeneous REE and HFSE compositions of the xenopumice could result from the hydrothermal alteration of trachyandesite or trachyte, consistent with the general depletion of elements and relative enrichment in SiO<sub>2</sub> that is typical of advanced argillic to silicic alteration facies. The veins facies are probably the remains of the protolith rock hydrothermal fluid circulation paths, in which mineral precipitation from the hydrothermal solutions prior pyrometamorphism is confirmed by the presence of hydrothermal quartz, zircon and REE-oxides aggregates in an Al-rich groundmass probably indicating advanced argillic alteration of the protolith.

According to the above evidence, trachyandesite-trachyte of the El Hierro submarine edifice was affected by acidic fluid circulation, which gave rise to heterogeneous leaching. Mineral aggregates, restitic phases, and the bulk trachyte *stricto sensu* composition characterizing the grey xenopumice facies, all probably represent parts of the protolith in which hydrothermal leaching was relatively weak (Figure 3.3). By contrast, the white xenopumice facies, were probably derived from strongly hydrothermally altered rocks in which original textures and mineral phases are (almost) completely obliterated. Before pyrometamorphic transformation induced by contact with basanitic magma, the xenopumice protolith was probably subjected to intermediate-advanced argillic alteration. It is probable that protolith rocks suffered hydrothermal alteration inside the volcanic edifice, as there are only a few traces of seabed hydrothermalism-metamorphism (i.e., the weak Ba enrichment; Rodriguez-Losada et al. 2014).

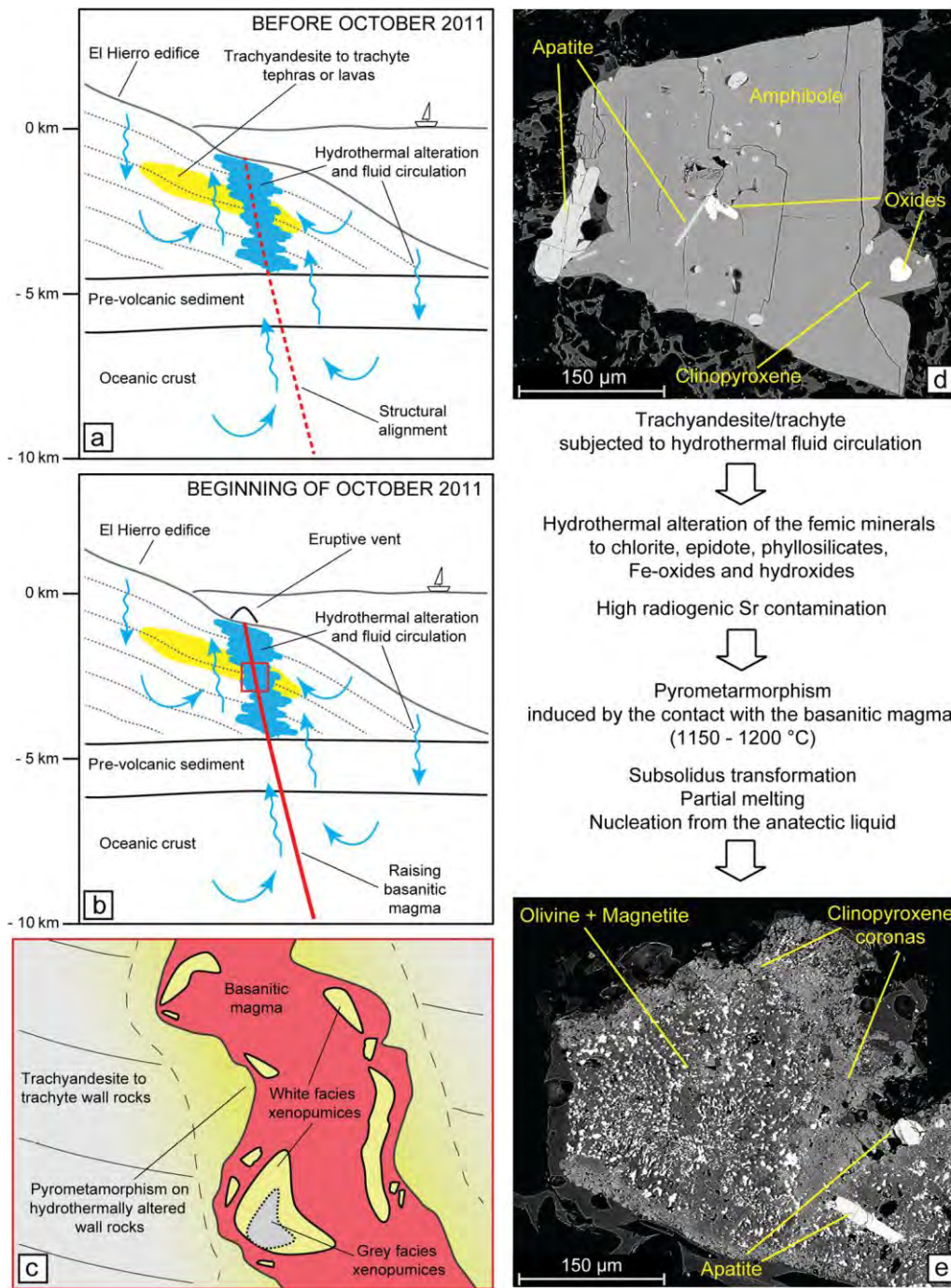


Figure 3.3. Simplified sketch summarizing the processes leading to xenopumice formation. (a) Hydrothermal fluid circulation locally altered trachyandesite/ trachyte products forming the El Hierro submarine edifice. (b) & (c) Hydrothermally altered wall rocks undergoing pyrometamorphism upon contact with the raising basanitic magma. (d) SEM-BSE image of mafic minerals in the Holocene subaerial El Hierro trachyte (inferred to be similar to some buried counterparts of the subvolcanic edifice). (e) SEM-BSE image of pseudomorphic minerals in the grey facies (after Del Moro et al., 2015).

The Sr, Nd, and Pb isotopic ratios of the analyzed xenopumice clearly indicate the magmatic nature and reflect processes of hydrothermal alteration (high  $^{87}\text{Sr}/^{86}\text{Sr}$  ratio of the grey facies, homogeneous  $^{143}\text{Nd}/^{144}\text{Nd}$  values for the white and grey facies, and grey facies Pb isotopic ratios close to the upper limit of the magmatic products of the volcano).

For the 2011 El Hierro eruption, crucial information regarding ascent dynamics was extracted from geophysical and geodetical data.

During the pre-eruptive period geophysical and geodetical signals indicate that magma was emplacing within the lower crust or close to the Moho discontinuity (López et al., 2012). The distribution and low-magnitude seismicity, combined with the deformation pattern, suggest that small-volume intrusions of magma, propagated in different direction possibly as fingers, took place at 8-12 km of depth in the centre, centre-south sectors of the island. The geometry of the intrusions was possibly controlled by pre-existing intrusive complexes and zones of structural weakness (González et al., 2013; Gorbatikov et al., 2013; García-Yeguas et al., 2014).

The drastic change both in the seismicity and ground deformation pattern occurred on early September likely indicates a change in the dynamics of magma movement. After relocation of seismic events it was clear that it represents a real migration with the hypocenters marking tight clusters. Seismic and ground deformation data indicate that, ten days before the onset of the eruption, a storage system was emplaced at depth (12-16 km), off the coast of El Julan. The 12 hours of seismic silence occurred between the major ML = 4.3 earthquake and the sudden appearance of seismic multiplets at <3 km of depth close to the future vent, were attributed to the interaction of the ascending magma with a stagnant magma pocket/s and hydrothermally altered volcanic rocks. The interaction (heating/pyrometamorphism) between the basanitic magma feeding the eruption, and the rocks/magma of the ductile zone would have initially resulted in an almost aseismic, horizontal expansion of the magma and later in the shallow seismicity. Materials resulting from this interaction were emitted and have been studied in this thesis.

A relatively low magnitude seismicity at depth of 10-14 km was registered for about 20 days after the onset of the eruption and again from early January to March 2012, interpreted as the readjustment of the stress field nearby the vent and the relaxation of the host rock when finally the eruption ceased, respectively. The deep seismicity in the northern part of the island consisted in two distinct swarms the first at 20-25 km since October 18 and the second, starting one week later at 15-20 km, respectively, indicating an emplacement of magma at depth without significant deflation of the plumbing system.

Regarding the information on ascent dynamics, that could be retrieved by the petrological data, it was observed that bulk rocks compositions varied significantly during the eruption with a progressive and continuous shift towards more mafic term, implying the existence of a zoned magma body that was progressively withdrawn during the eruption. The overall constancy of highly incompatible elements ratio (e.g. Rb/Nb, Rb/Th, Rb/Lb and Nb/La) *versus* time indicates that the process of magma differentiation responsible of such a zoning operated from a single parental magma (Figure 3.4). Although limited mixing processes may have occurred in shallow mantle depths, due to convective circulation, large-scale mixing process involving two reservoirs is unlikely since it is incompatible with regular compositional variations that were observed during the eruption (in accordance with Longpré et al., 2017).

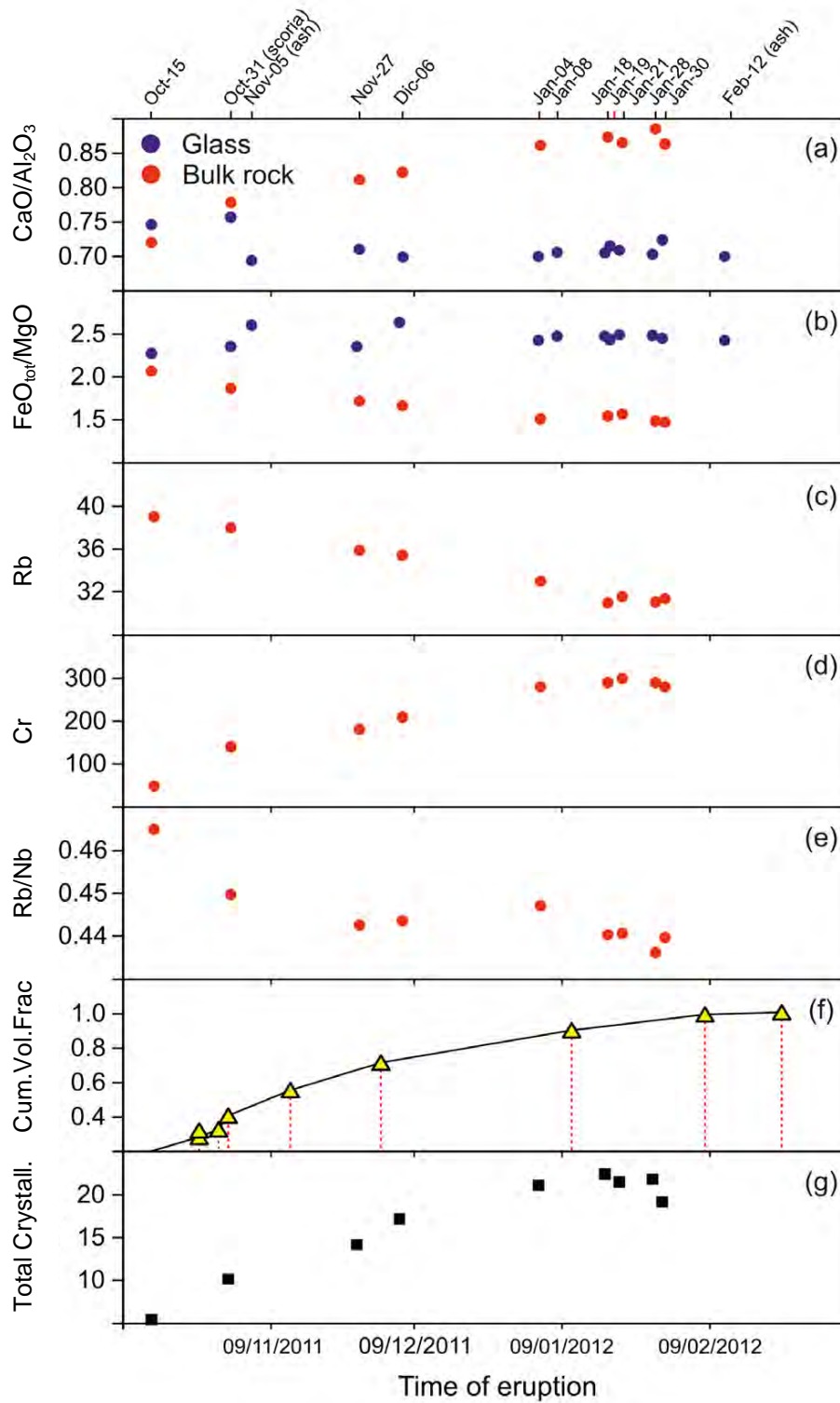


Figure 3.4. (a)  $\text{CaO}/\text{Al}_2\text{O}_3$  and (b)  $\text{FeO}_{\text{tot}}/\text{MgO}$  versus time for bulk rocks (red circles) and glasses (blue circles) composition. (c-e) Temporal variation diagrams of (c) Rb, (d) Cr and (e) Rb/Nb ratio (unit in ppm). (f) Cumulative volume fraction (yellow triangles) of erupted material after Rivera et al., 2013. (g) Total crystallinity (wt.%) obtained by mass balance calculation between bulk rocks and glass considering the average composition of minerals (after Meletlidis et al., 2015).

In fact, the full re-homogenization before the ascent and emplacement in a third crustal storage (10-15 km) would have been followed by an additional process of segregation and cumulus of mafic phases during the syn-eruptive ascent, in order to account for the regular variation observed in bulk rock composition.

The 1909 eruption of Chinyero was previously considered to be low intensity explosive Strombolian activity that did not represent a serious threat to the population or infrastructure of the time. This assumption mainly derives from the little photographic evidence of volcanic activity and from incomplete and fragmentary descriptions of the eruptive phenomena by eyewitnesses and scientists who observed the eruption only several hours after its onset or even weeks after it ended. However, data derived from the comprehensive review of historical sources and from early scientific reports, combined with field and laboratory data on deposits, reveal a very different scenario and clarify some crucial aspects regarding volcanic hazards in the modern Canary Islands.

The intense seismic activity, that preceded the eruption of Chinyero, and the contemporaneous formation of strong fumarole activity at the base of the Pico Viejo cone, could be associated with the intrusion and movement of an undefined volume of magma through the ocean crust and under the Tenerife volcanic complex, similarly to the 2011–2012 eruption of El Hierro (Martí et al., 2013a, b; Meletlidis et al., 2015). Also, the lack of time-related trends in crystal contents or in bulk rock, glass and minerals compositions, as resulted from the analysis, suggest that the whole eruption was fed by a single, relatively small, very homogeneous batch of magma. Additionally, the low phenocryst content, in both fallout pyroclastic deposits and lavas, suggests that the magma rapidly rose to the surface without stalling significantly along the route.

The initial opening phase was rapidly followed by energetic Strombolian activity that probably lasted between the onset of the eruption and the first observations by Ponte and Cologan in the early morning of 19 November. In this period, the monotonous sequence of well sorted, moderately to highly vesicular scoriaceous lapilli and ash was emplaced in the areas surrounding the volcano and up to several kilometres from the vent (Figure 3.4); the Chinyero scoria cone was also built and the first lava flow with a length of ca. 200 m was emplaced.

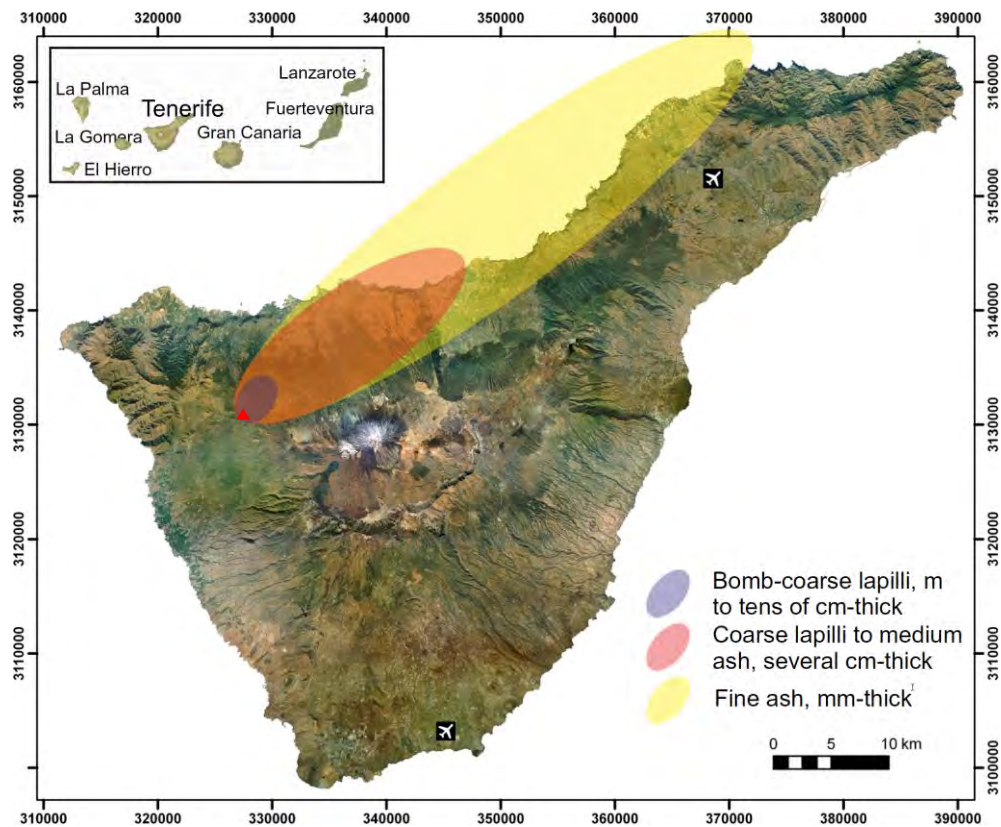


Figure 3.4. Map of Tenerife Island showing distribution of pyroclastic fall deposits reconstructed on the basis of historical reports and used to the approximate calculation of tephra volume. Red triangle indicates the Chinyero volcano and the airplane signs indicate Tenerife Norte (TFN) and Sur (TFS) airports (after Di Roberto et al., 2016).

The field relationships between pyroclastic products and lava flows suggest that the emission of ash and lapilli fallout from quasi-steady eruption plumes, alternated with the effusion of lavas (Brown et al., 2015). The rate of growth of the Chinyero cone (assuming a maximum duration of 17 h) is comparable or even higher than those of scoria cones built during violent Strombolian eruptions like Parícutín (Foshag and Gonzalez, 1956) or the 2001 eruption of Mt. Etna (Behncke and Neri, 2003).

Concerning the impact of the eruptions that have been discussed, and hazard implications, it is evident, through the global approach that has been carried out, that the composition of the magma is decisive in the style and magnitude of this type of eruption, but also factors such as the internal structure of the crust, magma/water interaction, localization and topography of the vent, pre- and syn-eruptive accompanied parameters, should be taken into account, in assessing the potential volcanic hazard on the islands.

Earlier works about the plumbing systems below Canary Islands consider magma pockets at different depths, result of intrusions that never reached the surface, due to low magma volume rate, local stress fields or discontinuities. These are responsible for islands evolution through the underplating process (Galipp, 2006; Carracedo, 2008 and 2015; Klügel, 2005; Stroncik, 2009) but, as it has also been shown, for complex processes that can change the eruption evolution and define certain patterns in the instrumental data that have to be considered. Magma/water interaction, due to surface or ground water availability, can be responsible for an increase in the energy of an explosive phase, but as seen in the Chinyero eruption where magma had a similar composition of the one of El Hierro eruption, moderate to violent activity is possible during the first hours/days of the eruption. Furthermore, if such an eruption occurs, air transport from/to the islands would likely be interrupted, causing substantial direct, indirect and induced impacts on industries dependent on air transport (e.g. travel and tourism, global exchange of goods, manufacturing supply chains). Note that tourism is presently the economic driving force for the archipelago and almost 90% of the daily consumer needs are covered through imports.

The succession of unrest episodes following the 2011 eruption and episodes in other islands, like the 2004 Tenerife unrest or the recent seismic activity nearby the Teide-Pico Viejo edifice, suggest that fresh magma keeps accumulating below the surface and both long- and short-term hazard assessments on the islands should take into account possible scenarios related to the eruption of basaltic magmas.

## 4. CONCLUSIONS

The 2011–2012 El Hierro eruption proved to be an excellent opportunity to study the monogenetic basaltic volcanism on the island, compare the products emitted with others from earlier eruptions, and apply techniques and instrumental data in order to achieve a comprehensive knowledge about the processes that take place before and during such types of eruption. This multidisciplinary approach provides new information about magma ascending, conditions and inner processes, basaltic eruptions, mechanisms of deposition, interaction scenarios and finally their products. These findings can play an important role in enhancing volcanic hazard assessment not only for El Hierro island but for the whole Canary archipelago and boost studies on basaltic monogenetic volcanism, which is definitely the most likely to occur in the next years.

- The 2011 El Hierro eruption was marked by a fast ascent of the basanitic magma from the depth of 12–14 km and at shallow depth interacted with trachytic magma pocket/s and with an associated alteration halo with rhyolitic composition. Trachytic magma and altered rocks were heated to various degrees, and they respectively generated the grey and white xenopumice. After the mingling and shortly before the extrusion, basanite and xenopumices shared a simultaneous event of bubble nucleation and growth followed by rapid cooling.
- The magmatic origin of the xenopumices is indicated by the presence of partially melted restitic minerals. Their mineralogy closely matches that of trachyandesite/ trachyte rocks and also shows geochemical magmatic signature comparable with representative trachyandesite and trachyte rocks of El Hierro. In addition, xenopumice Nd isotope ratios perfectly match the volcano's magmatics. Evidence of hydrothermal alteration suffered by the xenopumice protolith prior to pyrometamorphism can be found in the presence of zoned quartz, microcrystalline pseudomorphic aggregates, mineralized veins and variable xenopumice Sr and PB isotopic ratios.

Unlike the Malpaso Member, this pocket/s seemed not to have sufficient volume of trachytic magma, in order to change the dynamics of the eruption, although, during the first stages of the eruption and due to high volatile contents, a violent phase had taken place, that could be identified as a moderate Strombolian- type explosive activity. This is consistent with the shape and texture of the emitted products, the rapid construction of the submarine cone (Rivera et al., 2013) and the strong bubbling at the ocean surface.

The study of the sub-aerial deposit of Malpaso, originated from a base-surge-type explosive eruption with a subsequent radial emplacement of dilute PDCs from the vent, provides clues of the magma/water interaction influence on the dynamics of the eruption and also, with similar compositions to the 2011 eruption erupted products, indicate that basaltic intrusions have the potential for producing explosive eruptions.

According to geophysical and geodetical data the 2011 eruption was driven by a stepwise migration of a batch of magma between three main magmatic environments, including a deep reservoir, a crustal magma reservoir and a final shallow conduit and vent zone. When, on July 2011, magma reached the depth of 8-12 km, initially propagated as small-volume fingers or lobes, not capable of generating new fractures inside the volcanic edifice and its path was controlled by pre-existing intrusive complex and zones of structural weakness within the edifice, resulting in a typical distribution of earthquakes. On September 2011, the magma migrated southward forming a storage system off the coast of El Julan and changed the seismic activity depth (12-16 km). After a period of stagnation of about a month, the magma rapidly ascended to the final eruptive site, from where, a final aseismic ascent occurred, through relatively weak paths that could be identified as previous intrusions and small interconnected pockets of evolved magmas.

The stepwise ascent of magma of relatively small volume magma pockets (likely in the form of interconnected dyke and sills) is in agreement with that proposed by Stroncik et al. (2009) for El Hierro and other intraplate volcanoes, which includes multistage magma ascent with major crystal fractionation in the uppermost mantle and short-term stagnation at shallower levels (Figure 4.1).

From the petrological data can be deduced that the 2011 El Hierro eruption was fed by a single magma whose composition varied through a dominant process of crystals fractionation and crystals cumulus of mafic phases, in agreement with new results in Longpré et al. (2017). Unfortunately, thermodynamic modelling cannot discriminate if this process occurs in the mantle reservoir or in the crustal storage zone.

The same mechanism of magma ascent as in the El Hierro eruption, occurred in the 1909 Chinyero eruption, which was fed by a compositionally homogeneous batch of magma. Ascension was relatively fast from depth without significant stalling. At least in the early phases, the ascending magma produced a rather violent eruption. Rapidly pulsating or quasi-steady eruption columns produced the fallout of well-fragmented pyroclasts and scarce ballistic bombs. This type of activity produced the heavy fallout of lapilli and ash over the entire NE flank of the island of Tenerife, with fine ash reaching the island of Gran Canaria, situated more than 100 km from the vent.

The results of this dissertation confirm the importance of the study of the early products of an eruption, since they can contain crucial information on the volcano structure and the mechanism of magma ascent. Combining the petrological findings with the instrumental data is useful, in order to assess the state of the magmatic system and its possible evolution, and comparing it with passed eruptive activity can provide clues for future eruptions patterns.

Both long- and short-term hazard assessments for the islands, should take into account possible scenarios that include the 2011 submarine eruption, Malpaso felsic explosive eruption and its magma-water interaction and Chinyero, short but initially violent, basaltic eruption.

An extra effort to evaluate the real intensity and magnitude of past basaltic eruptions should be considered, as the study and comprehension of the processes leading to them are fundamental for a better understanding of the evolution of an active volcanic area such as the Canary Islands.

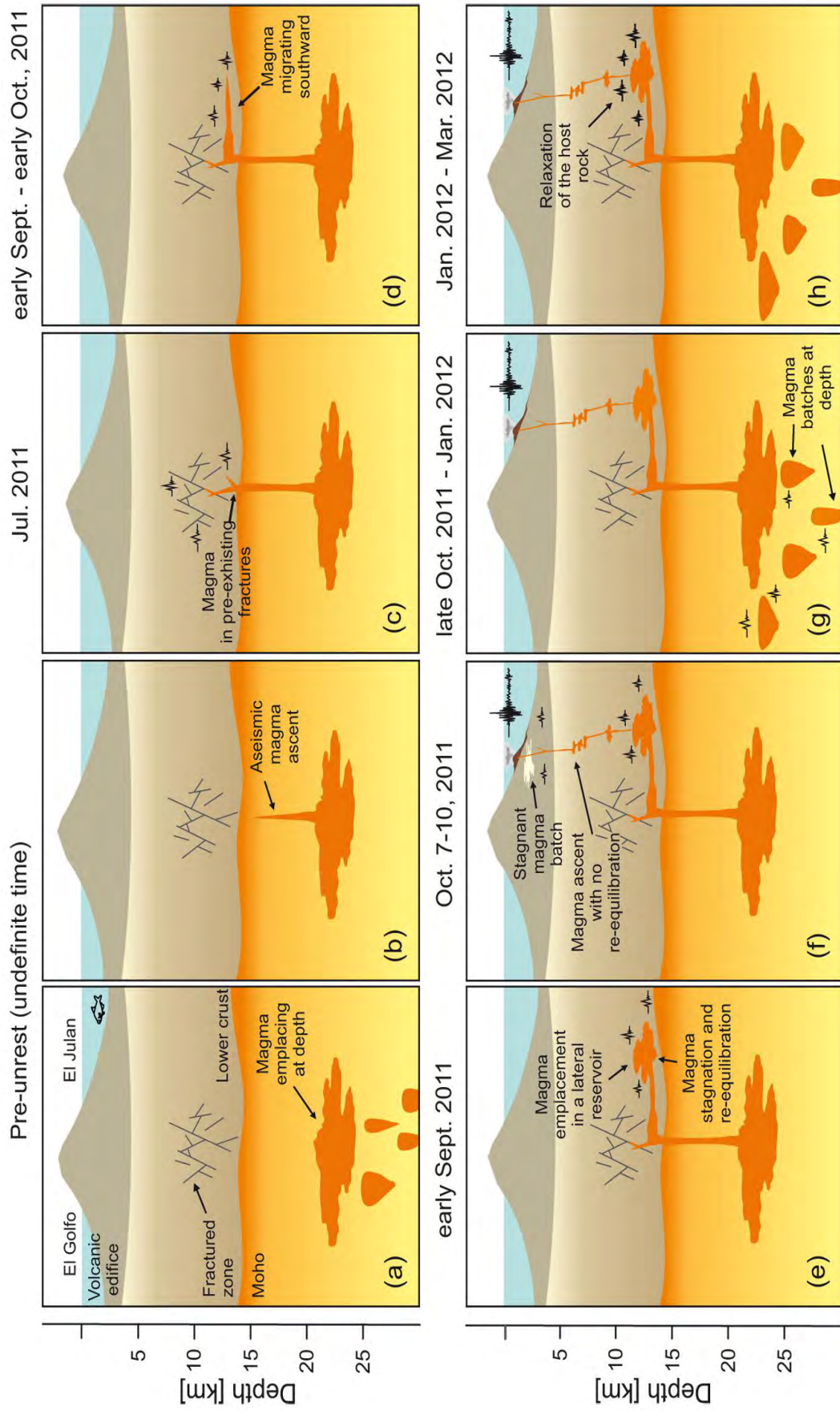


Figure 4.1. Cartoon interpretation (not to scale) of the volcanic system activated in El Hierro Island during the 2011-2012 unrest and eruption (along a north-south cross section). Panels (a-h) show in brief the main events that led to the eruption (after Meletlidis et al., 2015).

## 5. REFERENCES

- ❖ Ablay, G., 1997. Evolution of the Teide-Pico Viejo complex and magma system, Tenerife, Canary Islands. Ph.D. thesis, University of Bristol
- ❖ Ablay, G.J., Carroll, M.R., Palmer, M.R., Martí, J., Sparks, R.S.J., 1998. Basanite-phonolite lineages of the Teide-Pico Viejo Volcanic Complex, Tenerife, Canary Islands. *Journal of Petrology* 39 (5), 905-936.
- ❖ Acosta, J., Uchupi, E., Smith, D., Muñoz A., Herranz, P., Palomo, C., Llanes, P., and Ballesteros, M., 2003. Comparison of volcanic rifts on La Palma and El Hierro, Canary Islands and the Island of Hawaii, *Mar. Geophys. Res.*, 24, 59–90, doi:10.1007/s11001-004-1162-6.
- ❖ Albert, H., Perugini, D., Martí, J., 2015. Fractal analysis of enclaves as a new tool for estimating rheological properties of magmas during mixing: the case of Montaña Reventada (Tenerife, Canary Islands) *Pure Appl. Geophys.*, 172, pp. 1803–1814 <http://dx.doi.org/sire.ub.edu/10.1007/s00024-014-0917-5>
- ❖ Albert, H., Costa, F., Martí, J., 2015b. Timing of Magmatic Processes and Unrest Associated with Mafic Historical Monogenetic Eruptions in Tenerife Island. *Journal of Petrology*, v.56(10):1945-1965
- ❖ Albert, H., Costa, F., Martí, J., 2016. Years to weeks of seismic unrest and magmatic intrusions precede monogenetic eruptions. *Geology*. doi:10.1130/G37239.1
- ❖ Andújar, J., Costa, F. & Scaillet, B., 2013. Storage conditions and eruptive dynamics of central versus flank eruptions in volcanic islands: The case of Tenerife (Canary Islands, Spain). *Journal of Volcanology and Geothermal Research*, 260:62–79. ISSN 03770273. doi:10.1016/j.jvolgeores.2013.05.004.
- ❖ Anguita, F., Hernán, F., 1975. A propagating fracture model versus a hot spot origin for the Canary Islands. *Earth Planet. Sci. Lett.* 27, 11\_19.
- ❖ Anguita, F., Hernán, F., 2000. The Canary Islands origin: a unifying model. *J. Volcanol. Geoth. Res.* 103, 1\_26.

- ❖ Araña, V., and Ibarrola E., 1973. Rhyolitic pumice in the basaltic pyroclasts from the 1971 eruption of Teneguía volcano, Canary Islands, *Lithos*, 6, 273–278, doi:10.1016/0024-4937(73)90088-1.
- ❖ Araña, V. and Ortíz R., 1991. The Canary Islands: Tectonics, magmatism and geodynamic framework. En *Magmatism in extensional structural settings. The Phanerozoic African Plate*. Eds. A.B. Kampunzu y R.T. Lubala, 209-249. Springer- Verlag.
- ❖ Becerril, L., 2009. Approach to volcanic hazard and its effects 582 in coastal areas of the Canary Islands. Master's thesis, Universidad de Las Palmas de Gran Canaria, Spain
- ❖ Becerril, L., Cappello, A., Galindo, I., Neri, M., Del Negro, C., 2013. Spatial probability distribution of future volcanic eruptions at El Hierro Island (Canary Islands, Spain). *Journal of Volcanology and Geothermal Research* 257(0):21-30
- ❖ Behncke, B. & Neri, M., 2003. The July-August 2001 eruption of Mt. Etna (Sicily). *Bull Volcanol* 65:461–476. doi:10.1007/s00445-003-0274-1
- ❖ Biass, S., Bonadonna, C., 2014. TOTGS: total grainsize distribution of tephra fallout, <https://vhub.org/resources/3297>.
- ❖ Bonadonna, C., Houghton, B.F., 2005. Total grain-size distribution and volume of tephra-fall deposits. *Bull Volcanol* 67:441–456. doi:10.1007/s00445-004-0386-2
- ❖ Bonadonna, C. and Costa, A., 2013. Plume height, volume, and classification of explosive volcanic 630 eruptions based on the Weibull function. *Bulletin of volcanology* 75(8):1-19.
- ❖ Branne, M.J. and Kokelaar, P., 2002. Pyroclastic density currents and the sedimentation of 591 ignimbrites. *Geological Society of London Memoirs*, p 150
- ❖ Brown, R.J., Thordarson, T., Self, S., Blake, S., 2015. Disruption of tephra fall deposits caused by lava flows during basaltic eruptions. *Bull Volcanol* 77:90. doi:10.1007/s00445-015-0974-3
- ❖ Burchard, O., 1909. Ein neuer vulkanischer Ausbruch auf Teneriffa. *Globus: illustrierte Zeitschrift für Länder und Völkerkunde* 97:21–25
- ❖ Büttner, R., Dellino, P., Zimanowski, B., 1999. Identifying modes of magma/water interaction 597 from the surface features of ash particles. *Nature* 401:688-690

- ❖ Carracedo, J.C., Day, S.J., Guillou, H., Rodríguez Badiola, E., Canas, J.A., Pérez Torrado, F.J., 1998. Hotspot volcanism close to a passive continental margin: the Canary Islands. *Geol. Mag.* 135 (5), 591\_604.
- ❖ Carracedo, J.C., 1999. Growth, structure, instability and collapse of Canarian volcanoes and comparisons with Hawaiian volcanoes. *J. Volcanol. Geoth. Res.* 94, 1\_19.
- ❖ Carracedo, J.C., Rodríguez Badiola, E., Guillou, H., De La Nuez, J., and Pérez Torrado, F., 2001. Geology and volcanology of La Palma and El Hierro, Western Canaries, *Estud. Geol.*, 57, 175–273, doi:10.3989/egeol.01575-6134.
- ❖ Carracedo, J.C., Rodríguez Badiola, E., Pérez Torrado, F.J., Hansen, A., Rodríguez-González, A., Scaillet, S., et al., 2007a. La erupción que Cristóbal Colón vió en la isla de Tenerife (Islas Canarias). *Geogaceta* 41, 39\_42.
- ❖ Carracedo, J.C., Rodríguez Badiola, E., Guillou, H., Paterne, M., Scaillet, S., Pérez Torrado, F.J., et al., 2007b. Eruptive and structural history of Teide volcano and rift zones of Tenerife, Canary Islands. *Geol. Soc. Am. Bull.* 19, 1027\_1051.
- ❖ Carracedo, J.C., 2008b. *Canarian Volcanoes IV: La Palma, La Gomera y El Hierro*. Rueda, Madrid, p. 213
- ❖ Carracedo, J.C., Guillou, H., Nomade, S., Rodríguez-Badiola, E., Pérez-Torrado, F.J., Rodríguez-González, A., et al., 2011b. Evolution of ocean-island rifts: the northeast rift zone of Tenerife, Canary Islands. *Geol. Soc. Am. Bull.* 123, 562\_584.
- ❖ Carracedo, J.C., 2013. The last 2 ky of eruptive activity of the Teide volcanic complex: features and trends. In: Troll VR, Carracedo JC (eds) *Teide volcano*. Springer, Berlin, pp. 129–153
- ❖ Carracedo, J.C., Troll, V.R., Zaczek, K., Rodríguez-González, A., Soler, V., Deegan, F.M., 2015a. The 2011/ 2012 submarine eruption off El Hierro, Canary Islands: new lessons in oceanic island growth and volcanic crisis management. *Earth Sci. Rev.* 150, 168\_200.
- ❖ Cerdeña Domínguez, I., del Fresno, C., Rivera, L., 2011. New insight on the increasing seismicity during Tenerife's 2004 volcanic reactivation, *J. Volcanol. Geotherm. Res.*, 206 (2011), pp. 15–29
- ❖ Clarke, H., Troll, V.R., Carracedo, J.C., 2009. Phreatomagmatic to Strombolian eruptive activity of basaltic cinder cones: Montaña Los Erales, Tenerife, Canary Islands. *J Volcanol Geotherm Res*, 180, 225–45. Doi:10.1016/j.jvolgeores.2008.11.014.

- ❖ Cioni, R., Bertagnini, A., Santacroce, R., Andronico, D., 2008. Explosive activity and eruption scenarios at Somma-Vesuvius (Italy): towards a new classification scheme. *J Volcanol Geotherm Res* 178:331– 346. doi:10.1016/j.jvolgeores.2008.04.024
- ❖ Cioni, R., Bertagnini, A., D’Oriano, C., Pompilio, M., 2010. Past and present mid-intensity explosive eruptions of Italian volcanoes and their impact on human activity. *J Virt Expl.* doi:10.3809/jvirtex.2009.00229
- ❖ Collier, J.S., and A.B. Watts (2001). Lithospheric response to volcanic loading by the Canary Islands: constraints from seismic reflection data in their flexural moat, *Geophys. J. Int.*, 147, 660-676; doi:10.1046/j.0956-540x.2001.01506.x.
- ❖ Connor, C. B., Conway, F. M., 2000. Basaltic volcanic fields. *Encyclopedia of volcanoes*, pgs. 331–343.
- ❖ Fernández Navarro, L., 1911. Erupción volcánica del Chinyero (Tenerife) en noviembre de 1909. *Anales de la Junta para Ampliación de Estudios e Investigaciones Científicas*, V, Mem. 1, 99 pp.
- ❖ Fonseca, J. F., Faria, B. V., Lima, N. P., Heleno, S. I., Lazaro, C., d’Oreye, N. F., ... & Matos, J. L., 2003. Multiparameter monitoring of Fogo Island, Cape Verde, for volcanic risk mitigation. *Journal of volcanology and geothermal research*, 125(1), 39-56.
- ❖ Foshag, W.F., Gonzalez, R., 1956. Birth and development of Paricutin volcano Mexico. *Geological Survey Bulletin* 965-d
- ❖ Dach, R., Hugentobler, U., Fridez, P., Meindl, M., 2007. *Bernese GPS Software Version 5.0*, Astronomical Institute, University of Bern, Report.
- ❖ DelMoro, S., Renzulli, A., Tribaudino, M., 2011. Pyrometamorphic processes at the magma-hydrothermal system interface of active volcanoes: evidence from buchite ejecta of Stromboli (Aeolian Islands, Italy). *J Petrol* 52:541–564. doi:10.1093/petrology/egq090
- ❖ Donoghue, E., Troll, V., and Harris, C., 2010. Fluid-rock interaction in the Miocene, Post-Caldera, Tejada Intrusive Complex, Gran Canaria (Canary Islands): Insights from mineralogy, and O- and H-isotope geochemistry, *J. Petrol.*, 51, 2149–2176, doi:10.1093/petrology/egq052.
- ❖ Galipp, K., Klügel, A. and Hansteen, T.H., 2006. Changing depths of magma fractionation and stagnation during the evolution of an oceanic island volcano: La Palma (Canary Islands). *J. Volcanol. Geotherm. Res.*, 155(3-4): 285-306.

- ❖ García, O., Guzmán, S., Martí, J., 2014. Stratigraphic correlation of Holocene phonolitic explosive episodes of the Teide–Pico Viejo volcanic complex, Tenerife, *Journal of the Geological Society*, 171:375–387
- ❖ García, A., Fernandez-Ros, A., Berrocoso, M., Marrero, J.M., Prates, G., De la Cruz-Reyna, S., Ortiz, R., 2014. Magma displacements under insular volcanic fields, applications to eruption forecasting: El Hierro, Canary Islands, 2011-2013, *Geophys. J. Int.*; doi: 10.1093/gji/ggt505.
- ❖ García-Yeguas, A., Ibáñez, J.M., Koulakov, I., Jakolev, A., Romero-Ruiz, M.C., Rudencio, J., 2014. Seismic tomography model reveals mantle magma sources of recent volcanic activity at El Hierro Island (Canary Islands, Spain), *Geophys. J. Int.*, 199, 1739- 1750; doi:10.1093/gji/ggu339.
- ❖ Gee, M.J.R., Watts, A.B., Masson, D.G., and Mitchell, N.C., 2001. Landslides and the evolution of El Hierro in the Canary Islands, *Mar. Geol.*, 177, 271–293, doi: 10.1016/S0025-3227(01)00153-0.
- ❖ Geldmacher, J., Hoernle, K., Van den Bogaard, P., Duggen, S., Werner, R., 2005. New Ar-40/Ar-39 age and geochemical data from seamounts in the Canary and Madeira volcanic provinces: support for the mantle plume hypothesis. *Earth Planet. Sci. Lett.* 237, 85\_101.
- ❖ Ghiorso, M., and Sack, R., 1995. Chemical mass transfer in magmatic processes IV. A revised and internally consistent thermodynamic model for the interpolation and extrapolation of liquid-solid equilibria in magmatic systems at elevated temperatures and pressures, *Contrib. Mineral. Petrol.*, 119, 197–212, doi:10.1007/BF00307281.
- ❖ González, P.J., Samsonov, S.V., Pepe, S., Tiampo, S.F., Tizzani, P., Casu, F., Fernández, J., Camacho, A.G., Sansosti, E., 2013. Magma storage and migration associated with the 2011-2012 El Hierro eruption: Implications for crustal magmatic systems at oceanic island volcanoes, *J. Geophys. Res. Solid Earth*, 118, 1-17; doi:10.1002/jgrb.50289.
- ❖ Gorbatikov, A.V., Montesinos, F.G., Arnoso, J., Stepanova, M.Y., Benavent, M., Tsukanov, A.A., 2013. New Features in the Subsurface Structure Model of El Hierro Island (Canaries) from Low-Frequency Microseismic Sounding: An Insight into the 2011 Seismo-Volcanic Crisis, *Surv. Geophys.*, 34, 463-489; doi:10.1007/s10712-013-9240-4.
- ❖ Gottsmann, J., Wooller, L., Martí, J., Fernandez, J., Camacho, A., González, P., García, A., Rymer, H., 2006. New evidence for the reawakening of Teide volcano *Geophysical Research Letters*, 33 p. L20311

- ❖ Grapes, R.H., 1986. Melting and thermal reconstitution of pelitic xenoliths, Wehr volcano, East Eifel, Germany. *J Petrol* 27:343–396. doi:10. 1093/petrology/27.2.343
- ❖ Guillou, H., Carracedo, J.C., Pérez-Torrado, F.P., Badiola, E.R., 1996. K-Ar ages and magnetic stratigraphy of a hotspot-induced, fast grown oceanic island: El Hierro, Canary Islands. *J. Volcanol. Geoth. Res.* 73,141\_155.
- ❖ Guillou, H., Carracedo, J.C., Day, S.J., 1998. Dating the upper Pleistocene-Holocene volcanic activity of LaPalma using the unspiked K-Ar technique. *J. Volcanol. Geoth. Res.* 86, 137\_149.
- ❖ Guillou, H., Carracedo, J.C., Duncan, R., 2001. K-Ar,  $^{40}\text{Ar}/^{39}\text{Ar}$  Ages and magnetostratigraphy of Brunhes and Matuyama lava sequences from La Palma Island. *J. Volcanol. Geoth. Res.* 106, 175\_194.
- ❖ Guillou, H., Carracedo, J.C., Paris, R., Pérez-Torrado, F.J., 2004a. Implications for the early shield-stage evolution of Tenerife from K/Ar ages and magnetic stratigraphy. *Earth Planet. Sci. Lett.* 222, 599\_614.
- ❖ Guillou, H., Pérez Torrado, F.J., Hansen Machin, A.R., Carracedo, J.C.C., Gimeno, D., 2004b. The Plio-Quaternary volcanic evolution of Gran Canaria based on new K-Ar ages and magnetostratigraphy. *J. Volcanol. Geoth. Res.* 135 (3), 221\_246.
- ❖ Gutenberg, B., and Richter, C., 1954. *Seismicity of the Earth and Associated Phenomena* (Princeton University Press, Princeton, New Jersey), 2nd ed., 310 p.
- ❖ Heiken, G. and Wohletz, K., 1985. *Volcanic ash*. University of California Press, Berkeley. 246 pp
- ❖ Hiroi, Y. and Miyamoto, T., 2016. Relationship between eruptive style and vesicularity of juvenile clasts during eruptive episode A of Towada Volcano, Northeast Japan, *Journal of Volcanology and Geothermal Research*, Volume 325, Pages 86-97, ISSN 0377-0273, <http://dx.doi.org/10.1016/j.jvolgeores.2016.06.009>.
- ❖ Ibáñez, J.M., De Angelis, S., Díaz-Moreno, A., Hernández, P., Alguacil, G., Posadas, A., Pérez, N., 2012. Insights into the 2011-2012 submarine eruption off the coast of El Hierro (Canary Islands, Spain) from statistical analyses of earthquake activity, *Geophys. J. Int.*, 191, 659-670; doi:10.1111/j.1365-246X.2012.05629.x.
- ❖ Kereszturi, G., Németh, K., 2012. *Monogenetic Basaltic Volcanoes: Genetic Classification, Growth, Geomorphology and Degradation*, DOI: 10.5772/51387 in *Updates in Volcanology - New Advances in Understanding Volcanic Systems*, book edited by Karoly Nemeth, ISBN 978-953-51-0915-0

- ❖ Klügel, A., Hansteen, T.H., Schmincke, H.U., 1997. Rates of magma ascent and depths of magma reservoirs beneath La Palma (Canary Islands): *Terra Nova*, v. 9, p. 117–121, doi:10.1046/j.1365-3121.1997.d01-15.x.
- ❖ Klügel, A., Hoernle, K.A., Schmincke, H.-U., and White, J.D.L., 2000. The chemically zoned 1949 eruption on La Palma (Canary Islands): Petrologic evolution and magma supply dynamics of a rift zone eruption: *Journal of Geophysical Research*, v. 105, no. B3, p. 5997–6016.
- ❖ Klügel, A., Hansteen, T.H., Galipp, K., 2005. Magma storage and underplating beneath Cumbre Vieja volcano, La Palma (Canary Islands). *Earth Planet. Sci. Lett.* 236, 211\_226.
- ❖ Kouba, J., 2009. A guide to using International GNSS Service (IGS) products: IGS products; <http://igsb.jpl.nasa.gov/components/usage.html>.
- ❖ Le Corvec, N., Bebbington, M.S., Linsay, J.M., and McGee, L.E., 2013a. Age, distance, and geochemical evolution within a monogenetic volcanic field: analyzing patterns in the Auckland Volcanic Field eruption sequence. *Geochem. Geophys.Geosyst.* 14,3648–3665.
- ❖ Longpré, M.A., Klügel, A., Diehl, A., and Stix, J., 2014. Mixing in mantle magma reservoirs prior to and during the 2011-2012 eruption at El Hierro, Canary Islands, *Geology*; doi:10.1130/G35165.1
- ❖ Longpré, M.A., Stix, J., Klügel, A., Shimizu, N., 2017. Mantle to surface degassing of carbon- and sulphur-rich alkaline magma at El Hierro, Canary Islands. *Earth Planet. Sci. Lett.* 460, 268-280; doi:10.1016/j.epsl.2016.11.043
- ❖ López, C., Blanco, M.J., Abella, R., Brenes, B., Cabrera-Rodríguez, V.M., Casas, B., et al., 2012. Monitoring the volcanic unrest of El Hierro (Canary Islands) before the onset of the 2011\_2012 submarine eruption. *Geophys. Res. Lett.* 39, L13303
- ❖ Lorenz, V., 1986. On the growth of maars and diatremes and its relevance to the formation of tuff rings. *Bull.Volcanol.* 48,265–274.doi:10.1007/bf01081755
- ❖ Martí, J., Geyer, A., Andújar, J., Teixido, F., Costa, F., 2008. Assessing the potential for future explosive activity from Teide–Pico Viejo stratovolcanoes (Tenerife, Canary Islands), *J. Volcanol. Geotherm. Res.*, 178 (3), pp. 529–542
- ❖ Martí, J., Ortiz, R., Gottsmann, J., García, A., De La Cruz-Reyna, S., 2009. Characterising unrest during the reawakening of the central volcanic complex on Tenerife, Canary Islands, 2004–2005, and implications for assessing hazards and risk mitigation, *J. Volcanol. Geotherm. Res.*, 182, pp. 23–33

- ❖ Martí, J., and Felpeto, A., 2010. Methodology for the computation of volcanic susceptibility. An example for mafic and felsic eruptions on Tenerife (Canary Islands). *J. Volcanol. Geotherm. Res.* 195,69–77.
- ❖ Martí, J., Planagumà, L., Geyer, A., Canal, E., and Pedrazzi, D., 2011. Complex interaction between Strombolian and phreatomagmatic eruptions in the Quaternary monogenetic volcanism of the Catalan Volcanic Zone (NE of Spain). *J. Volcanol. Geotherm. Res.* 201,178–193.
- ❖ Martí, J., Pinel, V., López, C., Geyer, A., Abella, R., Tàrraga, M., et al., 2013a. Causes and mechanisms of the 2011–2012 El Hierro (Canary Islands) submarine eruption. *J. Geophys. Res. Solid Earth* 118,823–839.
- ❖ Martí, J., Castro, A., Rodríguez, C., Costa, F., Carrasquilla, S., Pedreira, R., Bolos, X., 2013b. Correlation of Magma Evolution and Geophysical Monitoring during the 2011-2012 El Hierro (Canary Islands) Submarine Eruption, *J. Pet.*, 54 (7), 1349-1373; doi:10.1093/petrology/egt014.
- ❖ Martí, J., López, C., Bartolini, S., Becerril, L. and Geyer, A., 2016b. Stress controls of monogenetic volcanism: a review, *Front. Earth Sci.* 4:106. doi:10.3389/feart.2016.00106
- ❖ Martí, J., Planagumà, L.I, Geyer, A., Aguirre-Díaz, G., Pedrazzi, D., Bolós, X., 2017, Basaltic ignimbrites in monogenetic volcanism: the example of La Garrotza volcanic field. *Bulletin of volcanology* 79:33, doi 10.1007/s00445-017-1113-0
- ❖ Mazzarini, F., Ferrari, L., and Isola, I., 2010. Self-similar clustering of cinder cones and crust thickness in the Michoacan-Guanajuato and Sierra de Chichinautzin volcanic fields, Trans-Mexican Volcanic Belt. *Tecnophysics.* 489: 55-64.
- ❖ Masson, D.G., 1996. Catastrophic collapse of the volcanic island of Hierro 15 ka ago and the history of landslides in the Canary Islands, *Geology*, 24(3), 231–234, doi:10.1130/0091-7613(1996)024<0231:CCOTVI>2.3.CO;2.
- ❖ Masson, D.G., Watts, A.B., Gee, M.J.R., Urgeles, R., Mitchell, N.C., Le Bas, T.P., and Canals, M., 2002. Slope failures on the flanks of the western Canary Islands, *Earth Sci. Rev.*, 57, 1–35, doi:10.1016/S0012-8252(01) 00069-1.
- ❖ Meletlidis, S., Di Roberto, A., Cerdeña, I., Pompilio, M., García-Cañada, M., Bertagnini, A., Benito-Saz, M.A., Del Carlo, P., Sainz-Maza Aparicio, S., 2015. New insight into the 2011-2012 unrest and eruption of El Hierro Island (Canary Islands) based on integrated geophysical, geodetical and petrological data, *Annals of Geophysics*, 58, 5, 2015, S0546; doi:10.4401/ag-6754

- ❖ Mogi, K., 1958. Relations between the eruptions of various volcanoes and the deformations of the ground surface around them, *Bull. Earthquake Res. Inst., University of Tokyo*, 36, 11-123.
- ❖ Newhall G.G. and S. Self S., 1982. The Volcanic Explosivity Index (VEI): An estimate of explosive magnitude of historic eruptions. *Journal of Geophysical Research* 87. 1231–1238
- ❖ Okada, Y., and Yamamoto, E., 1991. A model for the 1989 seismo-volcanic activity off Ito, Central Japan, derived from crustal movement data,” *J. Phys. Earth*, vol. 39, pp. 177– 195
- ❖ Olave Lacalle O., 2014. Análisis de la dispersión de ceniza de las erupciones del San Juan y El Teneguía en La Palma (Islas Canarias). Relación con las condiciones atmosféricas. Trabajo Fin de Grado, Dpto. de Geografía Física, ULL
- ❖ Pedrazzi, D., Martí, J., and Geyer, A., 2013. Stratigraphy, sedimentology and eruptive mechanisms in the tuff cone of El Golfo (Lanzarote, Canary Islands). *Bull Volcanol* 75:740, 2013.
- ❖ Pellicer MJ (1975) Estudio vulcanológico, petrológico y geoquímico de la isla de El Hierro (Archipiélago Canario). Tesis Doctoral. Facultad de Ciencias Geológicas. Universidad Complutense de Madrid:179 pp
- ❖ Pellicer, M.J., 1977. Estudio vulcanológico de la Isla de El Hierro (Islas Canarias) (Volcanological study of the island of El Hierro (Canary Islands). *Estud. Geol.* 33, 181\_197.
- ❖ Pérez, N.M., Padilla, G.D., Padrón, E., Hernández, P.A., Melián, G.V., Barrancos, J., Dionis, S., Nolasco, D., Rodríguez, F., Calvo, D., Hernández, I., 2012. Precursory diffuse CO<sub>2</sub> and H<sub>2</sub>S emission signatures of the 2011-2012 El Hierro submarine eruption: Canary Islands, *Geophys. Res. Lett.*, 39; doi:10.1029/2012GL052410.
- ❖ Pérez-Torrado, F.J., Rodríguez-González, A., Carracedo, J.C., Fernández-Turiel, J.L., Guillou, H., et al., 2011. Edades C-14 Del Rift ONO de El Hierro (Islas Canarias). In: Turu, V., Constante, A. (Eds.), *El Cuaternario en España y Areas Afines, Avances en 2011*. Asociación Española para el Estudio del Cuaternario (AEQUA), Andorra, pp. 101\_104.
- ❖ Perret, F.A., 1914. The volcanic eruption of Tenerife in the autumn of 1909. *Zeitschrift für Vulkanologie* 1:20–31
- ❖ Pioli, L., Erlund, E., Johnson, E., Cashman, K.V., Wallace, P., Rosi, M., Delgado Granados, H., 2008. Explosive dynamics of violent Strombolian eruptions: the eruption of Parícutin Volcano 1943–1952 (Mexico). *Earth Planet Sci Lett* 271:359–368. doi:10.1016 /j.epsl.2008.04.026

- ❖ Ponte and Cologán, A., 1911. Volcán del Chinyero. Memoria histórico descriptiva de esta erupción volcánica acaecida en 18 de noviembre de 1909. Tipolit, Tenerife, 61 pp.
- ❖ Pyle, D.M., 1989. The thickness, volume and grainsize of tephra fall deposits. *Bull Volcanol.* 51:1–15. doi: 10.1007%202FBF0108675
- ❖ Rivera, J., Lastras, G., Canals, M., Acosta, J., Arrese, B., Hermida, N., Micallef, A., Tello, O., Amblas, D., 2013. Construction of an oceanic island: Insights from the El Hierro (Canary Islands) 2011-2012 submarine volcanic eruption, *Geology*, 41 (3), 355-358; doi:10.1130/G33863.1.
- ❖ Rodríguez-Losada, J.A., Eff-Darwich, A., Hernández, L.E., Viñas, R., Pérez, N., Hernández, P., Melián, G., Martínez-Frías, J., Carmen Romero-Ruiz, M., Coello-Bravo, J.J., 2014. Petrological and geochemical highlights in the floating fragments of the October 2011 submarine eruption offshore El Hierro (Canary Islands): Relevance of submarine hydrothermal processes. *J Afric Earth Sci.* doi:10.1016/j.jafrearsci.2014.11.005
- ❖ Romero Ruiz, C., 1991. Las manifestaciones volcánicas históricas del Archipiélago Canario (2 Tomos). Gobierno de Canarias (Consejería de Política Territorial), Tenerife.
- ❖ Sainz-Maza Aparicio, S., Arnosó Sampedro, J., González Montesinos, F., Martí, J., 2014. Volcanic signatures in time gravity variations during the volcanic unrest on El Hierro (Canary Islands), *J. Geophys. Res. Solid Earth*, 119; doi:10.1002/2013JB 010795.
- ❖ Sheridan, M.F. and Wohletz, K.H., 1983. Hydrovolcanism: basic considerations and review *J. Volcanol. Geotherm. Res.*, 17 (1983), pp. 1–29
- ❖ Sigmarsson, O., Laporte, D., Carpentier, M., Devouard, B., Devidal, J.-L., Marti, J., 2013. Formation of U-depleted rhyolite from a basanite at El Hierro, Canary Islands. *Contrib. Mineral. Petrol.* 165 (3), 601\_622.
- ❖ Smith, P. M., and Asimow, P., 2005. Adibat\_1ph: A new public front-end to the MELTS, pMELTS, and pHMELTS models, *Geochem. Geophys. Geosyst.*, 6, Q02004, doi:10.1029/2004GC000816.
- ❖ Stroncik, N.A., Klügel, A., Hansteen, T.H., 2009. The magmatic plumbing system beneath El Hierro (Canary Islands): constraints from phenocrysts and naturally quenched basaltic glasses in submarine rocks. *Contrib. Mineral. Petrol.* 157 (5), 593\_607.

- ❖ Sobradelo, R., Martí, J., Mendoza-Rosas, A.T., and Gómez. G., 2011. Volcanic hazard assessment for the Canary Islands (Spain) using Extreme value theory. *Nat. Hazards Earth Syst. Sci.*, 11, 2741-2753, 2011. doi:10.5194/nhess-11-2741-2011.
- ❖ Surono, Jousset, P., Pallister, J., Boichu, M., Buongiorno, M. F., Budisantoso, A., Costa, F., Andreastuti, S., Prata, F., Schneider, D., Clarisse, L., Humaida, H., Bignami, C., Griswold, J., Carn, S., Oppenheimer, C., Lavigne, F., 2012. The 2010 explosive eruption of Java's Merapi volcano - A '100-year' event. - *Journal of Volcanology and Geothermal Research*, 241-242, pp. 121—135.
- ❖ Tous Meliá, J., 2011. La erupción del Chinyero a través de la cartografía, la fotografía y los documentos oficiales: (del 18 al 27 de noviembre de 1909). Tous Meliá J (ed), San Cristóbal de La Laguna, 335 pp.
- ❖ Troll, V.R., Klügel, A., Longpré, M.-A., Burchardt, S., Deegan, F.M., Carracedo, J.C., et al., 2012. Floating stones off El Hierro (Canary Islands, Spain): the peculiar case of the October 2011 eruption. *Solid Earth Discuss.* 3, 975\_999.
- ❖ Valentine, G.A., Perry, F.V., 2007. Tectonically controlled, time-predictable basaltic volcanism from a lithospheric mantle source (central Basin and Range Province, USA). *Earth Planet Sci Lett* 261:201–216
- ❖ Valentine, G.A., and Gregg, T.K.P., 2008. Continental basaltic volcanoes - Processes and problems. *J. Volcanol. Geother. Res.* 177,857–873.doi:10.1016/j.jvolgeores.2008.01.050
- ❖ Villasante-Marcos, V., and Pavón-Carrasco, F.J., 2014. Paleomagnetic constraints on the age of Lomo Negro volcanic eruption (El Hierro, Canary Islands). *Geophysical Journal International*199, 1497–1514. doi: 10.1093/gji/ggu346.
- ❖ Waldhauser, F., and Ellsworth, W.L., 2000. A double difference earthquake location algorithm: Method and application to the northern Hayward fault, *B. Seismol. Soc. Am.*, 90, 1353-1368; doi:10.1785/0120 000006.
- ❖ Walker, G.P.L., 2000. "Basaltic volcanoes and volcanic systems" in *Encyclopedia of Volcanoes*, ed. H. Sigurdsson(San Francisco, CA: Academic Press), 283–289.
- ❖ Wiesmaier, S., Deegan, F.M., Troll, V.R., Carracedo, J.C., Chadwick, J.P., Chew, D.M., 2011. Magma mixing in the 1100 AD Montña Reventada composite eruption, Tenerife, Canary Islands: interaction between rift zone and central volcano plumbing systems. *Contrib. Mineral. Petrol.* 162, 651\_669

- ❖ Wohletz, K.H. and Sheridan, M.F., 1983. Hydrovolcanic explosions II. Evolution of basaltic tuff rings and tuff cones *Am. J. Sci.*, 283 (1983), pp. 385–413
- ❖ Wood, C.A., 1980a. Morphometric analysis of cinder cone degradation. *J. Volcanol. Geotherm. Res.* 8, 137–160.
- ❖ *Wood, C.A., 1980b. Morphometric evolution of cinder cones. J. Volcanol. Geotherm. Res. 7, 387–413*

## 6. ANNEXES

*Annex 6.1*

*Xenopumices from the 2011-2012 submarine eruption of El Hierro (Canary Islands, Spain): Constraints on the plumbing system and magma ascent.*

*Meletlidis, S., A. Di Roberto, M. Pompilio, A. Bertagnini, I. Iribarren, A. Felpeto, P. A. Torres, and C. D'Oriano*

# Xenopumices from the 2011–2012 submarine eruption of El Hierro (Canary Islands, Spain): Constraints on the plumbing system and magma ascent

S. Meletlidis,<sup>1</sup> A. Di Roberto,<sup>2</sup> M. Pompilio,<sup>2</sup> A. Bertagnini,<sup>2</sup> I. Iribarren,<sup>1</sup> A. Felpeto,<sup>1</sup> P. A. Torres,<sup>1</sup> and C. D’Oriano<sup>2</sup>

Received 8 June 2012; revised 24 July 2012; accepted 24 July 2012; published 11 September 2012.

[1] Textures, petrography and geochemical compositions of products emitted during the onset of the 2011–2012 submarine eruption (15 October, 2011) off the coast of El Hierro have been investigated to get information on interaction mechanism between the first rising magma and the crust during the onset of the eruption as well as to get information on magma storage and plumbing systems beneath El Hierro volcano. Studied products consist of 5–50 cm bombs with an outer black to greenish, vesicular crust with bulk basanite composition containing pumiceous xenoliths (xenopumices). Our results show that xenopumices are much more heterogeneous than previously observed, since consist of a macro-scale mingling of a gray trachyte and white rhyolite. We interpreted xenopumices as resulting from the interaction (heating) between the basanitic magma feeding the eruption, a stagnant trachytic magma pocket/s and an associated hydrothermally altered halo with rhyolitic composition. Our findings confirm the importance of the study of the early products of an eruption since they can contain crucial information on the plumbing system geometry and the mechanism of magma ascent. **Citation:** Meletlidis, S., A. Di Roberto, M. Pompilio, A. Bertagnini, I. Iribarren, A. Felpeto, P. A. Torres, and C. D’Oriano (2012), Xenopumices from the 2011–2012 submarine eruption of El Hierro (Canary Islands, Spain): Constraints on the plumbing system and magma ascent, *Geophys. Res. Lett.*, 39, L17302, doi:10.1029/2012GL052675.

## 1. Introduction

[2] Products emitted during the early phases of a submarine eruption are usually lacking and impossible to sample since they are buried under subsequent deposits. Vice versa, the study of these early products may reveal important information about magma transfer dynamics and volcanic processes [Corsaro *et al.*, 2007]. In particular, the study of xenoliths may provide clues about possible interactions between the rising magma and the host rocks and valuable information as well about the chemistry, mineralogy and structure of the crust beneath the volcano, down to the mantle [Alletti *et al.*, 2005]. The 2011–2012 eruption on El Hierro

(Canary Islands, Spain), offered the rare opportunity to study these processes. The El Hierro eruption was preceded by ~3 months of relatively low energy seismicity accompanied by a surface deformation of at least 5 cm (data from www.ign.es). Earthquake foci, registered from Istituto Geografico National’s (IGN) monitoring network, were initially concentrated in the northern part of the island but progressively migrated southward remaining stable at 8–14 km of depth within the lower oceanic crust. On 9 October, after an event of 4.3 mbLg the day before, a swarm of small shallower earthquakes occurred about 5 km offshore South El Hierro and indicated that the magma was ascending toward the surface. On 10 October 2011, the onset of volcanic tremor, coupled 2 days later with the appearance of a dark water plume in the sea, testified that an eruption had started at about 2.5 km south off the coast of the village of La Restinga from the vent initially located at ~365 m depth (27°37.18′–17°59.58′; Figure S1 in the auxiliary material).<sup>1</sup> On 15 October, during a short but intensive degassing period, bi-colored, spindle-shaped ejecta ranging in size from 5 to 50 cm were observed floating and degassing on the surface. These ejecta resemble a “coconut” and consist of an outer black to greenish, vesicular crust (1–2 cm in thickness) with basanite bulk rock composition (data from www.ign.es) embedding gray to white colored, pumiceous xenoliths (hereafter called xeno-pumices as defined by Troll *et al.* [2011]) with trachytic to alkali rhyolitic bulk rock composition (data from www.ign.es). “Coconuts” bombs were only observed during the morning of 15 October 2011 (although small fragments <5 cm have been seen since the 12 Oct 2011). According to IGN/PEVOLCA data pumiceous xenoliths are volumetrically reduced if compared to basanite with an estimate ratio <1:10. Xenopumices similar to those emitted on 15 October were identified during the 1975 phreatomagmatic eruptions of Ruapehu volcano, New Zealand [Nairn *et al.*, 1979] and the 1989 submarine eruption off eastern Izu Peninsula, Japan [Yamamoto *et al.*, 1991]. Authors interpreted these products as resulting from the heating of volcanoclastic lake sediments and by vesiculation of a reheated felsic tuff derived from an older formation. Xenopumices have been also identified in volcanic deposits from several subaerial eruptions including the Grimsnés lavas, SW-Iceland [Jakobsonn, 1966], products of the 1943 eruption of Paricutin, Mexico [Milton, 1944] and those of the 1955 eruption of Nilahue maar, Chile [Muller and Veyl, 1957]. In the Canary archipelago felsic strongly fused glassy to pumiceous xenoliths were identified in products

<sup>1</sup>Centro Geofísico de Canarias, Instituto Geográfico Nacional, Santa Cruz de Tenerife, Spain.

<sup>2</sup>Istituto Nazionale di Geofisica e Vulcanologia, Pisa, Italy.

Corresponding author: A. Di Roberto, Istituto Nazionale di Geofisica e Vulcanologia, Sezione di Pisa, via della Faggiola 32, I-56126 Pisa, Italy. (diroberto@pi.ingv.it)

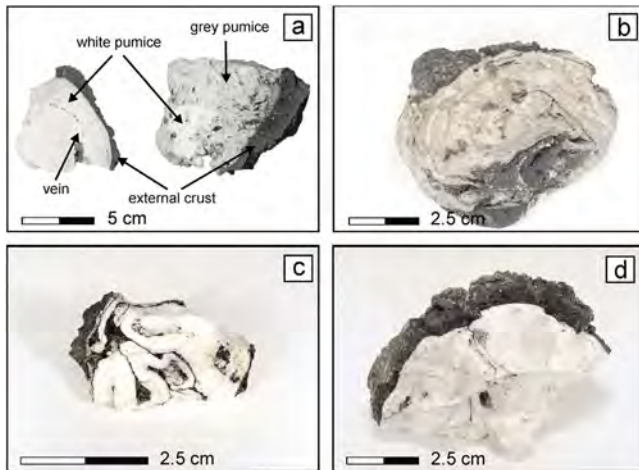


**Figure 1.** Images of products emitted on the morning of 15 October 2011 off El Hierro island coast. (a) Polished slide of gray and white xenopumices showing layering, folding and patchy mingling. (b) Intimate mingling between gray, white xenopumices and external basanite. (c) Folding in white xenopumices and mingling with basanite. (d) Sharp and abrupt contact between external crust and white xenopumice.

of the 1949 and 1971 eruptions in La Palma [Araña and Ibarrola, 1973; Klügel *et al.*, 1999]. In all the mentioned cases xenopumices were interpreted as fragments brought to the surface from various crustal depths within or below the volcano edifice and are representing fragments of volcanic or sub-intrusive felsic rocks melted and vitrified to a high degree. In the case of 15 October, El Hierro xenopumices, two main hypotheses have been suggested: 1) partial melting and vesiculation of pre-island sedimentary rocks that were picked up and heated by the ascending magma [Troll *et al.*, 2011] and 2) remobilization of a stagnant phonolitic melt present as late differentiate in the crust and successive variable interaction with old oceanic crust and the volcanic edifice [Sigmarsson *et al.*, 2012].

[3] In this article we report a detailed characterization of textural, petrographic and geochemical features of the rocks emitted during the 15 October 2011 with the aim of providing 1) new insights on mechanism of magma ascent and interactions with the crust during the onset of the eruption [Stronck *et al.*, 2009] and 2) information on magma storage and plumbing systems beneath this volcano. These data are crucial to interpret geophysical and geochemical signals collected during monitoring activities.

## 2. Geological Setting

[4] El Hierro, located at the SW end of the Canary archipelago (Figure S1 in the auxiliary material), is the emergent summit of a large volcanic shield (280 km<sup>2</sup>), which rises from about 4000 m of water depth and grows up to 1500 m above sea level. It is the youngest island of Canary archipelago and its subaerial volcanism dates back to 1.12 Ma [Guillou *et al.*, 1996]. El Hierro volcanic activity consists of three main cycles that correspond to successive volcanic edifices (Figure S1), i.e., 1) the Tiñor volcano edifice in the NE (0.88–1.12 Ma) characterized by picritic to hawaiitic-tephritic lavas, 2) El Golfo edifice in the NW (550–130 ka)

with products ranging from nephelinitic to trachytic compositions [Guillou *et al.*, 1996; Carracedo *et al.*, 2001] and 3) the late Quaternary rift volcanism (134 ka–AD1793) characterized by alkali picrites, basanites and tephrites, that can be observed in exceptional detail and it has been recognized on all three rifts (NE-, NW- and S-Ridge) of the island [Guillou *et al.*, 1996; Acosta *et al.*, 2003]. Tiñor and El Golfo volcanoes are separated by major tectonic events (gravitational collapses). The most recent eruption, Volcan de Lomo Negro (dubious AD1793 [Hernández-Pacheco, 1982]), occurred in the western part of the island, outside of the El Golfo landslide area, although the major holocenec subaerial activity has been concentrated in the southern part of the island (Figure S1).

## 3. Results

[5] Methods, instrumental conditions and analytical procedures are reported in the auxiliary material.

[6] As previously mentioned, studied products comprise “coconut-like” lava fragments with a dark-greenish external crust enveloping a light-colored xenopumice (Figure 1). Xenopumices are often heterogeneous at the macro-scale consisting of two materials that differ in vesicularity, texture and color, hereafter referred as 1) gray and 2) white xenopumice (Figure 1a). This material is often layered, with layers frequently folded and deformed into complex structures, chevron and box folds (Figure 1c). Mingling at macro-scale is ubiquitous both between gray and white xenopumices (complex patchy to intimate and folded texture; Figures 1a and 1b) and between xenopumices and the external basanitic crust (Figures 1b and 1c).

### 3.1. Textural and Petrographic Description

#### 3.1.1. External crust

[7] External crust is porphyritic with less than 15 vol. % of <500 μm, euhedral to anhedral (hopper), phenocrysts of olivine (Fo<sub>80-82</sub>), Fe-Ti spinels and minor clinopyroxene (swallow-tailed to hourglass morphology; Wo<sub>43-44</sub>En<sub>31-38</sub>) immersed in light-colored sideromelane (Figure 2a). Plagioclase (<100 μm; An<sub>63</sub>) is rare and occurs as laths in groundmass. Glass vesicularity is <57 vol. % with vesicles ranging in shape from mainly spherical to elliptical. Vesicles diameter ranges from few μm to 250 μm, with a vesicle size distribution characterized by a single mode around 10 μm (Figure S2). Bubbles size generally increases inward from the crust. Isolated bubbles up to 5 mm are also present.

#### 3.1.2. Xenopumice

[8] Gray xenopumice is highly vesicular (65–70 vol. %) with 1–400 μm, spherical to slightly elongated and irregularly shaped vesicles, showing a variable degree of coalescence. Vesicles size distribution is unimodal and asymmetrical (shifted toward larger size) with mode at 40 μm (Figure S2). Very large vesicles, up to 4 mm in size, also occur (Figures 2b and 2c). Chips of black basanitic glass (<5 mm) and black to greenish crystals (<5 mm) are embedded in this portion giving it a “salt and pepper” appearance. Gray xenopumices contain <5 vol. % of isolated phenocrysts of anorthoclase (<3 mm; Figure 2b) and variably amount of microphenocrysts (<100 μm) of anorthoclase, hopper to rounded olivine (Fo<sub>80</sub>), Fe-Ti spinels (Figure 2c), apatite and very minor clinopyroxene (Wo<sub>38-45</sub>En<sub>31-49</sub>) set in a glassy groundmass. Anorthoclases are shattered, fractured

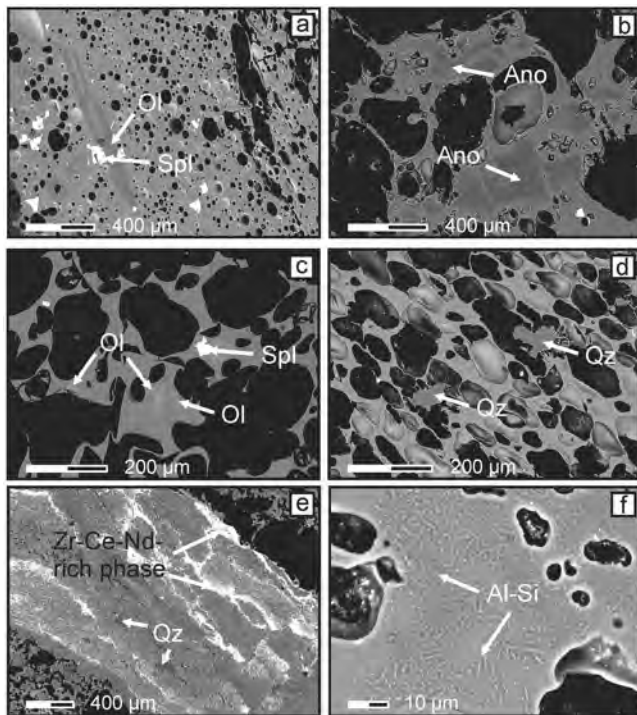


**Figure 2.** Scanning electron microscope backscattered (SEM-BSE) images representative of textures and main mineral assemblage identified in gray and white xenopumices. Mineral abbreviations after *Whitney and Evans* [2010]. (a) Microphenocrysts of olivine (Ol) and Fe-Ti spinels (Spl) within basanite. (b) Shattered, fractured and patchy anorthoclase (Ano) and (c) skeletal microcrystals of olivine and Fe-Ti spinels in gray xenopumice. (d) High vesicular white xenopumice bearing rounded microcrystals of quartz (Qz), (e) Zr-Ce-Nd-rich mineral phases and Al-silicate filling veins within white xenopumice and (f) Al-silicate within white xenopumice glass.

and patchy with saw-tooth rims at the glass interface (Figure 2b). Reaction rims and patches are less sodic and plot in the sanidine field of the ternary classification diagram Ab-An-Or. Sporadic relicts of former phlogopite were also observed as well as sparse euhedral zircon (Figure S2). In addition ribbon-shaped crystal clots (<5 mm) consisting of rounded anhedral olivine (Fo<sub>93-82</sub>) normally zoned, hourglass to patchy-zoned clinopyroxene (Wo<sub>41-48</sub>En<sub>27-51</sub>), Fe-Ti spinels, apatite and less commonly plagioclase (An<sub>38-51</sub>) occur (Figure S3). The contact between gray xenopumice and the external crust develops along a strip, few hundreds of microns-thick, where intimate mingling occurs (Figure S2). No abrupt changes in vesicularity, crystal content or glass texture were observed within this band (Figure S2).

[9] White xenopumices are made of highly vesicular material (56–70 vol. %) with 1–250  $\mu\text{m}$ , round to slightly elongated vesicles. Vesicles size distribution is unimodal and asymmetrical, with a mode at 50  $\mu\text{m}$  (Figure S2). Elongated bubbles often show a preferential alignment (Figure 2d). Xenopumices are composed of aphyric glass containing <200  $\mu\text{m}$ , anhedral crystals of quartz (Figure 2d). Rare microcrystals of Fe-Ti spinels and apatite were identified. Veins, as large as 3–4 mm cut the white xenopumices and stop over the external crust (Figure 2e). These are formed by

aggregates of Al-silicate crystals (likely mullite/sillimanite; Figure 2e), framboidal aggregates of Zr-rich minerals often bearing significant amounts of Ce and Nd and by pleonaste spinel (<50  $\mu\text{m}$ ). Glass along the veins contains abundant, <10  $\mu\text{m}$ , acicular crystals of the same Al-silicate (Figure 2f). The contact between external crust and xenopumice glass is abrupt (Figure S3).

### 3.1.3. Chemistry

[10] Bulk rock and glass composition of external crust plot in the basanite field of the Total Alkali versus Silica (TAS) diagram [*Le Maitre et al.*, 1989] (Figure S4). Xenopumices have trachytic to rhyolitic bulk rock composition, with SiO<sub>2</sub> ranging between 63.8 (gray xenopumice) and 69.5 wt. % (white xenopumice) and alkalis content respectively ranging between 12.6 and 8.8 wt. % (Figure S4). Glass compositions in gray xenopumice plot in the trachyte to rhyolite fields of the TAS diagram, while glass compositions of white xenopumice spread entirely over the rhyolite field (Figure S4). Trace elements pattern (bulk rock and glass) of the external crust are comparable with those of El Hierro volcanics [*Carracedo et al.*, 2001]. They show a relative enrichment of Th, Nb and LREE with respect to LILE (Ba, Rb) following a typical OIB trend and the characteristic pattern of the Canary Island basanites in the Primitive Mantle normalized spidergrams (Figure S5).

[11] According to their differentiated composition, gray trachytic xenopumices show high concentrations of incompatible elements and resemble final trachytic rocks in the El Golfo edifice (sample CIHI02 at 176 ka [*Carracedo et al.*, 2001]). Gray xenopumices show the same general trace element enrichment pattern of basanite although they are slightly depleted in Nb and Sr, have flat HREE distribution and a negative anomaly of Eu (Figure S5). White xenopumices show the same pattern as gray xenopumices, with a greater enrichment in U, Zr, Hf, Sm, and total HREE and Rb depletion. Xenopumice glasses are variably enriched in some incompatible elements although on the whole they show the same pattern and single element anomalies observed in bulk rock composition (i.e., depletion in Nb and Sr, flat HREE distribution and a negative anomaly of Eu), although glass of white xenopumice does not show the significant Zr and Hf enrichment observed in bulk rocks (Figure S5).

### 3.2. Thermodynamic Modeling

[12] Ascent and differentiation of magmas in the crust were simulated using alphaMELTS code [*Ghiorso and Sack*, 1995; *Smith and Asimow*, 2005] using both a basanite and gray xenopumice bulk rock starting composition (Tables S1 and S2). Paragenesis and mineral abundance observed in basanite were reproduced through polybaric differentiation from 400 MPa to 30 MPa, from 1190 to 1100°C of temperature (cooling rate of  $\approx 0.33^\circ$  per MPa) and in redox conditions of FMQ -1 (Table S1). On the opposite the differentiation within a magma reservoir has been reproduced simulating an isobaric cooling (T = 1200 to 1100°C) at P of 400, 200 and 100 MPa. Model predicts highly crystalline magmas and relative proportions between solid phases (e.g., Ol/Cpx) that are reversed compared to the natural assemblage. Vice-versa crystal content and mineral composition, observed in gray xenopumice, including the early crystallization of forsteritic olivine (Fo<sub>81</sub> at T = 1035°C) and late appearance of phlogopite (T = 920°C) can be modeled through an isobaric (P = 100 MPa) crystallization of a trachytic melt

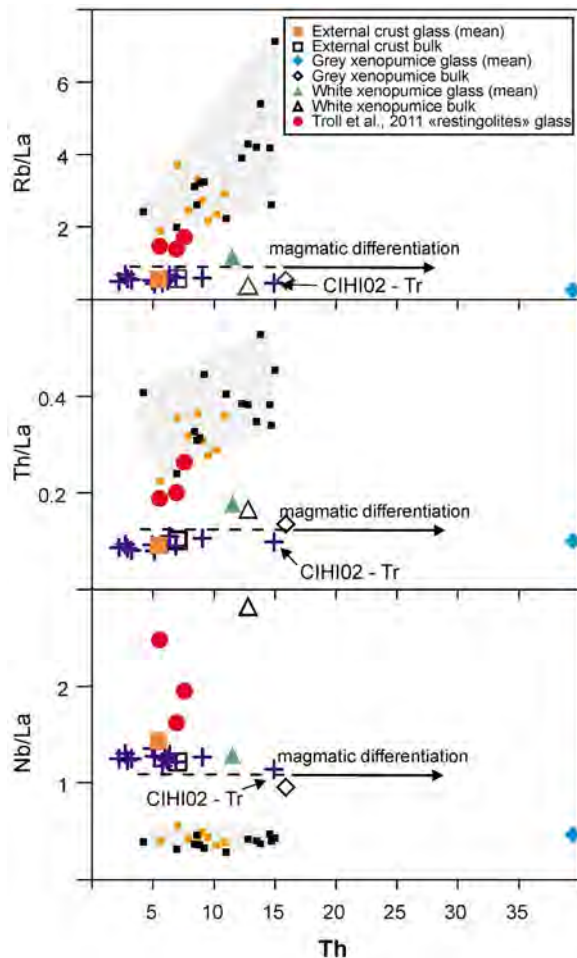


**Figure 3.** Ratios between trace elements (Rb/La, Th/La, Nb/La) differing in their compatibility and affinity for fluids (Rb for fluid-mobile, and Nb and Th for fluid-immobile elements) are plotted against highly incompatible elements (Th). The arrows indicate the direction of shifts due to magmatic differentiation from a common parental magma. Gray area represent compositional range of various sediments composites and averages (black full squares) and regional averages of Quaternary Loess (light brown full squares) reported by *McLennan* [2001]. Trachytic rocks in the El Golfo edifice from *Carracedo et al.* [2001] (CIHI02 - 176 ka age) are also reported.

that cools from 1035 to 900°C under a  $fO_2$  conditions of NNO (Table S2). On this basis we consider that paragenesis observed in investigated mafic and differentiated compositions reflects pre-eruptive equilibrium conditions.

#### 4. Discussion

[13] Our analyses demonstrate that products emitted during 15 October are heterogeneous in texture, mineralogy and chemical composition. Beside the basanite, which represents the “true” magma feeding the eruption, we identified two main types of enclaves: 1) gray trachytic xenopumices bearing magmatic minerals and 2) white trachytic xenopumices bearing quartz.

[14] Texture, mineral assemblage and composition observed in basanite results of thermodynamic modeling indicate a fast

ascent from a reservoir located at 400 MPa ( $\approx 12\text{--}14$  km) and the lack of prolonged pre-eruptive stationing in the crust. This is compatible with depths where most of the earthquake foci were clustered during both the late stages of the preceding unrest and the early phases of the eruption. The fast ascent is also in agreement with fast migration of hypocentres at shallower depths between 9 and 10 October, 2011 ([www.ign.es](http://www.ign.es)).

[15] The similarity of vesicles size distribution of the basanite and xenopumices suggest a concurrent, single event of bubble nucleation and growth. The differences between vesicles size can be ascribed to quenching processes. The external basanite contains many and small bubbles ( $N_{A_{tot}} = 1336 \text{ mm}^{-2}$ ) due to rapid quenching, whereas xenopumices continue to expand, showing larger bubbles often resulting from coalescence ( $N_{A_{tot}} = 341\text{--}560 \text{ mm}^{-2}$ ). Vesiculation patterns in xenopumices are thus different from those of Gran Canaria sedimentary xenoliths reported by *Troll et al.* [2011] which show a large variability in vesicle sizes and textures.

[16] In gray trachytic xenopumices ratios between highly incompatible elements (e.g., Rb/La, Th/La and Nb/La: Figure 3) indicate that they are co-magmatic with both the basanitic carrier magma, the white xenopumice and the whole differentiation series of El Hierro [*Carracedo et al.*, 2001] (Figure 3) and thus can be considered products of the same magmatic source. The mineral assemblage and compositions of gray trachytic xenopumices are compatible with those of a magma batch still hot ( $\approx 900^\circ\text{C}$ ) and differentiating at relative shallow depth ( $P \approx 100 \text{ MPa} \approx 4 \text{ km}$ ) probably stored in a small sill or a dike within the volcanic edifice. Reaction and resorption textures observed on some minerals as anorthoclase, phlogopite and in crystal clots, suggest a possible reheating induced by the interaction with carrier basanitic magma.

[17] Anomalous high content of some highly incompatible elements (U, Nb, Zr, Hf, Sm and HRE; Figure S5) observed in white xenopumices cannot be obtained by simple magmatic differentiation and require additional processes to be explained. Following previous hypotheses of *Araña and Ibarrola* [1973] on xenopumices found in the Teneguia lavas (La Palma), we suggest that white xenopumices may result from the total melting of an intensely altered volcanic rock, probably with a pristine trachytic composition. This could be reasonable considering that active volcanic systems like El Hierro are characterized by the development of hydrothermal systems where the circulation of fluids (either of magmatic and meteoric nature) can easily induce alteration of the volcanic rocks and the formation of a number of different alteration facies as has been demonstrated for Pliocene seamounts from La Palma [*Staudigel and Schmincke*, 1984] or for the Henry Seamounts close to the El Hierro [*Klügel et al.*, 2011]. Intense alteration of the trachytic rock in presence of hydrothermal fluid may also explain the presence of quartz that presently has not been identified in the magmatic mineral association of subaerial volcanics of El Hierro, i.e., that quartz may have precipitated from silica-rich fluids circulating in the altered rock complex before it was remelted by rising basanitic magma. A similar explanation for the presence of quartz within altered trachytic rocks is given for the products forming the intra-caldera cone sheets of the Tejada Intrusive Complex, Gran Canaria [*Donoghue et al.*, 2010]. High concentration of HFSE, notably Zr, Nb, and HREE as that observed within white xenopumices characterizes also

some evolved peralkaline igneous system. These features result from the combination of magmatic processes, that increase HFSE in the residual melt, and repeated hydrothermal alteration episodes at variable temperature that remobilize and further concentrate these elements [Salvi and Williams-Jones, 2006 and references therein].

[18] Hydrothermal alteration can also explain the quite high values of  $\delta^{18}\text{O}$  reported by Troll *et al.* [2011] for samples of rhyolitic xenopumices (9.1–11.6‰). In fact high temperature alteration (>350°C) of volcanic rocks in presence of fluids enriched in  $^{18}\text{O}$  (e.g., seawater) can produce altered rocks with higher  $\delta^{18}\text{O}$  values if compared to fresh rocks [Alt and Bach, 2006, and references therein]. Enrichment in  $\delta^{18}\text{O}$  can be also obtained during lower-temperature (<250°C) alteration [Alt and Bach, 2006, and references therein]. In addition, Javoy *et al.* [1986] report values of  $\delta^{18}\text{O}$  for volcanic rocks of La Palma that reach +11 ‰ and thus are similar to those found by Troll *et al.* [2011] in rhyolitic xenopumices. Therefore  $\delta^{18}\text{O}$  values of Troll *et al.* [2011] are not fully resolutive in ascribing xenopumices to a magmatic or sedimentary origin.

[19] In conclusion our data lead to exclude the melting of pre-island sedimentary rocks since both gray and white xenopumice have clear magmatic geochemical signature, which is distinctly different from that of sediments and loess from worldwide (Figure 3). In addition, the occurrence of magmatic minerals within gray pumice, which appear to be close to the equilibrium with a trachytic melt, lead us to exclude a protolith of sedimentary nature.

[20] Reheating and remobilization of a stagnant melt differentiating in the crust is a viable mechanism to explain the origin of xenopumice. A similar process has been proposed by Sigmarsson *et al.* [2012] who envisage the intrusion of gas-rich basanitic melt at the base of an evolved intrusion remobilizing a stagnant phonolitic melt present as late differentiate in the crust. Further interaction of phonolitic melts with old oceanic crust and the volcanic edifice, would have produced the rhyolitic composition. Being an abstract, it is difficult to evaluate in detail the proposed model; however our data doesn't support the presence of a phonolitic end-member.

[21] On the basis of petrologic data we are unable to constrain the size of the silicic stagnant melt. However, the occurrence of xenopumices only during the first days of the eruption leads us to figure that its volume should be rather small compared to that of basanite.

## 5. Conclusive Remarks

[22] 1. The onset of 2011–2012 El Hierro eruption was marked by a fast ascent of the basanitic magma from the depth of 12–14 km. Our results agree with earthquake hypocenters registered by IGN network during the initial phase of the eruption.

[23] 2. At shallow depth (<4 km and within the volcano edifice) the rising basanitic magma interacted with trachytic magma pocket/s and with an associated alteration halo with rhyolitic composition. Trachytic magma and altered rocks were heated to various degrees, and they respectively generated the gray and white xenopumice. Fluid shear stress during the ascent caused the intimate mingling between the basanite, gray xenopumice and white xenopumice.

[24] 3. After the mingling and shortly before the extrusion, basanite and xenopumices shared a simultaneous event of bubble nucleation and growth followed by rapid cooling.

[25] These findings confirm the importance of the study of the early products of an eruption since they can contain crucial information on the volcano structure and the mechanism of magma ascent. In this volcano as in others worldwide, geophysical signals need to be coupled with the study of progressively erupted products (petrologic monitoring) in order to assess the state of the magmatic system and its possible evolution.

[26] **Acknowledgments.** The authors wish to thank the IGN Volcanology Team for their efforts and assistance in sampling, Sergio Sanchez del Moral (National Museum of Natural History of Spain – CSIC) for sharing the results of his analyses on the El Hierro Xenopumices, the Sociedad de Salvamento y Seguridad Marítima (SASEMAR) for the efforts in and the Municipality of El Pinar (especially to Jesus Pérez Quintero) for their help on logistics.

[27] The Editor thanks Sharon Allen and Kimberly Genereau for assisting in the evaluation of this paper.

## References

- Acosta, J., E. Uchupi, A. Muñoz, P. Herranz, C. Palomo, and M. Ballesteros (2003), Geologic evolution of the Canarian Islands of Lanzarote, Fuerteventura, Gran Canaria and La Gomera and comparison of landslides at these island with those at Tenerife, La Palma and El Hierro, *Mar. Geophys. Res.*, *24*, 1–40, doi:10.1007/s11001-004-1513-3.
- Alletti, M., M. Pompilio, and S. Rotolo (2005), Mafic and ultramafic enclaves in Ustica Island lavas: Inferences on composition of lower crust and deep magmatic processes, *Lithos*, *84*(3–4), 151–167, doi:10.1016/j.lithos.2005.03.015.
- Alt, J. C., and W. Bach (2006), Oxygen isotope composition of a section of lower oceanic crust, ODP Hole 735B, *Geochem. Geophys. Geosyst.*, *7*, Q12008, doi:10.1029/2006GC001385.
- Araña, V., and E. Ibarrola (1973), Rhyolitic pumice in the basaltic pyroclasts from the 1971 eruption of Teneguía volcano, Canary Islands, *Lithos*, *6*, 273–278, doi:10.1016/0024-4937(73)90088-1.
- Carracedo, J. C., E. R. Badiola, H. Guillou, L. De La Nuez, and F. J. Perez Torrado (2001), Geology and volcanology of La Palma and El Hierro, western Canaries, *Estud. Geol.*, *57*, 175–273.
- Corsaro, R. A., L. Miraglia, and M. Pompilio (2007), Petrologic evidence of a complex plumbing system feeding the July–August 2001 eruption of Mt. Etna, Sicily, Italy, *Bull. Volcanol.*, *69*(4), 401–421, doi:10.1007/s00445-006-0083-4.
- Donoghue, E., V. Troll, and C. Harris (2010), Fluid-rock interaction in the Miocene, Post-Caldera, Tejada Intrusive Complex, Gran Canaria (Canary Islands): Insights from mineralogy, and O- and H-isotope geochemistry, *J. Petrol.*, *51*, 2149–2176, doi:10.1093/petrology/egq052.
- Ghiorso, M., and R. Sack (1995), Chemical mass transfer in magmatic processes IV. A revised and internally consistent thermodynamic model for the interpolation and extrapolation of liquid-solid equilibria in magmatic systems at elevated temperatures and pressures, *Contrib. Mineral. Petrol.*, *119*, 197–212, doi:10.1007/BF00307281.
- Guillou, H., J. C. Carracedo, F. Pérez Torrado, and E. Rodríguez Badiola (1996), K-Ar ages and magnetic stratigraphy of a hotspot-induced, fast grown oceanic island: El Hierro, Canary Islands, *J. Volcanol. Geotherm. Res.*, *73*, 141–155, doi:10.1016/0377-0273(96)00021-2.
- Hernández-Pacheco, A. (1982), On a possible eruption in 1793 in the island of El Hierro, Canary Islands, *Estud. Geol.*, *38*, 15–25.
- Jakobson, S. (1966), *The Grimsmés Lavas SW-Iceland*, *Acta Nat. Isl.*, vol. 2, 30 pp., Mus. Rerum Nat. Isl., Reykjavik.
- Javoy, M., C. J. Stillman, and F. Pineau (1986), Oxygen and hydrogen isotope studies on the basal complexes of the Canary Islands: Implications on the conditions of their genesis, *Contrib. Mineral. Petrol.*, *92*, 225–235, doi:10.1007/BF00375296.
- Klügel, A., H.-U. Schmincke, J. D. L. White, and K. A. Hoernle (1999), Chronology and volcanology of the 1949 multi-vent rift-zone eruption on La Palma (Canary Islands), *J. Volcanol. Geotherm. Res.*, *94*, 267–282, doi:10.1016/S0377-0273(99)00107-9.
- Klügel, A., T. H. Hansteen, P. van den Bogaard, H. Strauss, and F. Hauff (2011), Holocene fluid venting at an extinct Cretaceous seamount, Canary archipelago, *Geology*, *39*, 855–858, doi:10.1130/G32006.1.
- Le Maitre, R. W., et al. (1989), *A Classification of Igneous Rocks and Glossary of Terms: Recommendations of the International Union of Geological Sciences Subcommittee on the Systematics of Igneous Rocks*, 193 pp., Blackwell Sci., Oxford.

- McLennan, S. M. (2001), Relationships between the trace element composition of sedimentary rocks and upper continental crust, *Geochem. Geophys. Geosyst.*, 2(4), 1021, doi:10.1029/2000GC000109.
- Milton, C. (1944), Notes on volcanic rocks from Paricutin, Mexico, *Trans. Am. Geophys. Union*, 25, 618–621.
- Muller, G., and G. Veyl (1957), The birth of Nilahue, a new Maar type volcano at Rininahue, Chile, in *Chile Congreso Geológico Internacional*, pp. 375–396, Univ. de Chile, Santiago.
- Nairn, I. A., C. P. Wood, and C. A. Y. Hewson (1979), Phreatic eruptions of Ruapehu: April 1975, *N.Z. J. Geol. Geophys.*, 22, 155–170, doi:10.1080/00288306.1979.10424215.
- Salvi, S., and A. E. Williams-Jones (2006), Alteration, HFSE mineralisation and hydrocarbon formation in peralkaline igneous systems: Insights from the Strange Lake Pluton, Canada, *Lithos*, 91, 19–34, doi:10.1016/j.lithos.2006.03.040.
- Sigmarrsson, O., D. Laporte, J. Marti, B. Devouard, and N. Cluzel (2012), Mafic intrusion remobilising silicic magma under El Hierro, Canary Islands, *Geophys. Res. Abstr.*, 14, Abstract EGU2012-12251.
- Smith, P. M., and P. Asimow (2005), Adiatat\_1ph: A new public front-end to the MELTS, pMELTS, and pHMELTS models, *Geochem. Geophys. Geosyst.*, 6, Q02004, doi:10.1029/2004GC000816.
- Staudigel, H., and H.-U. Schmincke (1984), The Pliocene seamount series of La Palma/Canary Islands, *J. Geophys. Res.*, 89, 11,195–11,215, doi:10.1029/JB089iB13p11195.
- Stroncik, N. A., A. Klügel, and T. H. Hansteen (2009), The magmatic plumbing system beneath El Hierro (Canary Islands): Constraints from phenocrysts and naturally quenched basaltic glasses in submarine rocks, *Contrib. Mineral. Petrol.*, 157, 593–607, doi:10.1007/s00410-008-0354-5.
- Troll, V., et al. (2011), Floating sandstones off El Hierro (Canary Islands, Spain): The peculiar case of the October 2011 eruption, *Solid Earth Discuss.*, 3, 975–999, doi:10.5194/sed-3-975-2011.
- Whitney, D., and B. W. Evans (2010), Abbreviations for names of rock-forming minerals, *Am. Mineral.*, 95, 185–187, doi:10.2138/am.2010.3371.
- Yamamoto, T., T. Soya, S. Suto, K. Uto, A. Takada, K. Sakaguchi, and K. Ono (1991), The submarine eruption off eastern Izu Peninsula, Japan: Ejecta and eruption mechanisms, *Bull. Volcanol.*, 53, 301–308, doi:10.1007/BF00414526.

Auxiliary Material for Paper 2012GL052675

Xenopumices from the 2011-2012 submarine eruption of El Hierro (Canary Islands, Spain): Constraints on the plumbing system and magma ascent

S. Meletlidis

Centro Geofísico de Canarias, Instituto Geográfico Nacional,  
Santa Cruz de Tenerife, Spain

A. Di Roberto, M. Pompilio, and A. Bertagnini  
Istituto Nazionale di Geofisica e Vulcanologia,  
Pisa, Italy

I. Iribarren, A. Felpeto, and P. A. Torres  
Centro Geofísico de Canarias, Instituto Geográfico Nacional,  
Santa Cruz de Tenerife, Spain

C. D'Oriano  
Istituto Nazionale di Geofisica e Vulcanologia,  
Pisa, Italy

Meletlidis, S., A. Di Roberto, M. Pompilio, A. Bertagnini, I. Iribarren, A. Felpeto, P. A. Torres, and C. D'Oriano (2012), Xenopumices from the 2011-2012 submarine eruption of El Hierro (Canary Islands, Spain): Constraints on the plumbing system and magma ascent, *Geophys. Res. Lett.*, 39, L17302, doi:10.1029/2012GL052675.

## Introduction

Text S1 describes sampling techniques, analytical procedures (and analytical errors) for the analysis of products erupted on 15 October, 2011 from the submarine vent located off the coast of El Hierro island (Canary Islands, Spain). Geographic location of El Hierro island and shaded relief image of El Hierro island with highlighted the geological features described in the text are shown in Figure S1. Vesicles size distributions for basanite, grey and white xenopumices are shown in Figure S2. Scanning electron microscope backscattered (SEM-BSE) images representative of textures and main mineral assemblage identified in grey and white xenopumices are shown in Figure S3. Total Alkali versus Silica diagram for analyzed glass fragments and bulk rock are shown in Figure S4. Primitive Mantle [McDonough and Sun, 1995] normalized trace element pattern. Elements follow the order of incompatibility (bulk partition coefficients increasing from left to right) of elements with respect to the Depleted MORB Mantle [Workman & Hart, 2005]. Grey area represent variability observed in the whole El Hierro products (data from Carracedo et al., 2001). Result of the thermodynamic modeling of fractional crystallization during the ascent of a basanitic magma are given in Table S1. Result of the thermodynamic modeling of a isobaric ( $P=100\text{MPa}$ ) crystallization of a trachytic melt are given in Table S2.

1. 2012gl052675-txts01.txt

Text S1. Sampling and analytical procedures (and analytical errors) used for the analysis of products erupted on 15 October, 2011 from the submarine vent located off the coast of El Hierro island.

2. 2012gl052675-fs01.tif

Figure S1. Geographic location of El Hierro island at the southwestern edge of the Canary archipelago [Inset]. Shaded relief image of El Hierro island with highlighted the geological features described in the text. Location of the village of La Restinga (yellow full circle), the submarine vent (red star) and of the sampling sites of the products emitted during the 15 October, 2011 (orange full circles) are also indicated on the map. The green areas represents the “Mercedes star-type” rift zones where many well-preserved volcanic cones can be observed.

3. 2012gl052675-fs02.tif

Figure S2. Vesicles size distribution for basanite, grey and white xenopumices.

4. 2012gl052675-fs03.tif

Figure S3. Scanning electron microscope backscattered (SEM-BSE) images representative of textures and main mineral assemblage identified in grey xenopumices. Mineral abbreviations after Whitney and Evans (2010). a) Shattered, fractured and patchy microphenocrysts of anorthoclase (Ano), b) relicts of former phlogopite (Phl), c) microcrystals of zircon bearing few microns apatite inclusion, d) Amoeboid crystal clot consisting of anhedral microcrystals of clinopyroxene (Cpx), olivine (Ol), Fe-Ti spinels (Spl) and plagioclase (Pl) with interstitial glass, e) Close up of D, f) Pseudomorph over a former olivine crystal, g)  $\mu$ -scale mingling between basanite and gray xenopumice and h) Sharp and abrupt contact between external crust and rhyolitic glass within white xenopumice.

5. 2012gl052675-fs04.tif

Figure S4. TAS diagram for analyzed glass fragments and bulk rock. Filled symbols for glass compositions; open symbols for bulk rock compositions. For comparison bulk rock composition of subaerial rocks from El Hierro (grey field; GeoRoc data base-<http://georoc.mpch-mainz.gwdg.de/georoc/>) as well as other xenopumices samples [Troll et al., 2011 and data from [www.ign.es](http://www.ign.es)] are also given. Bulk rock composition of xenopumices from the 1949 multi-vent rift-zone eruption on La Palma are also reported [Arana and Ibarolla, 1973]; data were reported to 100 wt.% before plotting.

6. 2012gl052675-fs05.tif

Figure S5. Primitive Mantle [McDonough and Sun, 1995] normalized trace element pattern. Elements follow the order of incompatibility (bulk partition coefficients increasing from left to right) of elements with respect to the Depleted MORB Mantle [Workman & Hart, 2005]. Grey area represent variability observed in the whole El Hierro products (data from Carracedo et al., 2001).

7. 2012gl052675-ts01.xls

Table S1. Result of the thermodynamic modeling of fractional crystallization during the ascent of a basanitic magma (see Figure 2 for

Bulk rock compositions) following a gradient of 0.33 deg C/MPa using alphaMELTS code [Ghiorso and Sack, 1995; Smith and Asimow, 2005].

- 7.1 Column "P", megapascal, Pressure of the system.
- 7.2 Column "T", Celsius degree, temperature of the system.
- 7.3 Column "Melt fraction", grams/100 grams, melt fraction.
- 7.4 Column "Density liquid", grams/ml, density of liquid phase.
- 7.5 Column "Log viscosity liquid", Pas/s, viscosity of the liquid phase.
- 7.6 Column "aH2O", water activity.
- 7.7 Column "Mass liquid", grams, mass of liquid phase.
- 7.8 Column "Mass Ol", grams, mass of Olivine crystals.
- 7.9 Column "Composition Ol", composition of olivine crystals.
- 7.10 Column "Mass cpx", grams, mass of clinopyroxene crystals.
- 7.11 Column "Composition cpx", composition of clinopyroxene crystals.
- 7.12 Column "Mass Spl", grams, mass of spinel crystals.
- 7.13 Column "Composition Spl", composition of Spinel crystals.
- 7.14 Column "Mass Pl", grams, mass of plagioclase crystals.
- 7.15 Column "Composition pl", composition of plagioclase crystals.
- 7.16 Column "Mass H2O", grams, mass of water.

#### 8. 2012gl052675-ts02.xls

Table S2. Result of the thermodynamic modeling of a isobaric (P=100MPa) crystallization of a trachytic melt that cools from 1035 to 900 deg C alphaMELTS code [Ghiorso and Sack, 1995; Smith and Asimow, 2005].

- 8.1 Column "T", Celsius degree, temperature of the system.
- 8.2 Column "Melt fraction", grams/100 grams, melt fraction.
- 8.3 Column "Density liquid", grams/ml, density of liquid.
- 8.4 Column "Log viscosity liquid", viscosity of the liquid phase.
- 8.5 Column "aH2O", activity of water.
- 8.6 Column "Mass liquid", grams, mass of liquid phase.
- 8.7 Column "Mass Ol", grams, mass of olivine crystals.
- 8.8 Column "Composition Ol", composition of olivine.
- 8.9 Column "Mass Phl", grams, mass of phlogopite crystals.
- 8.10 Column "Composition Phl", Composition of phlogopite crystals.
- 8.11 Column "Mass Pl", grams, mass of plagioclase crystals.
- 8.12 Column "Composition Pl" composition of plagioclase crystals.
- 8.13 Column "Mass Spl", grams, mass of spinels crystals.
- 8.14 Column "Composition Spl" composition of Spinel crystals.
- 8.15 Column "Mass K-felds" grams, mass of K-feldspars crystals.
- 8.16 Column "Composition K-feldspar", composition of K-feldspar crystals.

#### References

Arana, V., and E., Ibarrola, (1973), Rhyolitic pumice in the basaltic pyroclasts from the 1971 eruption of Teneguía volcano, Canary Islands, Lithos 6, 273-278.

D'Oriano, C., Da Pelo, S., Podda, F., and Cioni, R., (2008), Laser-Ablation Inductively Coupled Plasma Mass Spectrometry (LA-ICP-MS):

setting operating conditions and instrumental performance, *Per. Mineral.*, 77(3), 65-74, doi:10.2451/2008PM0019.

Ghiorso, M., and R. Sack (1995), Chemical mass transfer in magmatic processes IV. A revised and internally consistent thermodynamic model for the interpolation and extrapolation of liquid-solid equilibria in magmatic systems at elevated temperatures and pressures, *Contrib. Mineral. Petr.*, 119, 197-212.

McDonough, W., and S.-S. Sun (1995), The composition of the earth, *Chem. Geol.*, 120, 223-253.

Smith, P. M., and P. Asimow (2005), *Adiabat\_1ph*: A new public front-end to the MELTS, pMELTS, and pHMELTS models, *Geochem. Geophys. Geosyst.*, 6(2), 1-8, doi:10.1029/2004GC000816.

Troll, V., A. Klügel, M. A. Longpré, S. Burchardt, S. M. Deegan, J.C. Carracedo, S. Wiesmaier, U. Kueppers, U. Dahren, L. S. Blythe, T. Hansteen, C. Freda, D. A. Budd, E. M. Jolis, E. Jonsson, E. Meade1, S. Berg, L. Mancini, L., and M. Polacci, (2011), Floating sandstones off El Hierro (Canary Islands, Spain): the peculiar case of the October 2011 eruption. *Solid Earth Discuss.* 3, 975-999, doi:10.5194/se-3-97-2012.

Workman, R., and S. Hart (2005), Major and trace element composition of the depleted MORB mantle (DMM), *Earth Planet. Sci. Lett.*, 231(1-2), 53-72, doi:10.1016/j.epsl.2004.12.005.

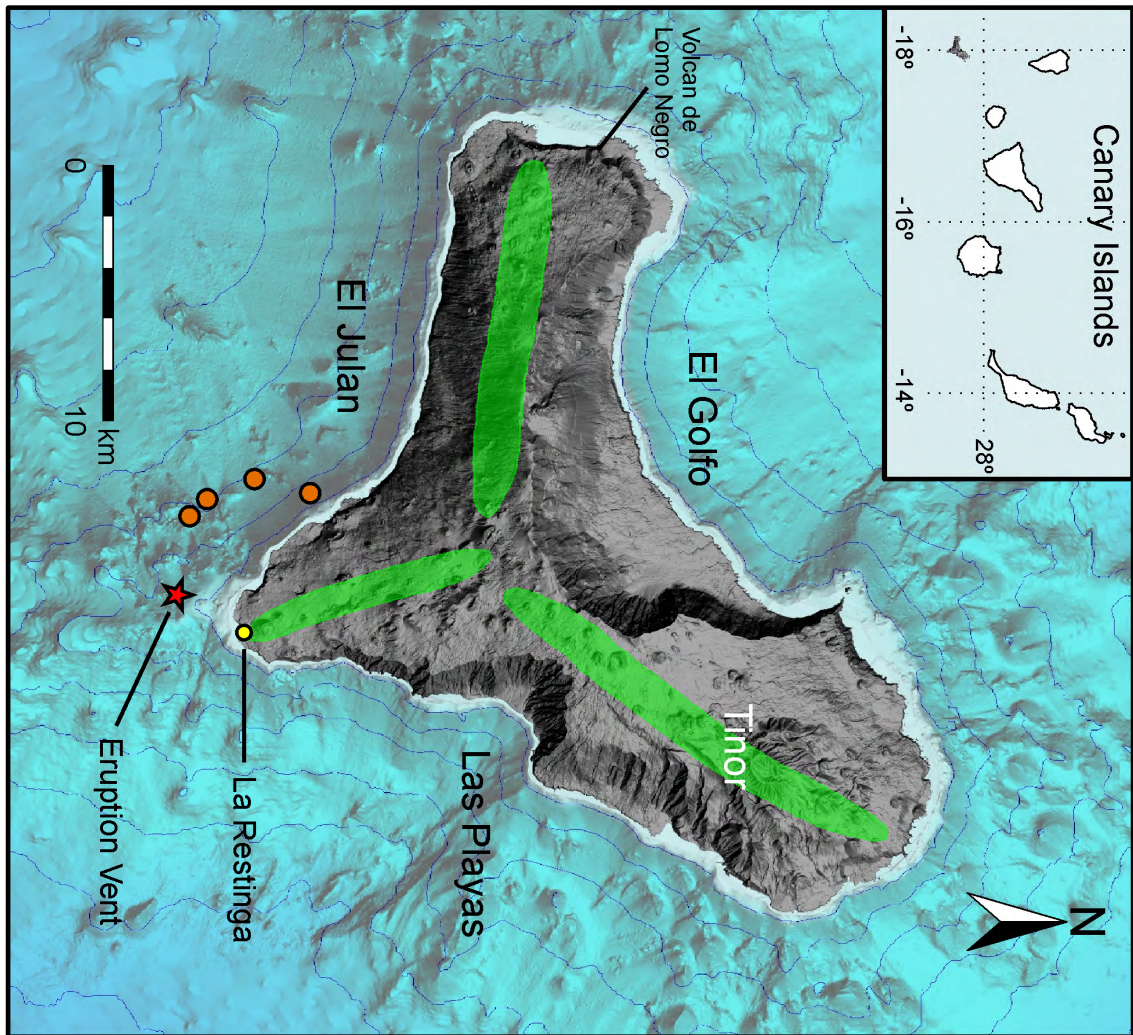
<http://dx.doi.org/10.1029/2012GL052675>

## 1. METHODS, INSTRUMENTAL CONDITIONS AND ANALYTICAL PROCEDURES

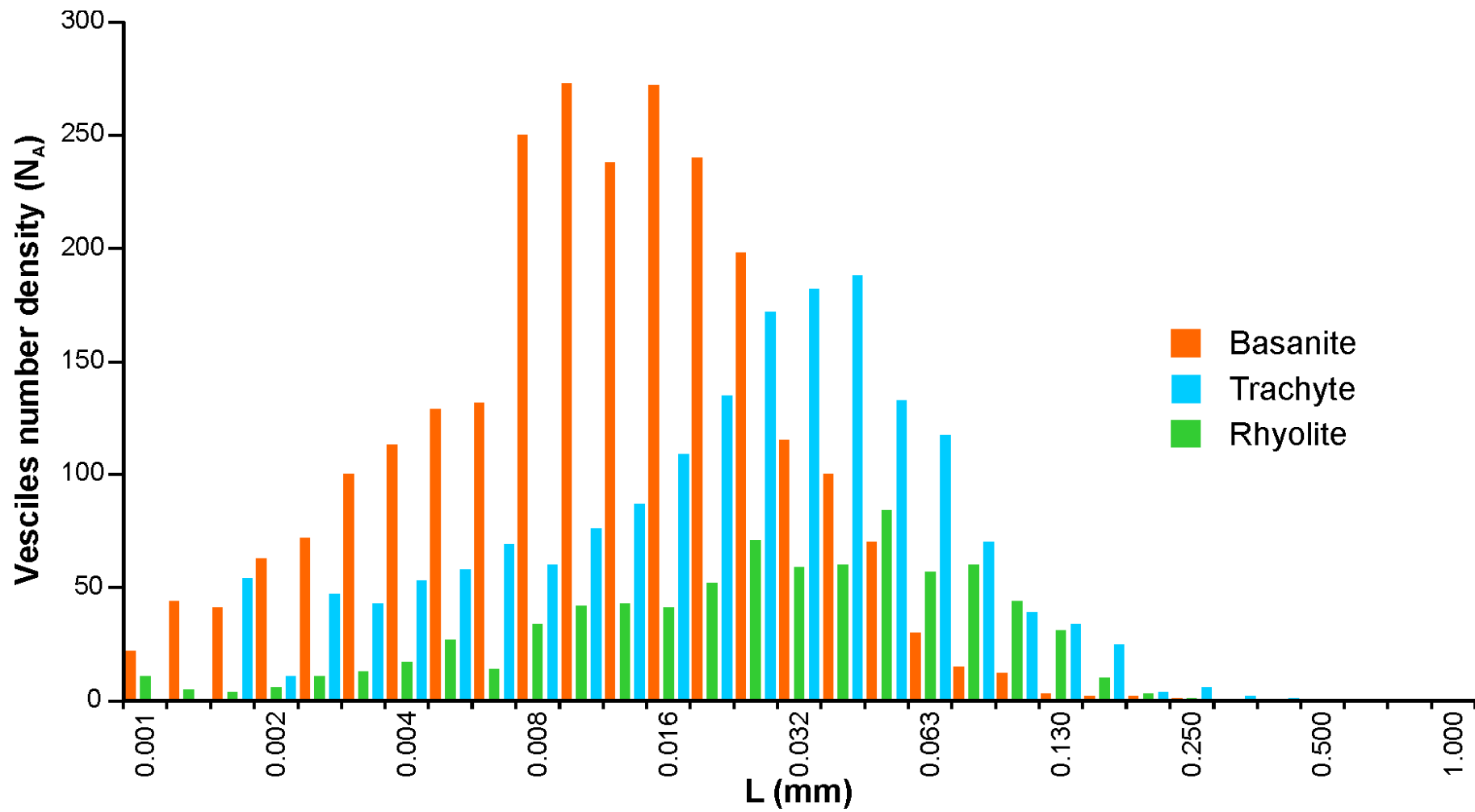
Morphological, micro-textural observations, micro-analysis of glass and mineral phases of the external crust and of xenopumices have been performed by means of optical microscope and scanning electron microscopy (SEM) at Istituto Nazionale di Geofisica e Vulcanologia (Sezione di Pisa) using a Zeiss EVO-MA-10 equipped with an Oxford ISIS microanalysis system. Instrumental conditions were: accelerating voltage 15 kV, working distance 8.5mm. The relative errors (1s) are <1% for SiO<sub>2</sub>, Al<sub>2</sub>O<sub>3</sub> and FeO, <0.5% for MgO and CaO and 2-3% for TiO<sub>2</sub>, MnO, Na<sub>2</sub>O, K<sub>2</sub>O and P<sub>2</sub>O<sub>5</sub>.

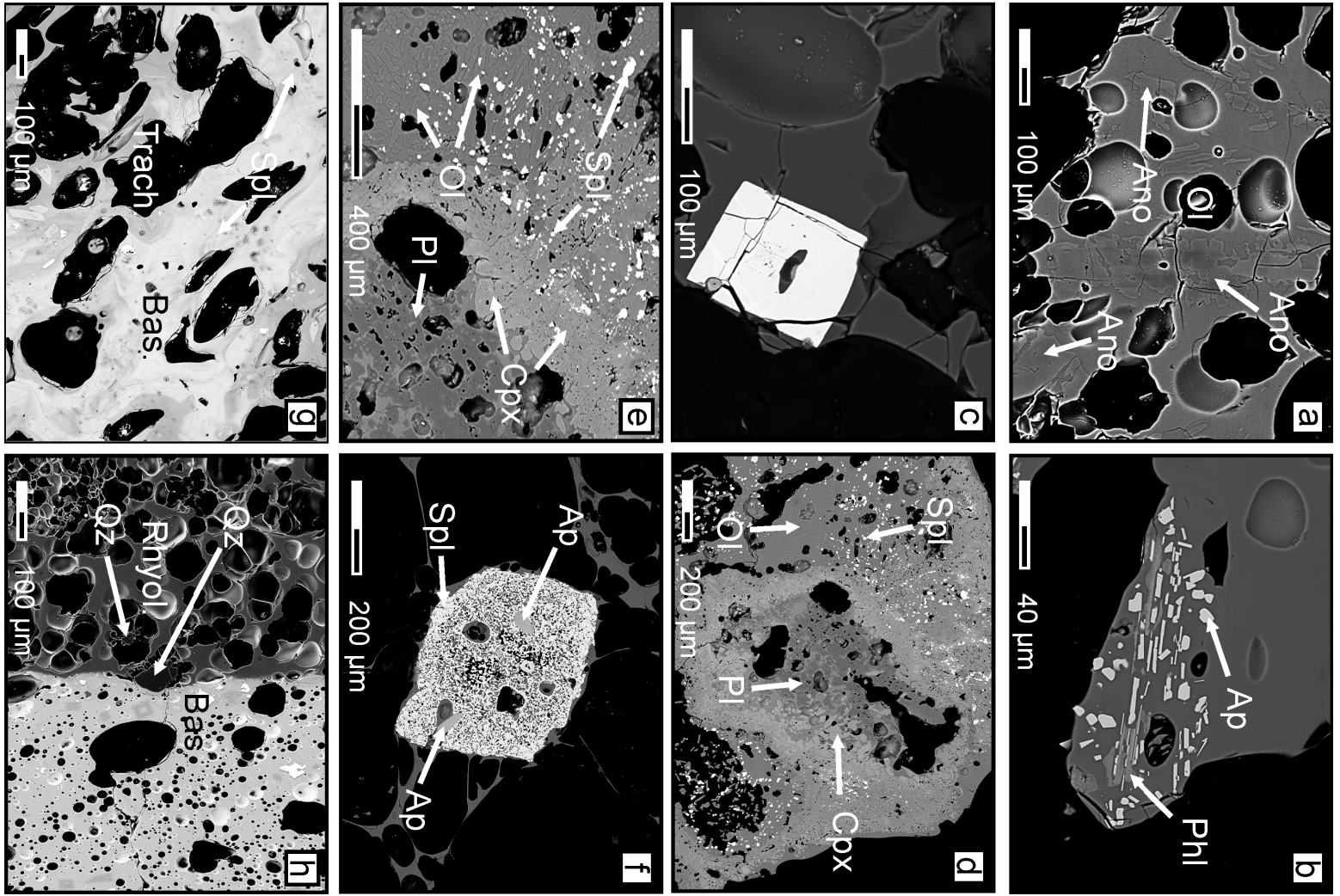
Whole rock chemical composition for major and trace elements (ICP for whole rock analyses and ICP/MS for trace elements) was determined respectively from the external crust and from the grey and white portions forming xenopumices. To perform whole rock chemical analysis original hand-sized samples were first crushed in a Teflon mill; homogeneous fragments were then selected and cleaned in an ultrasonic bath. Once cleaned each sample was crushed to a powder in an agate mill. The samples were analyzed by Activation Labs. Ltd, Ancaster, Canada using lithium metaborate/tetraborate fusion followed by ICP for whole rock analyses and ICP/MS for trace elements (Actlabs package WRA+WRA4B2). Analytical uncertainty was calculated within <3% and between 5% and 7%, for major and trace elements respectively.

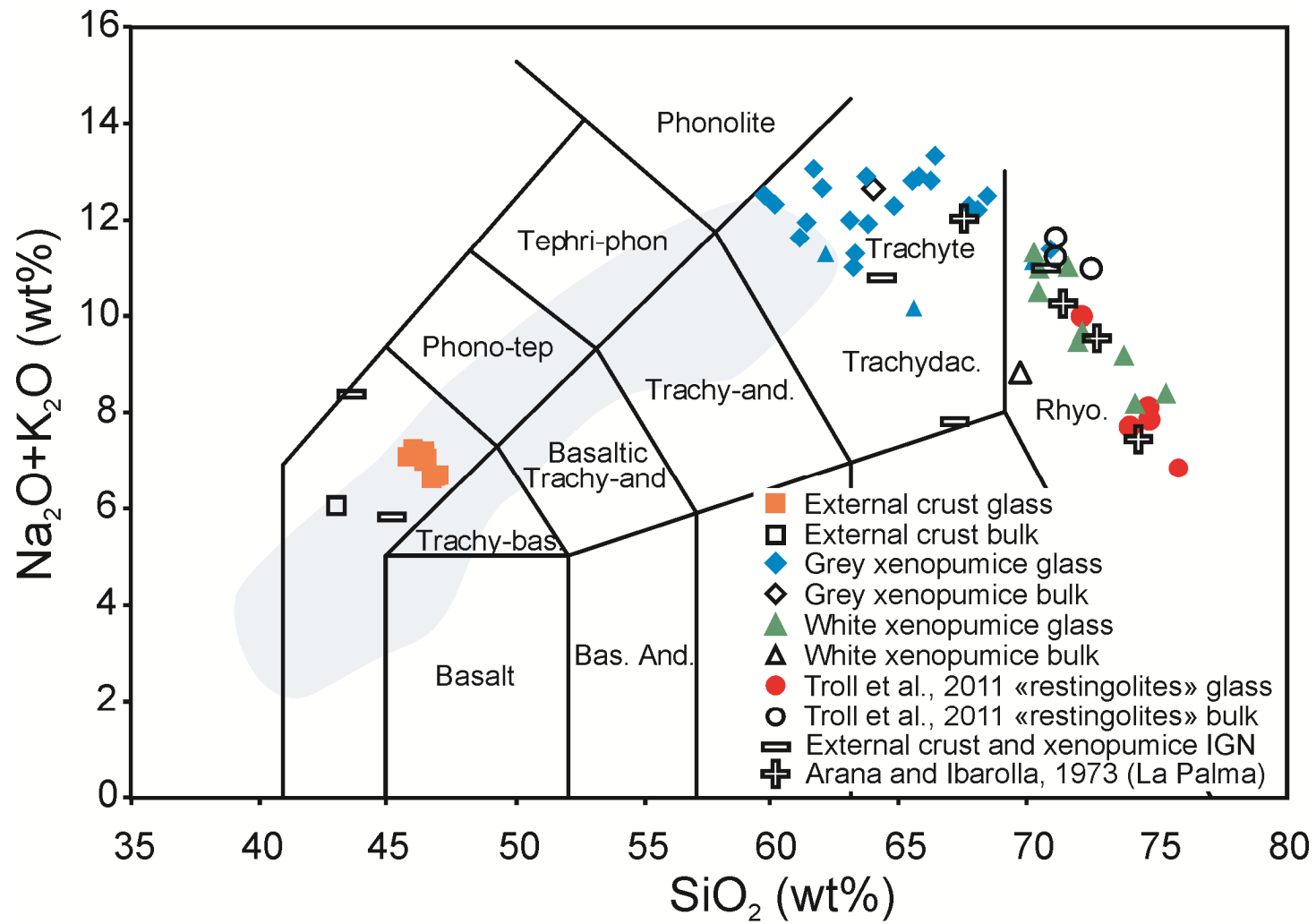
The concentration of thirty nine geochemically relevant trace elements, from <sup>7</sup>Li to <sup>238</sup>U, was determined in the external crust and in the grey and white portions forming xenopumices using the Laser Ablation Inductively Coupled Plasma Mass Spectrometry (LA-ICP-MS) instrumentation at the Department of Earth Sciences of the University of Cagliari (Italy). The device is a Quadrupole ICP-MS (Perkin Elmer Elan DRC-e) coupled with a 213 nm Nd:YAG laser probe (New Wave Research). The laser was operated at 10 Hz of repetition rate, laser output energy of 0.28 mJ, spot size of 30 - 40 μm and He as carrier gas in the ablation cell (D'Oriano et al., 2008). Selected elements were acquired in peak hopping mode with a dwell time of 10ms. Nist 612 and <sup>44</sup>Ca were adopted as external and internal standards, respectively. Precision and accuracy were evaluated on the USGS-BCR-2 reference materials; analytical accuracy is within 5% error level and precision is between 1% and 9%, at 40 μm of crater size for all elements (D'Oriano et al., 2008). Data reduction was performed by means of GLITTER® software (Macquarie Research Ltd.) developed by Van Achterberg et al. (2001; <http://www.glitter-gemoc.com/>). Vesicularity, bubble number densities and crystal content of selected samples was obtained by image analysis of SEM-backscatter images using ImageJ software (<http://rsbweb.nih.gov/ij/>).



2012g1052675-fs01.tif







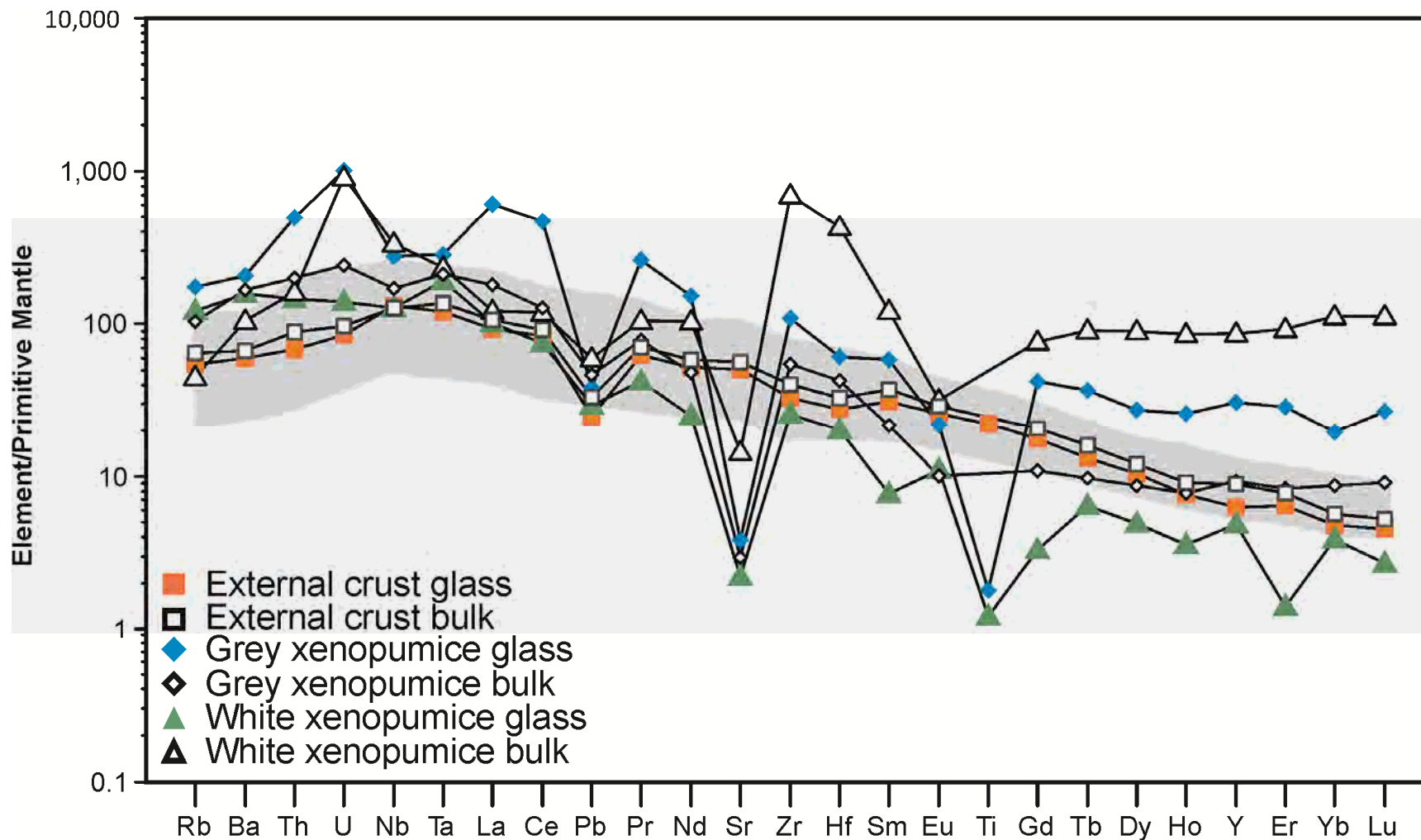


**Table S2. Thermodynamic modeling of a isobaric crystallization of a trachytic melt**

T (°C)	Melt fraction	$\rho$ liquid	Log $\eta$ liquid	Mass liq aH <sub>2</sub> O	Mass Ol	Composition Ol	Mass Phl	Composition Phl	Mass Pl	Composition Pl	Mass Spl	Composition Spl	Mass K- felds	Formula K-feldspar
1100	1,000	2,25	3,83	0,61	99,90									
1095	1,000	2,25	3,86	0,61	99,90									
1090	1,000	2,26	3,89	0,61	99,90									
1085	1,000	2,26	3,92	0,61	99,90									
1080	1,000	2,26	3,95	0,61	99,90									
1075	1,000	2,26	3,98	0,60	99,90									
1070	1,000	2,26	4,01	0,60	99,90									
1065	1,000	2,26	4,04	0,60	99,90									
1060	1,000	2,26	4,07	0,60	99,90									
1055	1,000	2,27	4,11	0,60	99,90									
1050	1,000	2,27	4,14	0,60	99,90									
1045	1,000	2,27	4,17	0,60	99,90									
1040	1,000	2,27	4,21	0,60	99,91									
1035	0,999	2,27	4,25	0,60	99,79	0,12		(Ca <sub>0,00</sub> Mg <sub>0,81</sub> Fe <sup>0,19</sup> ) <sub>2</sub> SiO <sub>4</sub>						
1030	0,999	2,27	4,29	0,59	99,67	0,11		(Ca <sub>0,00</sub> Mg <sub>0,80</sub> Fe <sup>0,19</sup> ) <sub>2</sub> SiO <sub>4</sub>						
1025	0,999	2,27	4,33	0,59	99,56	0,11		(Ca <sub>0,00</sub> Mg <sub>0,80</sub> Fe <sup>0,19</sup> ) <sub>2</sub> SiO <sub>4</sub>						
1020	0,999	2,27	4,37	0,59	99,46	0,11		(Ca <sub>0,00</sub> Mg <sub>0,80</sub> Fe <sup>0,20</sup> ) <sub>2</sub> SiO <sub>4</sub>						
1015	0,999	2,27	4,41	0,59	99,35	0,11		(Ca <sub>0,00</sub> Mg <sub>0,79</sub> Fe <sup>0,20</sup> ) <sub>2</sub> SiO <sub>4</sub>						
1010	0,999	2,27	4,45	0,59	99,25	0,10		(Ca <sub>0,00</sub> Mg <sub>0,79</sub> Fe <sup>0,21</sup> ) <sub>2</sub> SiO <sub>4</sub>						
1005	0,999	2,27	4,49	0,59	99,14	0,10		(Ca <sub>0,00</sub> Mg <sub>0,79</sub> Fe <sup>0,21</sup> ) <sub>2</sub> SiO <sub>4</sub>						
1000	0,999	2,27	4,54	0,59	99,04	0,10		(Ca <sub>0,00</sub> Mg <sub>0,78</sub> Fe <sup>0,21</sup> ) <sub>2</sub> SiO <sub>4</sub>						
995	0,999	2,28	4,58	0,59	98,95	0,10		(Ca <sub>0,00</sub> Mg <sub>0,78</sub> Fe <sup>0,22</sup> ) <sub>2</sub> SiO <sub>4</sub>						
990	0,999	2,28	4,62	0,59	98,85	0,10		(Ca <sub>0,00</sub> Mg <sub>0,77</sub> Fe <sup>0,22</sup> ) <sub>2</sub> SiO <sub>4</sub>						
985	0,999	2,28	4,66	0,59	98,76	0,10		(Ca <sub>0,00</sub> Mg <sub>0,77</sub> Fe <sup>0,23</sup> ) <sub>2</sub> SiO <sub>4</sub>						
980	0,999	2,28	4,71	0,59	98,66	0,09		(Ca <sub>0,00</sub> Mg <sub>0,77</sub> Fe <sup>0,23</sup> ) <sub>2</sub> SiO <sub>4</sub>						
975	0,999	2,28	4,75	0,59	98,57	0,09		(Ca <sub>0,00</sub> Mg <sub>0,76</sub> Fe <sup>0,23</sup> ) <sub>2</sub> SiO <sub>4</sub>						
970	0,999	2,28	4,79	0,58	98,48	0,09		(Ca <sub>0,00</sub> Mg <sub>0,76</sub> Fe <sup>0,24</sup> ) <sub>2</sub> SiO <sub>4</sub>						
965	0,999	2,28	4,84	0,58	98,40	0,09		(Ca <sub>0,00</sub> Mg <sub>0,75</sub> Fe <sup>0,24</sup> ) <sub>2</sub> SiO <sub>4</sub>						
960	0,999	2,28	4,88	0,58	98,31	0,09		(Ca <sub>0,00</sub> Mg <sub>0,75</sub> Fe <sup>0,25</sup> ) <sub>2</sub> SiO <sub>4</sub>						
955	0,935	2,28	4,80	0,63	91,90	0,19		(Ca <sub>0,00</sub> Mg <sub>0,74</sub> Fe <sup>0,25</sup> ) <sub>2</sub> SiO <sub>4</sub>					6,23	K <sub>0,61</sub> Na <sub>0,36</sub> Ca <sub>0,03</sub> Al <sub>1,03</sub> Si <sub>2,97</sub> O <sub>8</sub>
950	0,964	2,27	4,77	0,66	88,63	0,13		(Ca <sub>0,00</sub> Mg <sub>0,74</sub> Fe <sup>0,26</sup> ) <sub>2</sub> SiO <sub>4</sub>					3,13	K <sub>0,60</sub> Na <sub>0,37</sub> Ca <sub>0,03</sub> Al <sub>1,03</sub> Si <sub>2,97</sub> O <sub>8</sub>
945	0,965	2,27	4,75	0,68	85,49	0,12		(Ca <sub>0,00</sub> Mg <sub>0,73</sub> Fe <sup>0,26</sup> ) <sub>2</sub> SiO <sub>4</sub>			0,02	Fe <sup>0,98</sup> Mg <sub>0,24</sub> Fe <sup>1,37</sup> Al <sub>0,26</sub> Ti <sub>0,22</sub> O <sub>4</sub>	3,00	K <sub>0,59</sub> Na <sub>0,38</sub> Ca <sub>0,03</sub> Al <sub>1,03</sub> Si <sub>2,97</sub> O <sub>8</sub>
940	0,963	2,26	4,72	0,71	82,36	0,09		(Ca <sub>0,00</sub> Mg <sub>0,73</sub> Fe <sup>0,26</sup> ) <sub>2</sub> SiO <sub>4</sub>			0,11	Fe <sup>0,99</sup> Mg <sub>0,24</sub> Fe <sup>1,36</sup> Al <sub>0,19</sub> Ti <sub>0,22</sub> O <sub>4</sub>	2,93	K <sub>0,58</sub> Na <sub>0,39</sub> Ca <sub>0,04</sub> Al <sub>1,04</sub> Si <sub>2,96</sub> O <sub>8</sub>
935	0,964	2,26	4,70	0,74	79,37	0,09		(Ca <sub>0,00</sub> Mg <sub>0,74</sub> Fe <sup>0,26</sup> ) <sub>2</sub> SiO <sub>4</sub>			0,11	Fe <sup>0,99</sup> Mg <sub>0,24</sub> Fe <sup>1,35</sup> Al <sub>0,19</sub> Ti <sub>0,23</sub> O <sub>4</sub>	2,81	K <sub>0,56</sub> Na <sub>0,40</sub> Ca <sub>0,04</sub> Al <sub>1,04</sub> Si <sub>2,96</sub> O <sub>8</sub>
930	0,964	2,26	4,68	0,76	76,49	0,08		(Ca <sub>0,00</sub> Mg <sub>0,74</sub> Fe <sup>0,26</sup> ) <sub>2</sub> SiO <sub>4</sub>			0,10	Fe <sup>1,00</sup> Mg <sub>0,24</sub> Fe <sup>1,33</sup> Al <sub>0,19</sub> Ti <sub>0,24</sub> O <sub>4</sub>	2,69	K <sub>0,55</sub> Na <sub>0,41</sub> Ca <sub>0,04</sub> Al <sub>1,04</sub> Si <sub>2,96</sub> O <sub>8</sub>
925	0,964	2,25	4,65	0,79	73,73	0,08		(Ca <sub>0,00</sub> Mg <sub>0,74</sub> Fe <sup>0,26</sup> ) <sub>2</sub> SiO <sub>4</sub>			0,10	Fe <sup>1,00</sup> Mg <sub>0,24</sub> Fe <sup>1,32</sup> Al <sub>0,18</sub> Ti <sub>0,25</sub> O <sub>4</sub>	2,59	K <sub>0,53</sub> Na <sub>0,42</sub> Ca <sub>0,05</sub> Al <sub>1,05</sub> Si <sub>2,95</sub> O <sub>8</sub>
920	0,962	2,24	4,62	0,82	70,94	0,08		(Ca <sub>0,00</sub> Mg <sub>0,74</sub> Fe <sup>0,25</sup> ) <sub>2</sub> SiO <sub>4</sub>			0,10	Fe <sup>1,02</sup> Mg <sub>0,24</sub> Fe <sup>1,31</sup> Al <sub>0,18</sub> Ti <sub>0,26</sub> O <sub>4</sub>	2,03	K <sub>0,53</sub> Na <sub>0,42</sub> Ca <sub>0,05</sub> Al <sub>1,05</sub> Si <sub>2,95</sub> O <sub>8</sub>
915	0,962	2,24	4,59	0,86	68,26	0,08		(Ca <sub>0,00</sub> Mg <sub>0,74</sub> Fe <sup>0,25</sup> ) <sub>2</sub> SiO <sub>4</sub>			0,10	Fe <sup>1,02</sup> Mg <sub>0,24</sub> Fe <sup>1,29</sup> Al <sub>0,17</sub> Ti <sub>0,27</sub> O <sub>4</sub>	1,83	K <sub>0,53</sub> Na <sub>0,42</sub> Ca <sub>0,05</sub> Al <sub>1,05</sub> Si <sub>2,95</sub> O <sub>8</sub>
910	0,961	2,23	4,56	0,89	65,57		0,13	K(Fe <sup>0,00</sup> Mg <sub>1,00</sub> ) <sub>3</sub> AlSi <sub>3</sub> O <sub>10</sub> (OH) <sub>2</sub>			0,10	Fe <sup>1,03</sup> Mg <sub>0,24</sub> Fe <sup>1,28</sup> Al <sub>0,17</sub> Ti <sub>0,28</sub> O <sub>4</sub>	1,68	K <sub>0,54</sub> Na <sub>0,42</sub> Ca <sub>0,05</sub> Al <sub>1,05</sub> Si <sub>2,95</sub> O <sub>8</sub>
905	0,959	2,23	4,53	0,92	62,90		0,19	K(Fe <sup>0,01</sup> Mg <sub>0,99</sub> ) <sub>3</sub> AlSi <sub>3</sub> O <sub>10</sub> (OH) <sub>2</sub>			0,11	Fe <sup>1,05</sup> Mg <sub>0,23</sub> Fe <sup>1,27</sup> Al <sub>0,16</sub> Ti <sub>0,28</sub> O <sub>4</sub>	1,56	K <sub>0,54</sub> Na <sub>0,42</sub> Ca <sub>0,04</sub> Al <sub>1,04</sub> Si <sub>2,96</sub> O <sub>8</sub>
900	0,960	2,22	4,50	0,96	60,40		0,17	K(Fe <sup>0,01</sup> Mg <sub>0,99</sub> ) <sub>3</sub> AlSi <sub>3</sub> O <sub>10</sub> (OH) <sub>2</sub>			0,10	Fe <sup>1,07</sup> Mg <sub>0,23</sub> Fe <sup>1,27</sup> Al <sub>0,15</sub> Ti <sub>0,29</sub> O <sub>4</sub>	1,46	K <sub>0,54</sub> Na <sub>0,42</sub> Ca <sub>0,04</sub> Al <sub>1,04</sub> Si <sub>2,96</sub> O <sub>8</sub>

Table S1. Thermodynamic modeling of fractional crystallization of basanitic magma

P (Mpa)	T (°C)	Melt fraction	$\rho$ liquid	Log $\eta$ liquid	aH <sub>2</sub> O	Mass liquid	Mass Ol	Composition Ol	Mass cpx	Composition cpx	Mass Spl	Composition Spl	Mass Pl	Composition plagioclase	Mass H <sub>2</sub> O
400	1190	1	2,70	1,34	0,18	99,45									
390	1188	1	2,70	1,35	0,18	99,45									
380	1186	1	2,70	1,35	0,18	99,45									
370	1184	1	2,69	1,36	0,19	99,45									
360	1182	1	2,69	1,37	0,19	99,45									
350	1180	1	2,69	1,37	0,19	99,46									
340	1178	1	2,69	1,38	0,19	99,46									
330	1176	1	2,69	1,39	0,20	99,46									
320	1174	1	2,68	1,40	0,20	99,46									
310	1172	1	2,68	1,40	0,20	99,46									
300	1170	1	2,68	1,41	0,21	99,46									
290	1168	1	2,68	1,42	0,21	99,46									
280	1166	1	2,68	1,43	0,21	99,46									
270	1164	1	2,67	1,43	0,22	99,46									
260	1162	1	2,67	1,44	0,22	99,46									
250	1160	1	2,67	1,45	0,23	99,47									
240	1158	1	2,67	1,46	0,23	99,47									
230	1156	1	2,67	1,46	0,24	99,47									
220	1154	1	2,66	1,47	0,24	99,47									
210	1152	1	2,66	1,48	0,25	99,47									
200	1150	1	2,66	1,49	0,26	99,47									
190	1148	0,9994	2,66	1,50	0,27	99,41	0,06	(Ca <sub>0,01</sub> Mg <sub>0,81</sub> Fe <sup>0,18</sup> ) <sub>2</sub> SiO <sub>4</sub>							
180	1146	0,9856	2,64	1,57	0,27	98,00					1,44	Fe <sup>0,90</sup> Mg <sub>0,72</sub> Fe <sup>0,51</sup> Al <sub>0,25</sub> Ti <sub>0,62</sub> O <sub>4</sub>			
170	1144	0,9976	2,64	1,59	0,28	97,77					0,23	Fe <sup>0,90</sup> Mg <sub>0,72</sub> Fe <sup>0,51</sup> Al <sub>0,25</sub> Ti <sub>0,62</sub> O <sub>4</sub>			
160	1142	0,9974	2,63	1,60	0,29	97,53	0,02	(Ca <sub>0,01</sub> Mg <sub>0,81</sub> Fe <sup>0,18</sup> ) <sub>2</sub> SiO <sub>4</sub>			0,23	Fe <sup>0,90</sup> Mg <sub>0,72</sub> Fe <sup>0,51</sup> Al <sub>0,25</sub> Ti <sub>0,62</sub> O <sub>4</sub>			
150	1140	0,9972	2,63	1,62	0,30	97,26	0,06	(Ca <sub>0,01</sub> Mg <sub>0,81</sub> Fe <sup>0,18</sup> ) <sub>2</sub> SiO <sub>5</sub>			0,22	Fe <sup>0,90</sup> Mg <sub>0,72</sub> Fe <sup>0,51</sup> Al <sub>0,25</sub> Ti <sub>0,62</sub> O <sub>4</sub>			
140	1138	0,9972	2,62	1,64	0,32	96,99	0,06	(Ca <sub>0,01</sub> Mg <sub>0,81</sub> Fe <sup>0,18</sup> ) <sub>2</sub> SiO <sub>6</sub>			0,22	Fe <sup>0,90</sup> Mg <sub>0,71</sub> Fe <sup>0,52</sup> Al <sub>0,25</sub> Ti <sub>0,62</sub> O <sub>4</sub>			
130	1136	0,9972	2,62	1,66	0,33	96,72	0,06	(Ca <sub>0,01</sub> Mg <sub>0,81</sub> Fe <sup>0,18</sup> ) <sub>2</sub> SiO <sub>7</sub>			0,22	Fe <sup>0,90</sup> Mg <sub>0,71</sub> Fe <sup>0,52</sup> Al <sub>0,25</sub> Ti <sub>0,62</sub> O <sub>4</sub>			
120	1134	0,9972	2,61	1,68	0,35	96,46	0,05	(Ca <sub>0,01</sub> Mg <sub>0,81</sub> Fe <sup>0,18</sup> ) <sub>2</sub> SiO <sub>8</sub>			0,22	Fe <sup>0,90</sup> Mg <sub>0,71</sub> Fe <sup>0,52</sup> Al <sub>0,25</sub> Ti <sub>0,62</sub> O <sub>4</sub>			
110	1132	0,9972	2,61	1,70	0,37	96,19	0,05	(Ca <sub>0,01</sub> Mg <sub>0,81</sub> Fe <sup>0,18</sup> ) <sub>2</sub> SiO <sub>9</sub>			0,21	Fe <sup>0,90</sup> Mg <sub>0,71</sub> Fe <sup>0,53</sup> Al <sub>0,25</sub> Ti <sub>0,61</sub> O <sub>4</sub>			
100	1130	0,9972	2,60	1,72	0,40	95,93	0,05	(Ca <sub>0,01</sub> Mg <sub>0,81</sub> Fe <sup>0,18</sup> ) <sub>2</sub> SiO <sub>10</sub>			0,21	Fe <sup>0,90</sup> Mg <sub>0,71</sub> Fe <sup>0,53</sup> Al <sub>0,25</sub> Ti <sub>0,61</sub> O <sub>4</sub>			
90	1128	0,9972	2,60	1,74	0,43	95,67	0,05	(Ca <sub>0,01</sub> Mg <sub>0,81</sub> Fe <sup>0,18</sup> ) <sub>2</sub> SiO <sub>11</sub>			0,21	Fe <sup>0,90</sup> Mg <sub>0,71</sub> Fe <sup>0,54</sup> Al <sub>0,25</sub> Ti <sub>0,61</sub> O <sub>4</sub>			
80	1126	0,9972	2,59	1,76	0,47	95,42	0,05	(Ca <sub>0,01</sub> Mg <sub>0,81</sub> Fe <sup>0,18</sup> ) <sub>2</sub> SiO <sub>12</sub>			0,21	Fe <sup>0,90</sup> Mg <sub>0,70</sub> Fe <sup>0,54</sup> Al <sub>0,25</sub> Ti <sub>0,61</sub> O <sub>4</sub>			
70	1124	0,9973	2,59	1,78	0,53	95,16	0,05	(Ca <sub>0,01</sub> Mg <sub>0,81</sub> Fe <sup>0,18</sup> ) <sub>2</sub> SiO <sub>13</sub>			0,21	Fe <sup>0,90</sup> Mg <sub>0,70</sub> Fe <sup>0,55</sup> Al <sub>0,25</sub> Ti <sub>0,60</sub> O <sub>4</sub>			
60	1122	0,9889	2,58	1,81	0,60	94,11	0,09	(Ca <sub>0,01</sub> Mg <sub>0,81</sub> Fe <sup>0,18</sup> ) <sub>2</sub> SiO <sub>14</sub>	0,77	Na <sub>0,02</sub> Ca <sub>0,94</sub> Fe <sup>0,11</sup> Mg <sub>0,54</sub> Fe <sup>0,10</sup> Ti <sub>0,32</sub> Al <sub>0,66</sub> Si <sub>1,31</sub> O <sub>6</sub>	0,20	Fe <sup>0,91</sup> Mg <sub>0,69</sub> Fe <sup>0,55</sup> Al <sub>0,24</sub> Ti <sub>0,60</sub> O <sub>4</sub>			
50	1120	0,9925	2,58	1,83	0,70	93,41	0,07	(Ca <sub>0,01</sub> Mg <sub>0,81</sub> Fe <sup>0,19</sup> ) <sub>2</sub> SiO <sub>14</sub>	0,43	Na <sub>0,02</sub> Ca <sub>0,94</sub> Fe <sup>0,11</sup> Mg <sub>0,54</sub> Fe <sup>0,10</sup> Ti <sub>0,32</sub> Al <sub>0,65</sub> Si <sub>1,31</sub> O <sub>6</sub>	0,20	Fe <sup>0,91</sup> Mg <sub>0,69</sub> Fe <sup>0,55</sup> Al <sub>0,24</sub> Ti <sub>0,60</sub> O <sub>4</sub>			
40	1118	0,9927	2,57	1,85	0,86	92,74	0,07	(Ca <sub>0,01</sub> Mg <sub>0,81</sub> Fe <sup>0,19</sup> ) <sub>2</sub> SiO <sub>15</sub>	0,42	Na <sub>0,02</sub> Ca <sub>0,94</sub> Fe <sup>0,11</sup> Mg <sub>0,54</sub> Fe <sup>0,10</sup> Ti <sub>0,32</sub> Al <sub>0,65</sub> Si <sub>1,31</sub> O <sub>6</sub>	0,19	Fe <sup>0,91</sup> Mg <sub>0,68</sub> Fe <sup>0,57</sup> Al <sub>0,24</sub> Ti <sub>0,59</sub> O <sub>4</sub>			
30	1116	0,9808	2,57	1,91	1,00	90,96	0,19	(Ca <sub>0,01</sub> Mg <sub>0,81</sub> Fe <sup>0,19</sup> ) <sub>2</sub> SiO <sub>16</sub>	1,47	Na <sub>0,02</sub> Ca <sub>0,94</sub> Fe <sup>0,12</sup> Mg <sub>0,55</sub> Fe <sup>0,10</sup> Ti <sub>0,31</sub> Al <sub>0,64</sub> Si <sub>1,33</sub> O <sub>6</sub>	0,01	Fe <sup>0,92</sup> Mg <sub>0,66</sub> Fe <sup>0,59</sup> Al <sub>0,24</sub> Ti <sub>0,58</sub> O <sub>4</sub>			0,11
20	1114	0,9531	2,59	2,06	1,00	86,81	0,34	(Ca <sub>0,01</sub> Mg <sub>0,79</sub> Fe <sup>0,19</sup> ) <sub>2</sub> SiO <sub>16</sub>	3,50	Na <sub>0,02</sub> Ca <sub>0,94</sub> Fe <sup>0,12</sup> Mg <sub>0,57</sub> Fe <sup>0,11</sup> Ti <sub>0,28</sub> Al <sub>0,59</sub> Si <sub>1,38</sub> O <sub>6</sub>					0,43
10	1112	0,9391	2,61	2,25	1,00	81,93	0,25	(Ca <sub>0,01</sub> Mg <sub>0,78</sub> Fe <sup>0,21</sup> ) <sub>2</sub> SiO <sub>16</sub>	4,27	Na <sub>0,02</sub> Ca <sub>0,92</sub> Fe <sup>0,13</sup> Mg <sub>0,61</sub> Fe <sup>0,11</sup> Ti <sub>0,21</sub> Al <sub>0,50</sub> Si <sub>1,49</sub> O <sub>6</sub>					0,80
3	1100	0,8282	2,59	2,76	1,00	68,59	0,04	(Ca <sub>0,01</sub> Mg <sub>0,75</sub> Fe <sup>0,24</sup> ) <sub>2</sub> SiO <sub>16</sub>	8,71	Na <sub>0,02</sub> Ca <sub>0,90</sub> Fe <sup>0,16</sup> Mg <sub>0,68</sub> Fe <sup>0,10</sup> Ti <sub>0,10</sub> Al <sub>0,36</sub> Si <sub>1,68</sub> O <sub>6</sub>	2,94	Fe <sup>0,99</sup> Mg <sub>0,47</sub> Fe <sup>0,79</sup> Al <sub>0,29</sub> Ti <sub>0,46</sub> O <sub>4</sub>	1,36	K <sub>0,02</sub> Na <sub>0,33</sub> Ca <sub>0,65</sub> Al <sub>1,65</sub> Si <sub>2,35</sub> O <sub>8</sub>	1,17

*Annex 6.2*

*Explosive felsic volcanism on El Hierro (Canary Islands).*

*Pedrazzi, D., Becerril, L., Martí, J., Meletlidis, S., Galindo, I.*

# Explosive felsic volcanism on El Hierro (Canary Islands)

Dario Pedrazzi · Laura Becerril · Joan Martí ·  
Stavros Meletlidis · Inés Galindo

Received: 24 August 2013 / Accepted: 23 August 2014 / Published online: 7 September 2014  
© Springer-Verlag Berlin Heidelberg 2014

**Abstract** The Canary Islands consist of seven basaltic shield volcanoes whose submerged portion is much more voluminous than the subaerial part of each island. Like so many other volcanic oceanic islands, the indicative deposits of explosive felsic volcanism are not a common feature on the Canary archipelago. Hitherto, they have only been documented from the central islands of Gran Canaria and Tenerife, which are the largest volcanic complexes of the islands. On the other Canary Islands, the presence of felsic rocks is mostly restricted to intrusions and a few lava flows, generally within the succession in the oldest parts of individual islands. In this paper, we present a detailed stratigraphic, lithological and sedimentological study of a significant felsic pumice deposit on the island of El Hierro, referred here as the Malpaso Member, which represents the only explosive episode of felsic volcanism found on the Canary Islands (outside of Gran Canaria and Tenerife). The products of the eruption indicate a single eruptive event and cover an area of about 15 km<sup>2</sup>. This work provides a detailed stratigraphic and chronological framework for El

Hierro, and four subunits are identified within the member on the basis of lithological and granulometric characteristics. The results of this study demonstrate the importance of an explosive eruption in a setting where the activity is typified by effusive basaltic events. Given the style and the spatial distribution of the Malpaso eruption and its products, a future event with similar characteristics could have a serious impact on the population, infrastructure and economy of the island of El Hierro.

**Keywords** El Hierro · Canary Islands · Phreatomagmatism · Explosive volcanism · Volcanic hazard

## Introduction

The island of El Hierro (in the Canary Archipelago) is a typical basaltic shield volcano mainly constructed by effusive volcanism but also featuring phases of both Strombolian and Hawaiian activity. Most of the rocks that form the subaerial succession on El Hierro are of basic composition and include, above all, basanites, basalts and trachybasalts (Pellicer 1975; Balcells and Gomez 1997a, b; Carracedo et al. 2001). Although the presence of subordinate rocks with trachytic compositions on El Hierro has previously been reported (Pellicer 1975, Pellicer 1977; Fuster 1993; Balcells and Gomez 1997a, b; Carracedo et al. 2001), their relevance to the volcanological evolution of this island has never been discussed in detail, probably because these rocks are volumetrically subordinate to the island's mafic rocks. Felsic rocks are present as dikes and lava flows associated with the older parts of the island and include minor pumice deposits that are interbedded with basanitic lavas flows. These formations are more common in the upper part of the stratigraphic sequence that forms the shield edifice of El Golfo. The felsic formations have been interpreted as products of fractional crystallisation

---

Editorial responsibility: T. Thordarson

---

**Electronic supplementary material** The online version of this article (doi:10.1007/s00445-014-0863-1) contains supplementary material, which is available to authorized users.

---

D. Pedrazzi (✉) · L. Becerril · J. Martí  
Institute of Earth Sciences Jaume Almera, ICTJA-CSIC,  
Group of Volcanology, SIMGEO (UB-CSIC) Lluís Sole i Sabaris s/n,  
08028 Barcelona, Spain  
e-mail: d\_pedrazzi@yahoo.com

L. Becerril · I. Galindo  
Instituto Geológico y Minero de España (IGME) c/ Alonso Alvarado,  
43-2A 35003 Las Palmas de Gran Canaria, Spain

S. Meletlidis  
Centro Geofísico de Canarias, IGN, Santa Cruz de Tenerife, Spain

from an alkalic mafic parent (Carracedo et al. 2001). Radiometric ages ranging from  $8.69 \pm 0.15$  to  $8.13 \pm 0.06$  ka BP have been determined for the pumice deposits (Pellicer 1977; Perez-Torrado et al. 2011).

The submarine eruption that lasted from early October 2011 to the end of February 2012 about 2 km off the southern coast of El Hierro increased awareness of the possibility that felsic (i.e. more explosive) eruptions could take place on an island that is mostly characterised by mafic (i.e. less explosive) volcanism. Although this eruption mostly produced basanitic magmas in the form of submarine lava flows and pyroclastic fragments (Martí et al. 2013a, b), the first collected products were lava balloons having a highly vesiculated, low density aphyric white core, surrounded by a thin, highly vesicular basanitic carapace (Meletlidis et al. 2012; Sigmarrsson et al. 2013).

Knowledge of Holocene intrusive and volcanic activity is important for hazard assessment on the island because it has just entered into a period of renewed activity. Likewise, good understanding of felsic deposits is particularly relevant because magnitude VEI 3–5 explosive events would represent a major threat to the island. Also, previous studies would have identified deposits of certain extent, interpreted to be a formation representing one event/eruption or an episode made up from several events (Pellicer 1977; Balcells and Gomez 1997a, b; Carracedo et al. 2001; Perez-Torrado et al. 2011).

In this study, we describe a detailed stratigraphic, lithological and sedimentological study of these pumice deposits, which we name here as the Malpaso Member. We present the field descriptions and the petrographic and granulometric data of these felsic deposits and discuss their relative age, transport/depositional mechanisms, the corresponding eruption dynamics and implications for hazard assessment on the island of El Hierro.

## Geological setting

Located 100 km off the east coast of Africa, the Canary Archipelago is composed of seven major volcanic islands and a number of smaller islets and has a total surface area of almost 7,500 km<sup>2</sup> (Fig. 1). The islands are Neogene in age (Schmincke 1982; Araña and Ortiz 1991) and emerged at around 24 Ma (Robertson and Stillman 1979; Le Bas et al. 1986; Marinoni and Pasquare 1994; Marinoni and Gudmundsson 2000). El Hierro is the southwesternmost and smallest island in the archipelago, with an area of 269 km<sup>2</sup>. It has an estimated total edifice volume (subaerial and submarine) of 5,500 km<sup>3</sup> and rises about 5,500 m from its submarine base at a depth of 4,000 m (Schmincke 1990). The highest point on the island is Malpaso (1,501 m above sea level (a.s.l.)).

With its oldest subaerial deposits dated at 1.12 Ma, this island is considered to be the youngest in the Canary Archipelago (Fuster 1993; Guillou et al. 1996). Carracedo (1996) and Carracedo et al. (1998) have cited El Hierro as a classic case of a triple-armed rift system (Fig. 1) inasmuch as it is the result of three main volcanic cycles corresponding to the construction and partial destruction of successive volcanic edifices (Guillou et al. 1996; Balcells and Gomez 1997a, b). The first edifice corresponds to the Tiñor volcano (1.12–0.88 Ma), the second to El Golfo-Las Playas edifice (545–176 ka) and the third to the island's Rift volcanism (158 ka–Present time) (Fig. 1). Tiñor edifice mainly outcrops in the incised valleys and cliffs of the NE of the island showing during its last stages of growth an incipient development of the three rifts (Fig. 1). El Golfo-Las Playas edifice was constructed attached to the western flank of the remains of the previous edifice developing a clear three rift system (Fig. 1). The last growing stage of El Hierro was characterised by eruptions which occurred equally along the three rifts of the island (Fig. 1) (Balcells and Gomez 1997a, b; Carracedo et al. 2001). At least five debris avalanches have taken place during the construction of the volcano (Masson 1996; Urgeles et al. 1996, 1997; Carracedo et al. 1999, 2001; Masson et al. 2002; Longpré et al. 2011). These avalanches have notably changed its morphology. The ages of the debris avalanches range from <880 to 545–176 ka for the first at Tiñor and Las Playas I, and early avalanches were followed by landslides at Las Playas II (176–145 ka) and El Julan (>158 ka), located at SE and at SW of the island, respectively (Fig. 1). The most recent landslide corresponds to El Golfo, whose age has been recently proposed more precisely as between 87 and 39 ka (Longpré et al. 2011) (Fig. 1). The latest eruption took place on the submarine south rift in the sea off Las Calmas (Fig. 1) and lasted from 10 October 2011 to the end of February 2012 (Martí et al. 2013a, b).

The geology of the island reflects its formation by effusive magmatic eruptions of basic composition, as well as by Hawaiian-Strombolian episodes, fed by subvertical dykes (Becerril et al. 2013), combined with a number of hydromagmatic eruptions (Becerril 2009). The island's eruptions have been mainly basanitic in nature (Pellicer 1977; Carracedo et al. 2001). Examples of felsic deposits on the island are the trachytic lava flows near Las Puntas (176 ka; Guillou et al. 1996) and those present close to Playa del Pozo and on the uppermost part of the cliff of Las Playas (Balcells and Gomez 1997a, b) (Fig. 1). Pellicer (1977) identified trachytic pyroclastic deposits around Malpaso, which were dated by <sup>14</sup>C at an age of  $8.69 \pm 0.15$  ka BP (conventional radiocarbonic age) and attributed to an explosive eruption subsequent to the construction of the Tanganasoga edifice (Fig. 1). Balcells and Gomez (1997a, b) described these as laminated 'surge-type' trachytic deposits formed by a

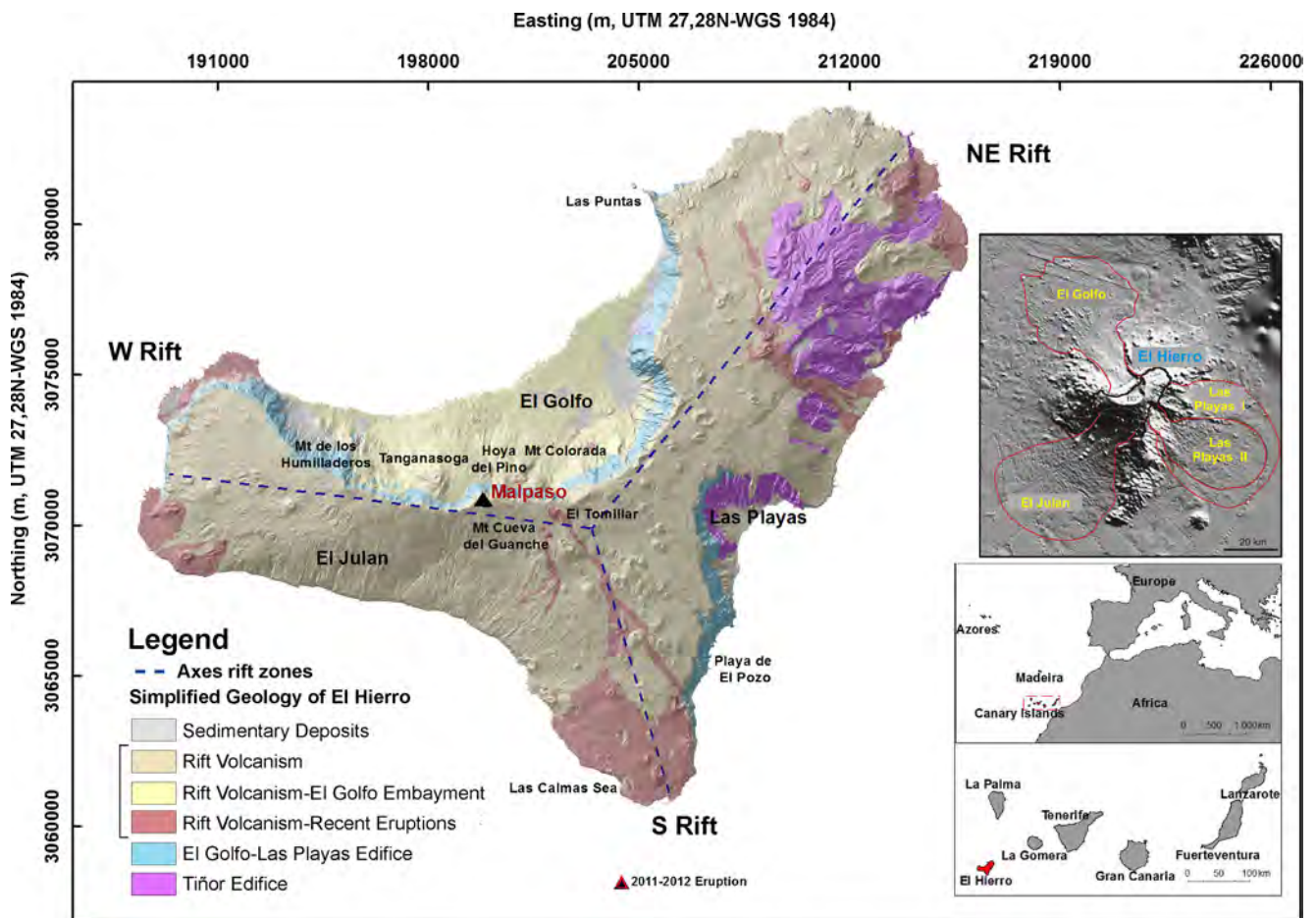


**Fig. 1** Location and simplified geological map of El Hierro. The main volcanic edifices (Tiñor, El Golfo-Las Playas and Rift Volcanism) and axis rift zones are shown. Differences in colour between legend and map are due to the overlaying of the DEM hillshade. Main topographic names

on text are placed in the figure. *Inset at the right bottom part* presents the location of the Canary Islands. *Shaded relief image of El Hierro at the right top part inset* shows areas affected by landslides (Modified from Masson et al. 2002)

previous eruption of Tanganasoga, probably related to the same volcanic complex. Carracedo et al. (2001) interpreted these deposits to represent an eruption of highly fractionated magma during the terminal stages of activity at El Golfo volcano (176 ka) prior to the establishment of the Rift volcanism. More recently, Perez-Torrado et al. (2011) obtained  $^{14}\text{C}$  age of  $8.13 \pm 0.06$  ka BP (conventional radiocarbonic age) for charcoal located in a paleosol under these deposits and suggested that their emplacement was coeval to the construction of Tanganasoga inside the landslide depression of El Golfo.

**Methods**

A preliminary study and interpretation of 1:5,000-scale orthophotos was carried out to obtain a complete overview of the area, to identify possible outcrops of interest and to discriminate between different landscape features occurring in the field. In order to understand the general geological framework of the area and to define the characteristics and extent of

the deposits, we undertook extensive field mapping at 1:5,000 scale in an area covering about 15 km<sup>2</sup>. The stratigraphic criteria used to distinguish different units included primarily sedimentary structures and the apparent component content (juvenile and lithic fragments), as well as characteristics such as grading, colour and sorting. Nomenclature used in the text for bed thickness, grain size and sorting of the pyroclastic deposits follows the one proposed by Sohn and Chough (1989).

In all, 152 stratigraphic sections were measured and used to document the geometry of the deposits and their component proportions (Online resource 1). Maximum clast sizes and thickness of the units were measured to create isopleth and isopach maps; sections with eroded tops were not considered for calculations. All data were managed and processed using the software ArcGIS 10.0 by ESRI<sup>®</sup> and Surfer 7. To obtain volumetric data from the maps, we used Kriging interpolation technic by Surfer 7, ArcGIS and the method proposed by Bonadonna and Costa (2013) to compare the results.

The geographical coordinates of relevant locations, as well as the stratigraphic sections and sampling points, were recorded using a portable Garmin Dakota-20 GPS to a precision of about 3 m (see Online resource 1). The reference zone used was the UTM projection Datum: D\_WGS\_1984, zone 27–28 N.

Binocular and electron microscopes were used to determine the main petrographic and textural characteristics of the juvenile components. As well, pumice particles ~125  $\mu\text{m}$  diameter from each unit were analysed with the scanning electron microscope (SEM; QUANTA 200-FEI) at the University of Barcelona (UB) to provide information on grain morphology in accordance with Dellino and La Volpe (1995). In addition, petrographic analyses were carried out in order to identify the mineralogy and general composition of the studied deposits.

The most representative levels of each stratigraphic unit were sampled and analysed (11 samples in total) for grain-size distribution and componentry. Grain-size analysis was performed by dry sieving at 1  $\phi$  ( $\Phi$ ) with sieves with aperture sizes ranging from 32 to 1/32 mm ( $-5\Phi$  to  $5\Phi$ ). The weight percentages of the sieved fractions were calculated and then plotted as cumulative curves to give grain-size distribution and the Inman parameters (median grain size ( $\text{Md}\Phi$ ) and sorting coefficient ( $\sigma\Phi$ )). The proportion of juveniles from  $-5\Phi$  to  $0\Phi$  was defined by hand picking and from  $0\Phi$  to  $5\Phi$  using a binocular microscope and image analysis techniques (e.g. ImageJ software). This point-counting method allows identifying the different components of each particle-size class using binocular microscope pictures.

## Stratigraphy

The Malpaso Member forms a succession of pyroclastic units with thicknesses from 3 to 81 cm that are exposed in the vicinity of Malpaso (1,500 m a.s.l.) (Figs. 2 and 3), the highest point on the island of El Hierro. These deposits overlie unconformably older massive-to-stratified Strombolian scoria fall deposits and associated lava flows originated from the uppermost part of the edifice of El Golfo (Carracedo et al. 2001) (Fig. 2). The Malpaso Member deposits are discontinuously covered by lava flows and fallout deposits associated with younger scoria cones located on the edge of El Golfo escarpment and by later fallout deposits from the Tanganasoga volcano and other nearby vents, all of which are constructed inside the embayment of El Golfo (Fig. 2). Well-developed paleosols are found throughout the sequence (Fig. 2), indicating that a significant period of time elapsed between the various eruptions.

The lower panel on Fig. 2 illustrates correlations among eight representative stratigraphic columns. In the vicinity of Malpaso (columns 1 and 2; Fig. 2), the Malpaso Member rests

on a paleosol developed on older mafic Strombolian deposits, in turn overlain by the Tanganasoga deposits. At these sites, the Malpaso Member consists of lithic-rich pumice deposits. Beyond the headwall of the landslide at El Golfo, on the northern flank of El Hierro, the Malpaso Member was not identified. In the eastern sector (columns 3–5; Fig. 2), a series of Strombolian deposits—including fallout material from Montaña Cueva del Guanche, and from the vents located inside the embayment of El Golfo (e.g. Hoya del Pino and Montaña Colorada) (Fig. 2)—and a lava flow originating from El Tomillar, overlie the Malpaso Member. The southern sector is mainly covered by lava flows and subordinate Strombolian deposits (columns 6 and 7; Fig. 2). The western side of the area shows a similar sequence with Strombolian and hydromagmatic deposits covering the Malpaso Member (column 8; Fig. 2).

The Malpaso Member consists of four units (characterised by different sedimentary structures and component content as well as grading, colour and sorting) (Fig. 3). These units extend over the whole of the terrain in the Malpaso area (Fig. 2) and tend to thicken in depressions and valleys. Investigations of 152 outcrops (Fig. 2) show that these deposits have a thickness maxima in the southeasterly, extending >2.5 km from Malpaso peak (Fig. 2). Simplified stratigraphic logs from 11 key localities are shown in Fig. 3. The area was divided into proximal (0–1 km), medial (1–2.5 km) and distal zones ( $\geq 2.5$  km) based on thickness and grain-size characteristics of the deposit (Fig. 2). The maximum observed thickness of the entire succession is in the range 40–81 cm at Malpaso peak and 3–5 cm in the most distal outcrops ( $\geq 2.5$  km). Anomalous thickness values were obtained from occasional depressions. The Malpaso Member is divided into four units (from base to top: N1, N2, N3 and N4) on the basis of lithology and depositional characteristics (Figs. 3 and 4).

### Unit N1

This unit is up to 21-cm thick (Figs. 3 and 4) and is composed mainly of well-sorted, clast-supported, thin medium pumice lapilli beds alternating with matrix-supported, poorly stratified thin beds of coarse ash with well-defined boundaries (Fig. 4). The pumice is light grey in colour and has small vesicles (millimetre to submillimetre in size) and lithic clasts consisting mainly of basalt lava fragments. The base of unit N1 is erosive as implied by undulating but sharp basal contact

**Fig. 2** Mapped on-land extent of the Malpaso Member deposits, with all the studied outcrops indicated. *Dashed lines* represent the extension of proximal (0–1 km), medial (1–2.5 km) and distal ( $\geq 2.5$  km) zones of the deposit (see text for further details). Selected stratigraphic columns (*bottom*) illustrate stratigraphic position and field relations of the Malpaso Member to older as well as younger deposits

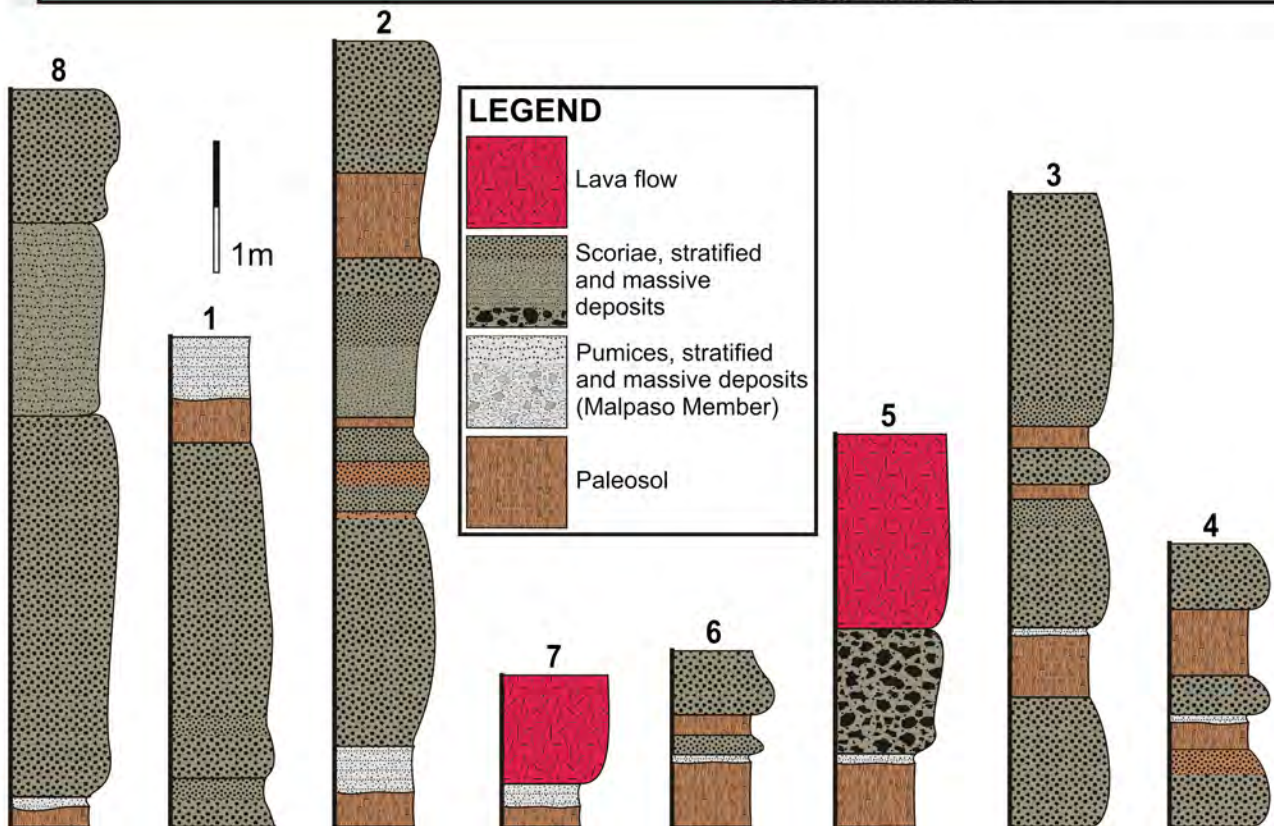
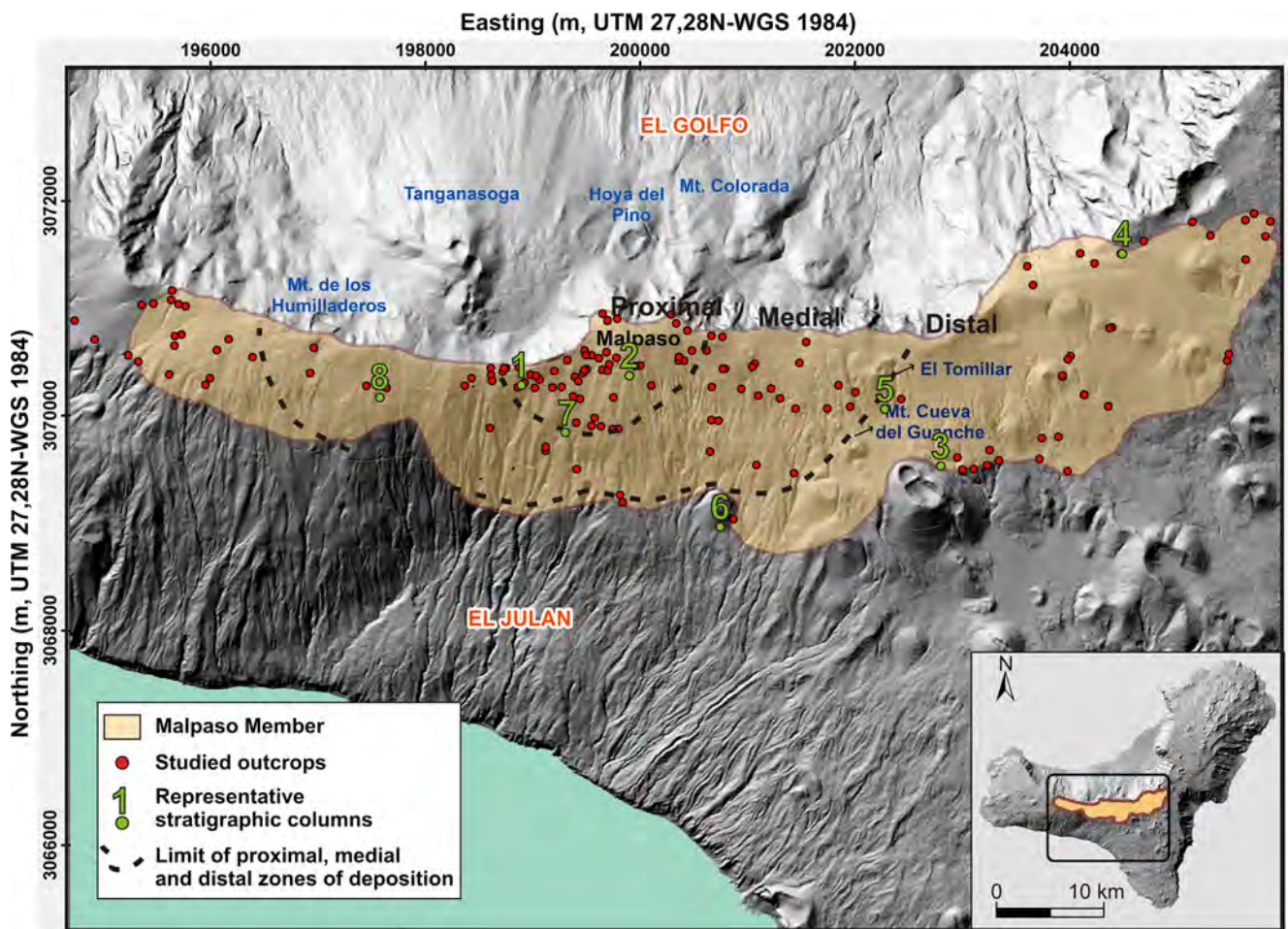


(Fig. 4a, b). Unit N1 rests directly on a paleosol that, according to radiocarbon ages given by Pellicer (1977) and Perez-Torrado et al. (2011), has an age of  $8.69 \pm 0.15$  and  $8.13 \pm 0.06$  ka BP (conventional radiocarbon age), respectively. To

the north, south and east, N1 thins out rapidly and is just a few centimetres thick at distances of  $\sim 2.5$  km.

Two subunits are distinguishable: N1a and N1b (Fig. 3). N1a at Malpaso reaches a maximum thickness of 8–10 cm and

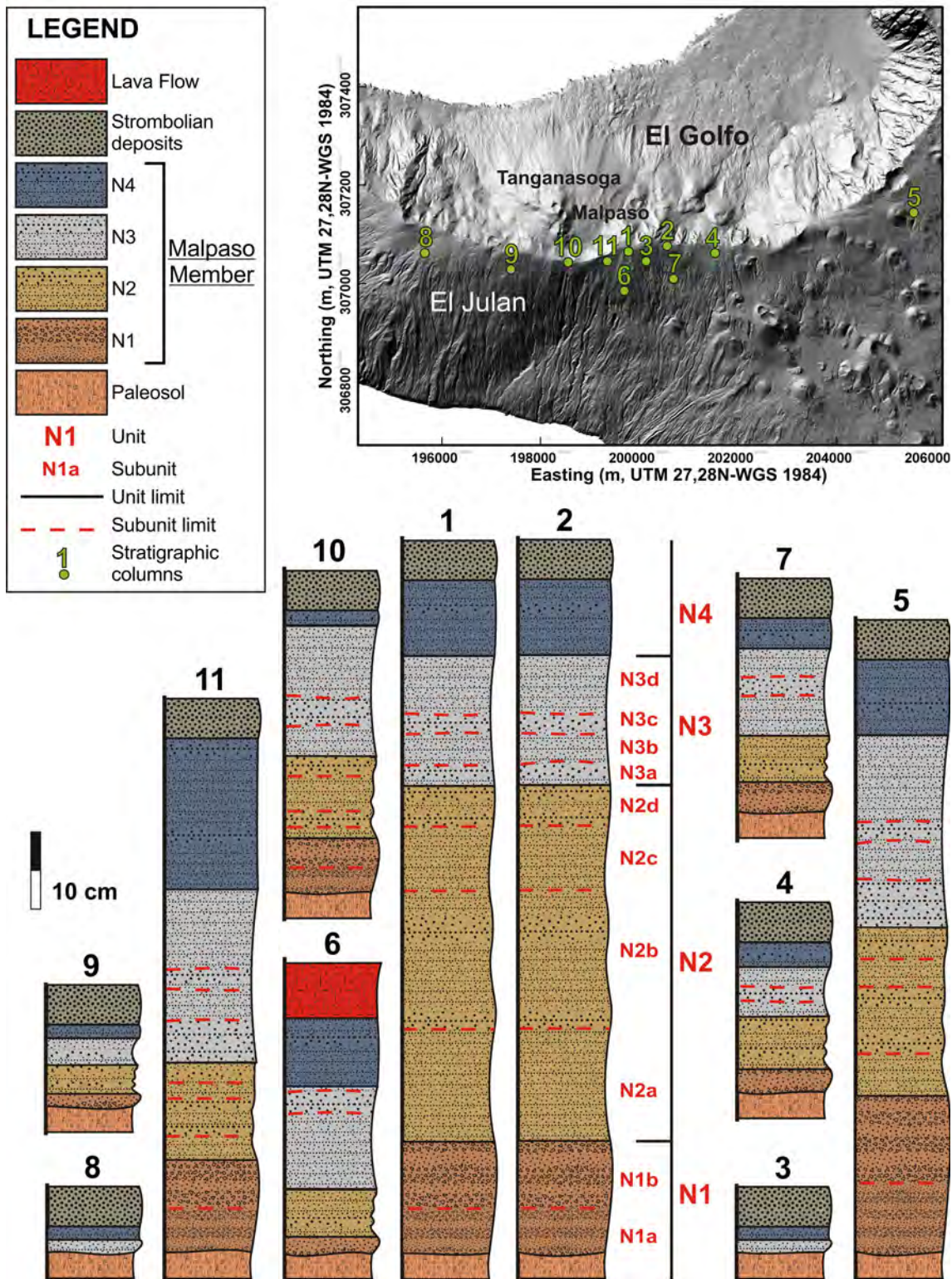


**Fig. 3** Composite stratigraphic sections of the Malpaso Member and its different units and subunits. See text for further details

comprised thin alternating beds of clast-supported pumice medium lapilli (<1 cm) and coarse ash-rich beds (1–2 cm). The deposit contains lava lithic fragments up to 2 cm in diameter. N1b is similar but shows a remarkable increase in the size of pumices, which reach up to 10 cm in diameter. The two subunits are well recognisable in the proximal zone (Figs. 2, 3 and 4a) while at the medial zone the distinction between the two subunits is unclear (Fig. 4b), and at distances  $\geq 2.5$  km (Fig. 2), the subunits are thinner and finer grained, which makes it very difficult to separate them (Fig. 4c).

Unit N2

The thickness of this unit in the proximal region ranges from 20 to a maximum of ~60 cm (Fig. 3). It consists of multiple, thin poorly stratified, dark-brown, matrix-supported ash beds with intercalated very thin (<0.5 cm) beds of poorly vesiculated pumice lapilli (Fig. 4a), and contains lava lithics of the same size. At proximal exposures (Fig. 3) it is possible to differentiate four subunits, labelled here as N2a, N2b, N2c and N2d. N2a is made up of 1–2-mm thick laminae that progressively exhibits an upward increase in grain size from fine ash to fine lapilli. N2a grades into N2b. The same pattern is

repeated in subunits N2c and N2d. Lithic fragments are up to 5 mm diameter in the lapilli-rich layers. At more distal exposures (Figs. 2 and 4b), it becomes progressively more difficult to distinguish the different subunits (Fig. 4c) until they disappear completely.

Unit N3

In the area around Malpaso (Fig. 3), unit N3 has a maximum thickness of 25 cm and is predominantly composed of stratified thin ash beds (3–5 cm). In the lower half, these ash beds are intercalated with minor fine-grained lapilli beds up to 5 cm. Lava lithic clasts up to few millimetres are also recognisable. N3 is lighter in colour than N2 with a sharp contact (Fig. 4a). Four subunits, N3a, N3b, N3c and N3d, are identified in proximal outcrops (Figs. 2 and 3) but are indistinguishable in the outermost distal zone (Fig. 2) where the unit becomes a single (2–3 cm) massive ash-dominated bed (Fig. 4c). N3a and N3c exhibit low-angle cross-bedding, with sets defined by fine lapilli lenses alternating with ash-grade lenses. N3b and N3d are characterised by plane-parallel bedding. In intermediate zones (Fig. 2), N3 has the same characteristics (Fig. 4b) as in the proximal outcrops although the

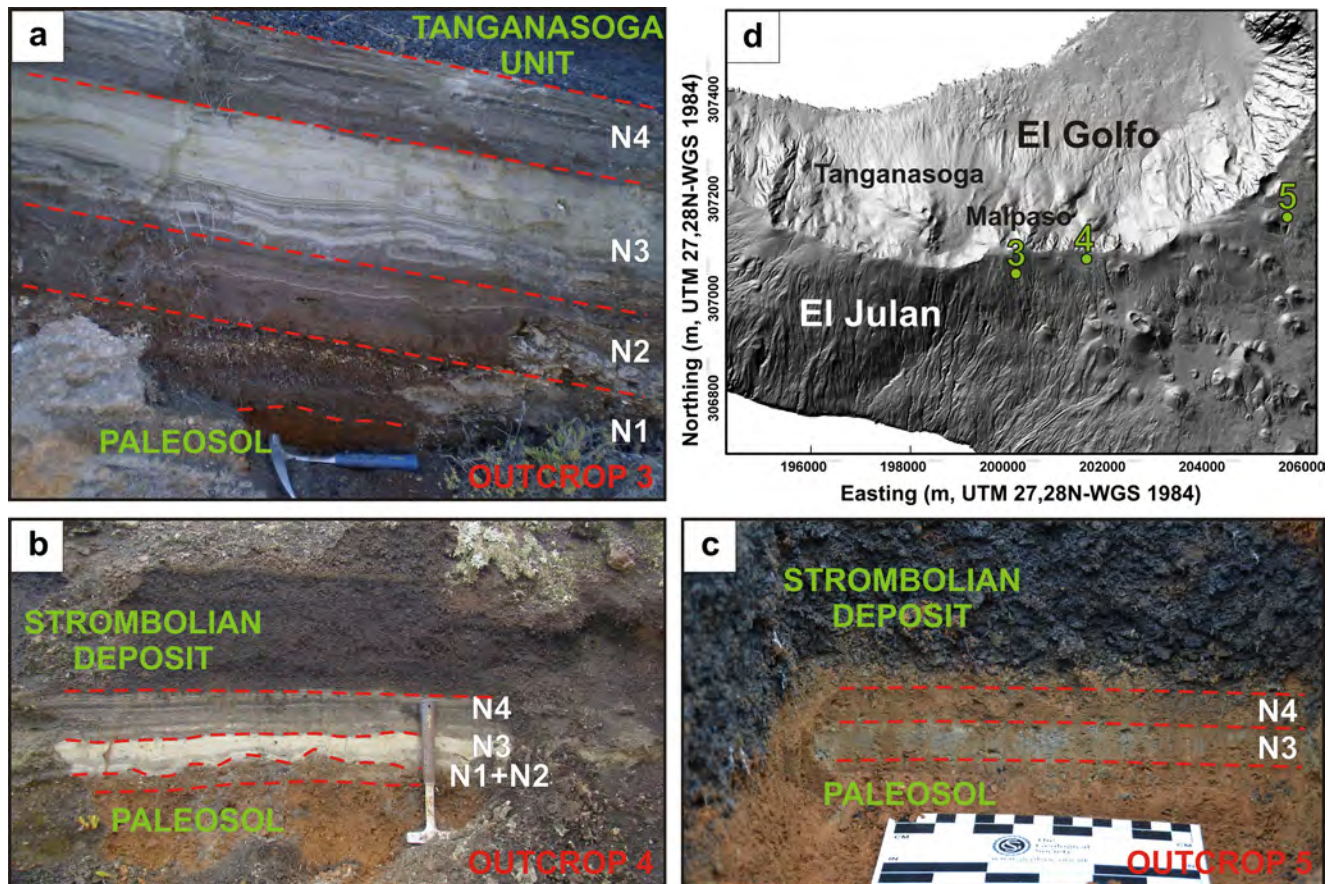


**Fig. 4** Malpaso Member deposits at **a** proximal, **b** medial and **c** distal outcrops. At the *right top part*, a map with the locations of the photographed outcrops is presented

deposit structure tends to be massive as observed in the distal area as well (Fig. 4c).

#### Unit N4

This unit is up to 20-cm thick in the proximal to medial outcrops (Fig. 3) and is composed of laminated ash and very thin (1–3 cm) lithic-rich lapilli thin beds with contacts ranging from sharp to gradational or diffuse and inverse grading. A general thinning upward sequence is observed. Millimetre- to centimetre-size lava lithic clasts are present throughout the entire unit and are responsible for its characteristic grey-black colour (Fig. 4a). Some white-coloured ash beds (like unit N3 in appearance) are also present. In most distal exposures (Fig. 3), it is 1–2-cm massive layer (Fig. 4c).

#### Isopach and isopleth maps

An isopach map of the Malpaso Member (Fig. 5a) was constructed from field measurements using 134 sections. This map illustrates that the thickness of the deposit changes sharply over short distances. The most abrupt change in thickness is observed between isolines 80 to 70 cm and 10 to 0 cm. The most distal exposure of Malpaso Member occurs 11 km from the thickest deposit outcrop. Thinning half distance (bt) of ~400 m has been obtained from the whole deposit. The isopach map gives a minimum deposit area of 15 km<sup>2</sup> and volume of about 1.7 · 10<sup>6</sup> m<sup>3</sup>, 1.8 · 10<sup>6</sup> m<sup>3</sup> and 1.9 · 10<sup>6</sup> m<sup>3</sup> through the Arcgis, Krigging and Bonadonna and Costa (2013) methods. The isopleth map is based on 30 measurements of the five largest pumice clasts in the subunit N1 (Fig. 5b). The largest pumice clast, ~10 cm in diameter, is present in the Malpaso area.

#### Componentry characteristics and grain-size distribution

The vertical variations in grain-size distribution and componentry of individual beds are presented on Fig. 6. Figure 7 shows plots of Md $\Phi$  and  $\sigma\Phi$  parameters and F1 (wt.% <1 mm diameter (0 $\Phi$ )) and F2 (wt.% <1/16 mm diameter (4 $\Phi$ )). The modal proportions of juvenile pumice, free crystals and accidental lithic fragments (mostly derived from older lava flows) are given for each grain-size fraction (or class) and their distribution among grain-size fractions as well as subunits is variable (Fig. 6). Lithics in N1 are present in almost all grain-size fractions with crystals and lithic fragments increasing in percentage in the 1 $\Phi$ –5 $\Phi$ -size range (Fig. 6). The amount of juvenile fragments (pumices and free crystals) in individual N1 samples ranges from 60 wt.% (N1BF) to a maximum of 75 wt.% (N1BG). N2 sample is finer grained than those of unit N1, while N2G sample shows a similar trend as the N1BG

sample. Both samples from unit N2 are made of ~70 wt.% of juvenile fragments. Unit N3 is significantly different in terms of sorting and overall finer-grained samples. Sample N3A is from the lowest part of the unit and exhibits the same trend as sample N2G (from top of N2) although somewhat finer grained (Fig. 6) with a 65 wt.% content of juvenile fragments. The grain-size distribution is also similar to N1BG (a lapilli unit in N1b) although shifted to finer-grain sizes but very different from the rest of the samples displayed from N1 and N2. The juvenile content increases upwards, hence the change in colour from dark to light grey occurs to a maximum value of approximately 90 wt.%. Free crystals make up 25 wt.% of the juvenile population (Fig. 6). The contact between N3 and N4 is marked by a distinct colour change from light grey to dark brown. An increase in lithic clasts abundance, with total values of 55–60 wt.% in almost all of the range in grain sizes is the most likely reason for this abrupt change in colour.

In terms of grain size, the two N1 subunits (i.e. N1A and N1B) at the base of Malpaso Member are characterised by alternating ash and lapilli layers and a general upward size increase in grain size in the lapilli (Fig. 6). In both subunits, the lapilli layers are well sorted ( $\sigma\Phi$  ~1.6–1.7; Fig. 7) and typified by unimodal samples (e.g. N1AG and N1BG). The ash-rich layers of each unit are poorly sorted ( $\sigma\Phi$  ~2.55; Fig. 7a) and typified by polymodal grain-size distribution (e.g. N1AF and N1BF on Fig. 6) N1AG and N1BG are characterised by 3 and 2 wt.% of fine ash (<63 mm), respectively, while N1AF and N1BF have significantly higher abundance of fine ash of 16 and 11 wt.%, respectively (Fig. 7b). The two samples (N2 and N2G) analysed from unit N2 exhibit similar grain-size characteristics as those from unit N1. Sample N2 is a polymodal poorly sorted fine ash ( $\sigma\Phi$ =2.39), with 28 wt.% of fine ash and sorting of  $\sigma\Phi$ =2.23. N2G is well sorted, unimodal with  $\sigma\Phi$ =1.61 and 4.6 wt.% as fine ash. Three samples were analysed for grain size from the N3 unit: N3A from the first subunit and N3C and N3D from the second (Fig. 7a). N3A and N3C are well-sorted lapilli ash with  $\sigma\Phi$  values in the range 1.46–1.63 (Fig. 7a). N3D is a well-sorted mainly made up of ash with  $\sigma\Phi$  values reaching 1.63 (Fig. 7a). N3D contains higher abundance of in fine ash (41 wt.%) than subunit N3A (28 wt.%) and N3C (14 wt.%) (Fig. 7b). Unit N4 is mainly made up of ash, although some lapilli-rich horizons can also be found toward its upper part. As observed in Figs. 6 and 7a, b, N4F is a polymodal, poorly sorted ( $\sigma\Phi$ =2.06) ash-rich layer with 25 % by weight of fine ash, while N4G is a unimodal, well-sorted ( $\sigma\Phi$ =1.59) lapilli-rich layer with 6.5 % of fine ash.

#### Grain shape of juvenile clasts

The morphology of juvenile clasts ~125  $\mu$ m in diameter was examined with the SEM in order to detect the magmatic vs.

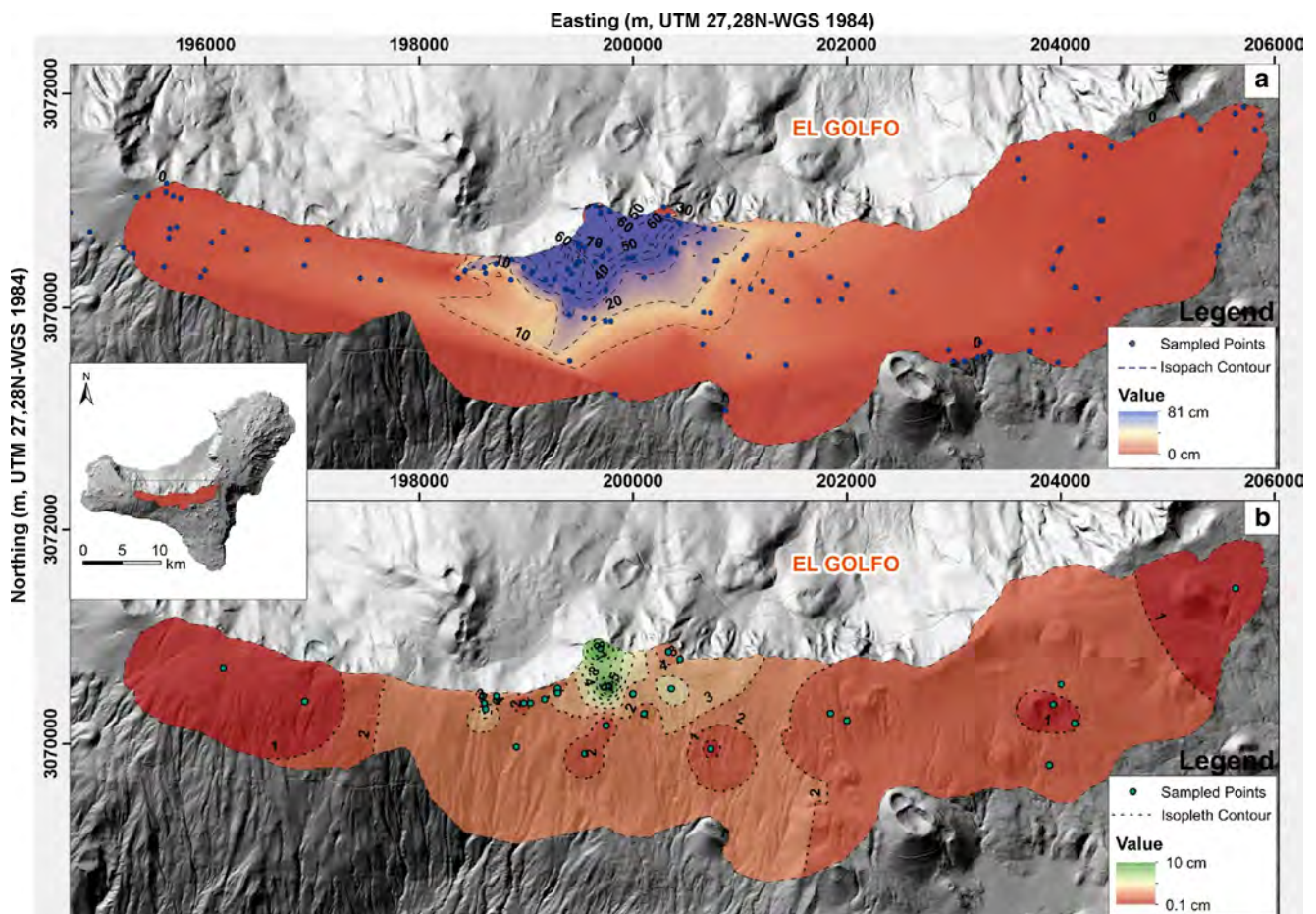


**Fig. 5** a Isopach map (cm) of the Malpaso Member; b isopleth map (cm) of the unit N1 of the Malpaso Member

hydromagmatic fragmentation style according to morphoscopy criteria (e.g. Heiken and Wohletz 1985; Dellino and La Volpe 1995, 1996; Palladino and Taddeucci 1998; Dellino et al. 2001; Polacci et al. 2003). Texturally, individual particles in levels N2–N4 are moderately to poorly vesicular and characterised by spherical to elongated vesicles, tending to have blocky and stepped morphologies (Fig. 8). Fine particles (<32  $\mu\text{m}$ ) commonly adhere to larger surface fragments as dust (Fig. 8c). Another characteristic feature of these particles is the presence of quenching cracks (Fig. 8e).

### Mineralogy

Juvenile components have identical mineralogy that suggests a trachiphonolitic composition throughout the whole Malpaso Member, but there are variations in texture between units. Pumice fragments are porphyritic, with 25–30 % of phenocrysts in volume that are surrounded by a glassy groundmass with a variable amount of vesicles of different sizes (6 to <0.05 mm) and forms (elongated and spherical). The mineral assemblage consists of euhedral-to-subhedral plagioclase, amphiboles and, to a lesser extent, clinopyroxene (Fig. 9). The

same phases were also found in the groundmass, along with oxides and glass. The maximum size of the phenocrysts is 2.5 mm (plagioclase) and 2 mm (amphiboles).

### Discussion

#### Physical volcanology of the Malpaso Member

The Malpaso Member covers an area of approximately 15 km<sup>2</sup> (Fig. 2), almost 5 % of the total area of El Hierro Island. Calculations of the volume of the exposed deposit is about  $1.8 \cdot 10^6$  m<sup>3</sup>. However, its original extent and volume is inferred to have been significantly larger as evidences indicate that large part of the original deposits have been removed by erosion, in particular by landslide at El Golfo. Stratigraphic relations and distribution of the Malpaso Member demonstrate that it was emplaced before 87–39 ka landslide (Longpré et al. 2011). Consequently, the mapped distribution of the Member does not represent its original extent. Despite these practical limitations, variations in distribution and thickness are observed, which in turn can be used to infer about mode of emplacement for the Malpaso member.

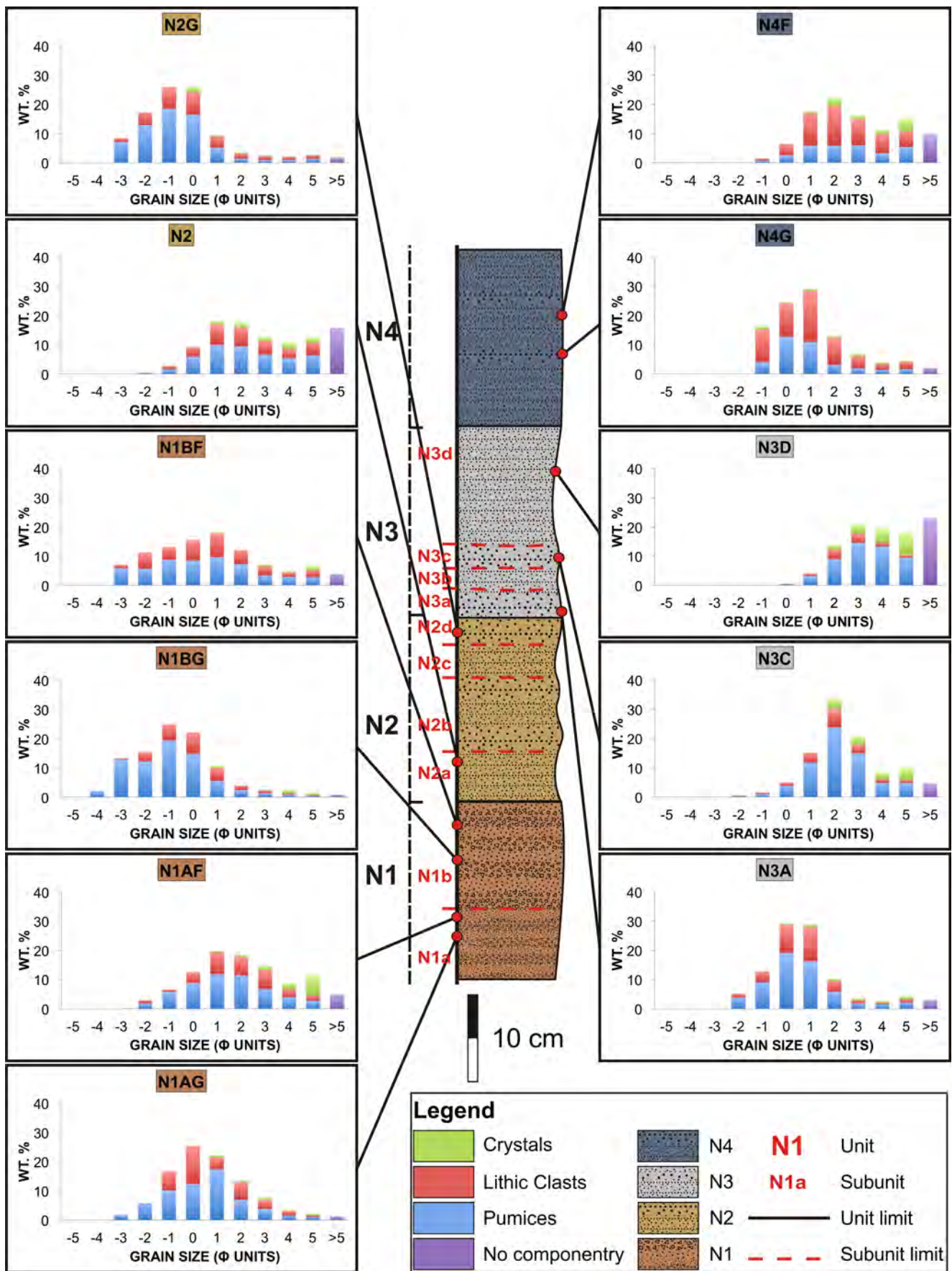


**Fig. 6** Grain-size distribution and modal composition of representative samples from the Malpaso Member. *N1* pumice lapilli layers alternating with poorly stratified ash layers, *N2* ash layers with loose pumice-lapilli-rich layers, *N3* massive poorly stratified ash beds with interbedded lapilli layers, *N4* ash and pumice-rich lapilli layers with abundant lava lithic clasts. The different subunits (e.g. *N1a*) are indicated on the *left side* of the stratigraphic log. Sample numbers are given at the *top of each bar graph*

The four recognised units (*N1*, *N2*, *N3* and *N4*) marked different phases of the eruption and can be interpreted in terms of changing of eruptive dynamics and of the transport and depositional systems.

Unit *N1* is characterised by an alternation of centimetre beds of well-sorted, fine-poor pumice lapilli and poorly sorted ash layers that feature a visible difference in grain size and sorting between the lapilli and ash-rich layers (Figs. 3 and 4). These characteristics could be interpreted to have resulted from either a pulsating pyroclastic surge or multiple but discrete closely pyroclastic density current (PDC)-spaced events (Dellino et al. 2004a). These types of deposits resemble the type 1a deposit described in Palladino and Simei (2002) in the Vulsini area (Italy). This deposit comprises normally graded, centimetre-to-decimetre-thick, ash-lapilli beds with coarse lithic and pumice lapilli that are normally graded and/or concentrate downward, in some cases to form clast-supported lower zones. The authors suggest a deposition by direct fallout from the gas-pyroclast suspension (Fisher 1966),

with the rate and style of sedimentation from a ground-hugging turbulent pyroclastic current strongly controlled by local substrate morphology. These deposits, thus, are likely to have been formed by deposition from a turbulent and low concentrated unsteady current with direct suspension sedimentation.

Unit *N2* shows similar characteristics respect to *N1*, but it is made of matrix-supported thin ash beds with interbedded very thin beds of fine pumice lapilli. Lapilli-poor layers with thin internal laminations could be indicative of grain-by-grain-dominated deposition of material transported by suspension in the dilute turbulent flow resulting in grain segregation, whereas lapilli-rich layers with crude associated stratification indicates that shearing was able to induce traction of larger particles that could not be transported in suspension (Arnott and Hand 1989).

Unit *N3* is characterised by laterally continuous stratified thin ash beds with undulating and plane-parallel laminations and minor fine-grained lapilli beds. In the lower part of unit *N3*, bedding is more distinct and individual beds are thicker than in the top half. This unit is interpreted as pyroclastic surge deposits based on plane-parallel and low-angle cross laminations (see Chough and Sohn 1990; De Rosa et al. 1992; Dellino et al. 2004b; Solgevik et al. 2007).

Unit *N4* is composed of single or a repetition of centimetre-ash and lithic-rich lapilli thin beds with continuous internal stratification with sharp or diffuse boundaries and inverse grading. Similar deposits were interpreted as fallout deposits or as pyroclastic surge and co-surge fallout deposits, due to the contemporaneous presence of characteristics normally pertaining to both fallout and surge deposits (e.g. Sohn 1997; Cole et al. 2001; Dellino et al. 2004a, b). It is difficult to discriminate between the two depositional mechanisms, but in this case, the general thinning upward internal sequence and the alternation between coarse and fine-grained layers could be interpreted as deposits emplaced from a single low-concentration PDC (see Sohn and Chough 1989; Sohn 1997; Dellino et al. 2004a, b).

These alternating fine- and coarse-grained beds might be the result of deposition under a tractive regime (e.g. Sohn 1997) similar to the type 2 deposit of Palladino and Simei (2002) at Vulsini Volcano.

The absence, in general, of any fall deposits at the base of each unit, rules out the possibility of a sustained-eruption-column phase supporting the idea that most of the studied deposits were formed directly from dilute PDCs radially expanding from the vent during vulcanian-type explosions with no rise of any sustained convective column. A second hypothesis might suggest a progressive feeding of the transporting system by continuous eruption column collapse as proposed for the Basal Unit of Sovana (BUS) at Vulsini Volcano (Italy) by Palladino and Taddeucci (1998). An interpretation as fallout origin is not favoured because of the

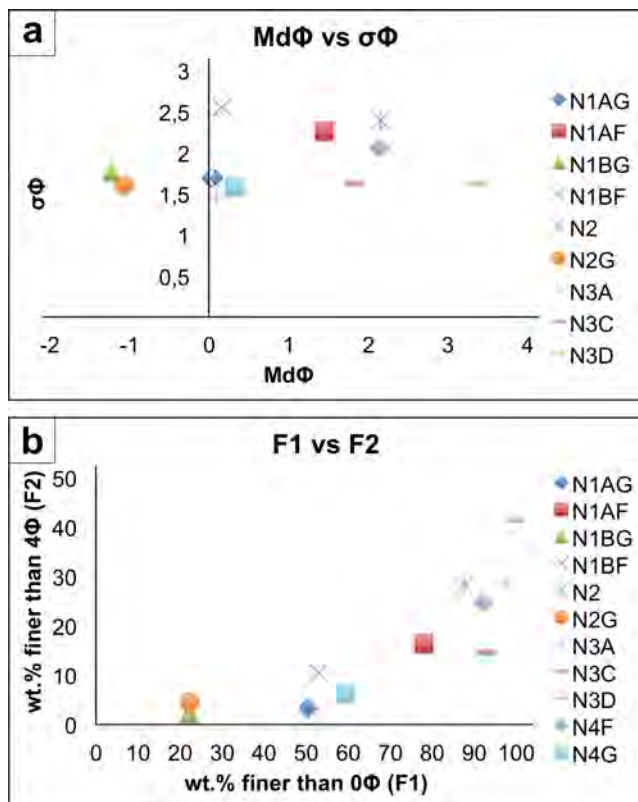
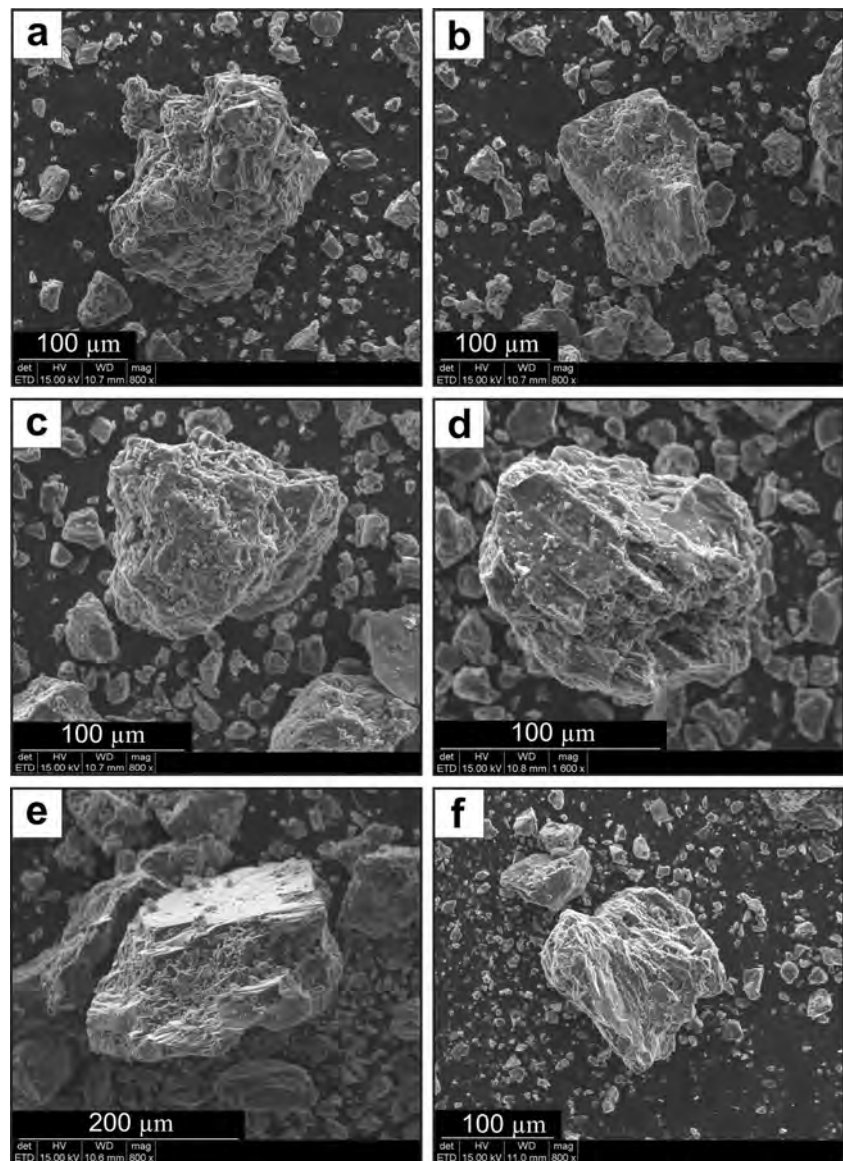


**Fig. 7** a Graphic standard deviation versus median diameter; b F2 (wt.% <1 mm diameter) versus F1 (wt.% <1/16 mm diameter)

**Fig. 8** Scanning electron microscope (SEM) images of pumice from units 2, 3 and 4. Clasts show little abrasion due to transport. Several examples of the most typical morphological features are shown. **a–b** Poorly vesiculated particles from unit N2 with mainly blocky morphologies; **c–d** poorly vesiculated clasts from unit N3 with tiny adhering particles and elongate vesicles; **e–f** dense and poorly vesiculated grains with blocky morphology, quenching crack structures and stepped textures



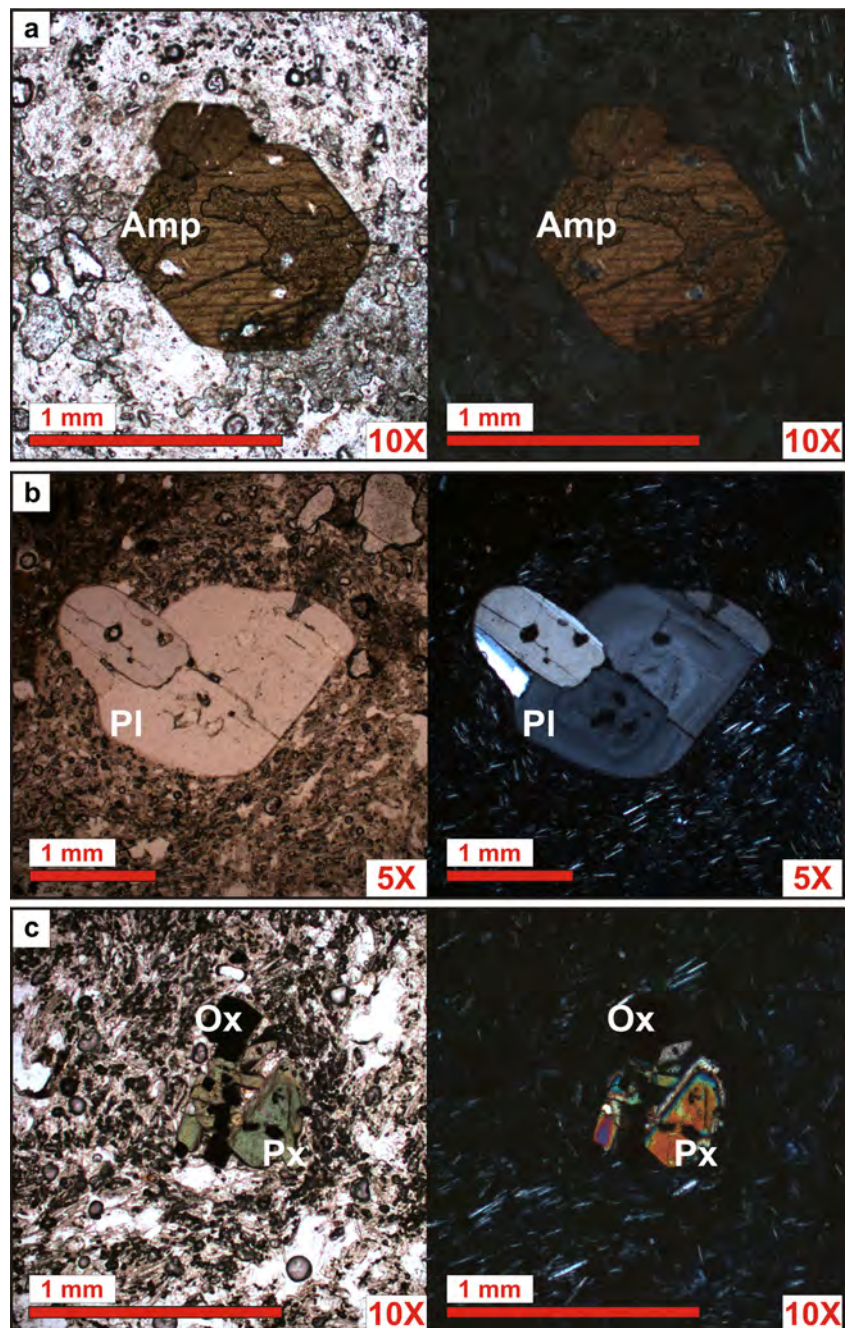
presence of depositional structures such as cross, planar and undulate laminations, tendency to fill channels of the pre-eruptive surface and units organisation. A further hypothesis might suggest a plume carried in opposite directions, with fallout deposits only present in the northern part of El Hierro Island that were later affected by El Golfo landslide. A similar eruption is for example the one of P17 at Sete Cidades Volcano-Sao Miguel Island (Cole et al. 2008) where fallout and PDC deposits of hydromagmatic origin were found in different areas around the volcano.

The sharp contacts with adjacent units demonstrate time-gap between deposition of individual units but not long enough for soil to form or for modifications of the surface of the underlying unit, thus, suggesting that the whole Malpaso member corresponds to the products of a single eruptive event with several pulses of PDC generation. The presence of subrounded/

rounded pumice clasts as observed in the field as well, lateral variations in thickness and depositional features such as undulate deposits tendency to fill channels of the pre-eruptive surface on outcrop scale suggest a lateral flow component of transport.

Grain-size data ( $Md\Phi$  and  $\sigma\Phi$ ; Fig. 7a) support the idea that the Malpaso Member was formed by PDCs.  $Md\Phi$  shows values between 0 and 3.5 while  $\sigma\Phi$  between 1.4 and 2.5 (Fig. 7a). These values are consistent with other surge deposits as, for example, the 1982 eruption at El Chichón Volcano (Sigurdsson et al. 1987) or 1980 eruption at Mount St. Helens (Druitt 1992) or similarly to the B-F facies related to the basal ash deposit of the Sovana Eruption at Vulcini Volcanoes-Italy, with the authors suggesting a deposition from turbulent, low particle concentration, thick pyroclastic current (Palladino and Taddeucci 1998).

**Fig. 9** Petrographic composition of juvenile samples from the eruption: **a** amphibole, **b** plagioclase and **c** pyroxene and oxide



However, some grain-size histograms seem to describe fall-out deposits as shown by granulometric curves (e.g. the samples N1AG, N1BG, N2G, N4G; Fig. 7a). Samples N1AG, N1BG, N2G and N4G refer to the thin coarse-grained layers observed throughout the sequence, but field evidence such as rounding of pumice, and lateral changes of texture and thickness on local scale, allow the distinction from fall deposits. Furthermore, a granulometrical shift toward finer values (negatively skewed distribution of the granulometric curves) is observed for some of the samples (e.g. N1AF, N3C and N4F) probably due to a selective transportation mechanism related to

turbulent suspension. This might be confirmed by the F1 vs. F2 diagram of Walker (1983) (Fig. 7b), showing a content of fine ash (<1/16 mm diameter ( $4\Phi$ )) for most of the finest level (e.g. samples N2, N3A, N3D and N4F) between 16 and 41 wt.%.

Field evidences (thinly laminated, fine- and coarse-grained beds) (Fig. 4), grain size and componentry of deposits (fine-grained, negatively skewed grain-size distribution, high lithic content; see Self and Sparks 1978; Barberi et al. 1989; Houghton and Schmincke 1989; Houghton and Smith 1993) (Fig. 6) and textural features of the juvenile fragments (shape of the fragments; presence of quenching cracks and fine

adhering dust on particle surfaces; see Heiken and Wohletz 1985; Büttner et al. 1999; Dellino and La Volpe 1995; Büttner et al. 2002) (Fig. 8) suggest magma/water interaction. This can occur at different times during a single eruption (e.g. Wohletz et al. 1995) as a function of many different factors. These include the availability of surface water and/or groundwater, the primary and/or secondary permeability and transmissivity of the aquifer and magma pressure within the conduit (Dobran and Papale 1993) that can in turn be related to the magma chemistry (Papale and Dobran 1994).

Unit N1 consists of clast-supported lapilli beds alternating with matrix-supported, poorly stratified thin beds of coarse ash, and unit N2 is made of multiple, thin poorly stratified, dark-brown, matrix-supported ash beds with intercalated very thin (<0.5 cm) beds of poorly vesiculated pumice lapilli. Lithic-rich pumice surge deposits of units 1 and 2 might suggest magma/water interaction and significant widening of the conduit during the first phases of the eruption, when the mass eruption rate was likely to have been low and the conduit still narrow, allowing groundwater to interact with the magma as reflected by the high lithic content of units N1 and N2 (between 25 and 40 wt.% of accidental lithics fragments for both units). In addition within the N2 unit (Figs. 3 and 4) layers are more fine-grained, reflecting a better efficiency in the magma/water interaction with an increase in the energy of the explosions (e.g. Wohletz 1986).

The transition from N2 to N3 seems gradual, although the evident change to a lighter grey colour in N3 (Fig. 4) reveals a rapid decrease in accidental lithics of around 10 wt.% (Fig. 6). This type of deposits might be associated with sharp increases in magma discharge and/or changes in upper conduit-crater geometries as observed in the case of Mt. Pinatubo (Hoblitt et al. 1996), Greenish eruption of Somma-Vesuvius (Cioni et al. 2003), Montserrat (Formenti et al. 2003) or Pollena (Sulpizio et al. 2005). In any case, unit N3, which is predominantly composed of stratified thin ash beds, shows similar characteristic as the lower subunit of the WTT Cupa eruptive unit at Roccamonfina Volcano, Italy (Giordano 1998), which is a white, very fine-grained deposit with clasts generally less than 1 mm and exhibits parallel to low-angle cross-stratification interpreted as a base surge of hydromagmatic origin. The lithological features of the N3 deposit (finer fine-grained tephra than the other units) might suggest efficient fragmentation of the magma (Wohletz 1986). The absence of bedforms in the upper part of this unit might be due to cohesiveness of depositing wet ash, as proposed for turbulent gravity current with a fall component as in the case of the ash-rich beds associated with the AD 180 Hatepe Plinian pumice fall deposit at Taupo, New Zealand (Talbot et al. 1994). The lithic-poor nature of the N3 phreatomagmatic deposits also suggests that the water interacting with the magma was probably not related to groundwater as proposed for example for the WTT Cupa

and WTT Galluccio, and possibly WTT S. Clemente eruptive sequences at Roccamonfina Volcano (Giordano 1998).

A clearly defined limit marks the transition from N3 to N4 with a rapid change in the overall aspect of the deposit, which is composed of laminated ash and very thin (1–3 cm) lithic-rich (lava lithics up to 55–60 wt.%) lapilli thin beds (Fig. 4). As proposed by Sulpizio et al. (2005), the presence of lithic-enriched layers can reflect the clearing of the conduit and restoration of the pristine magma discharge conditions. In such cases, density of the erupting mixture increases due to incorporation of large amounts of cold and heavy lithics. In any case, the general fine-grained aspect and the high accidental lithics of the N4 deposits would rather suggest a renewed efficiency of magma/water interaction with overpressure conditions following the entrance of large quantities of steam in the conduit (Barberi et al. 1989).

Groundwater was, most likely, the main source leading to magma/water interaction. Hydrogeological models of shield volcanoes, as the case of El Hierro Island, are generally poorly constrained, and contrasting models have been proposed in different areas as for example the Hawaiian model (Peterson 1972; Macdonald et al. 1983), and the Canary Island model (Custodio 1978, 1989). Recent works as the one carried out at Piton de la Fournaise volcano-Reunion Island (Join et al. 2005) demonstrates that the geological structure of active shield volcano provides sufficient hydrogeologic conditions to produce a high water table in the interior of the island, creating the conditions for similar eruptions as the one of the Malpaso Member at El Hierro Island.

#### Age of the Malpaso Member and of the landslide at El Golfo

The authors who have mentioned the presence of the trachytic pumice deposit on El Hierro have offered contrasting explanations for its origin, significance and age. Pellicer (1977) attributed this deposit to an explosive eruption subsequent to the Tanganasoga eruption (dated at  $8.69 \pm 0.15$  ka BP), while Balcells and Gomez (1997a, b) described this deposit as a laminated surge-type deposit originating during an eruption that predates Tanganasoga. Carracedo et al. (2001) assumed that this deposit represents later evolutionary stages of the El Golfo volcano construction, thereby interpreting it as a pre-El Golfo sector collapse dated around 176 ka. Finally, Perez-Torrado et al. (2011) dated a paleosol at the base of the pumice deposit at  $8.13 \pm 0.06$  ka BP attributing the overlying deposit to Tanganasoga.

Given the new stratigraphy described in this paper, the dates hitherto ascribed to this deposit and their interpretations do not match the stratigraphic position of the Malpaso Member. Bearing in mind that Tanganasoga and other vents (e.g. Hoya del Pino, Montaña Colorada) postdate the landslide of El Golfo, and that their deposits cover the pumice products, no stratigraphic evidence exists to support the idea that the

Malpaso Member was associated with Tanganasoga or to any subsequent eruptions. Therefore, stratigraphically speaking, the Malpaso Member must belong to the final episodes in the construction of the composite El Golfo volcano, as has been suggested by Carracedo et al. (2001). However, between the deposition of the Malpaso Member and the deposits on Tanganasoga, there is no paleosol that could indicate any significant time lapse between the two events. This implies that the eruption of the Malpaso Member, the landslide of El Golfo and the eruption (and construction) of Tanganasoga occurred sequentially in a relatively short period of time. Furthermore, it is also possible that the eruption of the Malpaso Member was the cause behind the landslide of El Golfo. The construction of Tanganasoga could correspond to a volumetrically significant postcollapse eruptive episode that was triggered by the decompression of the deep magmatic system caused by the massive removal of part of El Golfo. This matches well with the model proposed by Manconi et al. (2009) and similar successions of events that have occurred after the formation of volcanic landslides on other oceanic volcanic islands (Lipman et al. 1990; Presley et al. 1997; Hildenbrand et al. 2004).

These stratigraphic constraints also generate an inconsistency with published data regarding the date of the landslide at El Golfo. Using radiogenic isotopic dating (K–Ar), the age of this event has been proposed to lie within  $134 \pm 4$  and  $21 \pm 3$  ka (Guillou et al. 1996; Szérméta et al. 1999; Carracedo et al. 1999, 2001). Marine geological studies, primarily concerned with the age of turbidite deposits associated with the massive landslide avalanche, give an age of 17–13 ka (Masson 1996; Urgeles et al. 1997; Masson et al. 2002). A more recent study using new radiogenic isotope data ( $^{40}\text{Ar}/^{36}\text{Ar}$ ) from pre- and postlandslide materials from El Golfo valley dates the event at between  $87 \pm 8$  and  $39 \pm 13$  ka (Longpré et al. 2011). However, if the emplacement of the Malpaso Member took place around  $8.13 \pm 0.06$  ka BP—as suggested by Perez-Torrado et al. (2011) and as demonstrated above, it clearly predates the formation of the landslide on El Golfo and, thus, the age of this destructive event must be at least the same as that of the Malpaso Member or younger. Consequently, the age attributed to the landslide in previous study is mistaken or the inferred age of the Malpaso Member (Perez-Torrado et al. 2011) is incorrect. We only found charcoal samples in the paleosol near Malpaso (same location of previous  $^{14}\text{C}$  dates) and found no evidence of any charcoal in the paleosol in distal parts of the deposits. This finding, coupled with the facts that in proximal and intermediate areas the Malpaso member is overlain by several pyroclastic deposits of local eruptions, and that these deposits are separated by well-developed paleosols (e.g. columns 2 and 3; Figs. 2 and 10), suggesting that between these eruptions occur long periods of repose that once thought between the emplacement of the Malpaso Member and the present day. In addition, morphological characteristics of the

paleosol, where the charcoal dated by Perez-Torrado et al. (2011) was found, indicate that it is an Andosol (Padrón 1993). The formation of this type of soils requires between several tens of thousands to hundreds of thousands of years ( $\sim 150$  ka) in areas as Hawaii (Tom et al. 1997). If we assume that El Hierro has similar climatic characteristics as Hawaii (mild temperatures, although lower rainfall rates), we can think that the paleosol formation required more than a few thousand years. This suggests that the ages obtained by Perez-Torrado et al. (2011) could be younger and the charcoal that they used may correspond to a charcoal from younger plant roots growing on Malpaso or to younger deposits. It is a very common fact that forest fires occur on the island as those recorded during the last decade in 2003 and 2006 (<http://www.gobiernodecanarias.org/istac/>), producing new carbonic material not directly related to eruptions.

The distribution of the pumice deposits (in particular the isopach map), variations in lateral grain size and the isopleth map (Fig. 5a, b) suggest that the position now occupied by Tanganasoga is the most suitable location for the vent of the Malpaso Member. This would be consistent with the distribution of all the products from El Golfo in the area and with the location of Tanganasoga itself and would provide a site for the main vent of El Golfo and its eruptive activity in the area.

#### Volcanic hazard implications

The style and magnitude of this type of eruption is clearly of great importance in assessing the potential volcanic hazard on El Hierro. The presence of similar compositions in the erupted products during the recent 2011–2012 eruption raises the question as to whether this felsic magma represents an assimilated product from a previous eruption or whether it represents a juvenile component (i.e. differentiated product) from the last eruption. Needless to say, the most important question to answer is whether or not El Hierro's magmas have the potential to generate a large volume of eruptable felsic magma. The sequence of unrest episodes following this very recent eruption, characterised by heightened seismicity mostly located at a depth of about 20–25 km and significant surface deformation that has already accumulated more than 25 cm of total vertical uplift ([www.ign.es](http://www.ign.es)), suggests that fresh magma has continued to accumulate below the surface of the island.

These petrological issues are beyond the scope of this paper but nevertheless still should be investigated in detail. From the results obtained, we can see that an eruption of similar characteristics to that of the Malpaso Member does not require a large amount of eruptable magma and that its associated hazards are much greater than those related to the mafic volcanism that has characterised most of the recent eruptions on El Hierro. The results of our study show that the pumice deposits reached a radial distance of at least 3 km from the hypothetical vent site (Fig. 3), and it seems likely that the

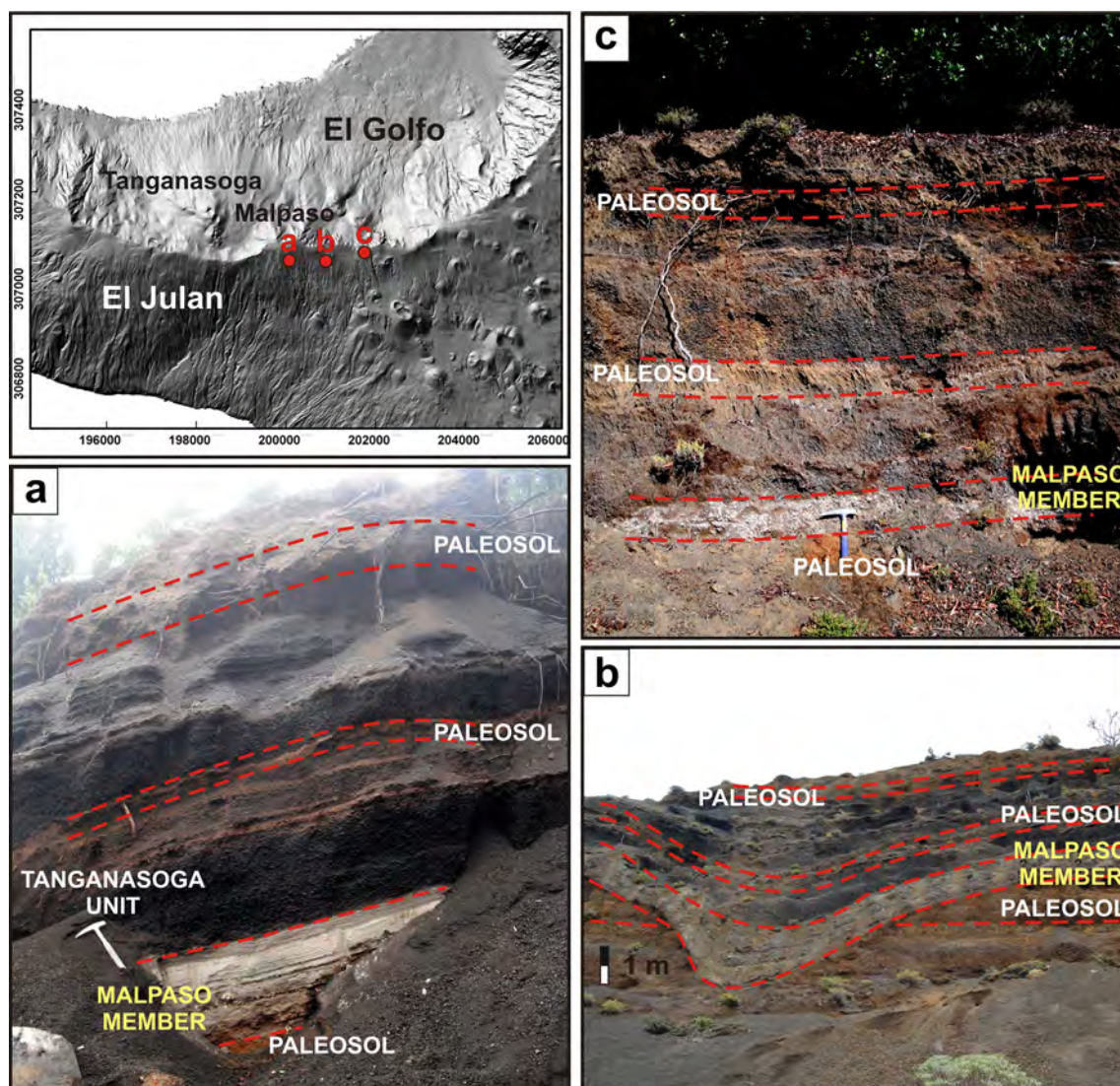


**Fig. 10** Pyroclastic deposits produced by younger, local Strombolian eruptions overlying the Malpaso tephra deposit (*light coloured*). Note that individual units are separated by well-developed paleosols

PDCs that produced these deposits could have travelled much further. The degree of hazard depends on the location of the vent and the topography of the surrounding area, as well as the initial energy in the flow. Our data suggest that the vent area of the Malpaso Member eruption was located in a similar position to that currently occupied by Tanganasoga, probably due to the position of the main feeding system from the previous El Golfo volcano. However, the characteristics of the 2011–2012 eruption and of the preceding episode of unrest (Martí et al. 2013a, b) suggest that the position of future vents (i.e. current volcanic susceptibility; see Becerril et al. 2013) is not controlled by the same stress configuration as during the construction of El Golfo and Tanganasoga. This introduces additional uncertainty into the evaluation of hazards on El Hierro and thus is an indication that both long- and short-term hazard assessments on the island should take into account possible scenarios related to the eruption of felsic magmas.

## Conclusions

In this study, we conducted a detailed stratigraphic, lithological and sedimentological study of a felsic pumice deposit, named here as the Malpaso Member. This deposit originated from a base-surge-type explosive eruption with a subsequent radial emplacement of dilute PDCs from the vent that would have been located in a similar position to the volcano of Tanganasoga. The low vesicularity of juvenile fragments and the morphological characteristics of the fine particles, as well as the high proportion of lithic fragments and the ash-rich nature of the deposit, suggest that magma/water interaction controlled the dynamics of the eruption.

In the light of the new stratigraphy described in this paper and previously available data, we thus conclude that the Malpaso Member was not associated with the eruption of Tanganasoga or any subsequent eruption and instead

corresponds to the final episodes in the construction of the composite volcano of El Golfo.

The presence of similar compositions in the erupted products of the recent 2011–2012 eruption indicates that the magmas from El Hierro could have the potential for producing a large volume of eruptable felsic magma, a finding that obliges both long- and short-term hazard assessments to take into account possible scenarios that include the eruption on El Hierro of felsic magmas.

**Acknowledgements** This research was partially funded by the MINECO grant CGL2011-16144-E and the European Commission (FT7 Theme: ENV.2011.1.3.3-1; grant 282759: ‘VUELCO’). The authors are grateful to the Cabildo of El Hierro for permission to undertake this research and, above all, to the Consejo Insular de Aguas de El Hierro for its support and to Orlando Hernandez, Xavier Bolós, Daniele Giordano, Jose Morales de Francisco and Llorenç Planagumà for their assistance in the field, as well as Olaya García, Pedro Agustín Padrón and Quico Burjachs for their suggestions during this research. We are also grateful to the Editor James White, the Associated Editor Thorvaldur Thordarson, to the reviewer Roberto Sulpizio and the two anonymous reviewers for their constructive reviews of this manuscript. The English text was corrected by Michael Lockwood.

## References

- Araña V, Ortiz R (1991) The Canary Islands: tectonics, magmatism and geodynamic framework. In: Kampunzu AB, Lubala RT (eds) *Magmatism in extensional structural settings*. Springer, Berlin, pp 209–249
- Amott RWC, Hand BM (1989) Bedforms, primary structures and grain fabric in the presence of suspended sediment rain. *J Sediment Petrol* 59:1062–1069
- Balcells R, Gomez JA (1997a) Memorias y mapas geológicos del Plan MAGNA a escala 1:25.000 de las Hojas correspondientes a la isla de El Hierro. Hoja de Frontera, Instituto Geológico y Minero de España, Spain
- Balcells R, Gomez JA (1997b) Memorias y mapas geológicos del Plan MAGNA a escala 1:25.000 de las Hojas correspondientes a la isla de El Hierro. Hoja de Sabinosa, Instituto Geológico y Minero de España, Spain
- Barberi F, Cioni R, Rosi M, Santacroce R, Sbrana A, Vecci R (1989) Magmatic and phreatomagmatic phases in explosive eruptions of Vesuvius as deduced by grain-size and component analysis of the pyroclastic deposits. *J Volcanol Geotherm Res* 38(3–4):287–307
- Becerril L (2009) Approach to volcanic hazard and its effects in coastal areas of the Canary Islands. Master's thesis, Universidad de Las Palmas de Gran Canaria, Spain
- Becerril L, Cappello A, Galindo I, Neri M, Del Negro C (2013) Spatial probability distribution of future volcanic eruptions at El Hierro Island (Canary Islands, Spain). *J Volcanol Geotherm Res* 257:21–30
- Bonadonna C, Costa A (2013) Plume height, volume, and classification of explosive volcanic eruptions based on the Weibull function. *Bull Volcanol* 75(8):1–19
- Büttner R, Dellino P, Zimanowski B (1999) Identifying modes of magma/water interaction from the surface features of ash particles. *Nature* 401:688–690
- Büttner R, Dellino P, La Volpe L, Lorenz V, Zimanowski B (2002) Thermohydraulic explosions in phreatomagmatic eruptions as evidenced by the comparison between pyroclasts and products from Molten Fuel Coolant Interaction experiments. *J Geophys Res: Solid Earth* 107(B11):2277
- Carracedo JC (1996) Morphological and structural evolution of the western Canary Islands: hotspot-induced three-armed rifts or regional tectonic trends? *J Volcanol Geotherm Res* 72(1–2):151–162
- Carracedo JC, Day S, Guillou H, Rodríguez Badiola E, Canas JA, Pérez Torrado FJ (1998) Hotspot volcanism close to a passive continental margin: the Canary Islands. *Geol Mag* 135(05):591–604
- Carracedo JC, Day SJ, Guillou H, Pérez Torrado FJ (1999) Giant Quaternary landslides in the evolution of La Palma and El Hierro, Canary Islands. *J Volcanol Geotherm Res* 94(1–4):169–190
- Carracedo JC, Rodríguez Badiola E, Guillou H, de La Nuez HJ, Pérez Torrado FJ (2001) Geology and volcanology of the western Canaries: La Palma and El Hierro. *Estud Geol* 57:171–295
- Chough SK, Sohn YK (1990) Depositional mechanics and sequences of base surges, Songaksan tuff ring, Cheju Island, Korea. *Sedimentology* 37(6):1115–1135
- Cioni R, Sulpizio R, Garruccio N (2003) Variability of the eruption dynamics during a Subplinian event: the Greenish Pumice eruption of Somma–Vesuvius (Italy). *J Volcanol Geotherm Res* 124(1–2):89–114
- Cole PD, Guest JE, Duncan AM, Pacheco JM (2001) Capelinhos 1957–1958, Faial, Azores: deposits formed by an emergent Surtseyan eruption. *Bull Volcanol* 63(2–3):204–220
- Cole PD, Pacheco JM, Gunasekera R, Queiroz G, Gonçalves P, Gaspar JL (2008) Contrasting styles of explosive eruption at Sete Cidades, São Miguel, Azores, in the last 5000 years: hazard implications from modelling. *J Volcanol Geotherm Res* 178(3):574–591
- Custodio E (1978) *Geohidrología de terrenos e islas volcánicas (Hydrogeology of volcanic lands and islands)*. Instituto de Hidrología Centro de Estudios Hidrográficos Publ 128 Madrid:1–303
- Custodio E (1989) Groundwater characteristics and problems in volcanic rock terrains. In: *Isotope techniques on the study of the hydrology of fractured and fissured rocks*. International Atomic Energy Agency STI/PUB 790 Vienna: 87–137
- De Rosa R, Frazzetta G, La Volpe L (1992) An approach for investigating the depositional mechanism of fine-grained surge deposits. The example of the dry surge deposits at “La Fossa di Vulcano”. *J Volcanol Geotherm Res* 51(4):305–321
- Dellino P, La Volpe L (1995) Fragmentation versus transportation mechanisms in the pyroclastic sequence of Monte Pilato-Rocche Rosse (Lipari, Italy). *J Volcanol Geotherm Res* 64(3):211–231
- Dellino P, La Volpe L (1996) Image processing analysis in reconstructing fragmentation and transportation mechanisms of pyroclastic deposits. The case of Monte Pilato-Rocche Rosse eruptions, Lipari (Aeolian Islands, Italy). *J Volcanol Geotherm Res* 71(1):13–29
- Dellino P, Isaia R, La Volpe L, Orsi G (2001) Statistical analysis of textural data from complex pyroclastic sequences: implications for fragmentation processes of the Agnano-Monte Spina Tephra (4.1 ka), Phlegraean Fields, southern Italy. *Bull Volcanol* 63(7):443–461
- Dellino P, Isaia R, La Volpe L, Orsi G (2004a) Interaction between particles transported by fallout and surge in the deposits of the Agnano-Monte Spina eruption (Campi Flegrei, Southern Italy). *J Volcanol Geotherm Res* 133(1–4):193–210
- Dellino P, Isaia R, Veneruso M (2004b) Turbulent boundary layer shear flows as an approximation of base surges at Campi Flegrei (Southern Italy). *J Volcanol Geotherm Res* 133(1–4):211–228
- Dobran F, Papale P (1993) Magma-water interaction in closed systems and application to lava tunnels and volcanic conduits. *J Geophys Res: Solid Earth* (1978–2012) 98(B8):14041–14058
- Druitt TH (1992) Emplacement of the 18 May 1980 lateral blast deposit ENE of Mount St. Helens, Washington. *Bull Volcanol* 54(7):554–572
- Fisher RV (1966) Mechanism of deposition from pyroclastic flows. *Am J Sci* 264(5):350–363

- Formenti Y, Druitt TH, Kelfoun K (2003) Characterisation of the 1997 Vulcanian explosions of Soufrière Hills Volcano, Montserrat, by video analysis. *Bull Volcanol* 65(8):587–605
- Fuster JM (1993) Geochronología de la Isla de El Hierro (Islas Canarias). *Bol R Soc Esp Hist Nat (Sec Geol)* 88(1–4):85–97
- Giordano G (1998) Facies characteristics and magma–water interaction of the White Trachytic Tuffs (Roccamonfina Volcano, southern Italy). *Bull Volcanol* 60(1):10–26
- Guillou H, Carracedo JC, Torrado FP, Badiola ER (1996) K-Ar ages and magnetic stratigraphy of a hotspot-induced, fast grown oceanic island: El Hierro, Canary Islands. *J Volcanol Geotherm Res* 73(1–2):141–155
- Heiken G, Wohletz K (1985) *Volcanic ash*. University of California Press, Berkeley. 246 pp
- Hildenbrand A, Gillot P-Y, Le Roy I (2004) Volcano-tectonic and geochemical evolution of an oceanic intra-plate volcano: Tahiti-Nui (French Polynesia). *Earth Planet Sci Lett* 217(3–4):349–365
- Hoblitt R, Wolfe E, Scott W, Couchman M, Pallister J, Javier D (1996) The preclimatic eruptions of Mount Pinatubo, June 1991. In: Newhall CG, Punongbayan RS (eds) *Fire and mud: eruptions and lahars of Mount Pinatubo*, Philippines. Philippines Institute of Volcanology and Seismology, Quezon 766 City and University of Washington Press, Seattle, pp 457–511
- Houghton BF, Schmincke HU (1989) Rothenberg scoria cone, East Eifel: a complex Strombolian and phreatomagmatic volcano. *Bull Volcanol* 52(1):28–48
- Houghton BF, Smith RT (1993) Recycling of magmatic clasts during explosive eruptions: estimating the true juvenile content of phreatomagmatic volcanic deposits. *Bull Volcanol* 55(6):414–420
- Join JL, Folio JL, Robineau B (2005) Aquifers and groundwater within active shield volcanoes. Evolution of conceptual models in the Piton de la Fournaise volcano. *J Volcanol Geotherm Res* 147(1):187–201
- Le Bas MJ, Rex DC, Stillman CJ (1986) The early magmatic chronology of Fuerteventura, Canary Islands. *Geol Mag* 123:287–298
- Lipman P, Rhodes JM, Dalrymple G (1990) The Ninole Basalt—implications for the structural evolution of Mauna Loa volcano, Hawaii. *Bull Volcanol* 53(1):1–19
- Longpré M-A, Chadwick JP, Wijbrans J, Iping R (2011) Age of the El Golfo debris avalanche, El Hierro (Canary Islands): new constraints from laser and furnace  $^{40}\text{Ar}/^{39}\text{Ar}$  dating. *J Volcanol Geotherm Res* 203(1–2):76–80
- Macdonald GA, Abbott AT, Peterson FL (1983) *Volcanoes in the sea: the geology of Hawaii*. University of Hawaii Press: pp 523
- Manconi A, Longpré M-A, Walter TR, Troll VR, Hansteen TH (2009) The effects of flank collapses on volcano plumbing systems. *Geology* 37(12):1099–1102
- Marinoni LB, Gudmundsson A (2000) Dykes, faults and palaeostresses in the Teno and Anaga massifs of Tenerife (Canary Islands). *J Volcanol Geotherm Res* 103(1–4):83–103
- Marinoni LB, Pasquarè G (1994) Tectonic evolution of the emergent part of a volcanic ocean island: Lanzarote, Canary Islands. *Tectonophysics* 239(1–4):111–137
- Martí J, Castro A, Rodríguez C, Costa F, Carrasquilla S, Pedreira R, Bolos X (2013a) Correlation of magma evolution and geophysical monitoring during the 2011–2012 El Hierro (Canary Islands) submarine eruption. *J Petrol* 54(7):1349–1373
- Martí J, Pínel V, López C, Geyer A, Abella R, Tarraga M, Blanco MJ, Castro A, Rodríguez C (2013b) Causes and mechanisms of the 2011–2012 El Hierro (Canary Islands) submarine eruption. *J Geophys Res: Solid Earth* 118(3):823–839
- Masson DG (1996) Catastrophic collapse of the volcanic island of Hierro 15 ka ago and the history of landslides in the Canary Islands. *Geology* 24:231–234
- Masson DG, Watts AB, Gee MJR, Urgeles R, Mitchell NC, Le Bas TP, Canals M (2002) Slope failures on the flanks of the western Canary Islands. *Earth Sci Rev* 57(1–2):1–35
- Meletlidis S, Di Roberto A, Pompilio M, Bertagnini A, Iribarren I, Felpeto A, Torres PA, D’Oriano C (2012) Xenopumices from the 2011–2012 submarine eruption of El Hierro (Canary Islands, Spain): constraints on the plumbing system and magma ascent. *Geophys Res Lett* 39(17), L17302
- Padrón P (1993) Estudio edafológico de la isla de El Hierro. In: Tesis Doctoral inédita. Departamento de Edafología y Geología. Universidad de La Laguna. 285 p.+mapas
- Palladino DM, Simei S (2002) Three types of pyroclastic currents and their deposits: examples from the Vulcini Volcanoes, Italy. *J Volcanol Geotherm Res* 116(1–2):97–118
- Palladino DM, Taddeucci J (1998) The basal ash deposit of the Sovana Eruption (Vulsini Volcanoes, central Italy): the product of a dilute pyroclastic density current. *J Volcanol Geotherm Res* 87(1):233–254
- Papale P, Dobran F (1994) Magma flow along the volcanic conduit during the Plinian and pyroclastic flow phases of the May 18, 1980, Mount St. Helens eruption. *J Geophys Res: Solid Earth* (1978–2012) 99(B3):4355–4373
- Pellicer MJ (1975) Estudio vulcanológico, petrológico y geoquímico de la isla de El Hierro (Archipiélago Canario). Tesis Doctoral, Facultad de Ciencias Geológicas, Universidad Complutense de Madrid: 179 pp
- Pellicer MJ (1977) Estudio vulcanológico de la Isla de El Hierro, Islas Canarias. *Estud Geol* 33:181–197
- Perez-Torrado FJ, Rodríguez-González A, Carracedo JC, Fernández-Turiel JL, Guillou H, Hansen A, Rodríguez Badiola E (2011) Edades C-14 Del Rift ONO de El Hierro (Islas Canarias). In: Turu V, Constante A (eds) *El Cuaternario en España y Áreas Afines*. Asociación Española para el Estudio del Cuaternario (AEQUA), Andorra, pp 101–104
- Peterson FL (1972) Water development on tropic volcanic islands—type example: Hawaii. *Groundwater* 10(5):18–23
- Polacci M, Pioli L, Rosi M (2003) The Plinian phase of the Campanian Ignimbrite eruption (Phlegrean Fields, Italy): evidence from density measurements and textural characterization of pumice. *Bull Volcanol* 65(6):418–432
- Presley TK, Sinton JM, Pringle M (1997) Postshield volcanism and catastrophic mass wasting of the Waianae Volcano, Oahu, Hawaii. *Bull Volcanol* 58(8):597–616
- Robertson AHF, Stillman CJ (1979) Late Mesozoic sedimentary rocks of Fuerteventura, Canary Islands: implications for West African continental margin evolution. *J Geol Soc* 136(1):47–60
- Schmincke H-U (1982) Volcanic and chemical evolution of the Canary Islands. In: Rad U, Hinz K, Samthein M, Seibold E (eds) *Geology of the Northwest African continental margin*. Springer, Berlin, pp 273–306
- Schmincke HU (1990) *Geology and geological field guide of Gran Canaria*. Pluto Press, Kiel, 212 pp
- Self S, Sparks RSJ (1978) Characteristics of widespread pyroclastic deposits formed by the interaction of silicic magma and water. *Bull Volcanol* 41(3):196–212
- Sigmarsson O, Laporte D, Carpentier M, Devouard B, Devidal J-L, Martí J (2013) Formation of U-depleted rhyolite from a basanite at El Hierro, Canary Islands. *Contrib Mineral Petrol* 165(3):601–622
- Sigurdsson H, Carey SN, Fisher RV (1987) The 1982 eruptions of El Chichón volcano, Mexico (3): physical properties of pyroclastic surges. *Bull Volcanol* 49(2):467–488
- Sohn YK (1997) On traction-carpet sedimentation. *J Sediment Res* 67(3): 502–509
- Sohn YK, Chough SK (1989) Depositional processes of the Suwolbong tuff ring, Cheju Island (Korea). *Sedimentology* 36(5):837–855
- Solvegvik H, Mattsson HB, Hermelin O (2007) Growth of an emergent tuff cone: fragmentation and depositional processes recorded in the Capelas tuff cone, São Miguel, Azores. *J Volcanol Geotherm Res* 159(1):246–266
- Sulpizio R, Mele D, Dellino P, Volpe L (2005) A complex, Subplinian-type eruption from low-viscosity, phonolitic to tephri-phonolitic

- magma: the AD 472 (Pollena) eruption of Somma-Vesuvius, Italy. *Bull Volcanol* 67(8):743–767
- Székely N, Laj C, Guillou H, Kissel C, Mazaud A, Carracedo J-C (1999) Geomagnetic paleosecular variation in the Brunhes period, from the island of El Hierro (Canary Islands). *Earth Planet Sci Lett* 165(3–4):241–253
- Talbot JP, Self S, Wilson CJN (1994) Dilute gravity current and rain-flushed ash deposits in the 1.8 ka Hatepe Plinian deposit, Taupo, New Zealand. *Bull Volcanol* 56(6–7):538–551
- Tom MS, Trumbore SE, Chadwick OA, Vitousek PM, Hendricks DM (1997) Mineral control of soil organic carbon storage and turnover. *Nature* 389(6647):170–173
- Urgeles R, Canals M, Baraza J, Alonso B (1996) The submarine “El Golfo” debris avalanche and the Canary debris flow, West Hierro Island: the last major slides in the Canary archipelago. *Geocata* 20:390–393
- Urgeles R, Canals M, Baraza J, Alonso B, Masson DG (1997) The most recent megaslides on the Canary Islands: the El Golfo Debris Avalanche and the Canary Debris Flow, west El Hierro Island. *J Geophys Res* 102:20305–20323
- Walker GPL (1983) Ignimbrite types and ignimbrite problems. *J Volcanol Geotherm Res* 17(1–4):65–88
- Wohletz K (1986) Explosive magma-water interactions: thermodynamics, explosion mechanisms, and field studies. *Bull Volcanol* 48(5): 245–264
- Wohletz K, Orsi G, De Vita S (1995) Eruptive mechanisms of the Neapolitan Yellow Tuff interpreted from stratigraphic, chemical, and granulometric data. *J Volcanol Geotherm Res* 67(4):263–290

<b>Studied outcrop Number</b>	<b>Coordinates (UTM)</b>		<b>Thickness (cm)</b>
	<b>X</b>	<b>Y</b>	
<b>1</b>	201065	3070484	22
<b>2</b>	200791	3070436	27
<b>3</b>	200408	3070513	45
<b>4</b>	199997	3070466	61
<b>5</b>	199063	3070334	21
<b>6</b>	199696	3070885	60
<b>7</b>	199712	3070479	81
<b>8</b>	199549	3070564	30
<b>9</b>	199686	3070592	61
<b>10</b>	200000	3070467	65
<b>11</b>	199503	3070433	67
<b>12</b>	199469	3070396	53
<b>13</b>	199482	3070425	55
<b>14</b>	199956	3070461	68
<b>15</b>	201043	3070455	19
<b>16</b>	200770	3070438	19
<b>17</b>	200357	3070513	53
<b>18</b>	200361	3070546	62
<b>19</b>	199779	3070540	73
<b>20</b>	199785	3070903	70
<b>21</b>	199696	3070891	55
<b>22</b>	199484	3070609	69
<b>23</b>	199495	3070564	62
<b>24</b>	199647	3070427	26,7

<b>Studied outcrop Number</b>	<b>Coordinates (UTM)</b>		<b>Thickness (cm)</b>
	<b>X</b>	<b>Y</b>	
<b>25</b>	200336	3070861	55
<b>26</b>	200439	3070793	75,5
<b>27</b>	200664	3070744	39,5
<b>28</b>	200765	3070734	32
<b>29</b>	200619	3070607	29,5
<b>30</b>	200482	3070606	45
<b>31</b>	201219	3070252	12
<b>32</b>	201304	3070160	10
<b>33</b>	201446	3070064	7,5
<b>34</b>	201743	3070065	7
<b>35</b>	201432	3069465	9
<b>36</b>	201083	3069542	7,5
<b>37</b>	200651	3069666	3
<b>38</b>	199409	3069503	21,5
<b>39</b>	194840	3031098	0
<b>40</b>	199393	3070361	54
<b>41</b>	199183	3070261	42
<b>42</b>	199020	3070259	0
<b>43</b>	198862	3070265	8
<b>44</b>	198924	3070308	0
<b>45</b>	199425	3070321	44
<b>46</b>	199375	3070179	46
<b>47</b>	199438	3070157	58
<b>48</b>	199750	3070170	61

Studied outcrop Number	Coordinates (UTM)		Thickness (cm)
	X	Y	
49	200104	3070282	29
50	200668	3070267	23
51	199438	3070157	31
52	200942	3070247	21
53	201546	3070687	9
54	201546	3070687	15
55	201956	3070083	3
56	201100	3070185	10,5
57	200728	3069953	20
58	200663	3069959	21
59	199797	3069876	23
60	199744	3069873	25
61	199634	3069900	25
62	199547	3069905	38
63	199406	3069933	14
64	199270	3070267	40
65	201483	3070491	10
66	199614	3070536	0
67	199322	3070517	62
68	198720	3070410	24
69	198610	3070378	21
70	198870	3070450	30
71	204689	3071626	0
72	204476	3071507	0

Studied outcrop Number	Coordinates (UTM)		Thickness (cm)
	X	Y	
73	204233	3071417	2,5
74	203659	3071217	1
75	203606	3071390	2
76	204098	3071510	1
77	201848	3070283	5
78	202005	3070218	5
79	202432	3070153	5
80	203933	3070365	3
81	204132	3070195	4
82	203897	3069802	3
83	203741	3069790	3
84	203254	3069681	3
85	202955	3069612	2
86	204397	3070823	1
87	204373	3070817	1
88	204009	3070555	2
89	203984	3070525	1
90	203934	3070374	2
91	204138	3070195	1
92	204359	3070085	1
93	205467	3070514	0
94	205483	3070573	0
95	205311	3071677	0
96	205640	3071454	2

<b>Studied outcrop Number</b>	<b>Coordinates (UTM)</b>		<b>Thickness (cm)</b>
	<b>X</b>	<b>Y</b>	
<b>97</b>	198367	3070279	0
<b>98</b>	198431	3070350	0
<b>99</b>	198622	3070325	32
<b>100</b>	198980	3070379	32
<b>101</b>	199032	3070370	31
<b>102</b>	199200	3070415	25
<b>103</b>	199698	3070417	22
<b>104</b>	198751	3070444	31
<b>105</b>	198733	3070441	0
<b>106</b>	198609	3070445	26
<b>107</b>	198609	3070445	0
<b>108</b>	196927	3070397	6
<b>109</b>	197450	3070277	5
<b>110</b>	198445	3070268	20
<b>111</b>	198601	3069885	10
<b>112</b>	199576	3069976	16
<b>113</b>	199119	3069674	0
<b>114</b>	199120	3069708	0
<b>115</b>	199814	3069263	30
<b>116</b>	196167	3070712	3
<b>117</b>	195768	3071020	2
<b>118</b>	195701	3071041	1
<b>119</b>	195632	3071079	0
<b>120</b>	195468	3071043	0

<b>Studied outcrop Number</b>	<b>Coordinates (UTM)</b>		<b>Thickness (cm)</b>
	<b>X</b>	<b>Y</b>	
<b>121</b>	195357	3071033	0
<b>122</b>	195640	3071167	0
<b>123</b>	196960	3070632	3
<b>124</b>	197635	3070261	7
<b>125</b>	196389	3070546	2
<b>126</b>	196058	3070611	2
<b>127</b>	195729	3070755	2
<b>128</b>	195666	3070742	2
<b>129</b>	195662	3070653	2
<b>130</b>	195996	3070349	2
<b>131</b>	195952	3070287	2
<b>132</b>	195614	3070383	2
<b>133</b>	195327	3070504	0
<b>134</b>	195232	3070563	0
<b>135</b>	194920	3070711	0
<b>136</b>	194733	3070887	0
<b>137</b>	199839	3069194	0
<b>138</b>	200870	3069036	0
<b>139</b>	203002	3069499	0
<b>140</b>	203104	3069505	0
<b>141</b>	203231	3069538	0
<b>142</b>	203340	3069585	0
<b>143</b>	203719	3069598	0
<b>144</b>	203980	3069485	0

<b>Studied outcrop Number</b>	<b>Coordinates (UTM)</b>		<b>Thickness (cm)</b>
	<b>X</b>	<b>Y</b>	
<b>145</b>	205141	3071803	0
<b>146</b>	205637	3071820	0,5
<b>147</b>	205718	3071881	0
<b>148</b>	205823	3071670	0
<b>149</b>	205870	3071808	0
<b>150</b>	206077	3071549	0
<b>151</b>	200289	3070943	0
<b>152</b>	199650	3070950	0

\*Geographical coordinates of relevant locations, as well as stratigraphic sections and sampling points

*Annex 6.3*

*Xenopumice erupted on 15 October 2011 offshore of El Hierro (Canary Islands): a subvolcanic snapshot of magmatic, hydrothermal and pyrometamorphic processes.*

*S. Del Moro, A. Di Roberto, S. Meletlidis, M. Pompilio, A. Bertagnini, S. Agostini, F. Ridolfi, A. Renzulli*

# Xenopumice erupted on 15 October 2011 offshore of El Hierro (Canary Islands): a subvolcanic snapshot of magmatic, hydrothermal and pyrometamorphic processes

S. Del Moro<sup>1</sup> · A. Di Roberto<sup>2</sup> · S. Meletlidis<sup>3</sup> ·  
M. Pompilio<sup>2</sup> · A. Bertagnini<sup>2</sup> · S. Agostini<sup>4</sup> · F. Ridolfi<sup>1</sup> ·  
A. Renzulli<sup>1</sup>

Received: 23 December 2014 / Accepted: 21 May 2015 / Published online: 31 May 2015  
© Springer-Verlag Berlin Heidelberg 2015

**Abstract** On 15 October 2011, a submarine eruption offshore of El Hierro Island gave rise to floating volcanic products, known as xenopumices, i.e., pumiceous xenoliths partly mingled and coated with the juvenile basanitic magma. Over the last few years, no consensus in the scientific community in explaining the origin of these products has been reached. In order to better understand the formation of xenopumice, we present a textural, mineralogical, and geochemical study of the possible magmatic, hydrothermal, and pyrometamorphic processes, which usually operate in the plumbing systems of active volcanoes. We carried out a comprehensive SEM investigation and Sr-Nd-Pb isotope analyses on some samples representative of three different xenopumice facies. All the data were compared with previous studies, new data for El Hierro extrusives and a literature dataset of Canary Islands igneous and sedimentary rocks. In the investigated xenopumices, we emphasize the presence of restitic magmatic phases as well as crystallization of minerals (mainly olivine+pyroxene+

magnetite aggregates) as pseudomorphs after pre-existing mafic phenocrysts, providing evidence of pyrometamorphism induced by the high-T juvenile basanitic magma. In addition, we identify veins consisting of zircon+REE-oxides+mullite associated with Si-rich glass and hydrothermal quartz, which indicate the fundamental role played by hydrothermal fluid circulation in the xenopumice protolith. The petrological data agree with a pre-syneruptive formation of the xenopumice, when El Hierro basanite magma intruded hydrothermally altered trachyandesite to trachyte rocks and triggered local partial melting. Therefore, the El Hierro xenopumice represents a snapshot of the transient processes at the magma-wall rock interface, which normally occurs in the feeding system of active volcanoes.

**Keywords** Xenopumice · El Hierro · Hydrothermal process · Pyrometamorphism · Subvolcanic

Editorial responsibility: J.E. Gardner

✉ A. Renzulli  
alberto.renzulli@uniurb.it

<sup>1</sup> Dipartimento di Scienze della Terra, della Vita e dell'Ambiente, Università degli Studi di Urbino Carlo Bo, Campus Scientifico, "Enrico Mattei", Via Cà le Suore 2-4, I-61029 Urbino, Italy

<sup>2</sup> Istituto Nazionale di Geofisica e Vulcanologia, Sezione di Pisa, Via della Faggiola 32, I-56126 Pisa, Italy

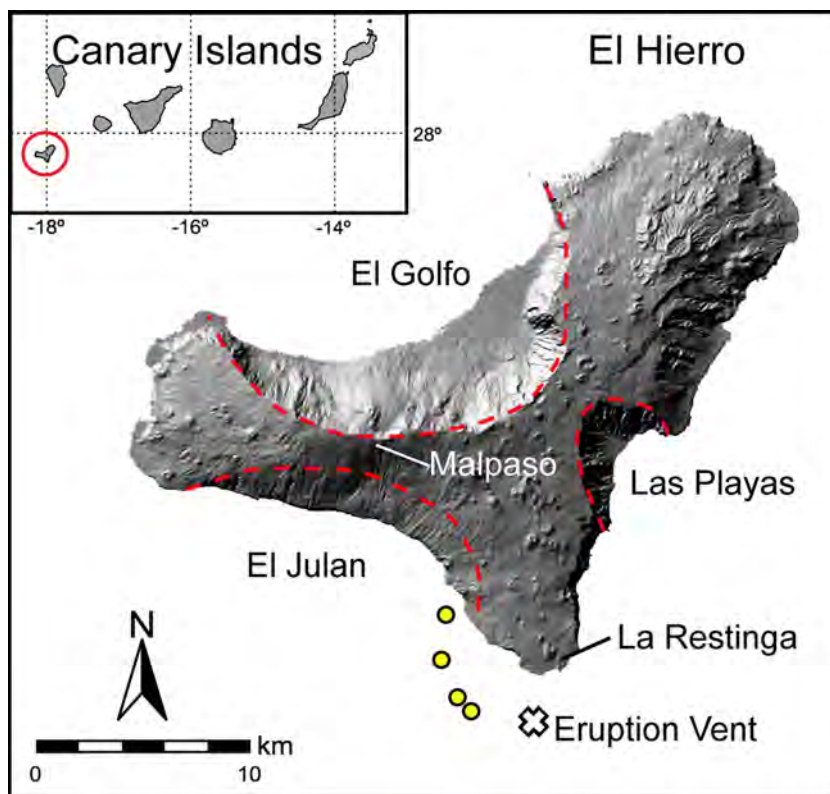
<sup>3</sup> Centro Geofísico de Canarias, Instituto Geográfico Nacional, c/La Marina, 20, 38001 Santa Cruz de Tenerife, Spain

<sup>4</sup> Istituto di Geoscienze e Georisorse - CNR, Via Moruzzi 1, I-56124 Pisa, Italy

## Introduction

In this paper, we are investigating the products erupted during the onset of El Hierro 2011–2012 submarine eruption, known as xenopumices or "restingolites" (Troll et al 2012; Rodríguez-Losada et al. 2014), sampled on the 15th October 2011 floating offshore from the small village of La Restinga along the south coast of the island (Fig. 1). They consist of whitish to grey, highly vesiculated xenoliths, with SiO<sub>2</sub> contents ranging from 62 to 71 wt.% (Meletlidis et al. 2012; Troll et al. 2012; Sigmarsson et al. 2013; Rodríguez-Losada et al. 2014). They are plastically convoluted with thin bands and coated by a few-centimeter-thick crust of the juvenile basanite magma that fed the eruption (Fig. 2).

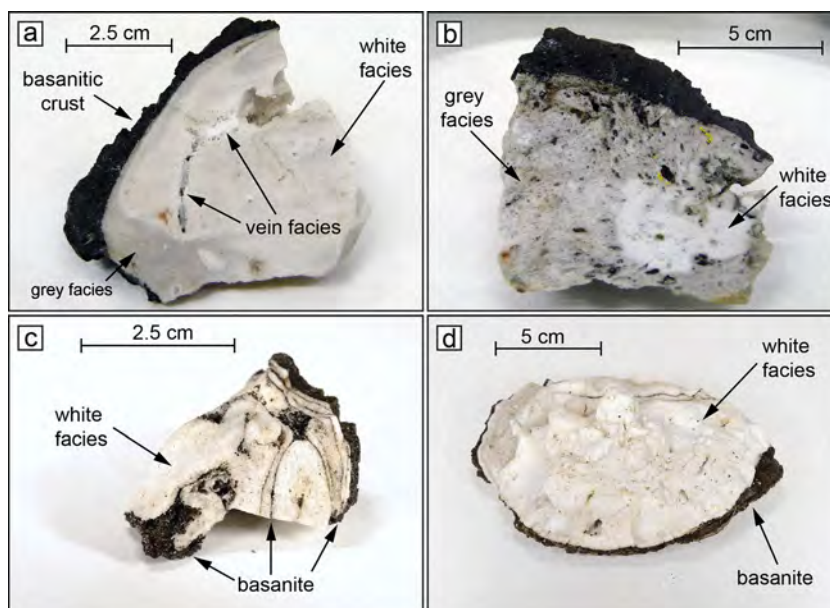
**Fig. 1** El Hierro island. Flank collapse scars are highlighted by red broken lines. Yellow full circles are the xenopumice sampling sites



The nature of these rocks is still a matter of discussion in the scientific community. Troll et al. (2012) suggested that xenopumices are xenoliths originating from the sedimentary deposits of the pre-island oceanic crust, which have been melted and transported by the ascending basanitic magma. In contrast, Meletlidis et al. (2012) suggested that they originated when the basanitic magma interacted with a pocket of shallow trachytic magma and an associated halo of altered

rock of rhyolitic composition. Similarly, Sigmarsson et al. (2013) proposed that the xenopumices are products of the remobilization of a small, differentiated felsic magma body, slightly contaminated with quartz-rich sediments, by the ascending basanitic magma. Recently, Rodriguez-Losada et al. (2014) embraced the hypothesis of a sedimentary origin of the xenopumice, but they pointed out a hydrothermal contribution in their formation. However, none of the models proposed for

**Fig. 2** Images of products erupted on the morning of 15 October 2011 offshore of El Hierro. **a, b** Polished slide xenopumice showing patchy mingling between white and grey facies and milky porcelain-like veins (vein facies). **c** Intimate mingling and folding between the xenopumice and the basanite. **d** Elliptical bomb formed almost completely of xenopumice and coated by a very thin crust of basanite



the origin of El Hierro 2011 xenopumice fully account for their texture, mineralogy, and geochemistry.

In this study, we attempt to reconcile all the petrological data presented by the abovementioned authors and provide support for our interpretation with new isotopic, textural, mineral chemistry, and glass analyses. We believe that the xenopumice formed from the interplay of magmatic, hydrothermal, and pyrometamorphic processes commonly occurring within the plumbing system of active volcanoes. In fact, active volcanic edifices are typically characterized by fluids moving along fractures and by porosity forming the hydrothermal system. Hydrothermal fluids leach subvolcanic and extrusive rocks, transport elements in the form of ions, complex ions, etc., as well as suspensions, and condense as brine or precipitate as solid phases, leading to profound physical and chemical transformation of the rocks forming the volcanic edifice (Wohletz and Heiken 1992). These processes are easily recognizable when dealing directly with hydrothermally altered volcanic samples, but they can be very hard to identify when obliterated by pyrometamorphism (Grapes 2006), i.e., very high-T low-P metamorphism inducing the partial or complete melting of the protolith rock. Hydrothermally altered volcanic rocks subjected to pyrometamorphic processes induced by contact with high-T magmas in active volcanoes (Wood 1994; Grapes 2006; Del Moro et al. 2011) usually appear as partly to completely glassy rocks (buchites), characterized by rare minerals and heterogeneous bulk rock composition. Since trachyte rocks are inferred to represent the most likely volcanic equivalents of the xenopumice before hydrothermal alteration and pyrometamorphism, we also describe the petrography and the bulk rock and glass compositions of trachyte pumice (subaerial Holocene trachyte) from a pyroclastic deposit sampled along the El Golfo landslide crown outcropping in the Malpaso area (1500 m a.s.l.), which is related to Holocene explosive volcanism of the volcano (Pedrazzi et al. 2014).

### Geological setting and chronology of the 2011–2012 El Hierro eruption

El Hierro and La Palma are part of the Western Canary Islands and are representative of the younger magmatism characterizing the archipelago. El Hierro is the youngest volcano. It is located at the SW margin of the archipelago and reaches a height of 1500 m a.s.l. (Fig. 1). Subaerial activity started with the growth of Tiñor volcano (0.88–1.12 Ma), in the NE sector of the island, characterized by lavas ranging in composition from picrite to hawaiite-tephrite (Guillou et al. 1996; Carracedo et al. 2001). El Golfo volcanic edifice, in the NW sector, is younger (550–130 ka) and shows a wider compositional variation of erupted products, from nephelinite to trachyte (Guillou et al. 1996; Carracedo et al. 2001). Quaternary

activity of El Hierro consists mainly of alkali picrites, basanites, and tephrites (Carracedo et al. 2001) that have been recognized in all the three rifts of the island (Guillou et al. 1996; Acosta et al. 2003). El Hierro rift zones (NE-rift, NW-rift, and S-ridge) are separated by deep scars produced by flank collapses, giving the volcano its characteristic star shape (Carracedo et al. 2001; Fig. 1).

The submarine part of El Hierro, which represents over 90 % of the island, is not well studied. Nevertheless, as reported by Sigmarsson et al. (2013), it is probably composed of mainly basaltic to basanitic lavas, repeatedly erupted during the shield-stage activity proposed by Carracedo et al. (2001). The submarine volcanic cone rises from a depth of 4000 m. It was built upon a Jurassic oceanic crust (Schmincke and Sumita 1998) covered by pre-island pelagic sediments interstratified with terrigenous sediments from the African continental margins (Krautel and Schmincke 2002; Sigmarsson et al. 2013).

The geometry of the volcano feeding system has recently been constrained by both thermobarometric (Stroncik et al. 2009) and passive seismic (Gorbatikov et al. 2013 and references therein) investigations. It is located between a depth that likely exceeds 35 km and the base of the oceanic crust. Stroncik et al. (2009) suggested a lack of a large magma reservoir beneath El Hierro. The plumbing system is more likely composed of interconnected magma pockets, sills, and dikes, allowing for an almost constant mixing and homogenization of magma between picritic and trachytic end members, from which magma rises directly, without significant stagnation within crustal reservoirs, during eruptions.

Models proposed to describe magma ascent dynamics prior to the 2011–2012 eruption suggest a stepwise migration of magma from an upper mantle source (Martí et al. 2013a; Martí et al. 2013b; Domínguez Cerdeña et al. 2014; García et al. 2014; Longpré et al. 2014). Magma originated at 20–25 km in the upper mantle and ascended aiseisimally to the base of the crust, where it has been accumulating since July 2011 (Martí et al. 2013a, b; Longpré et al. 2014). After a southward lateral migration within the lower crust (8–16 km of depth), which occurred from early September 2011 to the first week of October, the intruded magma finally ascended to shallower depths, approaching the surface on 10 October 2011 and triggering the eruption (López et al. 2012).

The onset of the eruption was characterized by the appearance of a dark water plume associated with bubbling gas activity (Carracedo et al. 2012; Meletlidis et al. 2012; Troll et al. 2012). On 15 October, xenopumice, coated by and mingled with a basanitic crust, were first observed floating and degassing on the surface of the sea above the eruptive center, resembling bombs up to 50 cm in size. Eruption of the xenopumice lasted for only 1 day (Meletlidis et al. 2012), to be replaced by the appearance of floating basanitic lava balloons, often over 1 m in diameter (Troll et al. 2012).

By the end of the eruption (first week of March 2012), the newborn submarine volcano had reached a height of 220 m from the sea floor (Rivera et al. 2013).

## Methods

Polished thin sections were prepared from different parts (in terms of physical features) of the eight investigated xenopumice samples and from two subaerial Holocene trachyte pumices. Sample texture and major element compositions of glass and mineral phases were investigated by scanning electron microscopy (SEM) at the Istituto Nazionale di Geofisica e Vulcanologia (Sezione di Pisa) using a Zeiss EVO-MA-10 equipped with an Oxford ISIS microanalysis system (accelerating voltage 15 kV, beam current 400–500 pA, 1–2  $\mu\text{m}$  beam diameter, 100 s of acquisition time, ZAF, and natural minerals as calibration standards). Analytical errors were estimated from mineral and natural glass standards and are, respectively, less than 1 % for concentrations above 15 wt.%, 2 % for concentrations between 5 and 15 wt.%, 10 % for concentrations between 1 and 5 wt.%, and 30 % for concentrations <1 wt.%.

Whole-rock compositions for major and trace elements were determined by ALS Minerals (Sevilla, Spain) using lithium metaborate/lithium tetraborate fusion followed by ICP-AES for whole-rock analyses (ALS package ME-ICP06) and ICP-MS for trace elements (ALS package ME-MS81). Before bulk rock analysis, selected samples were cleaned in an ultrasonic bath and then crushed and pulverized in an agate mill to avoid contamination.

Sr, Nd, and Pb isotope analyses were performed using a Finnigan MAT 262V multicollector mass-spectrometer at IGG-CNR, Pisa (Italy). Sr and Nd isotopes were measured in the dynamic mode, after Sr, REE, and Nd purification through conventional anion-ion exchange resins. Measured  $^{87}\text{Sr}/^{86}\text{Sr}$  ratios were normalized to  $^{86}\text{Sr}/^{88}\text{Sr}=0.1194$ . Replicate analyses of NIST SRM 987 ( $\text{SrCO}_3$ ) standard (Avanzinelli et al. 2005) gave an average value of  $0.710211 \pm 12$  (2SD,  $n=47$ ). Published values are adjusted to  $^{87}\text{Sr}/^{86}\text{Sr}=0.710250$ . Replicate analyses of the J Nd i-1 (La Jolla) standard (Avanzinelli et al. 2005) gave an average value of  $0.512103 \pm 12$  (2SD,  $n=36$ ); thus, no correction was made of published values. Sr and Nd blanks were negligible for the analyzed samples.

Pb isotope analyses were performed operating in static mode, after lead extraction from the matrix by chromatographic ion exchange in Dowex 1 anion resin, using standard HBr and HCl elution procedures. Replicate analyses of Pb isotope ratios are accurate to within 0.025 % (2SD) per mass unit, after applying mass discrimination corrections of  $0.15 \pm 0.01$  % per mass unit relative to the NIST SRM 981 reference composition of Todt et al. (1993). Pb blanks were on the order of 0.2–

0.4 ng during the period of chemistry processing, and no blank correction was made.

## Results

The investigated xenopumice consist of eight separate samples (from those already described by Meletlidis et al. 2012). They are pumiceous xenoliths coated with a few-centimeter-thick crust of basanitic magma which also forms few-millimeter-thick bands associated and plastically convoluted with the xenopumice (Fig. 2). The contact between the xenolith and basanitic magma is always sharp and the zone of mingling is confined to a few tens of microns. The basanitic crust consists of vesiculated sideromelane-bearing phenocrysts and microphenocrysts of olivine ( $\text{Fo}_{80-82}$ ), Fe-Ti oxides, minor clinopyroxene ( $\text{Wo}_{43-44}$ ,  $\text{En}_{31-38}$ ), and rare plagioclase ( $\text{An}_{63}$ ) (see also Meletlidis et al. 2012). The geochemistry and mineralogy of the juvenile magma erupted during the 2011–2012 El Hierro crisis, already described by Martí et al. (2013b), closely match major-trace elements and modal composition of the basanite coating the xenopumice studied in this work (Meletlidis et al. 2012).

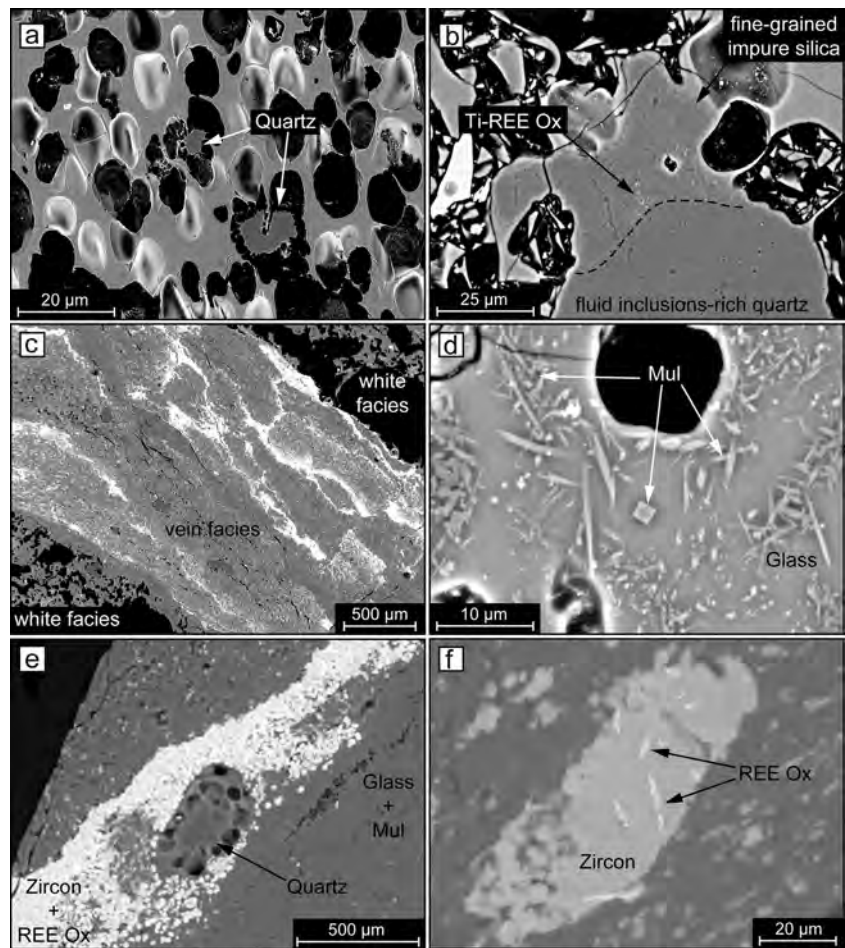
## Xenopumice

From our study of eight xenopumice samples, it is possible to recognize three main facies: white, vein, and grey, which differ in terms of composition, mineralogy, and texture.

### White facies

These parts of the xenopumice are almost completely glassy and highly vesicular (56–70 vol.%) with vesicles mostly ranging from a few micrometers up to 250  $\mu\text{m}$  in size and from sub-rounded to slightly elongated in shape (Meletlidis et al. 2012; Fig. 3a). As shown in Table 1, glass composition is rather heterogeneous, with  $\text{SiO}_2=64.5$  to 76 wt.%,  $\text{Al}_2\text{O}_3=15$  to 18 wt.%,  $\text{Na}_2\text{O}=4.5$  to 6.7 wt.%,  $\text{K}_2\text{O}=3.7$  to 4.8 wt.%, and minor amounts of CaO, MgO, and FeO. Rare restitic phases, ranging in size from tens to hundreds of micron, include partially dissolved plagioclase ( $\text{An}_{38-51}$ ; Table 2), zircon, biotite, apatite, and quartz. Quartz is the most abundant phase (although <1 vol.%) consisting of <100  $\mu\text{m}$  rounded to amoeboid, partially melted crystals characterized by abundant fluid inclusions. Some of the crystals show concentric multiple zoning, consisting of layers of fine-grained, impure silica (Sigmarsson et al. 2013) weakly enriched in alkalis and aluminum. In these impure silica layers, a few microns of Ti-REE-oxides also occur (Fig. 3b).

**Fig. 3** SEM-BSE images of **a** quartz crystals from the white xenopumice facies with **b** detail of quartz textures. **c** Vein facies in which flux structures are well recognizable; **d** detail of the mullite (Mul)+Si-rich glass forming the vein facies groundmass, **e** microcrystalline zircon+REE-oxides (REE Ox) flux structure around a partially melted quartz, and **f** detail of zircon and REE oxides in the vein facies



**Vein facies**

Some of the studied samples are characterized by the presence of veins as large as 4 mm (Figs. 2a and 3c). At the mesoscale,

the veins appear filled by milky white material with no apparent vesiculation. Nevertheless, large voids are locally present. They mostly cut the white facies, forming few branches and following the convoluted structure of the rock stopping

**Table 1** Representative glass analyses of: white facies (1–3), grey facies (4–5), grey facies in the pseudomorphic mineral aggregates associated with partially melted plagioclase (6) and olivine+magnetite+

pyroxene (7–8), vein facies associated with mullite (9), and Holocene subaerial trachyte residual glass (10–11)

wt.%	WF 1	WF 2	WF 3	GF 4	GF 5	GF 6	GF 7	GF 8	VF 9	TRAC 10	TRAC 11
SiO <sub>2</sub>	64.57	70.67	74.09	70.6	61.1	56.22	62.29	56.26	76.59	59.65	63.65
TiO <sub>2</sub>	0.85	0.23	0.18	0.01	0.26	0.19	0.51	0.09	0.07	0.74	0.82
Al <sub>2</sub> O <sub>3</sub>	15.93	16.67	15.13	15.7	18.26	15.49	17.54	19.11	15.17	18.14	18.7
FeO <sup>a</sup>	3.31	0.89	0.47	1.52	3.59	4.7	3.13	4.68	0.38	4.25	3.09
MnO	0.18	0.07		0.09	0.2	0.27	0.12			0.23	0.28
MgO	1.61	0.37	0.15	0.25	1.72	0.81	1.64	2.01	0.48	0.73	0.69
CaO	2.19	0.57	0.18	0.24	2.68	10.9	1.84	4.72	0.49	2.11	1.44
Na <sub>2</sub> O	6.26	6.36	4.55	4.83	6.21	5.03	6.3	6.58	4.11	7.08	6.73
K <sub>2</sub> O	3.75	4.65	3.69	6.51	5.69	4.45	5.55	4.83	2.98	5.33	4.79
Total	98.65	100.48	98.44	99.75	99.71	98.06	98.92	98.28	100.27	98.26	100.19

<sup>a</sup> Total iron as FeO

**Table 2** Representative feldspar analyses calculated on the basis of eight oxygens: restitic plagioclase in the white facies (1); partially melted plagioclase in grey facies mineral aggregates (2); restitic core (3–5), partially melted rim (6–7) and associated glass (8) of the jigsaw fit anorthoclase restitic phenocryst of grey facies; and Holocene subaerial trachyte feldspar (9–11)

wt.%	WF 1	GF 2	GF 3	GF 4	GF 5	GF 6	GF 7	GF 8	TRAC 9	TRAC 10	TRAC 11
SiO <sub>2</sub>	56.02	57.85	65.93	66.74	65.56	65.92	65.32	65.09	59.64	64.80	61.17
Al <sub>2</sub> O <sub>3</sub>	26.79	26.36	20.95	19.41	20.23	19.75	19.51	19.21	25.95	21.61	23.73
FeO	0.41	0.67	0.17		0.11	0.28	0.02	0.31	0.31	0.35	0.36
CaO	9.86	7.58	1.20	0.09	1.02	0.74	0.58	0.62	6.81	2.56	4.82
Na <sub>2</sub> O	5.63	6.02	8.64	7.27	6.64	6.37	4.90	5.73	7.33	9.08	7.99
K <sub>2</sub> O	0.50	1.43	2.96	6.35	6.30	6.99	9.20	7.29	0.48	1.73	0.91
Total	99.21	99.91	99.85	99.86	99.86	100.05	99.53	98.25	100.52	100.13	98.98
Si	2.543	2.601	2.920	2.983	2.937	2.954	2.962	2.969	2.648	2.867	2.746
Al	1.434	1.397	1.094	1.022	1.068	1.043	1.043	1.033	1.358	1.127	1.256
Fe <sup>2+</sup>	0.014	0.023	0.006		0.004	0.009	0.001	0.011	0.010	0.012	0.012
Ca	0.480	0.365	0.057	0.004	0.049	0.036	0.028	0.030	0.324	0.121	0.232
Na	0.496	0.525	0.742	0.630	0.577	0.554	0.431	0.507	0.631	0.779	0.696
K	0.029	0.082	0.167	0.362	0.360	0.400	0.532	0.424	0.027	0.098	0.052
Total	5.00	4.99	4.99	5.00	5.00	5.00	5.00	4.97	5.00	5.00	4.99
An	47.76	37.57	5.89	0.43	4.97	3.59	2.84	3.15	32.98	12.16	23.67
Ab	49.35	53.99	76.79	63.23	58.51	55.98	43.46	52.72	64.25	78.05	71.01
Or	2.88	8.44	17.31	36.34	36.53	40.42	53.69	44.13	2.77	9.79	5.32

abruptly at the contact with the basanitic crust. Microscale observations revealed that the veins consist of microcrystalline zircon (~25 vol.%), quartz (<5 vol.%), REE-oxides (<1 vol.%), and rare rutile, immersed in a groundmass of high-Si glass (SiO<sub>2</sub>=76.6 wt.%; Table 1)+crypto to rarely microcrystalline mullite (Fig. 3d). Zircon forms few micron, sub-rounded, irregular to elongated aggregates, usually aligned in the vein direction (Fig. 3c, e). REE (mostly Ce, Nd, La, Pr, Sm) oxides grow interstitially or are included in zircons, forming spotted lamellae whose size (<20 μm) makes them impossible to be quantitatively analyzed without zircon or groundmass interference (Fig. 3e, f). In this facies, quartz consists of isolated subhedral to anhedral crystals, rarely exceeding 200 μm and showing the same features as in the white facies (Fig. 3e). Rutile is rare in the veins, resembling pseudomorphs probably after spinel or ilmenite. The veins are also characterized by elongated trains of vesicles a few microns across, running approximately parallel to the vein edges. The contact between the veins and the white facies of the xenopumice is restricted within a few tens of micron-thick mullite-free vesiculated glass (Fig. 3c).

### Grey facies

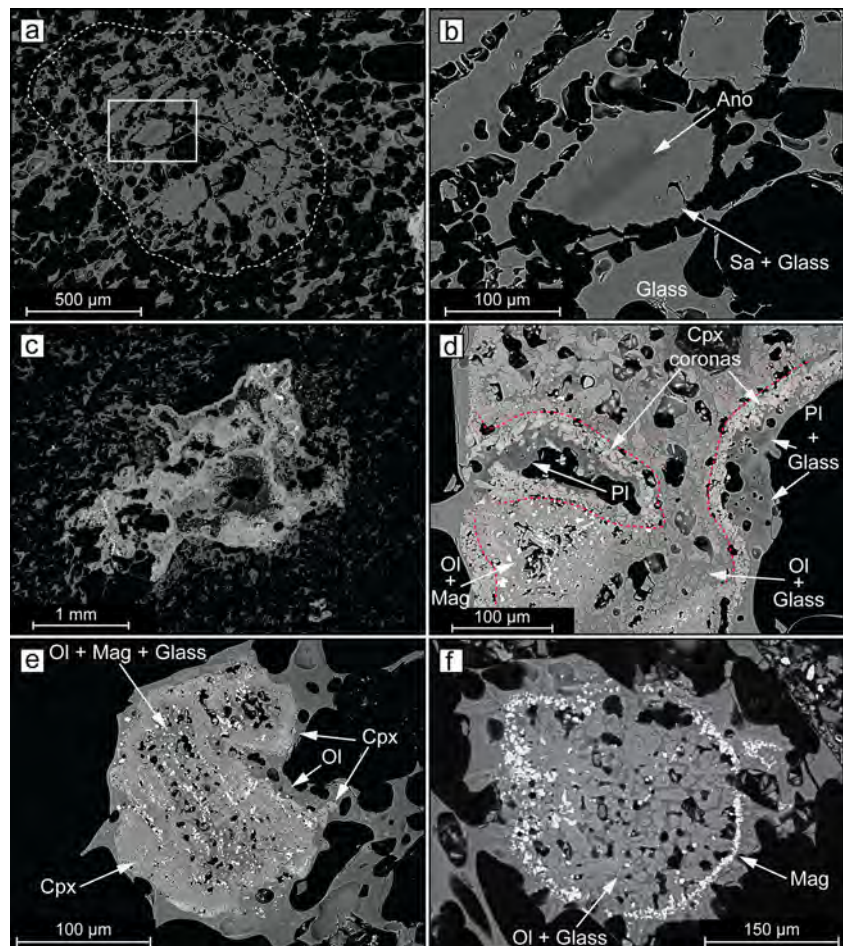
There is no sharp contact zone between the white and grey facies; besides the color, the transition is mainly suggested by small differences in vesicularity (65–70 vol.% for this facies), glass chemistry, and the presence (in the grey facies) of both

restitic and newly formed mineral aggregates. Among the investigated samples, the grey facies is volumetrically less abundant relative to the white facies and approximately represents less than 20 vol.% of the xenopumice.

The grey facies is characterized by an abundance of partially melted restitic anorthoclase ranging in size from about 300 μm to <4 mm. The anorthoclase is usually isolated, showing jigsaw-fit texture, probably separated along pre-existing fractures (Fig. 4a). Anorthoclase fragments are linked by thin stringers of glass forming the wall of sub-rounded to irregular degassing bubbles which seems to be responsible for the feldspar displacements (Fig. 4b). Fragments generally preserve anorthoclase composition at the core (An<sub>0-10</sub>, Ab<sub>58-77</sub>, Or<sub>13-37</sub>) and have sanidine rims (An<sub>1-6</sub>, Ab<sub>43-64</sub>, Or<sub>34-54</sub>) characterized by partial melting textures (i.e., fritted margins; Fig. 4b; Table 2). Glass composition close to the fringed rim of the crystals is almost indistinguishable from that of sanidine (Fig. 5a; Table 2), providing a transient snapshot of alkali feldspar congruent melting. Restitic plagioclase is also present, consisting of irregular spots with andesine composition (An<sub>37-45</sub>) immersed in a vesicular, Ca-Al-enriched glass (Fig 4d; Table 2).

The grey facies is also typified by the presence of hundreds of microns to a few millimeter-sized mineral aggregates that resemble pseudomorphs after pre-existing minerals or glomerophytic aggregates, consisting of clinopyroxene, olivine, magnetite, plagioclase, apatite, and rare Ti-magnetite, orthopyroxene, and zircon (Fig. 4c–f). These are mostly confined to an outer clinopyroxene (Wo<sub>41-50</sub>, En<sub>35-52</sub>; Table 3)

**Fig. 4** SEM-BSE images of the xenopumice grey facies. **a** *Broken line contour* contains a jigsaw-fit restitic feldspar with the *inset b* showing restitic anorthoclase (Ano) composition at the core of a partially melted crystal fragment having sanidine (Sa) composition. **c** Mineral+glass aggregate; **d** detail of an aggregate showing clinopyroxene (Cpx) coronas formed by zoned crystals, around partially melted plagioclase (Pl) and olivine (Ol) associated with glass and magnetite (Mag); **e** pseudomorph of olivine+magnetite+glass surrounded by clinopyroxene after pre-existing primary mafic phase (possibly amphibole or clinopyroxene); **f** pseudomorph of magnetite+olivine+glass (possibly after amphibole)



corona with tabular to squat microcrystals ranging in size from a few microns to a few tens of microns (Fig. 4d, e). In some cases, aggregates of sub-rounded to rounded crystals of olivine ( $Fe_{71-90}$ ; Table 3) within a vesiculated glass rimmed by pyroxene coronas are also present (Fig. 4d). More often, olivine is associated with clinopyroxene, magnetite, rare Ti-magnetite, and orthopyroxene ( $Wo_{0.6-1.3}$ ,  $En_{65-68}$ ; Table 3), with voids or glass between the crystals (Fig. 4d, e, f). Oxide phases are generally clustered, often showing a preferential arrangement following the cleavage, or the rim of pre-existing mineral phases (Fig. 4e, f). Occasionally, when coronas surround partially melted plagioclase, clinopyroxenes are strongly zoned, showing partially reabsorbed cores enriched in FeO ( $Wo_{46-50}$ ,  $En_{20-29}$ ) and  $Al_2O_3$  (2.9–8.8 wt.%; Fig. 4d; Fig. 5b; Table 3). Glass compositions of the grey facies are lower in  $SiO_2$  (56–71 wt.%; Table 1) with respect to the white facies.

### Subaerial Holocene trachyte

The occurrence of trachytes within the Holocene explosive products of El Hierro has been previously reported (Pellicer 1979, 1980; Fuster 1993; Carracedo et al. 2001; Day et al. 2010; Pedrazzi et al. 2014). The pumices here investigated

are porphyritic with ~25 vol.% of phenocrysts in a hyalopilitic groundmass (representative glass compositions are reported in Table 1). Feldspar is the main phenocryst phase, as showing euhedral to subhedral zoned crystals characterized by partially resorbed cores and sub-rounded rims. They are less than 3 mm in size and range in composition from anorthoclase to andesine ( $An_{12-33}$ ,  $Ab_{64-78}$ ,  $Or_{3-11}$ ; Fig. 5a; Table 2). Amphibole is the main mafic phase, with euhedral crystals (<2 mm in size) of weakly zoned Mg-hastingsites, usually with inclusions of glass, spinel, and/or apatite. Minor clinopyroxene ( $Wo_{45-50}$ ,  $En_{23-44}$ ; Fig. 5b; Table 3), tens to hundreds of microns in size, are usually associated with Mg-hastingsite. Tabular biotite is also present. Microlites in the groundmass mainly consist of feldspar laths, whose composition ( $An_{10-24}$ ,  $Ab_{71-76}$ ,  $Or_{5-15}$ ) is slightly more evolved with respect to the phenocrysts. Minor accessory zircon and oxides are also present.

### Bulk rock geochemistry

The bulk-rock chemical compositions of the grey and white xenopumice facies (Meletlidis et al. 2012), the other available

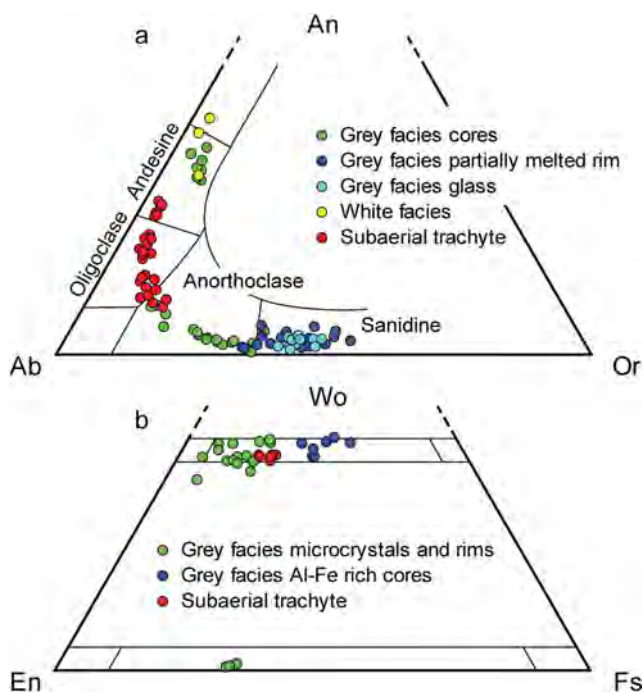


**Fig. 5** **a** Feldspar ternary diagram showing the compositions of restitic and partially melted feldspars in the xenopumice. Grey facies sanidine and glass compositions are representative of the partial melting of anorthoclase as shown in Fig. 4b. Holocene El Hierro subaerial trachyte feldspars are also plotted. **b** Pyroxene ternary diagram showing the composition of grey facies coronas and microcrystals in the aggregates compared with pyroxene composition of the Holocene El Hierro subaerial trachyte

xenopumice geochemical data (Troll et al. 2012; Sigmarsson et al. 2013; Rodriguez-Losada et al. 2014), and the compositions of two samples of Holocene subaerial trachyte representative of the most evolved eruptive products of El Hierro activity are reported in Table 4.

On the basis of the major-oxide compositions ( $\text{SiO}_2 = 66.3$  wt.%;  $\text{Al}_2\text{O}_3 = 18.6$  wt.%; alkalis = 8.4 wt.%), the white facies can be classified as a trachyte, showing only a minor amount of alkalis and silica with respect to the xenopumice literature data, which range from trachyte to alkali rhyolite (Fig. 6a). Trace element concentrations are rather different (Table 4). The flat pattern of the REE spider diagrams (Fig. 6b) is only interrupted by the usual Eu-negative anomaly, highlighting weak enrichment in LREE and strong enrichment in HREE.

The grey facies is less “evolved” ( $\text{SiO}_2 = 62.3$  wt.%;  $\text{Al}_2\text{O}_3 = 16.8$  wt.%; alkalis = 12.4 wt.%) with respect to the white facies and closely matches the compositions of the most evolved trachyte rocks and glasses of El Hierro as shown by both TAS (Fig. 6a) and REE spider diagram patterns (Fig. 6b). Although xenopumice compositions from Troll et al. (2012), Sigmarsson et al. (2013), and Rodriguez-Losada et al. (2014) show LREE patterns comparable with the grey facies (Meletlidis et al. 2012), the HREE patterns are different: flat

for the grey facies and slightly sloping for the other xenopumices.

Strong similarities between the El Hierro subaerial trachyte and xenopumice can also be seen in the incompatible elements (Fig. 6c). The rocks show the same patterns: characterized by positive Th, Zr, and Hf anomalies (very strong for the white facies xenopumice) and Sr, P, and Ti troughs. The heterogeneous U contents of the xenopumice samples, ranging from 1.08 ppm (Sigmarsson et al. 2013) to 42.1 ppm (Rodriguez-Losada et al. 2014), is also worth noting.

## Isotopes

Sr, Nd, and Pb whole rock isotope ratios of the grey and white xenopumice facies as well as of a representative sample of Holocene subaerial trachyte (Trac 2) are given in Table 5. Sr isotope ratios of the xenopumice are variable, showing  $^{87}\text{Sr}/^{86}\text{Sr} \sim 0.70643$  and  $\sim 0.71013$  for the white and grey facies, respectively. By contrast,  $^{143}\text{Nd}/^{144}\text{Nd}$  ratios of xenopumice samples appear rather homogeneous (white facies  $\sim 0.51298$  and grey facies  $\sim 0.51290$ ) and are comparable with the xenopumice Nd isotope ratio of  $\sim 0.51293$  reported by Sigmarsson et al. (2013). Pb isotope ratios of samples of the white xenopumice facies are  $^{206}\text{Pb}/^{204}\text{Pb} \sim 21.688$ ,  $^{207}\text{Pb}/^{204}\text{Pb} \sim 15.709$ , and  $^{208}\text{Pb}/^{204}\text{Pb} \sim 39.774$ , whereas for the grey facies, they are  $^{206}\text{Pb}/^{204}\text{Pb} \sim 20.051$ ,  $^{207}\text{Pb}/^{204}\text{Pb} \sim 15.678$  and  $^{208}\text{Pb}/^{204}\text{Pb} \sim 39.788$ .

Compared with the xenopumice, Holocene trachyte shows a lower  $^{87}\text{Sr}/^{86}\text{Sr}$  ( $\sim 0.70303$ ) value and a similar  $^{143}\text{Nd}/^{144}\text{Nd}$  ( $\sim 0.51295$ ) ratio.  $^{206}\text{Pb}/^{204}\text{Pb}$  ( $\sim 19.451$ ),  $^{207}\text{Pb}/^{204}\text{Pb}$  ( $\sim 15.578$ ), and  $^{208}\text{Pb}/^{204}\text{Pb}$  ( $\sim 39.096$ ) are slightly lower with respect to xenopumice ratios. Troll et al. (2012) and Rodriguez-Losada et al. (2014) also report  $\delta^{18}\text{O}$  xenopumice analyses in the range of 9.1–11.6 and 12–12.7‰.

## Discussion

Despite the occurrence of xenopumice reported by many authors studying the 2011–2012 El Hierro eruption, hypotheses on their origin were only proposed by Meletlidis et al. (2012), Troll et al. (2012), Sigmarsson et al. (2013), and Rodriguez-Losada et al. (2014). Meletlidis et al. (2012) reported the presence of texturally and compositionally different parts forming the xenopumice, also recognizing residual magmatic mineral phases. By contrast, other authors did not report any compositional or textural heterogeneities among the xenopumice samples they examined. Major oxide chemistry and textural data of the samples studied by the above authors equate to the white facies reported in this work (Fig. 6a). However, trace element variations of the xenopumices differ (Fig. 6b, c; Table 4).

**Table 3** Representative mafic mineral analyses of: grey facies olivine in the mineral aggregates (1–3), grey facies unzoned clinopyroxene and crystal rims (4–5) and Al-Fe rich zoned clinopyroxene cores (6–7) in the mineral aggregates, orthopyroxene associated with olivine (8); and clinopyroxene (9) and calcium amphibole (10–11) from the Holocene subaerial trachyte

wt.%	GF 1	GF 2	GF 3	GF 4	GF 5	GF 6	GF 7	GF 8	TRAC 9	TRAC 10	TRAC 11
SiO <sub>2</sub>	41.42	38.01	39.25	55.08	51.56	47.92	44.30	53.28	50.05	40.51	40.28
TiO <sub>2</sub>					0.56		0.61		0.82	4.65	4.51
Al <sub>2</sub> O <sub>3</sub>				0.07	2.05	5.42	8.70	0.27	2.73	12.15	11.98
FeO <sup>a</sup>	6.30	22.20	16.20	4.24	8.71	13.85	16.78	20.51	9.21	14.46	15.08
MnO	0.59	0.81	0.71	0.48	0.70	0.64	0.76	1.07	0.90	0.38	0.43
MgO	52.18	38.91	43.63	16.66	14.55	9.20	6.44	24.66	13.12	11.62	11.51
CaO	0.25	0.22	0.30	24.15	20.68	22.04	21.80	0.31	21.87	11.32	11.31
Na <sub>2</sub> O				0.47	0.92	1.63	1.19		1.29	3.22	3.06
K <sub>2</sub> O										0.99	1.11
Total	100.74	100.15	100.09	101.15	99.73	100.70	100.58	100.10	99.99	98.31	98.16
Si	0.994	0.990	0.994	1.991	1.911	1.793	1.688	1.960	1.856	5.998	5.984
Ti					0.016		0.017		0.023	0.518	0.504
Al				0.003	0.090	0.239	0.391	0.012	0.119	2.120	2.098
Fe <sup>2+</sup>	0.126	0.484	0.343	0.075	0.147	0.138	0.249	0.562	0.071	1.722	1.764
Fe <sup>3+</sup>				0.054	0.123	0.295	0.285	0.069	0.215	0.068	0.109
Mn	0.012	0.018	0.015	0.015	0.022	0.020	0.025	0.033	0.028	0.039	0.054
Mg	1.867	1.511	1.647	0.898	0.804	0.513	0.366	1.352	0.725	2.565	2.549
Ca	0.006	0.006	0.008	0.939	0.830	0.906	0.912	0.012	0.885	1.796	1.800
Na				0.033	0.066	0.118	0.088		0.093	0.925	0.881
K										0.187	0.210
Total	3.01	3.01	3.01	4.01	4.01	4.02	4.02	4.00	4.02	15.94	15.95
Fo	93.66	75.75	82.76								
Wo				47.33	42.84	47.75	49.03	0.60	45.54		
En				45.43	41.93	27.73	20.15	66.66	38.01		
Fs				7.23	15.23	24.52	30.81	32.74	16.45		

<sup>a</sup> Total iron as FeO

A general depletion of medium and heavy REE was reported by Troll et al. (2012), Sigmarsson et al. (2013), and Rodriguez-Losada et al. (2014). Xenopumice samples studied by Sigmarsson et al. (2013) are depleted in U, Sr, and Pb, whereas those reported by Troll et al. (2012) show a wide range of variation for these trace elements. Samples investigated by Rodriguez-Losada et al. (2014) are strongly enriched in U and show the same Pb variation range reported by Troll et al. (2012). Although the samples studied by Sigmarsson et al. (2013) are generally depleted in HREE and HFSE with respect to those of the other authors, they reported a few EMP spot analyses with anomalously high Zr, Th, and HFSE, which is consistent with the white facies composition (Meletlidis et al. 2012). The REE and HFSE enrichment of the white xenopumice facies is probably related to the presence of the veins, which are also enriched in aluminum, as shown by the presence of mullite. Troll et al. (2012) did not report anomalously high REE and HFSE, although their XRD data indicated the presence of smectite and mica/illite

suffering thermal decomposition, highlighting the presence of Al-rich parts of the protolith.

In order to elucidate the origin of the xenopumice (which is inhomogeneous in texture and geochemistry), Fig. 6 shows a comparison of bulk rock and glass compositions of El Hierro xenopumice and extrusives. In addition, radiogenic isotope compositions of xenopumice samples (Table 5) are compared in Fig. 7 with: El Hierro and La Palma (Canary Islands) magmatic extrusive and intrusive rocks (Ovchinnikova et al. 1995; Hoernle 1998; Neumann et al. 2000; Abratis et al. 2002; Praegel and Holm 2006; Gurenko et al. 2006, 2009; Day et al. 2010; Geldmacher et al. 2011); Jurassic oceanic crust beneath Gran Canaria (Canary Islands; Hoernle 1998); pelagic and terrigenous sediments from Gran Canaria (Hoernle 1998), from the 121DK (24°53'N, 21°42' W) and 65GTV (35°20'N, 15°20'W) east Atlantic Ocean dredging sites reported in Abouchami et al. (1999), and the ODP658C (20°95'N, 18°35'W) drilling site representative of the composition of Sahara dust (Cole et al. 2009).

**Table 4** Major oxide (wt.%), and volatile and trace element (ppm) compositions of xenopumice from the available literature data, compared with pumices representative of the Holocene subaerial trachyte (Trac 1 and Trac 2)

	Meletlidis et al. (2012)		Sigmarrsson et al. (2013)	Troll et al. (2012)			Rodriguez-Losada et al. (2014)			This work	
	White Facies	Grey Facies	EH 1-A	H12110	EH2510-1	EH2110-2	EH-W	igme_W1	igme_W2	Trac 1	Trac 2
SiO <sub>2</sub>	66.35	62.27	67.7	69.19	71.03	68.61	66.76	71.17	70.76	62.3	60
TiO <sub>2</sub>	0.26	0.28	0.22	0.22	0.18	0.21	0.25	0.25	0.40	0.28	0.81
Al <sub>2</sub> O <sub>3</sub>	18.61	16.75	16.6	15.76	15.10	15.43	15.22	15.63	14.74	16.55	18.15
Fe <sub>2</sub> O <sub>3</sub> <sup>a</sup>	0.91	2.78	1.54	0.73	0.69	0.71	0.99	0.81	1.37	2.73	3.75
MnO	0.02	0.07	0.02	0.01	0.02	0.02	0.02	0.04	0.04	0.07	0.18
MgO	0.33	1.66	0.51	0.31	0.12	0.55	0.34	0.11	0.42	1.66	0.71
CaO	0.44	1.37	0.54	0.48	0.31	0.47	0.64	0.84	1.23	1.32	2.63
Na <sub>2</sub> O	5.1	6.31	6.74	6.09	6.11	6.52	5.7	5.77	5.77	6.45	7.4
K <sub>2</sub> O	3.31	6.05	3.64	4.88	4.73	4.78	4.25	4.31	4.14	5.74	3.62
P <sub>2</sub> O <sub>5</sub>	0.15	0.07	0.06	0.07	0.04	0.05	0.11	0.05	0.09	0.07	0.15
LOI	2.3	2.52	2.1	1.19	1.06	1	5.66	1.02	1.04	2.97	2.06
Total	97.78	100.13	99.67	98.93	99.39	98.35	99.87	100.01	100	100.14	99.46
F			282–449								
Cl			118–222	7660	4160	13,342					
S			26–59								
Li			11–11.2								
Sc	8	1	2.21–2.4				1				
Be	4	4					3	12.1	9.7		
V	7	13		0.99	0.47	1.51	10	5.14	16.4	8	36
Cr	<20	<20		5.65	0.52	1.11	20	9	9	10	10
Co	<1	2		1.1	1.02	0.63	2	2.13	4.3		
Ni	<20	70		2.08	1.66	10.3	30	7.33	13.7		
Cu	<10	20	2.5–2.58	9.71	2.61	6.43	10	20.6	27.8		
Zn	30	130	46.9–47.7	21.54	37.4	38.01	30	57.8	51.9		
Rb	27	62	43.3–44	42.98	49.34	48.29	39	44	47	62.3	129.5
Sr	287	59	128–131	90.44	79.39	135.03	250			61.4	861
Y	373	39.9	13.1–13.4	9.98	5.78	4.67	22.9	23.4	25.7	39.1	35.8
Zr	7310	574	488–518	237	220	212	527			633	934
Nb	221	112	116–118	72.51	56.21	56.05	101			121	204
Cs	<0.1	<0.1					0.1			0.05	1.68
Ba	691	1099	865–889	436	543	496	871	2014	1748	1035	852
La	78.6	117	76.9–81.5	29.23	28.84	34.57	51.2	57.5	57.8	115	128.5
Ce	200	213	152–158	77.76	62.95	85.16	111	127	133	194.5	216
Pr	26.7	19.8	16.8–17.4	7.19	7.55	7.99	11.6	15.4	16.3	18.6	20.7
Nd	130	60.6	57.4–58.6	23.85	21.26	25.52	41.9	52.4	53.9	58.3	66.8
Sm	49.6	8.8	9.41–9.46	4.14	4.74	4.15	8.3	9.5	9.7	8.36	10.5
Eu	4.87	1.56	1.43–1.44	0.76	0.8	0.82	1	1.3	1.3	1.65	3.15
Gd	41.8	5.95	5.71–5.8	2.63	2.38	2.49	6.4	7.2	7.4	6.31	7.99
Tb	8.93	0.96	0.775–0.781	0.39	0.3	0.3	0.9	0.9	1	0.98	1.23
Dy	60.6	5.85	3.75–3.79	2.13	1.57	1.56	4.5	4.8	5.3	5.99	6.44
Ho	12.8	1.16	0.585–0.594	0.37	0.27	0.22	0.8	0.8	1	1.22	1.22
Er	40.4	3.64	1.44–1.45	0.97	0.62	0.52	2	2.3	2.5	3.65	3.41
Tm	7.19	0.571		0.18	0.09	0.09	0.3	0.3	0.3	0.57	0.5
Yb	49.6	3.82	1.46–1.47	1.15	0.6	0.65	1.7	2	2.1	3.92	3.15
Lu	7.59	0.615	0.204–0.206	0.17	0.08	0.09	0.3	0.3	0.3	0.61	0.5
Hf	122	12	11.6–12	5.83	6.84	7.24	10.9			13.3	18.9

**Table 4** (continued)

	Meletlidis et al. (2012)		Sigmarsson et al. (2013)	Troll et al. (2012)			Rodriguez-Losada et al. (2014)			This work	
	White Facies	Grey Facies	EH 1-A	H12110	EH2510-1	EH2110-2	EH-W	igme_W1	igme_W2	Trac 1	Trac 2
Ta	8.63	7.78	7.49–7.59	3.93	4.81	4.79	7.4			8.3	11.2
Pb	9	7	5.73–5.91	7.26	14.25	7.14	13	6.8	6.6		
Th	12.8	15.9	10.5–10.7	5.53	7.58	6.93	9.4	12.9	11.7	15.5	23.8
U	18.5	4.9	1.08–1.09	23.9	11.8	3.28	35.6	35.4	42.1	4.27	6.02

<sup>a</sup> Total iron as Fe<sub>2</sub>O<sub>3</sub>

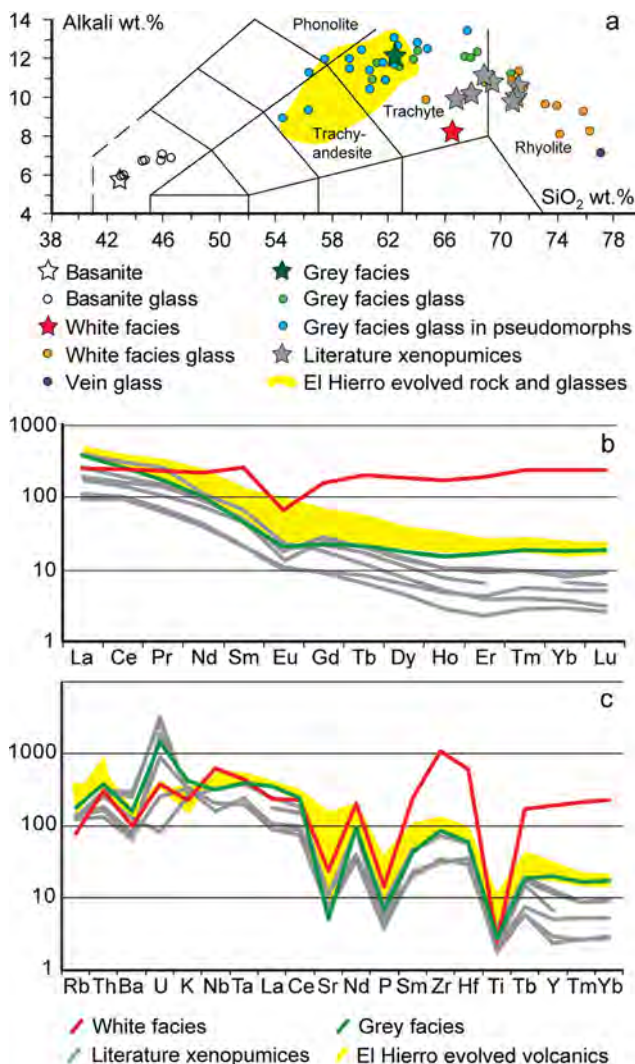


**Fig. 6** **a** TAS diagram (Le Maitre et al. 1989) showing bulk rock (stars) and glass (circles) compositions of the various studied rocks. **b** REE and **c** incompatible elements spider diagrams (normalization values from Nakamura 1974 and Thompson et al. 1984) comparing white and grey facies compositions with xenopumice data from literature (Table 4) and historical El Hierro evolved volcanic products. Glass analyses are from this work (Table 1). El Hierro basanite compositions are from Meletlidis et al. (2012); the trachyandesite-trachyte data (El Hierro evolved rock and glasses) are from this work, Pellicer (1980), Carracedo et al. (2001) and Day et al. (2010)

Below, we discuss the compositional, textural, and isotopic evidence to demonstrate how volcanic rocks of trachyandesite to trachyte composition are the preferred candidates for the xenopumice protolith, emphasizing the role played by hydrothermal and pyrometamorphic processes in generating these rocks.

**The effect of hydrothermal alteration on mineralogy, chemistry, and Sr, Nd, and Pb isotopes**

Active volcanoes are characterized by an acid-sulfate hydrothermal system (Wohletz and Heiken 1992) responsible for the circulation of acidic fluids through rock porosity or along fractures and discontinuities. When rocks forming an active volcano edifice are subjected to acidic fluid circulation, leaching occurs. Rock transformations induced by hydrothermal alteration depend on temperature, pH, and time of exposure to acidic fluids and can result in argillic to silicic alteration facies (Wohletz and Heiken 1992; Fulignati et al. 1998; Robb 2005; Pirajno 2009).

Clues to the volcanic origin of the xenopumice are preserved in the partially molten feldspars (anorthoclase+plagioclase) as well as in the remnants of biotite, which are among the phases that better survive hydrothermal alteration (Wohletz and Heiken 1992), and are present both in grey (mainly) and white facies. Besides indicating a magmatic origin of the protolith, these restitic phases are compatible with a trachyandesite or trachyte mineralogy. Preservation and habit of the two feldspars in the xenopumice, which remain as partially melted jigsaw-fit texture anorthoclase and few tens to hundreds of micron-sized patchy andesine, can be ascribed to the different sizes of these minerals in the trachytic protolith, probably containing millimetric anorthoclase and smaller plagioclase (Fig. 4a, b, d).

A trachyandesitic or trachytic xenopumice protolith was probably characterized by a similar composition and mineralogy to the subaerial Holocene trachyte here investigated, in which mafic phases are calcic amphiboles (Leake et al. 1997; Ridolfi et al. 2010) of the pargasite-Mg-hastingsite solid

**Table 5** Isotope ratio analyses performed on white and grey xenopumice facies and on the El Hierro subaerial trachyte, compared with Nd isotopic ratio of xenopumice analyzed by Sigmarsson et al. (2013). In-run errors are shown for isotope ratios

Radiogenic isotope ratios	El Hierro xenopumices		El Hierro trachyte	
	Literature data	This work		
	Sigmarsson et al. (2013)	White facies	Grey facies	Trac 2
$^{87}\text{Sr}/^{86}\text{Sr}$		0.706426±6	0.710134±6	0.703029±6
$^{143}\text{Nd}/^{144}\text{Nd}$	0.512931±8	0.512978±7	0.512905±8	0.512948±8
$^{206}\text{Pb}/^{204}\text{Pb}$		21.6875±9	20.0511±40	19.4510±40
$^{207}\text{Pb}/^{204}\text{Pb}$		15.7092±6	15.6778±31	15.5787±10
$^{208}\text{Pb}/^{204}\text{Pb}$		39.7738±16	39.7877±80	39.0962±31

solution with minor clinopyroxene and biotite. Hydrothermal alteration after calcic amphibole led to the formation of chlorite, epidote, calcite, minor phyllosilicates (smectites, illite, etc.), Fe-oxides and hydroxides, quartz, and rutile (Deer et al. 1997a). Secondary phases after clinopyroxene (Deer

et al. 1997b) and biotite (Wohletz and Heiken 1992) are similar, consisting mainly of Mg-Fe phyllosilicates, Fe-oxides and hydroxides, calcite, and anhydrite. As mentioned before, biotite, illite, and smectites surviving high-T induced by the contact with basanitic magma are reported in xenopumices by Meletlidis et al. (2012) and Troll et al. (2012).

The role of hydrothermal alteration in transforming an inferred trachytic protolith is supported by the presence of quartz characterized by concentric layers of “impurities” (this work; Sigmarsson et al. 2013) and inclusions of Ti-REE phases (Fig. 3b). These zoned quartz grains provide strong evidence of argillic and/or silicic alteration (Wohletz and Heiken 1992; Fulignati et al. 1998, 1999). According to this evidence, quartz does not have a sedimentary origin as suggested by Troll et al. (2012), Sigmarsson et al. (2013), and Rodriguez-Losada et al. (2014), as quartz in submarine sediments around Canary Islands come mainly from the Saharan dust (Cole et al. 2009) formed by the degradation of intrusive/metamorphic rocks.

The heterogeneous REE and HFSE compositions of the xenopumice (Meletlidis et al. 2012; Troll et al. 2012; Sigmarsson et al. 2013 and Rodriguez-Losada et al. 2014; Fig. 6b, c) could result from the hydrothermal alteration of trachyandesite or trachyte, consistent with the general depletion of elements and relative enrichment in  $\text{SiO}_2$  that is typical of advanced argillic to silicic alteration facies (Salvi and Williams-Jones 1996; Fulignati et al. 1999). Fulignati et al. (1999) have shown how LREE and HREE are virtually immobile during weak leaching processes. Nevertheless, severe alteration (leading to advanced argillic facies) may be associated with REE and HFSE mobility. Salvi and Williams-Jones (1996) and Salvi et al. (2000) demonstrated how hydrothermal fluid circulation can play a significant role in the depletion/accumulation of REE and HFSE in alkaline and peralkaline igneous complexes. A number of authors have studied REE and HFSE mobility during high temperature acidic fluid circulation and that of ligands, such as  $\text{Cl}^-$ ,  $\text{SO}_4^{2-}$  (Wood 1990; Haas et al. 1995; Fulignati et al. 1999; Gysi and Williams-Jones 2013), and  $\text{F}^-$  (Salvi and Williams-Jones 1996; Fulignati et al. 1999; Salvi et al. 2000; Migdisov et al. 2009). The very high chlorine ( $\text{Cl}=4160\text{--}13,342$  ppm;

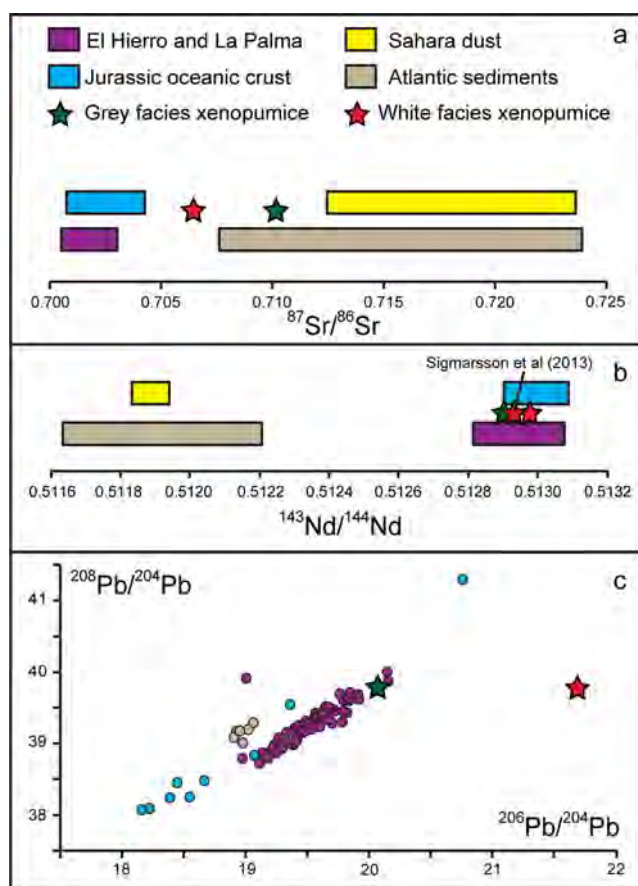


**Fig. 7** Representative  $^{87}\text{Sr}/^{86}\text{Sr}$  (a),  $^{143}\text{Nd}/^{144}\text{Nd}$  (b), and  $^{208}\text{Pb}/^{204}\text{Pb}$  vs  $^{206}\text{Pb}/^{204}\text{Pb}$  (c) ratios of white and grey xenopumice facies compared with: El Hierro and La Palma (Canary Islands) magmatic extrusive and intrusive rocks (Ovchinnikova 1995; Hoernle et al. 1998; Neumann 2000; Abratis 2002; Praegel and Holm 2006; Gurenko 2006, 2009; Day et al. 2010; Geldmacher 2011), which also include the Holocene subaerial trachyte presented in this work; the Jurassic oceanic crust beneath Gran Canaria (Canary Islands; Hoernle 1998); pelagic and terrigenous sediments (Hoernle 1998; Abouchami et al. 1999), and Sahara dust (Cole et al. 2009)

Table 4) content in the xenopumice analyzed by Troll et al. (2012) seems to confirm the hypothesis of REE and HFSE mobility induced by fluid circulation.

The products of hydrothermal activity to which the xenopumice protolith has been subjected prior to partial melting/pyrometamorphism are represented by the vein facies. The veins are probably the remains of the protolith rock hydrothermal fluid circulation paths, which now appears as a few-millimeter-wide channel-like fluidal structure (Figs. 2a and 3c), in which mineral precipitation from the hydrothermal solutions prior pyrometamorphism is confirmed by the presence of hydrothermal quartz, zircon and REE-oxides aggregates in an Al-rich groundmass (Fig. 3d, e, f), probably indicating advanced argillic alteration of the protolith.

According to the above evidence, trachyandesite-trachyte of the El Hierro submarine edifice was affected by acidic fluid circulation, which gave rise to heterogeneous leaching. Mineral aggregates, restitic phases, and the bulk trachyte *stricto sensu* composition characterizing the grey xenopumice facies, all probably represent parts of the protolith in which hydrothermal leaching was relatively weak. By contrast, the white xenopumice facies, as well as the samples studied by Troll et al. (2012), Sigmarsson et al. (2013), and Rodriguez-Losada et al. (2014), were probably derived from strongly hydrothermally altered rocks in which original textures and mineral phases are (almost) completely obliterated.

Before pyrometamorphic transformation induced by contact with basanitic magma, the xenopumice protolith was probably subjected to intermediate-advanced argillic alteration (Wohletz and Heiken 1992; Fulignati et al. 1999; Robb 2005). Thus, prior to their eruption, the xenopumice protolith rocks consisted of amorphous silica and/or silica phases, clay minerals, hydroxides, probably sulfates, chlorides, and fluorides together with relic magmatic phases. Parts of the rocks suffered less intense hydrothermal alteration in which feldspars were altered to secondary minerals (sericite?) along the rims and fractures, while mafic minerals were completely replaced by phyllosilicates and hydroxides. Acidic fluid circulation formed veins, and REE and HFSE sulfate, chloride and/or fluoride probably crystallized (Salvi and Williams-Jones 1996; Fulignati et al. 1999; Salvi et al. 2000), as well as phyllosilicates and silica phases (Wohletz and Heiken 1992; Fulignati et al. 1999). It is probable that protolith rocks suffered hydrothermal alteration inside the volcanic edifice, as there are only a few traces of seabed hydrothermalism/metamorphism (i.e., the weak Ba enrichment; Rodriguez-Losada et al. 2014). Seabed hydrothermal alteration is generally characterized by high mobility of Ba and abundance of carbonates, as reported by Klugel et al. (2011) and Staudigel and Schmincke (1984) for dredged trachytic rocks from the Henry Seamount (located south east off the coast of El Hierro) and the submarine sequence outcropping on La Palma (Canary archipelago).

The Sr, Nd, and Pb isotopic ratios of the analyzed xenopumice samples could be very difficult to explain without taking into account the effects of hydrothermal alteration.  $^{87}\text{Sr}/^{86}\text{Sr}$  values of white ( $\sim 0.70643$ ) and grey ( $\sim 0.71013$ ) facies are notably different, and also differ from the Holocene subaerial trachyte ( $\sim 0.70303$ ), which closely matches other El Hierro magmatic products (Fig. 7a). The variation in the xenopumice Sr isotope ratios cannot be explained by seawater contamination alone. Values characterizing the present day oceans are within the range of 0.7091–0.7092 (e.g., Kuznetsov et al. 2012 and references therein) and although a large amount of seawater contamination could lead to the white facies  $^{87}\text{Sr}/^{86}\text{Sr}$  value, it would not be able to explain the higher  $^{87}\text{Sr}/^{86}\text{Sr}$  ratio of the grey facies. Magma contamination induced by quartz-rich sediments as suggested by Sigmarsson et al. (2013), or the sedimentary origin of the xenopumice proposed by Troll et al. (2012) and Rodriguez-Losada et al. (2014), could also partially explain their Sr isotopic ratios. Nevertheless, the above hypotheses are not consistent with the homogeneous  $^{143}\text{Nd}/^{144}\text{Nd}$  values of  $\sim 0.51298$  for the white facies,  $\sim 0.51290$  for the grey facies, and  $\sim 0.51293$  for the xenopumice analyzed by Sigmarsson et al. (2013). These Nd isotopic values clearly show a magmatic signature for the xenopumice, with no detectable contribution from pelagic or terrigenous sediments (Fig. 7b). Compared with the Nd isotopic values, the Sr isotopic ratios of the xenopumice are best explained by hydrothermal alteration, given the relatively greater mobility of Sr compared with Nd. The high mobility of Rb and Sr during both low- and high-T hydrothermal alteration is a commonly reported process that usually results in anomalous  $^{87}\text{Sr}/^{86}\text{Sr}$  ratios (Spooner et al. 1977; Manziés and Seyfried 1979; Verma 1992; Cousens et al. 1993; Glodny and Grauert 2009; Nobre Silva et al. 2010). In contrast, Nd is relatively immobile during alteration processes (Verma 1992; Cousens et al. 1993; Nobre Silva et al. 2010).

Lead isotope analyses (Table 5) also reflect the role of hydrothermal alteration of the xenopumice protolith. Grey facies Pb isotopic ratios are close to the upper limit of the magmatic products of the volcano (Fig. 7c). In contrast, the white facies has a  $^{208}\text{Pb}/^{204}\text{Pb}$  value of  $\sim 39.774$ , comparable with the El Hierro dataset (Fig. 7c), whereas  $^{206}\text{Pb}/^{204}\text{Pb}$  and  $^{207}\text{Pb}/^{204}\text{Pb}$  (respectively,  $\sim 21.688$  and  $\sim 15.709$ ; Table 4) are anomalous with respect to the magmatic and sedimentary rocks considered (Fig. 7c). Since  $^{206}\text{Pb}$ ,  $^{207}\text{Pb}$ , and  $^{208}\text{Pb}$  are the products of  $^{238}\text{U}$ ,  $^{235}\text{U}$ , and  $^{232}\text{Th}$  radioactive decay, respectively, the variation of the white facies Pb isotopic ratios may be explained by the preferential and inhomogeneous leaching of U-bearing minerals with respect to Th-rich phases by hydrothermal fluids, as demonstrated by the wide range of U in the xenopumice samples.

According to our hypothesis, leaching occurred during upward migration of acidic fluids through the volcano edifice,

saturating the fluids with medium and heavy REE as well as some HFSE, and contaminating rocks with a high  $^{87}\text{Sr}/^{86}\text{Sr}$  ratio. When the fluids reached shallower levels of the volcano, different conditions (lower pressure and temperature and higher oxygen fugacity) induced precipitation from the super-saturated fluids of REE- and HFSE-bearing phases in veins and as mineral aggregates. Continuous acidic fluid circulation could have contaminated the original  $^{87}\text{Sr}/^{86}\text{Sr}$  ratio of the trachyandesite/trachyte protolith to the anomalously high values reported for the white and grey xenopumice facies. High radiogenic Sr contaminating the hydrothermal fluids during their upward migration could have been derived from terrigenous and pelagic sediments with  $^{87}\text{Sr}/^{86}\text{Sr}$  in the range of 0.709–0.715 (Hoernle 1998) forming the base of the El Hierro submarine edifice. Alternatively, the contamination may have been caused by extensive leaching of high  $^{87}\text{Sr}/^{86}\text{Sr}$  minerals (such as biotite and/or feldspar) from differentiated intrusive alkaline rocks (e.g., syenite enriched in incompatible elements such as REE and HFSE; Troll and Schmincke 2002) within the volcanic edifice.

### Pyrometamorphism after hydrothermal alteration

Pyrometamorphism at the contact between basic magma and sedimentary or metamorphic rocks (Grapes 1986, 2006; Graham et al. 1988; Preston et al. 1999; Renzulli et al. 2003; Salvioli-Mariani et al. 2005; Harlov et al. 2006), as well as hydrothermally altered volcanics (Wood 1994; Wood and Browne 1996; Grapes 2006; Del Moro et al. 2011, 2013), usually results in partially to completely vesiculated glassy rocks of the sanidinite facies (i.e., buchite; Grapes 2006 and references therein). Partial melting and subsequent crystallization from the anatectic liquid, as well as subsolidus mineral reactions, are the main processes of pyrometamorphism (Grapes 1986; Graham et al. 1988; Clark and Peacor 1992; Preston et al. 1999; Sokol et al. 1998; Grapes 2006; Del Moro et al. 2011, 2013).

In agreement with the evidence presented above, the high temperature of the basanitic magma triggered pyrometamorphism of hydrothermally altered trachyandesite/trachyte forming the wall rocks of the newly formed El Hierro eruptive conduit. The rapid rise of magma engulfed and transformed the original altered rocks, resulting in the eruption of xenopumice at the beginning of the October 2011 event (Fig. 8).

The temperature of the basanitic magma is estimated to have been about 1150–1200 °C (Sigmarsson et al. 2013; Martí et al. 2013b) under oxygen fugacity conditions close to the NNO buffer (Martí et al. 2013b). The magma temperature was therefore hot enough to induce the almost complete dehydration melting of the hydrous and hydroxyl mineral assemblage of the argillic to silicic alteration facies of the

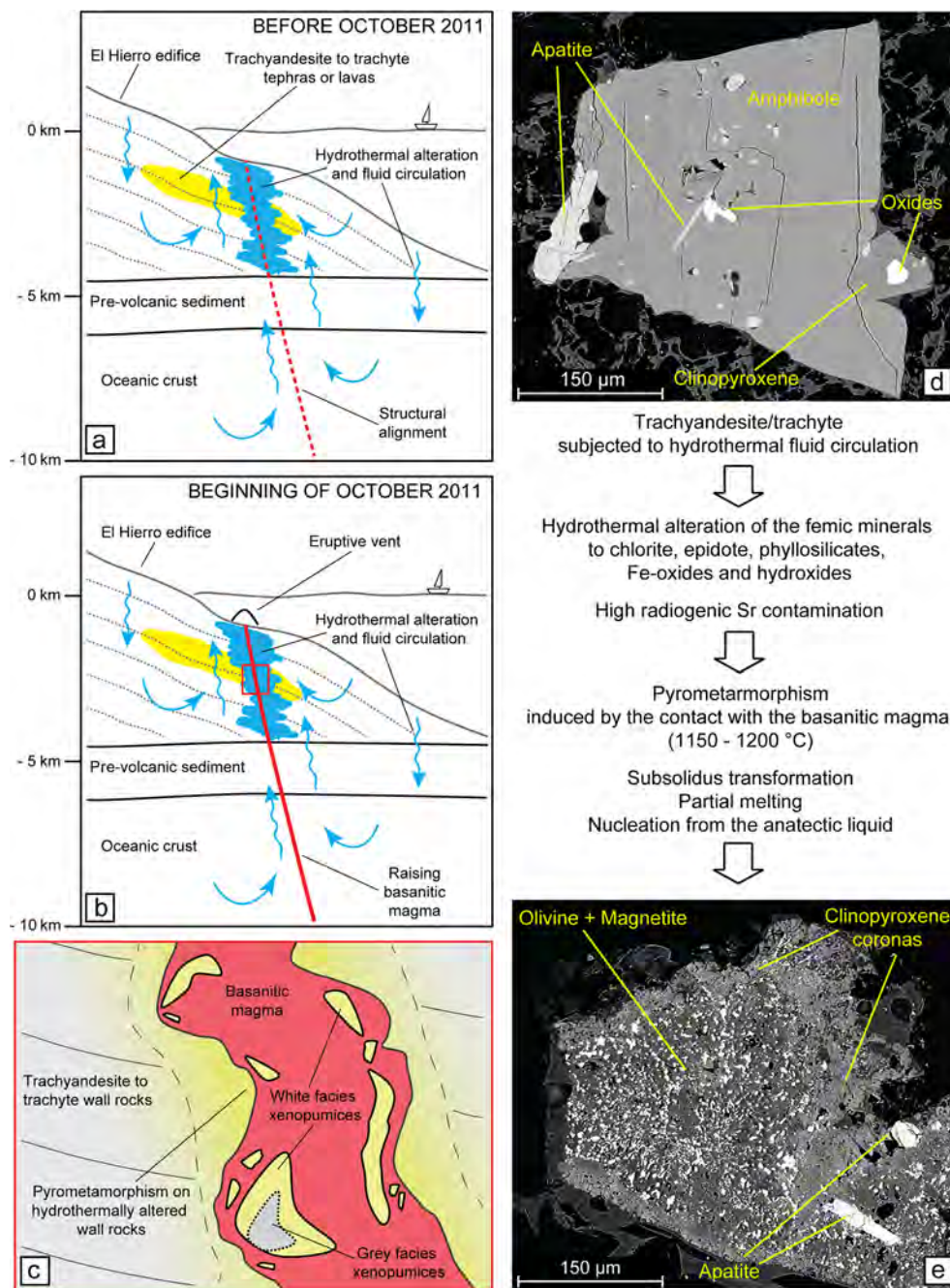
xenopumice protolith. Evidence of partial melting is preserved in restitic anorthoclase phenocrysts of the grey xenopumice facies. Since melting normally proceeds inwards from rims and along fractures, the anorthoclase jigsaw-fit texture (Fig. 4a, b) is probably due to gas expansion related to thermal dissolution of hydrous alteration minerals (possibly sericite and/or kaolinite) formed along cracks within the feldspar phenocrysts. Temperatures were hot enough (i.e.,  $>850\text{ °C}/\leq 1\text{ kbar}$ ) to induce partial melting of anorthoclase ( $\text{Ab}_{58-77}$ ), which is compositionally close to the eutectic of Bowen and Tuttle (1950).

Heating experiments on clays (Schomburg 1991) reported the formation of forsterite after Mg-chlorite at temperatures  $>800\text{--}830\text{ °C}$ . The association olivine+pyroxene+spinel/hercynite+volatiles was observed by Waldron et al. (1993) and Rathossi and Pontikes (2010) during high-T breakdown of chlorite, in which Ca was provided by calcite. Similar reactions can be invoked for the crystallization of the olivine+clinopyroxene+magnetite assemblages, forming the microcrystalline aggregates observed in the grey facies (Fig. 4c–f), from secondary phases (possibly chlorite+illite/smectite+Fe-hydroxides+quartz+calcite/anhydrite) that have replaced the original mafic minerals (i.e., calcic amphibole+clinopyroxene+biotite).

Textural evidence from the xenopumice suggests that olivine+magnetite formed after subsolidus breakdown of pre-existing mineral phases (such as secondary chlorite+Fe-hydroxides after amphibole; Fig. 8e). Olivine is also observed as single microlites surrounded by glass and suggesting nucleation from the melt (Fig. 4d, f). According to Gee and Sack (1988), Toplis (2005) and Putirka (2008), the Fe-Mg exchange coefficient between olivine and liquid depends on the silica and alkali content of the melt, increasing with  $\text{SiO}_2$  and decreasing with alkalis, with a nearly constant  $K_D(\text{Fe-Mg})^{\text{ol-liq}}((X_{\text{Fe}}^{\text{ol}}X_{\text{Mg}}^{\text{liq}})/(X_{\text{Mg}}^{\text{ol}}X_{\text{Fe}}^{\text{liq}}))=0.30\pm 0.03$  for basaltic liquids. According to calculations based on olivine and related glass compositions of the grey facies aggregates,  $K_D(\text{Fe-Mg})^{\text{ol-liq}}$  varies from 0.02 to 0.24, highlighting a transient metastable nucleation of olivine rather than crystallization under equilibrium conditions. In fact, the occurrence of rare orthopyroxene in the aggregates (olivine+magnetite+orthopyroxene) may be the result of metastable olivine reacting with the Si-rich anatectic liquid.

The formation of clinopyroxene coronas is common during partial melting at the interface between silica-rich phases or melts and less evolved liquids (Bowen 1928; Searle 1962; Sato 1975; Preston et al. 1999; Del Moro et al. 2011). Clinopyroxene coronas in the grey xenopumice facies may have formed from thermal decomposition of secondary minerals after calcic amphibole and/or clinopyroxene alteration (possibly chlorite+calcite/anhydrite+smectite+illite). Aluminum-rich compositions, such as those observed in the core of some clinopyroxene crystals (Table 3), could have

**Fig. 8** Simplified sketch summarizing the processes leading to xenopumice formation. **a** Hydrothermal fluid circulation locally altered trachyandesite/trachyte products forming the El Hierro submarine edifice; **b, c** Hydrothermally altered wall rocks undergoing pyrometamorphism upon contact with the raising basanitic magma; **d** SEM-BSE image of mafic minerals in the Holocene subaerial El Hierro trachyte (inferred to be similar to some buried counterparts of the subvolcanic edifice); **e** SEM-BSE image of pseudomorphic minerals in the grey facies



been formed from the dissolution of illite-chlorite (Rathossi and Pontikes 2010). However, as clinopyroxene usually forms coronas around partially melted plagioclase (Fig. 4d), it could have crystallized from Ca-Al-enriched liquid locally present around partially melted andesine.

Mullite is a common product during contact metamorphism and pyrometamorphism of pelitic rocks through the breakdown of muscovite, and besides being a good indicator of temperature (higher than 800–850 °C), it also indicates pressure of 1 kbar or less (Kitchen 1984; Cosca et al. 1989; Clark and Peacor 1992; Wood 1994; Preston et al. 1999;

Grapes 2006; Del Moro et al. 2011). Mullite associated with silica-rich glass is only present in the vein xenopumice facies in which alteration of the protolith prior to pyrometamorphism was more intense. Therefore, this association probably takes place after high-T breakdown of Al-bearing alteration phases, such as illite (Schomburg 1991) or smectite. Layered quartz is also present in the veins (as well as in the white facies) and was probably the result of pyrometamorphism of amorphous silica or hydrothermal quartz.

Zircon and REE-oxides characterizing the vein facies may have been derived from the thermal breakdown of sulfate/

chloride/fluoride-bearing minerals. Such phases can concentrate REE and Zr and are usually stable at low-T and relatively oxidized conditions (Archibald et al. 2001; Jugo 2009). Under magmatic or pyrometamorphic conditions, S, Cl, and F are volatilized or dissolved in the silicate melt (Wood 1994; Wood and Browne 1996). This should have allowed the formation of REE-oxides and zircon (this latter being possible through the interaction with the Si-rich melt).

## Conclusions

In order to elucidate the origin of xenopumice erupted on 15 October 2011, after the formation of a submarine vent on the El Hierro S-ridge, we have presented a detailed dataset of whole rock geochemistry, Sr-Nd-Pb isotopes, mineral, and glass analyses and textural investigation of the xenopumice and Holocene trachyte from El Hierro subaerial activity.

1. The magmatic origin of the xenopumice protolith is indicated by the presence of partially melted restitic minerals, such as anorthoclase, andesine, and biotite. This restitic mineralogy closely matches that of trachyandesite/trachyte rocks. Xenopumice also shows a geochemical magmatic signature comparable with representative trachyandesite and trachyte rocks of El Hierro as highlighted by REE and incompatible elements spider diagrams. In addition, xenopumice Nd isotope ratios perfectly match the volcano's magmatic products and therefore further support the magmatic origin of the xenopumice protolith, as  $^{143}\text{Nd}/^{144}\text{Nd}$  is usually not affected by hydrothermal alteration.
2. Evidence of hydrothermal alteration suffered by the xenopumice protolith prior to pyrometamorphism includes the following:
  - (i) The presence of zoned quartz characterized by layers enriched in alkalis, aluminum, fluid, and Ti-REE-oxide inclusions, which was probably formed through pyrometamorphism of amorphous silica or hydrothermal quartz.
  - (ii) Microcrystalline pseudomorphic aggregates of olivine+clinopyroxene+magnetite+glass have been recognized to be the pyrometamorphic products of alteration phases (possibly chlorite+illite/smectite+Fe-hydroxide+quartz+calcite/anhydrite), which replaced the primary mafic phases of the xenopumice protolith mainly consisting of calcic amphibole, clinopyroxene, and biotite.
  - (iii) Subvolcanic hydrothermal processes affecting the protolith can explain the variable xenopumice Sr and Pb isotopic ratios, which are not compatible

with either magmatic or sedimentary rocks or contamination models among them.

- (iv) Mineralized veins consisting of zircon+REE-oxides+mullite+zoned quartz+Si-rich glass are the result of pyrometamorphism after alteration minerals such as illite+smectites+amorphous silica or hydrothermal quartz+Zr- and REE-sulfate and/or chloride and/or fluoride.

On the basis of the above evidence, we propose that basanitic magma, rising inside the volcano edifice, intruded hydrothermally altered trachyandesitic to trachytic pyroclasts or lavas. The hydrothermally altered wall rock fragments were pyrometamorphosed and entrained in the basanitic magma. The anatectic melt of the xenoliths mingled with the basanitic magma and quenched as xenopumice during the eruption.

Studying lithotypes of xenolithic derivation such as xenopumice can be a powerful tool in defining the plumbing system of active volcanoes. These lithotypes represent a snapshot of the (usually) transient phenomena occurring inside active volcanoes; however, their study and the comprehension of the processes leading to their formation are fundamental for a better understanding of the evolution of active volcanoes.

**Acknowledgments** This work was financially supported by INGV-Pisa and Dipartimento di Scienze della Terra, della Vita e dell' Ambiente of the University of Urbino (A. Renzulli). We are grateful to B. Scaillet for his comments and suggestions of an early version of the manuscript. We also would like to thank R.H. Grapes and an anonymous referee for their critical review of the article.

## References

- Abouchami W, Galer SJG, Koschinsky A (1999) Pb and Nd isotopes in NE Atlantic Fe-Mn crusts: proxies for trace metal paleosources and paleocean circulation. *Geochim Cosmochim Acta* 63:1489–1505. doi:10.1016/S0016-7037(99)00068-X
- Abratis M, Schmincke H-U, Hansteen T (2002) Composition and evolution of submarine volcanic rocks from the central and western Canary Islands. *Int J Earth Sci* 91:562–582. doi:10.1007/s00531-002-0286-7
- Acosta J, Uchupi E, Smith D, Munoz A, Herranz P, Palomo C, Llanes P, Ballesteros M, Group ZW (2003) Comparison of volcanic rifts on La Palma and El Hierro, Canary Islands and the Island of Hawaii. *Mar Geophys Res* 24:59–90. doi:10.1007/s11001-004-1162-6
- Archibald SM, Migdisov AA, Williams-Jones AE (2001) The stability of Au-chloride complexes in water vapor at elevated temperatures and pressures. *Geochim Cosmochim Acta* 65:4413–4423. doi:10.1016/S0016-7037(01)00730-X
- Avanzinelli R, Boari E, Conticelli S, Francalanci L, Guarnieri L, Perini G, Petrone CM, Tommasini S, Ulivi M (2005) High precision Sr, Nd, and Pb isotopic analyses using the new generation Thermal Ionisation Mass Spectrometer ThermoFinnigan Triton-Ti<sup>®</sup>. *Per Miner* 74:147–166
- Bowen NL (1928) *The evolution of the igneous rocks*. Princeton University Press, Princeton

- Bowen NL, Tuttle OF (1950) The system  $\text{NaAlSi}_3\text{O}_8\text{--KAlSi}_3\text{O}_8\text{--H}_2\text{O}$ . *J Geol* 58:489–511
- Carracedo JC, Badiola ER, Guillou H, De La Nuez J, Pérez Torrado FJ (2001) Geology and volcanology of La Palma and El Hierro, Western Canaries. *Estud Geologicos* 57:175–273
- Carracedo JC, Pérez Torrado F, Rodríguez González A, Soler V, Fernández Turiel JL, Troll VR, Wiesmaier S (2012) The 2011 submarine volcanic eruption in El Hierro (Canary Islands). *Geol Today* 28:53–58. doi:10.1111/j.1365-2451.2012.00827.x
- Clark BH, Peacor DR (1992) Pyrometamorphism and partial melting of shales during combustion metamorphism: mineralogical, textural, and chemical effects. *Contrib Mineral Petrol* 112:558–568. doi:10.1007/BF00310784
- Cole JM, Goldstein SL, deMenocal PB, Hemming SR, Grousset FE (2009) Contrasting compositions of Sahara dust of eastern Atlantic Ocean during the last deglaciation and African Humid Period. *Earth Plan Sci Lett* 278:257–266. doi:10.1016/j.epsl.2008.12.011
- Cosca MA, Essene EJ, Geissman JW, Simmons WB, Coates DA (1989) Pyrometamorphic rocks associated with naturally burned coal beds, Powder River Basin, Wyoming. *Am Min* 74:85–100
- Cousens BL, Spera FJ, Dobson PF (1993) Post-eruptive alteration of silicic ignimbrites and lavas, Gran Canaria, Canary Island: strontium, neodymium, lead and oxygen isotopic evidence. *Geochim Cosmochim Acta* 57:631–640. doi:10.1016/0016-7037(93)90374-6
- Day JMD, Pearson DG, Macpherson CG, Lowry D, Carracedo JC (2010) Evidence for distinct proportions of subducted oceanic crust and lithosphere in HIMU-type mantle beneath El Hierro and La Palma, Canary Islands. *Geochim Cosmochim Acta* 74:6565–6589. doi:10.1016/j.gca.2010.08.021
- Deer WA, Howie RA, Zussman J (1997a) Rock forming minerals, Volume 2B, double chain silicates, 2nd edn. The Geological Society, London
- Deer WA, Howie RA, Zussman J (1997b) Rock forming minerals, Volume 2A, single chain silicates, 2nd edn. The Geological Society, London
- Del Moro S, Renzulli A, Tribaudino M (2011) Pyrometamorphic processes at the magma-hydrothermal system interface of active volcanoes: evidence from buchite ejecta of Stromboli (Aeolian Islands, Italy). *J Petrol* 52:541–564. doi:10.1093/petrology/egq090
- Del Moro S, Renzulli A, Landi P, La Felice S, Rosi M (2013) Unusual lapilli tuff ejecta erupted at Stromboli during the 15 March 2007 explosion shed light on the nature and thermal state of rocks forming the crater system of the volcano. *J Volcanol Geotherm Res* 254:37–52. doi:10.1016/j.jvolgeores.2012.12.017
- Domínguez Cerdeña I, del Fresno C, Gomis Moreno A (2014) Seismicity patterns prior to the 2011 El Hierro eruption. *B Seismol Soc Am*. doi:10.1785/0120130200
- Fulignati P, Gioncada A, Sbrana A (1998) Geologic model of the magmatic–hydrothermal system of Vulcano (Aeolian islands, Italy). *Mineral Petrol* 62:195–222. doi:10.1007/BF01178029
- Fulignati P, Gioncada A, Sbrana A (1999) Rare-earth element (REE) behaviour in the alteration facies of the active magmatic - hydrothermal system of Vulcano (Aeolian Island, Italy). *J Volcanol Geotherm Res* 88:325–342. doi:10.1016/S0377-0273(98)00117-6
- Fuster JM (1993) Geochronología de la Isla de El Hierro (Islas Canarias). *Bol R Soc Esp Hist Nat (Sec Geol)* 88(1-4):85–97
- García A, Fernández-Ros A, Berrocoso M, Marrero JM, Prates G, De la Cruz-Reyna S, Ortiz R (2014) Magma displacements under insular volcanic fields, applications to eruption forecasting: El Hierro, Canary Island, 2011–2013. *Geophys J Int* 197:322–334. doi:10.1093/gji/ggt505
- Gee LL, Sack RO (1988) Experimental petrology of melilite nephelinites. *J Petrol* 29:1233–1255
- Geldmacher J, Hoernle K, Hanan BB, Blichert-Toft J, Hauff F, Gill JB, Schmincke H-U (2011) Hafnium isotopic variations in East Atlantic intraplate volcanism. *Contrib Mineral Petrol* 162:21–36. doi:10.1007/s00410-010-0580-5
- Glodny J, Grauert B (2009) Evolution of a hydrothermal fluid-rock interaction system as recorded by Sr isotopes: a case of study from the Schwarzwald, SW Germany. *Mineral Petrol* 95:163–178. doi:10.1007/s00710-008-0034-1
- Gorbatikov AV, Montesinos FG, Amoso J, Yu Stepanova M, Benavent M, Tsukanow AA (2013) New features in the subsurface structure model of El Hierro Island (Canaries) from low-frequency microseismic sounding: an insight into the 2011 seismo-volcanic crisis. *Surv Geophys* 34:463–489. doi:10.1007/s10712-013-9240-4
- Graham IJ, Grapes RH, Kifle K (1988) Buchitic metagreywacke xenoliths from Mount Ngauruhoe, Taupo volcanic zone, New Zealand. *J Volcanol Geotherm Res* 35:205–216. doi:10.1016/0377-0273(88)90017-0
- Grapes RH (1986) Melting and thermal reconstitution of pelitic xenoliths, Wehr volcano, East Eifel, Germany. *J Petrol* 27:343–396. doi:10.1093/petrology/27.2.343
- Grapes RH (2006) Pyrometamorphism. Springer, Berlin
- Guillou H, Carracedo JC, Pérez Torrado FJ, Badiola ER (1996) K–Ar ages and magnetic stratigraphy of a hotspot-induced, fast grown oceanic island: El Hierro, Canary Islands. *J Volcanol Geotherm Res* 73:141–155. doi:10.1016/0377-0273(96)00021-2
- Gurenko AA, Hoernle KA, Hauff F, Schmincke H-U, Han D, Miura YN, Kaneoka I (2006) Major, trace element and Nd–Sr–Pb–O–He–Ar isotope signatures of shield stage lavas from the central and western Canary Islands: insights into mantle and crustal processes. *Chem Geol* 233:75–112. doi:10.1016/j.chemgeo.2006.02.016
- Gurenko AA, Sobolev AV, Hoernle KA, Hauff F, Schmincke H-U (2009) Enriched, HIMU-type peridotite and depleted recycled pyroxenite in the Canary plume: a mixed-up mantle. *Earth Planet Sci Lett* 277:514–524
- Gysi AP, Williams-Jones AE (2013) Hydrothermal mobilization of pegmatite-hosted REE and Zr at Strange Lake, Canada: a reaction path model. *Geochim Cosmochim Acta* 122:324–352. doi:10.1016/j.gca.2013.08.031
- Haas JR, Shock EL, Sassani DC (1995) Rare earth elements in hydrothermal systems: estimates of standard partial molal thermodynamic properties of aqueous complexes of the rare earth elements at high pressures and temperatures. *Geochim Cosmochim Acta* 59:4329–4350. doi:10.1016/0016-7037(95)00314-P
- Harlov D, Renzulli A, Ridolfi F (2006) Iron-bearing chlor-fluorapatites in crustal xenoliths from the Stromboli volcano (Aeolian Islands, southern Italy): an indicator of fluid processes during contact metamorphism. *Eur J Mineral* 18:233–241. doi:10.1127/0935-1221/2006/0018-0233
- Hoernle K (1998) Geochemistry of Jurassic ocean crust beneath Gran Canaria (Canary Islands): implications for crustal recycling and assimilation. *J Petrol* 39:859–880. doi:10.1093/petroj/39.5.859
- Jugo PJ (2009) Sulfur content at sulfide saturation in oxidized magmas. *Geology* 37:415–418. doi:10.1130/G25527A.1
- Kitchen D (1984) Pyrometamorphism and the contamination of basaltic magma at Tieveragh. *Co Antrim J Geol Soc Lond* 141:733–745. doi:10.1144/gsjgs.141.4.0733
- Klügel A, Hansteen TH, van den Bogaard P, Strauss H, Hauff F (2011) Holocene fluid venting at an extinct Cretaceous seamount, Canary archipelago. *Geology* 39:855–858. doi:10.1130/G32006.1
- Krastel S, Schmincke H-U (2002) Crustal structure of northern Gran Canaria, Canary Islands, deduced from active seismic tomography. *J Volcanol Geotherm Res* 115:153–177. doi:10.1016/S0377-0273(01)00313-4
- Kuznetsov AB, Semikhatov MA, Gorokhov IM (2012) The Sr isotope composition of the world ocean, marginal inland seas: implication for the Sr isotope stratigraphy. *Stratigr Geol Correl* 20:501–515. doi:10.1134/S0869593812060044

- Le Maitre RW, Bateman P, Dudek A, Keller J, Lameyre Le Bas MJ, Sabine PA, Schmid R, Sorensen H, Streckeisen A, Woolley AR, Zanettin B (1989) A classification of igneous rocks and glossary of terms. Blackwell, Oxford
- Leake BE, Woolley AR, Arps CES, Birch WD, Gilbert MC, Grice JD, Hawthorne FC, Kato A, Kisch JJ, Krivovichev VG, Linthout K, Laird J, Mandarino J, Maresch WV, Nickel EH, Schumaker JC, Smith DC, Stephenson NCN, Ungaretti L, Whittaker EJW, Youzhi G (1997) Nomenclature of amphiboles: report of the subcommittee on amphiboles of the International Mineralogical Association Commission on New Minerals and Mineral Names. *Can Mineral* 35:219–246
- Longpré MA, Klügel A, Diehl A, Stix J (2014) Mixing in mantle reservoirs prior to and during the 2011–2012 eruption at El Hierro, Canary Island. *Geology* 42:315–318. doi:10.1130/G35165.1
- López C et al (2012) Monitoring the unrest of El Hierro (Canary Islands) before the onset of the 2011 submarine eruption. *Geophys Res Lett* 39, L13303. doi:10.1029/2012GL051846
- Manzies M, Seyfried WE (1979) Basalt-seawater interaction trace element and strontium isotopic variations in experimentally altered glassy basalt. *Earth Planet Sci Lett* 44:463–472. doi:10.1016/0012-821X(79)90084-0
- Martí J, Castro A, Rodríguez C, Costa F, Carrasquilla S, Pedreira R, Bolos X (2013a) Correlation of magma evolution and geophysical monitoring during the 2011–2012 El Hierro (Canary Islands) submarine eruption. *J Petrol* 54:1349–1373. doi:10.1093/petrology/egt014
- Martí J, Pínel V, López C, Geyer A, Abella R, Tárraga M, Blanco MJ, Castro A, Rodríguez C (2013b) Causes and mechanisms of the 2011–2012 El Hierro (Canary Islands) submarine eruption. *J Geophys Res: Solid Earth* 118:823–839. doi:10.1002/jgrb.50087
- Meletlidis S, Di Roberto A, Pompilio M, Bertagnini A, Iribarren I, Felpeto A, Torres PA, D’Orlando C (2012) Xenopumices from the 2011–2012 submarine eruption of El Hierro (Canary Islands, Spain): Constraints on the plumbing system and magma ascent. *Geophys Res Lett* 39. doi: 10.1029/2012GL052675
- Migdisov AA, Williams-Jones AE, Wagner T (2009) An experimental study of the solubility and speciation of the Rare Earth Elements (III) in fluoride- and chloride- bearing aqueous solutions at temperatures up to 300 °C. *Geochim Cosmochim Acta* 73:7087–7109. doi:10.1016/j.gca.2009.08.023
- Nakamura N (1974) Determination of REE, Ba, Fe, Mg, Na and K in Carbonaceous and ordinary chondrites. *Geochim Cosmochim Acta* 38:757–775. doi:10.1016/0016-7037(74)90149-5
- Neumann ER, Sørensen V, Simonsen SL, Johnsen K (2000) Gabbroic xenoliths from La Palma, Tenerife and Lanzarote, Canary Islands: evidence for reactions between Canary Islands melts and old oceanic crust. *J Volcanol Geother Res* 103:313–342. doi:10.1016/S0377-0273(00)00229-8
- Nobre Silva IG, Weis D, Scoates JS (2010) Effects of acid leaching on the Sr-Nd-Hf isotopic compositions of ocean island basalts. *Geochim Geophys Geosyst* 11. doi:10.1029/2010GC003176
- Ovchinnikova GV, Belyatskii BV, Vasil’eva IM, Levskii LK, Grachev AF, Arana V, Mithavala J (1995) Sr–Nd–Pb isotope characteristics of the mantle sources of basalts from the Canary Islands. *Petrology* 3:172–182
- Pedrazzi D, Becerril L, Martí J, Meletlidis S, Galindo I (2014) Explosive felsic volcanism on El Hierro (Canary Islands). *Bull Volcanol* 76:1–19
- Pellicer MJ (1979) Geochemical study of volcanism on Hierro, Canary Islands. *Estud Geologicos* 35:15–29
- Pellicer MJ (1980) Comportamiento de los elementos menores y modelo de fusión parcial para las lavas de la isla de Hierro, (A. Canario). *Bol R Soc Esp Hist Nat* 78:175–189
- Pirajno F (2009) Hydrothermal processes and mineral systems. Springer, Perth
- Praegel NO, Holm PM (2006) Lithospheric contributions to high-MgO basanites from the Cumbre Vieja volcano, La Palma, Canary Islands and evidence for temporal variation in plume influence. *J Volcanol Geotherm Res* 149:213–239. doi:10.1016/j.jvolgeores.2005.07.019
- Preston RJ, Dempster TJ, Bell BR, Rogers G (1999) The petrology of mullite-bearing peraluminous xenoliths: implications for contamination processes in basaltic magmas. *J Petrol* 40:549–573. doi:10.1093/petroj/40.4.549
- Putirka KD (2008) Thermometers and barometers for volcanic systems. *Rev Min Geochem* 69:61–120. doi:10.2138/rmg.2008.69.3
- Rathossi C, Pontikes Y (2010) Effect of firing temperature and atmosphere on ceramics made of NW Peloponnese clay sediments. Part I: Reaction paths, crystalline phases, microstructure and colour. *J Eur Ceram Soc* 30:1841–1851. doi:10.1016/j.jeurceramsoc.2010.02.003
- Renzulli A, Tribaudino M, Salvioli-Mariani E, Serri G, Holm PM (2003) Cordierite-anorthoclase hornfels xenoliths in Stromboli lavas (Aeolian Islands, Sicily) an example of a fast cooled contact aureole. *Eur J Mineral* 15:665–679. doi:10.1127/0935-1221/2003/0015-0665
- Ridolfi F, Renzulli A, Puerini M (2010) Stability and chemical equilibrium of amphibole in calc-alkaline magmas: an overview, new thermobarometric formulations and application to subduction-related volcanoes. *Contrib Mineral Petrol* 160:45–66
- Rivera J, Lastras G, Canals M, Acosta J, Arrese B, Herrida N, Micallef A, Tello O, Amblas D (2013) Construction of an oceanic island: insights from the El Hierro (Canary Islands). *Geology*. doi:10.1130/G33863.1
- Robb L (2005) Introduction to ore-forming processes. Blackwell Publishing
- Rodriguez-Losada JA, Eff-Darwich A, Hernandez LE, Viñas R, Pérez N, Hernandez P, Melián G, Martínez-Frías J, Carmen Romero-Ruiz M, Coello-Bravo JJ (2014) Petrological and geochemical highlights in the floating fragments of the October 2011 submarine eruption offshore El Hierro (Canary Islands): Relevance of submarine hydrothermal processes. *J Afric Earth Sci*. doi:10.1016/j.jafrearsci.2014.11.005
- Salvi S, Williams-Jones AE (1996) The role of hydrothermal processes in concentrating high-field strength elements in the Strange Lake peralkaline complex, northeastern Canada. *Geochim Cosmochim Acta* 60:1917–1932. doi:10.1016/0016-7037(96)00071-3
- Salvi S, Fontan F, Monchoux P, Williams-Jones AE, Moine B (2000) Hydrothermal mobilization of high field strength elements in alkaline igneous systems: Evidence from the Tamazeght complex (Morocco). *Econ Geol* 95:559–576. doi:10.2113/95.3.559
- Salvioli-Mariani E, Renzulli A, Serri G, Holm PM, Toscani L (2005) Glass-bearing crustal xenoliths (buchites) erupted during recent activity of Stromboli (Aeolian Islands). *Lithos* 81:255–277. doi:10.1016/j.lithos.2004.12.001
- Sato H (1975) Diffusion coronas around quartz xenocrysts in andesite and basalt from the Tertiary Volcanic Region in northeastern Shikoku, Japan. *Contrib Mineral Petrol* 50:49–64. doi:10.1007/BF00385221
- Schmincke H-U, Sumita M (1998) Volcanic evolution of Gran Canaria reconstructed from apron sediments: synthesis of VICAP project drilling. In: Weaver Philip PE, Schmincke Hans U, Firth John V, Duffield W (eds) Proceedings ocean drilling program, Scientific Results, vol 157, pp 443–469
- Schomburg J (1991) Thermal reactions of clay minerals: their significance as “archaeological thermometers” in incipient potteries. *App Clay Sci* 6:215–220
- Searle EJ (1962) Xenoliths and metamorphosed rocks associated with the Auckland basalts. *N Z J Geol Geophys* 5:384–403. doi:10.1080/00288306.1962.10420095
- Sigmarrsson O, Laporte D, Carpentier M, Devouard B, Devidal JL, Martí J (2013) Formation of U-depleted rhyolite from basanite at El

- Hierro, Canary Islands. *Contrib Mineral Petrol* 165:601–622. doi:10.1007/s00410-012-0826-5
- Sokol E, Volcova N, Lepezin G (1998) Mineralogy of pyrometamorphic rocks associated with naturally burned coal-bearing spoil-heaps of the Chelyabinsk coal basin, Russia. *Eur J Mineral* 10:1003–1014. doi:10.1127/ejm/10/5/1003#\_blank
- Spooner ETC, Chapman HJ, Smewing JD (1977) Strontium isotopic contamination and oxidation during ocean floor hydrothermal metamorphism of the ophiolitic rocks of the Troodos Massif, Cyprus. *Geochim Cosmochim Acta* 41:873–890. doi:10.1016/0016-7037(77)90147-8
- Staudigel H, Schmincke HU (1984) The Pliocene seamount series of La Palma/Canary Islands. *J Geophys Res Solid Earth* 89:11195–11215. doi:10.1029/JB089iB13p11195
- Stroncik NA, Klügel A, Hansteen TH (2009) The magmatic plumbing system beneath El Hierro (Canary Islands): constraints from phenocrysts and naturally quenched basaltic glasses in submarine rocks. *Contrib Mineral Petrol* 157:593–607. doi:10.1007/s00410-008-0354-5
- Thompson RN, Morrison MA, Hendry GL, Parry SJ (1984) An assessment of the relative roles of crust and mantle in magma genesis: an elemental approach. *Philos Trans R Soc Lond A3*(10):549–590. doi:10.1098/rsta.1984.0008
- Todt W, Cliff RA, Hanser A, Hofmann AW (1993) Re-calibration of NBS lead standards using a <sup>202</sup>Pb-<sup>205</sup>Pb double spike. *Terra Abstracts supplement 1 to Terra Nov.* 5 (1): 396
- Toplis MJ (2005) The thermodynamics of iron and magnesium partitioning between olivine and liquid: criteria for assessing and predicting equilibrium in natural and experimental systems. *Contrib Mineral Petrol* 149:22–39. doi:10.1007/s00410-004-0629-4
- Troll VR, Schmincke HU (2002) Magma mixing and crustal recycling recorded in ternary feldspar from compositionally zoned peralkaline ignimbrite 'A', Gran Canaria, Canary Islands. *J Petrol* 43:243–270. doi:10.1093/petrology/43.2.243
- Troll VR, Klügel A, Longpré MA et al (2012) Floating stones off El Hierro, Canary Islands: xenoliths of pre-island sedimentary origin in the early products of the October 2011 eruption. *Solid Earth* 3:97–110. doi:10.5194/se-3-97-2012
- Verma SP (1992) Seawater alteration effects on REE, K, Rb, Cs, Sr, U, Th, Pb and Sr-Nd-Pb isotope systematics of Mid-Ocean Ridge Basalt. *Geochem J* 26:159–177
- Waldron KA, Droop GTR, Champness PE (1993) Kinetic controls on the formation of metastable phases during experimentally induced breakdown of chlorite. *Mineral Mag* 57:141–156. doi:10.1180/minmag.1993.057.386.14
- Wohletz K, Heiken G (1992) *Volcanology and Geothermal energy*. University of California Press, Berkeley
- Wood SA (1990) The aqueous geochemistry of the rare earth elements and yttrium: 2. Theoretical prediction of speciation in hydrothermal solutions to 350°C at saturation water vapor pressure. *Chem Geol* 88:99–125. doi:10.1016/0009-2541(90)90106-H
- Wood CP (1994) Mineralogy at the magma-hydrothermal system interface in andesite volcanoes, New Zealand. *Geology* 22:75–78
- Wood CP, Browne PRL (1996) Chlorine-rich pyrometamorphic magma at White Island volcano, New Zealand. *J Volcanol Geotherm Res* 72:21–35. doi:10.1016/0377-0273(95)00085-2

*Annex 6.4*

*New insight into the 2011-2012 unrest and eruption of El Hierro Island (Canary Islands) based on integrated geophysical, geodetical and petrological data.*

*S. Meletlidis, A. Di Roberto, I. Domínguez Cerdeña, M. Pompilio, L. García-Cañada, A. Bertagnini, M. A. Benito-Saz, P. Del Carlo, S. Sainz-Maza Aparicio.*

# New insight into the 2011-2012 unrest and eruption of El Hierro Island (Canary Islands) based on integrated geophysical, geodetical and petrological data

Stavros Meletlidis<sup>1</sup>, Alessio Di Roberto<sup>2,\*</sup>, Itahiza Domínguez Cerdeña<sup>1</sup>, Massimo Pompilio<sup>2</sup>, Laura García-Cañada<sup>3</sup>, Antonella Bertagnini<sup>2</sup>, Maria Angeles Benito-Saz<sup>3</sup>, Paola Del Carlo<sup>2</sup>, Sergio Sainz-Maza Aparicio<sup>3</sup>

<sup>1</sup> Centro Geofísico de Canarias, Instituto Geográfico Nacional, Santa Cruz de Tenerife, Spain

<sup>2</sup> Istituto Nazionale di Geofisica e Vulcanologia, Sezione di Pisa, Pisa, Italy

<sup>3</sup> Observatorio Geofísico Central, Instituto Geográfico Nacional, Madrid, Spain

## Article history

Received March 2, 2015; accepted September 25, 2015.

## Subject classification:

Volcano seismology, Mineralogy and petrology, Geological and geophysical evidences of deep processes, Rock geochemistry, Measurements and monitoring, El Hierro, Magma ascent, Volcano Monitoring.

## ABSTRACT

A shallow water eruption started on October 10, 2011, ~2 km south off the coast of El Hierro (Canary Islands, Spain). The eruption lasted about five months and ended by early March 2012. Three months of unrest preceded this event with more than 10,000 localized earthquakes and up to 6 cm of vertical ground deformation. In the Canary Islands, this is the first eruption to be monitored by the network of Instituto Geográfico Nacional (IGN) since the very beginning of the seismic unrest. This provided unprecedented time series that include geophysical (seismic and gravimetric), geodetic, geochemical and petrological data. In this work we discuss and interpret these data in order to describe the mechanisms of 2011-2012 El Hierro eruption, including ascent from magmatic source, a crustal storage, and the final intrusion in the South Rift before the eruption. Our research approach provides a multidisciplinary view of the dynamics of magma ascent and improves previous interpretations formulated during or shortly after the end of the eruption. According to our results, a major intrusion occurred beneath and around preexisting high-density magmatic bodies, localized at depth below the central part of the island. After a failed attempt to reach the surface through a low fractured zone located below the central-northern part of the island, the ascending magma finally found its way nearby the El Hierro South Rift Zone and erupted off the coast of La Restinga village, 350 m below sea level. The eruption was fed by the ascent of an important volume of material from the upper mantle that was emplaced near the crust-mantle boundary and progressively tapped during the eruption.

## 1. Introduction

The shallow submarine eruption that took place between October 10, 2011, and March 5, 2012, off the

coast of La Restinga village in the south of El Hierro puts an end to the non-eruptive period of the Canary Islands that had lasted over 40 years, since the 1971 eruption in La Palma Island.

The lack of information about the eruptive activity of El Hierro Island, and more generally on shallow water volcanic eruptions, led the scientific community to invest a great effort on the meticulous registration of geophysical and geodetical time series for this unprecedented eruption. This was possible thanks to the monitoring network of Instituto Geográfico Nacional (IGN) that was present on the island before the onset of eruptive unrest and that was promptly enhanced during the crisis. Notwithstanding this prompt and large monitoring effort, uncertainties derived from incomplete scientific knowledge and limited data described for shallow water eruptions have resulted in difficulties for managing the eruptive crisis and a severe impact on the island's economy. Recently some models have been proposed to describe the dynamics of magma intrusion and ascent driving to the 2011-2012 eruption [see Martí et al. 2013a, Martí et al. 2013b, García et al. 2014, Longpré et al. 2014]. These models are based on the analysis of seismic data registered in the IGN seismic catalogue ([www.ign.es](http://www.ign.es)), ground deformation detected by GPS network and on the petrological study of erupted products. With only minor differences between them, these researches propose that the eruption was driven by the ascent of a mantle-derived magma [Martí et al. 2013a,

Martí et al. 2013b, Longpré et al. 2014] initially accumulated in a reservoir located at a depth of about 20-25 km below the El Hierro Island and possibly originated by the mixing and hybridization of two magmas from distinct mantle reservoirs [Longpré et al. 2014]. This magma would have ascended aseismically and progressively accumulated in the lower crust (during about two months), reaching a level of stagnation at 10-15 km. After a ~15 km-long subhorizontal migration toward the SE, the magma would have finally ascended to the eruption site, off the coast of La Restinga village [Martí et al. 2013a, Martí et al. 2013b, García et al. 2014, Longpré et al. 2014].

In this paper we combine the temporal analysis of seismic events, ground deformation patterns and gravity data with a detailed mineralogical and geochemical analysis of products systematically sampled during the eruption and with the thermodynamical modeling of magma differentiation. We use the hypocentral positions recently relocated by Domínguez Cerdeña et al. [2014]. This research approach allows to give a multidisciplinary view of the dynamics of magma ascent and improves previous interpretations formulated during or shortly after the end of the eruption. According to our model the eruption was fed by a single batch of

mantle-derived magma progressively tapped at variable rates from October 2011 to March 2012. Magma feeding the eruption experienced a stepwise migration between three main magmatic environments, including a deep reservoir, a crustal magma reservoir and a final shallow conduit and vent zone.

## 2. Geological background

El Hierro, located at the south-western end of the Canary Islands (Figure 1), is the emergent summit (~1500 m) of a much wider volcanic shield (280 km<sup>2</sup>), which rises from a water depth of 3800-4000 m. It is the youngest island of the Canary Archipelago, with the oldest subaerial rocks cropping out on the island that have been dated at 1.12 Ma [Guillou et al. 1996]. The subaerial part of El Hierro is formed by two main volcanic edifices, the Tiñor volcano on the north-east flank of the island, built approximately between 0.88-1.12 Ma and El Golfo volcano in the north-west flank, built between 550-130 ka. Products belonging to Tiñor volcano

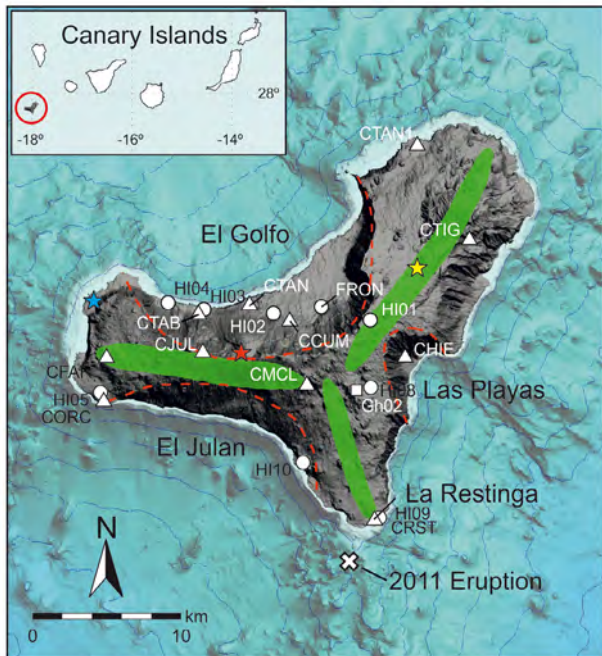


**Figure 1.** Map of El Hierro Island with highlighted the main morphological features. Green shaded zones: rift lines. Red dashed lines: Landslides scars. Stars indicate the most recent eruptions on the island; yellow star: Las Chamuscas, red star: Tanganasoga and blue star: Lomo Negro. White cross: location of the vent of the 2011-2012 eruption. In map are also highlighted the position of instruments of multiparametric monitoring network that was deployed on the island by Instituto Geográfico Nacional: triangles - Seismic stations; circles - permanent GPS stations; squares - permanent gravimetric station.

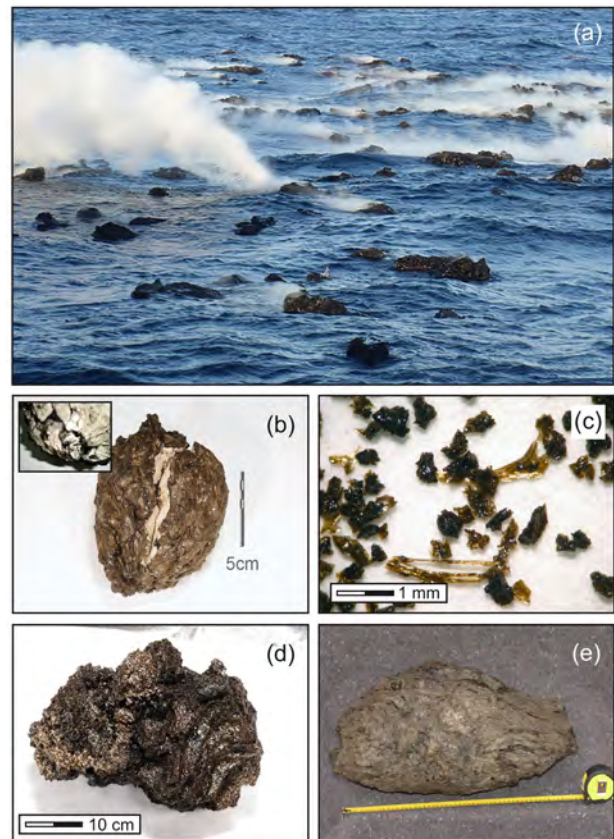


**Figure 2.** Images of volcanic products emitted during the 2011-2012 eruption. (a) Hot scoriaceous blocks and "lava balloons" floating on the sea surface during the eruption; (b) "coconut-like" bomb consisting of an outer basanite crust embedding a pumiceous xenolith [Troll et al. 2011, Meletlidis et al. 2012, Sigmarsson et al. 2012, Del Moro et al. 2015]; (c) example of the juvenile ash and fine lapilli sampled in water column on November 5, 2011, and February 12, 2012; (d) floating lava block erupted during the first days of the eruption; (e) elliptical-shaped "lava balloon".

mainly consist of picritic to hawaiitic-tephritic massive lavas whereas El Golfo volcano is characterized by nephelinitic to trachytic composition [Carracedo et al. 2001]. These two main edifices are separated by the gravitational collapse of the Tiñor volcano occurred at ca. 0.88 Ma [Guillou et al. 1996, Carracedo et al. 2001, Münn and Klügel 2006]. The last eruptive stage, known as Quaternary rift volcanism, has been very active since 134 ka, and it is characterized by alkali picrites, basanites and tephrites that can be observed in exceptional detail all along the three rifts (NE-, W- and S-Ridge) of the island [Guillou et al. 1996, Acosta et al. 2003]. This volcanic activity has produced a large number of cones in the emerged part of El Hierro Island and an even greater number on its submarine flanks as shown by recent investigations [Rivera et al. 2013]

The most recent subaerial eruption, Volcán de Lomo Negro occurred in the western part of the island, outside of El Golfo landslide area (Figure 1), possibly between 115 BC and 1602 AD [Villasante-Marcos and Pavón-Carrasco 2014]. More recently, in 1793 AD a seismic crisis occurred at El Hierro and was likely related to an event of magma intrusion at depth or to a submarine eruption at the southern off-shore ridge of the island [Villasante-Marcos and Pavón-Carrasco 2014].

### 3. The 2011-2012 unrest and eruption

During the second fortnight of July 2011, the seismic stations of IGN started to register anomalous seismicity (up to 200 events *per* day) with hypocenters preliminarily located in the area of El Golfo and at depths of 8-12 km (IGN Seismic Bulletin). In the following two months, there was only a minor migration of the seismic hypocenters accompanied by ground deformation, diffuse emission of CO<sub>2</sub>, anomalous values of the magnetic field and Rn<sup>222</sup> and H<sub>2</sub>S efflux [Lopez et al. 2012, Pérez et al. 2012]. In the last days of September seismicity clearly migrated to the south and finally the eruption started on October 10, 2011, after at least 10,000 localized seismic events and a maximum vertical deformation of up to 6 cm. The onset of the eruption was accompanied by harmonic volcanic tremor recorded by the seismic network of IGN in the western Canaries and 48 hours later by the appearance of a plume of stained and discolored water at ~2 km south the coast of La Restinga village (27°37.18 - 17°59.58 ; Figure 1) off the southern tip of the island. Repeated multibeam surveys revealed that the eruption occurred in a gully aligned in a NE-SW direction, almost perpendicular to the South Rift and at water depths between ~363 and 89 m, with several vents that functioned simultaneously [Rivera et al. 2013]. Data document repeated cycles of collapse and subsequent

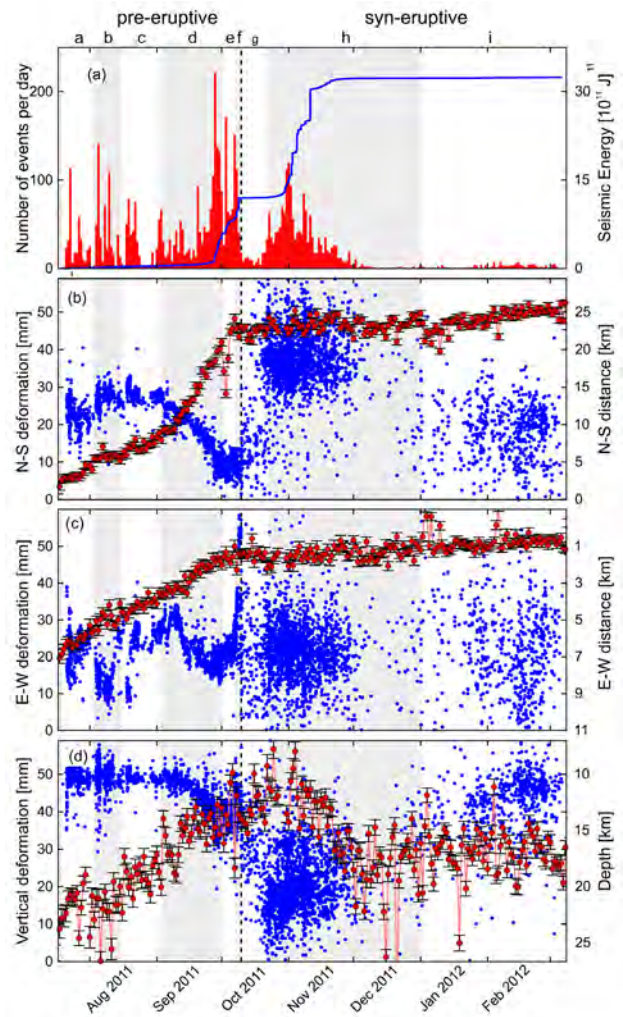


**Figure 3.** (a) Temporal evolution of the daily number of earthquakes with magnitude >1.5 (red histograms) and the accumulated energy curve (blue line). (b-d) Blue dots: temporal evolution of the (b) North-South and (c) East-West distances (km) to the vent and of the (d) depth (km) of the earthquakes after relocation of Domínguez Cerdeña et al. [2014]; red dots (with the axis error) N-S, E-W and vertical components of ground deformation recorded at GPS station FRON (the only station that was active since the very onset of the unrest) during the pre-eruptive and syn-eruptive phases of the 2011-2012 El Hierro eruption. Black dashed line indicates the onset of the eruption. Shaded and white alternating areas indicate the nine phases in which authors divided the pre-eruptive unrest and eruptive activity.

regrowth of the cone with a total accumulated volume in the order of  $329 \times 10^6$  NDRE m<sup>3</sup> [Rivera et al. 2013]. The eruption produced a variety of volcanic material; some of the pyroclastic products were floating and therefore it was possible to sample them extensively on the sea surface during the entire duration of the eruption (Figure 2). First massive emission of volcanic materials occurred on October 15, 2011 even though small fragments (<5 cm) had been observed floating since October 12, 2011. Products included anomalous “coconut-like” bombs (Figure 2b), consisting of a vesicular crust with bulk basanite composition enveloping a pumiceous xenolith with trachytic to rhyolitic compo-

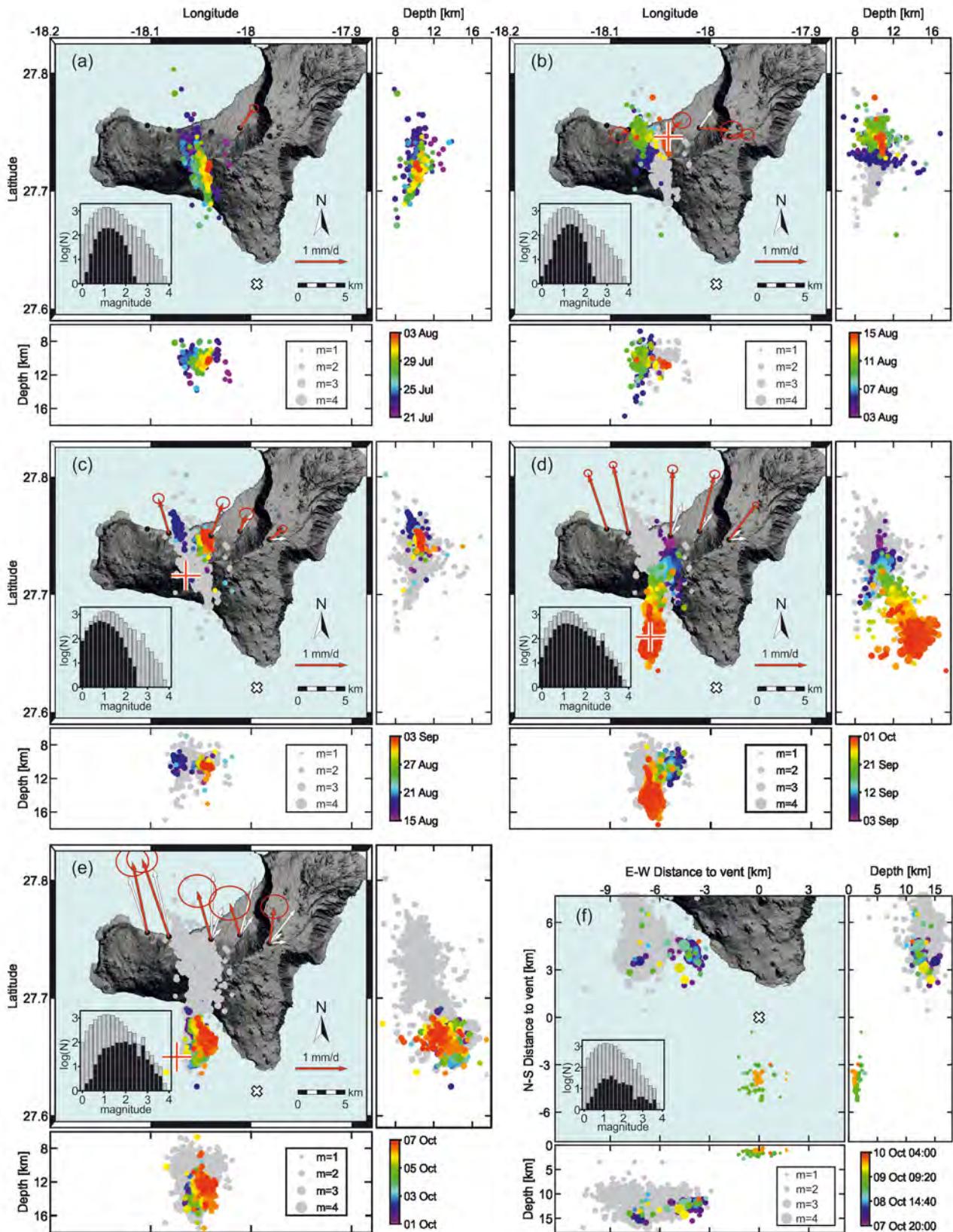


**Figure 4.** Temporal evolution of the latitude, longitude and depth (km) of the earthquakes with magnitude  $>1.5$  (time scale of events is reported in the color bar and in grey are reported the earthquakes occurred during the previous phases) along with the evolution of the horizontal deformation registered by GPS stations (red arrow for the period in analysis and white arrow for the previous periods) during the pre-eruptive phase of 2011-2012 eruption of El Hierro Island. In grey are reported the earthquakes occurred in the previous phases. Red cross indicates the position of deformation source according to Mogi model and white X marks the vent of 2011-2012 eruption. Inner plots give the histograms of the number of located events *versus* magnitude for the each phase (black) and for the full period (grey shaded). Seismic data are after relocation of Domínguez Cerdeña et al. [2014].

sition [Troll et al. 2011, Meletlidis et al. 2012, Sigmarsson et al. 2012, Del Moro et al. 2015]. This type of products was emitted exclusively during the first days of the eruption and the main volume was produced on October 15, 2011. In late October and in the first days of November the eruption consisted of intense degassing episodes producing strong bubbling (up to 15 m-high bubble emerged on the sea surface) accompanied with the emission of abundant ash and floating scoriaceous fragments (Figure 2c-d) [Santana-Casiano et al. 2013]. On November 27, and for the next three months, lava balloons were observed while floating and degassing on the sea surface (Figure 2a). These are unusual products consisting of an internal gas-filled cavity surrounded by a few centimeters-thick crust of quenched vesicular lava (Figure 2e). In El Hierro they range in size between 30 and 200 cm. The emission of lava balloons continued until February 23, 2012. The eruption lasted for  $\sim 5$  months and was officially declared ended on March 5, 2012, with the top of the new submarine cone reaching the depth of 89 m b.s.l. [Rivera et al. 2013].

#### 4. Methods and materials

Geophysical and geodetical signals acquisition methods and processing techniques as well as methods for the sampling and study of erupted products are reported in the Supplementary materials.

#### 5. Results

##### 5.1. Time variation of geophysical signals

The analysis of seismic activity, gravity changes and ground deformation allowed to distinguish six pre-eruptive and three syn-eruptive phases during the unrest and the following eruption (Figures 3-6).

##### 5.1.1. Pre-eruptive

*Phase A; July 21, 2011 - August 3, 2011* (Figure 4a). The first seismic swarm was recorded on July 21, 2011 and was characterized by low-energy earthquakes located at depth of 8-14 km beneath the south-central sector of the island. During this phase the seismic activity suffered a  $\sim 3$  km, short-term horizontal migration at depths of 10-12 km and toward the north. This occurred

through repeated, low-energy and intermittent swarms (Figure 3a). Since 7 July, 2011, and for the whole period, the only GPS station operating on the island (FRON) registered a ground deformation vector directed to the NE (red arrow in Figure 4a) [López et al. 2012].

*Phase B; August 3, 2011 - August 15, 2011* (Figure 4b). Low-energy seismic activity registered in the previous phase continued with hypocenters located at 9-10 km. Earthquake swarms were again intermittent and separated by periods of relative repose (Figure 3a). GPS network registered a radial distribution of ground deformation; in fact, HI01, HI02 and FRON stations, located in the central part of the island, recorded ground displacements towards E and NE whereas HI03 station, located in the western sector of the island, registered a movement towards W.

Calculation of Mogi [1958] source parameters indicated that the deformation center (red/white cross) was located beneath the central part of the island at depth of  $\sim 5$  km. The volume was estimated in the order of  $10 \times 10^6 \text{ m}^3$  (Table 1).

*Phase C; August 15, 2011 - September 3, 2011* (Figure 4c). In this period the second highest b-value ( $> 2$ ) [Gutenberg and Richter 1954] for the whole seismic unrest was achieved, as reported by Ibáñez et al. [2012] and Martí et al. [2013a, 2013b]. The earthquakes were clustered mainly at the margins of the area previously affected by the seismic activity and were located at depths shallower than 12 km (Figure 4c). The HI03 and HI02 GPS stations showed a strong increase in the ground deformation and a change in the vector direction towards NNW and NNE, respectively (Figure 4c). The source of deformation was determined to lay  $\sim 5$  km beneath the center of the island and its volume was estimated in ca.  $30 \times 10^6 \text{ m}^3$  (Table 1).

*Phase D; September 3, 2011 - October 1, 2011* (Figure 4d). In this period, the seismic events were initially located at depths of 10-12 km, on the eastern margin of the area previously affected by seismic activity. On late September, after a brief period of relatively low seismic activity, the number and magnitude of seismic events resumed, and hypocenter locations progressively migrated south and deepened at 12-16 km. All the GPS stations recorded strong acceleration in the ground de-

Period	Longitude	Latitude	Depth (km)	Volume ( $\text{m}^3$ )
August 3, 2011 - August 15, 2011	-18,042	27,746	4.9	$10 \times 10^6$
August 15, 2011 - September 3, 2011	-18,065	27,716	4.9	$30 \times 10^6$
September 3, 2011 - October 1, 2011	-18,06	27,664	3.8	$160 \times 10^6$
October 1, 2011 - October 7, 2011	-18,074	27,65	5.0	$50 \times 10^6$

**Table 1.** Position (latitude, longitude and depth) of deformation sources and volume calculated according to Mogi [1958] model.

Month/day of emission	October	November	December	January	February
1		S	LB	LB	LB
2		S			LB
3		S		LB	
4		S	LB	LB*	
5		D/Ash*			
6		D/Ash*	LB*	LB	LB
7			LB	LB	
8		D		LB*	LB
9					
10			LB		
11			LB		
12					Ash*
13					
14		LB*	LB		
15	Xen*				
16		LB*			
17					
18				LB*	
19		LB		LB*	
20				LB	
21				LB*	
22				LB	
23					LB
24					
25				LB	
26		LB		LB	
27		LB*		LB*	
28				LB*	
29	S			LB	
30			LB	LB*	
31	S*		LB	LB	

**Table 2.** Calendar with the days of emission and sampling of volcanic ash (in the water column), floating scoria and lava balloons. The days of intense degassing are included as well. Xen = xenopumice; Ash = volcanic ash in water column; S = scoriaceous blocks; D = days with intense degassing; LB = lava balloons. Asterisks indicate days when sampling of products was possible.

formation with vectors showing a radial pattern (Figure 4d). The deformation center moved further toward the south, following the migration path of hypocenters and was determined to lay off the coast of El Julan depression at depth of  $\sim 3.8$  km, approximately 1 km shallower than in the previous phase (Table 1). The volume was calculated in  $160 \times 10^6 \text{ m}^3$ , which is the highest estimated value for the entire eruption (Table 1).

*Phase E; October 1, 2011 - October 7, 2011* (Figure 4e). Seismic events drastically increased in magnitude and clearly migrated in southeast direction and at depths of 10-11 km. During this phase more than 50% of the total seismic energy of the unrest phase was released (Figure 3a). The direction of deformation vectors changed and almost all the stations registered vectors directed to-

wards NNW. The deformation center was calculated to lay still offshore the coast of El Julan, at depth of  $\sim 5$  km and  $\sim 1$  km deeper than in the previous phase, with an estimated volume in the order of  $50 \times 10^6 \text{ m}^3$  (Table 1).

From 22:24 UTC on October 7 to  $\sim 05:00$  UTC, on October 8, a sequence of anomalies in the gravimeter sensors were registered including: a) an initial small increment in the gravity value of  $3 \mu\text{Gal}$ , b) a very strong movement of the ground lasting for at least 30 minutes and followed by c) continuous tilting of the sensor (Figure 5).

*Phase F; October 7, 2011 - October 10, 2011* (Figure 4f). After  $\sim 12$  hours of relative seismic silence, on October 8, 2011, at 20:34 UTC a seismic event with  $M_L=4.3$  was recorded off the SW coast of the island at a depth

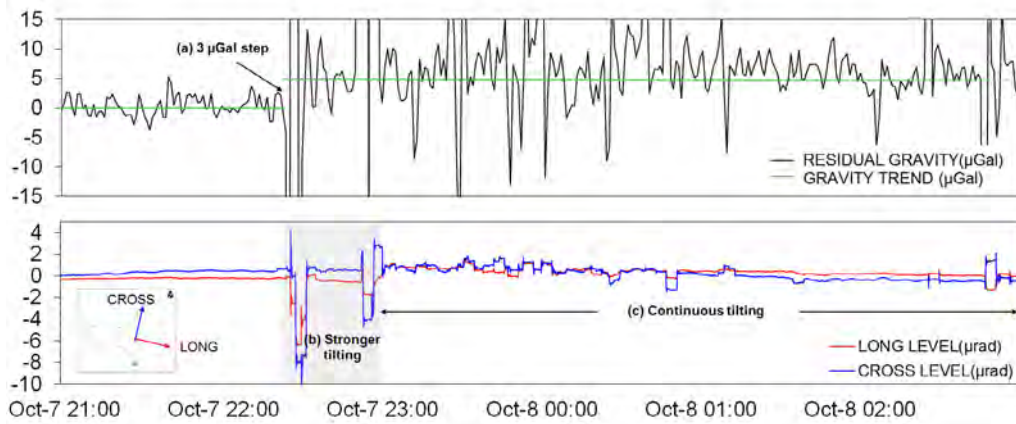


**Figure 5.** (a) Residual gravity record ( $\mu\text{Gal}$ ) filtered at 1 minute and (b) long and cross level values ( $\mu\text{rad}$ ) in the period between the night of October 7, and the early morning of October 8, 2011. The inset in the lower part of the plot shows, the cross and long directions of the two levels within the gravimeter.

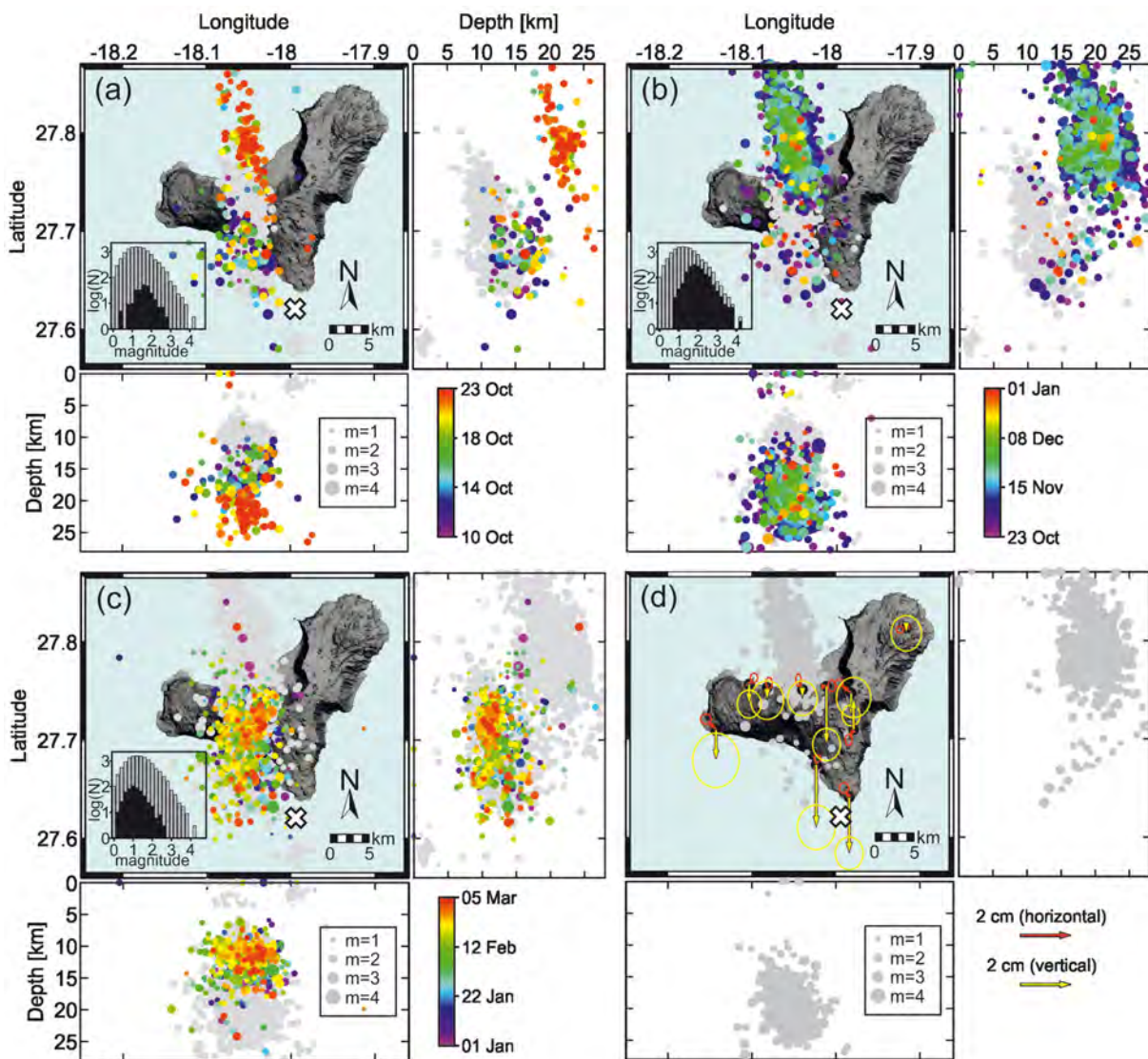


**Figure 6.** (a-c) Temporal evolution of the latitude, longitude and depth (km) of the earthquakes with magnitude  $>1.5$  (time scale of events is reported in the color bar and in grey are reported earthquakes occurred in the previous phases) during the syn-eruptive phase of 2011-2012 eruption of El Hierro Island. White X marks the vent position for the 2011-2012 eruption. In grey are reported earthquakes occurred in the previous phases. Inner plots give the histograms of the number of located events versus magnitude for the each phase (black) and for the full period (grey shaded). Seismic data are after relocation of Domínguez Cerdeña et al. [2014]. (d) Red and yellow vectors show horizontal and vertical ground displacement respectively from November 6, 2011, to January 1, 2012 (within eruptive phase F) during which a minor episode of gradual ground deflation was registered by GPS network. Arrows are tipped with 75% confidence ellipses/circles and seismicity for the same period is plotted as grey circles. The white cross in all panels marks the position of vent for the 2011-2012 eruption.

of ~12 km. This was the largest event registered since the beginning of the seismic unrest and marked the transition toward a new trend in the hypocentral characteristics of the following earthquakes. In fact after this event, the seismicity showed a sharp migration to the south, and reached a position located at a horizontal distance of ~13 km from the previous position and at a depth shallower than 3 km. During the first 26 hours of this phase the earthquakes were randomly spaced over an area of 18 km<sup>2</sup> (green dots in Figure 4f) and later, they were characterized by a lower mean magnitude (*mbLg*) and were clustered at depth of 1 km in area of ca. 3 km<sup>2</sup> (orange dots in Figure 4f). Ground deformation, which had rapidly and continuously increased since the onset of the seismic unrest, suddenly slowed on October 8, 2011 (Figure 3a,b).

### 5.1.2. Syn-eruptive activity

*Phase G; October 10, 2011 - October 23, 2011* (Figure 6a). Since the beginning of the eruption and for about one week, seismic activity was localized mainly off the coast of El Julan, at depths of 10-14 km (Figure 6a). In this period seismicity was also registered at depth of 20-25 km off the El Golfo depression (Figure 6a).

*Phase H; October 23, 2011 - January 1, 2012* (Figure 6b). During the last week of October until early January, seismic activity was localized in the central-northern part of the island and had the highest magnitudes ever registered (except for the *ML*=4.3 event of October 8, 2011). This seismicity developed at two different depths, with a first swarm at a ca. 20-25 km and the second one, which began a week later, at 15-20 km. Both swarms shared some common signal characteristics,

consisting of an initial, persistent and progressive increase in the magnitude and number of seismic events culminating in relatively large events and followed by a drop in both the parameters [García et al. 2014]. Rare earthquakes occurred at depths of 10-14 km in the center-southern part of the island.

On early November a minor episode of gradual ground deflation was registered by GPS network (Figure 6d). This event lasted only four weeks and was registered especially in HI09 and HI10 stations located in the south of the island (Figure 6d) and FRON (in El Golfo) whereas most of the other stations showed no significant changes (above the background noise level) in the ground deformation vector until the end of the eruption.

*Phase I; January 1, 2012 - March 5, 2012* (Figure 6c). In the final stage of the eruption, from early January to March, the seismic activity was again located in the central-southern part of the island with hypocenters at depth of 10-15 km. Except for negligible fluctuations, no significant deflation was observed in the horizontal and vertical components of ground deformation (Figure 3b,c).

### 5.2. Textures, mineral phases and composition of erupted products

All samples are porphyritic rocks. Products emitted during from 15 to 31 October, 2011, have a low phenocrysts content <5 vol. %, whereas since early November phenocryst content gradually increased reaching values of ca. 20 vol. %. Phenocrysts include clinopyroxene, olivine and spinel. Groundmass shows the same mineral assemblage. In floating scoriaceous fragments and lava balloons, the outer portion that was originally

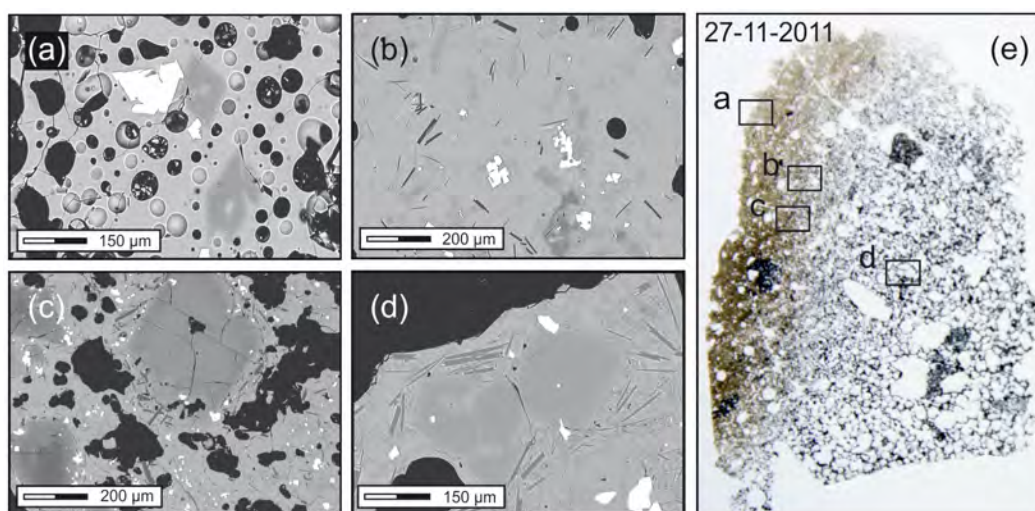


**Figure 7.** Scanning electron microscope (SEM) backscattered and optical microscope images representative of groundmass textures observed in floating scoriaceous fragments and of lava balloons. (a) External portion originally in contact with seawater showing a completely glassy groundmass. (b-c) intermediate portion of the external crust with abundant microphenocrysts of olivine, clinopyroxene, spinel and plagioclase and skeletal microlites mostly of clinopyroxene. (d) Groundmass with intersertal texture made of microlites of clinopyroxene, spinels and plagioclase. (e) Positions where a-d images have been acquired.

in contact with seawater, is almost completely glassy and microlite-free (Figure 7a,e). This portion grades into a glassy groundmass with abundant microphenocrysts of olivine, clinopyroxene, spinel and plagioclase as large as 200-300  $\mu\text{m}$ , and skeletal microlites consisting mostly of clinopyroxene and minor spinels and plagioclase (Figure 7b,c,e). The abundance of skeletal microlites progressively increases as distance from the external crust increases. In the internal portion of samples, groundmass shows an intersertal texture (Figure 7d,e). All studied samples exhibit the zoned texture described above with the only exception of the scoriaceous and glassy crust (<3 cm) embedding the xenopumices erupted on October 15, 2011 and of ash samples recovered in the water column that are completely glassy.

Olivine occurs as isolated phenocrysts (<1 mm) and micro-phenocrysts (<500  $\mu\text{m}$ ) and in glomeroporphyritic aggregates with interstitial clinopyroxene and

spinel (Supplementary Figure 1). Morphology of the crystals is highly variable (Supplementary Figure 1) including embayed boundaries, skeletal or faceted shapes indicating rapid growth of the crystals.

As a whole, olivine phenocryst exhibit little variation in composition between cores and rims with more than 75% of measured composition peaked around  $\text{Fo}_{79-81}$ . Larger olivine phenocrysts are usually normally zoned with Mg-rich  $\text{Fo}_{78-88}$  cores and  $\text{Fo}_{78-83}$  rims (Supplementary Figure 1). Mg-rich cores are often associated with tiny euhedral to podiform crystals of Cr-rich spinels and melt inclusions that are often completely crystallized. Oscillatory zoning is uncommon and remains confined in a narrow compositional range ( $\text{Fo}_{83-80}$ ). Olivine micro-phenocrysts are usually more homogeneous than phenocrysts and have cores with composition peaked around  $\text{Fo}_{80}$  approximating the composition of phenocryst rims (Figure 8).

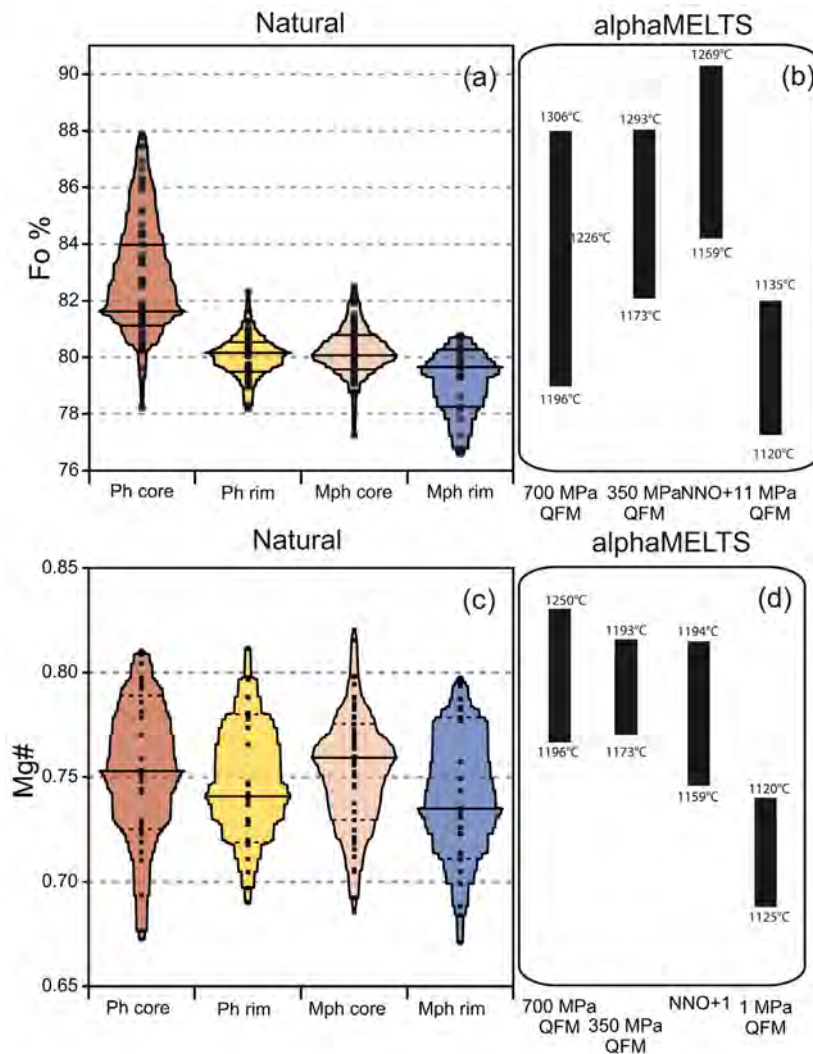


**Figure 8.** (a-c) Box percentile plots of Forsterite % and Mg# ( $\text{MgO}/\text{MgO}+\text{FeO}_{\text{tot}}$  on molar basis) respectively in natural olivine and clinopyroxenes erupted during 2011-12 El Hierro eruption grouped on the basis of size of the minerals (Phenocrysts  $\geq 500 \mu\text{m}$  = Ph; Microphenocrysts  $\leq 500 \mu\text{m}$  = Mph) and position (core-mantle and rim). Width of the box is proportional to the distribution height. Median (solid), 25th, and 75th percentiles (dotted) are marked with line segments across the box; (b-d) Range of Forsterite % and Mg# composition obtained from thermodynamical modeling of fractional crystallization at different pressure and oxidizing conditions in the reported temperature range.

Clinopyroxene is the most abundant phase and occurs as phenocrysts, micro-phenocrysts and microlites within the groundmass (Supplementary Figure 1). Phenocrysts are up to 4 mm and range in morphology from subequant euhedral to subhedral. Microphenocrysts in groundmass range in shape from subequant euhedral and elongated to polyhedral. Groundmass microlites, as large as few microns, are dendritic to skeletal and feathery. Clinopyroxene composition is almost confined within the diopside field, though all crystals exhibit well developed zoning (Figure 8). Patchy and oscillatory zoning is typical of larger phenocrysts whereas sector and hourglass zoning is common in microphenocrysts. Compositional zoning reflects changes in Mg# and in the Ti, Al and Si contents. On the whole phenocrysts core and rim show same Mg# range on values peaked around 0.75, while they differ for Ti/Si cation ratio. Cores show low values of Ti/Si peaked around 0.03 whereas rims exhibit a wider range and are peaked around 0.07.

Cores in microphenocrysts show Mg# values and distribution comparable with those of phenocrysts, with rims extending toward Mg# values as low as 0.70. In addition cores and rims differ for the Ti/Si ratio, with rim showing median values of Ti/Si higher than in cores.

Spinel occurs as <100  $\mu\text{m}$  microphenocrysts and

microlites with variable morphologies (Supplementary Figure 1) and comprise minerals belonging to Magnetite-Ulvöspinel series. High-Cr spinels were not found as isolated phenocrysts or microphenocrysts as *vice versa* reported by Marti et al. [2013b].

Microphenocrysts of plagioclase <200  $\mu\text{m}$  are common only in samples erupted after October 15, 2011. These crystals show mainly an acicular shape (Supplementary Figure 1) with textures typical of fast growth (i.e. swallow-tailed, belt-buckle, chain, acicular bended shape). Their composition ranges between  $\text{An}_{60}$  and  $\text{An}_{72}$ . Few large, 200-300  $\mu\text{m}$  plagioclase crystals occur with patch zoned cores ( $\text{An}_{51-58}$ ) as large as few microns and rims with composition  $\text{An}_{60-72}$ . Plagioclase also form rare holocrystalline aggregates with pyroxene and spinel.

### 5.3. Bulk rock and glass composition

All studied samples have a basanite major element bulk rock composition, with  $\text{SiO}_2$  ranging between 42.2 and 44.2 wt. % and alkali content ranging between 5.13 and 6.07 wt. % (Table 3). These compositions overlap those of products emitted during the Quaternary rift volcanism of El Hierro [Carracedo et al. 2001]. In addition, trace element bulk rock composition patterns are fully comparable with those of El Hierro volcanics showing a relative enrichment of Th, Nb and LREE with respect to LILE (Ba, Rb) and following a typical OIB trend and the characteristic pattern of the Canary Island basanites. Bulk rock compositions plot with a limited scatter along a differentiation trend in  $\text{CaO}/\text{Al}_2\text{O}_3$  vs  $\text{FeO}_{\text{tot}}/\text{MgO}$  diagram controlled by the precipitation of olivine and clinopyroxene. Glass composition partially overlaps this trend extending toward lower  $\text{CaO}/\text{Al}_2\text{O}_3$  and higher  $\text{FeO}_{\text{tot}}/\text{MgO}$  values.

Ratios between highly incompatible trace elements (e.g. Rb/Ba, Rb/Th and Rb/La) are quite constant with the exception of the sample of October 15, 2011, that slightly exceeds the analytical error accounting for limited contamination of magma by xenophomites. These ratios do not vary with the magma differentiation (Figure 9) pointing to a simple differentiation process starting from a single magma parent and excluding mixing between magma with distinct geochemical features.

Bulk rocks compositions show a progressive and continuous shift toward more mafic compositions starting from the very first day of eruption up to late January (Tables 3 and 4; Figure 10a). In particular the less differentiated samples were emitted on January 28, 2012, whereas the most evolved products were erupted during the first day of eruption, on October 15, 2011. This is witnessed by the regular increase in the  $\text{CaO}/\text{Al}_2\text{O}_3$

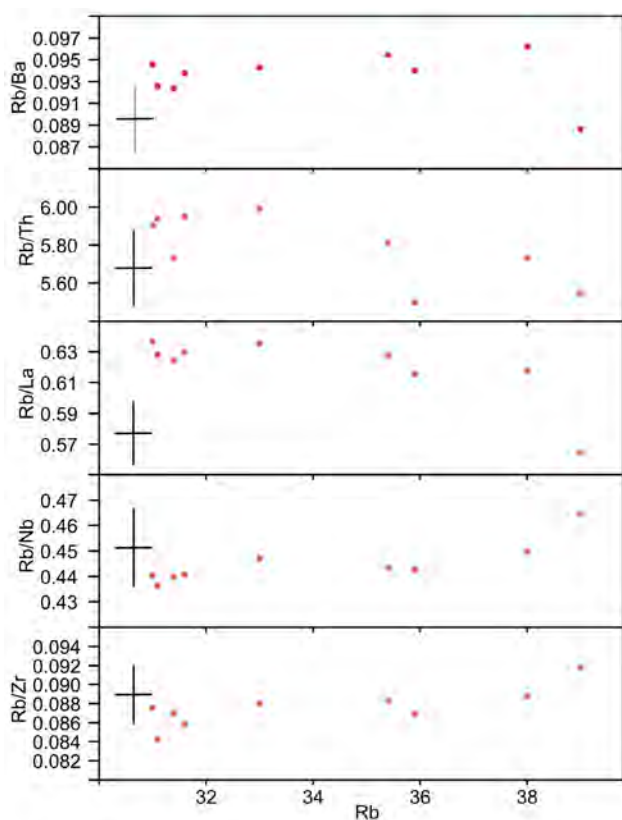


**Figure 9.** Variation diagrams (unit in ppm) for bulk rock Rb/Ba, Rb/Th, Rb/La, Rb/Nb and Rb/Zr ratio versus Rb during the 2011-12 El Hierro eruption. Error bars (black crosses) represent 1 sigma.

THE 2011-2012 UNREST AND ERUPTION OF EL HIERRO

Date (dd/mm/yyyy)	15/10/2011	31/10/2011	27/11/2011	06/12/2011	04/01/2012	18/01/2012	21/01/2012	28/01/2012	30/01/2012
SiO <sub>2</sub>	42.96	44.20	43.60	42.80	43.10	42.20	42.50	43.10	43.30
TiO <sub>2</sub>	4.28	4.42	4.74	4.70	4.70	4.50	4.61	4.76	4.69
Al <sub>2</sub> O <sub>3</sub>	14.15	13.50	13.25	12.95	12.55	12.2	12.55	12.15	12.40
Fe <sub>2</sub> O <sub>3</sub>	14.42	14.75	14.40	14.15	14.35	14.45	14.75	14.35	14.20
CaO	10.19	10.50	10.75	10.65	10.8	10.65	10.85	10.75	10.7
MgO	6.28	7.11	7.55	7.64	8.54	8.43	8.47	8.67	8.66
Na <sub>2</sub> O	4.44	3.95	4.11	4.16	3.83	4.17	3.81	3.83	4.10
K <sub>2</sub> O	1.63	1.49	1.44	1.40	1.34	1.28	1.32	1.30	1.32
MnO	0.20	0.20	0.20	0.19	0.20	0.18	0.19	0.19	0.19
P <sub>2</sub> O <sub>5</sub>	1.00	0.91	0.88	0.85	0.81	0.73	0.76	0.77	0.78
LOI	0.82	0.19	0.21	0.32	0.14	1.08	0.70	0.49	0.66
Total	100.36	101.22	101.13	99.81	100.36	99.87	100.51	100.36	101.00
SrO	---	0.13	0.13	0.12	0.12	0.11	0.11	0.11	0.11
BaO	---	0.05	0.06	0.05	0.05	0.04	0.04	0.05	0.05
Cs	0.5	0.47	0.41	0.39	0.4	0.34	0.35	0.36	0.37
Rb	39	38	35.9	35.4	33	31	31.6	31.1	31.4
Ba	440	395	382	371	350	328	337	336	340
W	9.2	2	1	2	1	1	1	1	1
Th	7.03	6.63	6.53	6.09	5.51	5.25	5.31	5.24	5.48
U	1.96	1.71	1.58	1.56	1.37	1.3	1.36	1.32	1.38
Nb	83.9	84.5	81.1	79.8	73.8	70.4	71.7	71.3	71.4
Ta	5.05	5.1	4.9	4.9	4.5	4.3	4.3	4.4	4.3
La	69.1	61.5	58.3	56.4	51.9	48.7	50.2	49.5	50.3
Ce	153	128.5	122.5	118	110	103.5	107.5	104.5	106.5
Pr	18	15.6	14.9	14.45	13.45	12.5	13	12.95	13
Sr	1118	1075	1025	1025	960	916	941	932	936
Nd	73.2	64.6	62.5	61.7	56.8	53.6	55.4	54.4	55
Sm	15.1	13.8	13.2	13.1	12.15	11.75	11.75	11.9	11.75
Zr	425	428	413	401	375	354	368	369	361
Hf	9.3	9.8	9.4	9.4	8.8	8.4	8.5	8.9	8.5
Eu	4.5	4.37	4.27	4.26	3.87	3.75	3.93	3.88	3.99
Sn	3	3	3	3	3	3	3	3	3
Gd	11.3	11.7	11.65	11.6	10.15	10.45	10.45	10.3	10.6
Tb	1.59	1.54	1.54	1.57	1.41	1.37	1.4	1.43	1.43
Dy	8.18	7.96	7.7	7.81	7.24	6.98	7.07	7.23	7.23
Y	38.3	35.3	34.6	34.1	31.8	30.6	31.2	31.2	31.2
Ho	1.36	1.36	1.33	1.36	1.23	1.21	1.22	1.2	1.21
Er	3.41	3.2	3.13	3.2	2.94	2.77	2.86	2.81	2.92
Tm	0.438	0.41	0.39	0.4	0.36	0.34	0.35	0.35	0.35
Yb	2.49	2.28	2.24	2.17	2.08	1.95	1.96	1.99	1.96
Lu	0.354	0.31	0.32	0.31	0.28	0.27	0.28	0.27	0.27
Tl	0.05	<0.5	<0.5	<0.5	<0.5	<0.5	<0.5	<0.5	<0.5
Ga	28	25.9	24.9	25.2	24.2	23.5	24.5	24.1	23.7
V	341	355	367	378	382	373	386	385	381
Cr	50	140	180	210	280	290	300	290	280

Table 3. Bulk rock major and trace elements chemical composition of studied products.



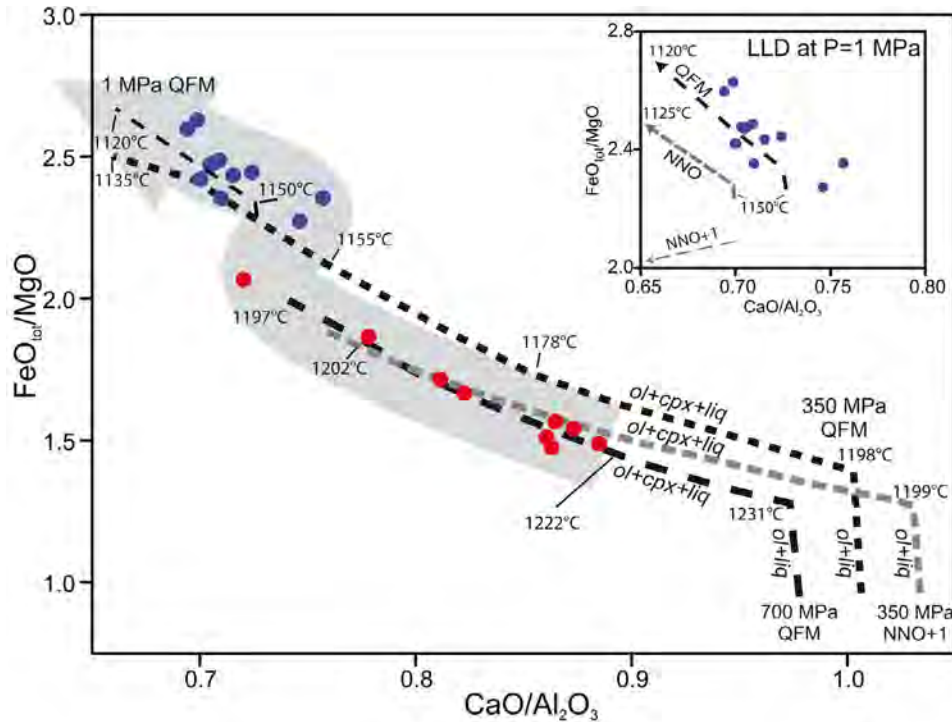


**Figure 11.** Comparison between compositions of bulk rocks (red solid circles), glass (blue solid circles) and liquid lines of descent (LLD) obtained by thermodynamic modeling of cooling (range of temperature are reported) and fractional crystallization at different pressures (700–1 MPa) under distinct oxidation conditions (from QFM to NNO+1). Gray arrow describe possible ascent path of magma that starts to crystallize at 700 MPa (between 1300 and 1200°C under QFM) or at 350 MPa (between 1199 and 1160°C under NNO+1), moves at lower pressure and finally quench at temperatures between 1150°C down to 1120°C, close to the surface. Inset shows liquid line of descent at  $P = 1$  MPa (water depth of 100 m) under different oxidizing conditions and glass compositions measured during the 2011–12 El Hierro eruption.

#### 5.4. Thermodynamic modeling

Large variations in bulk rocks composition accompanied by variability in crystal content and significant zoning in crystals possibly indicates that magma experienced several magmatic environments and complex magmatic processes along the ascent. As a consequence, thermodynamic modeling techniques [Ghiorso and Sack 1995] have been employed to track the whole history of the magma, using a combination of geophysical and petrological data as initial and as boundary conditions.

Relocated depths of hypocentral foci by Domínguez Cerdeña et al. [2014] and local lithosphere and density structure [Collier and Watts 2001] have been used as first guesses to constrain pressure ranges where magma might have resided before the eruption. Accordingly, we simulated cooling and crystallization of mantle derived melts respectively in a deep magmatic reservoir at mantle pressure of 700 MPa (corresponding to a seismic source at 20–25 km) and in a crustal storage zone at pressure of 350 MPa (corresponding to a seismic source at 8–12 km). Final cooling at pressure of 1 MPa corresponding to water column of about 100 m has been also modeled. We selected as starting material a magma with the composition equal to that of rocks erupted on October 31, 2011. In fact in these samples the compositions of glass and bulk rock almost match,

thus indicating that this sample possibly represents a magmatic liquid. From this starting composition we estimated the composition of a parental liquid in equilibrium with mantle conditions using the Amoeba routine of AlphaMELTS [Smith and Asimov 2005]. This routine varies the parental melt composition until isobaric forward fractionation yields a specified target (here considered as the composition of October 31, 2011). From this parental melt we simulated, again using AlphaMELTS, an isobaric cooling and crystal fractionation processes at 700, 350 and 1 MPa under distinct  $fO_2$  paths variable from 1 log unit more oxidizing than those of the NiNiO buffer from (NNO+1) to QFM (quartz-fayalite-magnetite) redox buffers. In this way we were able to investigate and reproduce the liquid line of descent (LLD) of the whole suite from the mantle to the final stages of the ascent, through crustal magma storage. Comparison between simulated liquid line of descent and composition of erupted products is shown in  $CaO/Al_2O_3$  vs  $FeO_{tot}/MgO$  diagram of Figure 11. Bulk rocks compositions match the evolution of magma precipitating olivine  $Fo_{85-81}$  and clinopyroxene with  $Mg\# = 0.80-0.77$  at  $P = 700$  MPa, at temperatures between 1220 and 1190°C and under a QFM buffer. The same compositional trend is also compatible with the cooling of a magma and crystallization of olivine  $Fo_{87-84}$  and clinopyroxene with  $Mg\# = 0.80-0.74$

at temperature between 1180 and 1160°C and at  $P = 350$  MPa under NNO+1 buffer.

Glass compositions plot across the liquid line of descent resulting from crystallization of the same phases (olivine  $\text{Fo}_{80-79}$  and clinopyroxene with  $\text{Mg\#} = 0.74-0.73$ ) plus spinel at 350 MPa between 1155-1150°C and at 1 MPa between 1145 to 1120°C ( $\text{Fo}_{79-77}$ ;  $\text{Mg\#} = 0.70-0.69$ ) under QFM redox conditions. Composition of precipitated phases in equilibrium (Figure 8) match the range observed in natural products.

Comparisons between liquid line of descent, mineral composition calculated by thermodynamic modeling and compositional variations observed in bulk rocks and glasses show that:

- assuming a parental magma in equilibrium with a mantle mineral assemblage, as that retrieved by alphaMELTS, large part of the crystallization ( $\approx 50\%$ ) is controlled by phase equilibria that occur in a storage system that result to be very deep in case of reducing condition (located in the mantle at 700 MPa at  $f\text{O}_2 = \text{QFM}$ ) or in the crust if oxidizing condition are considered (at 350 MPa and  $f\text{O}_2 = \text{NNO}+1$ ). Glass composition reflects final precipitation ( $\approx 5\%$ ) during the quenching in the last stage of the ascent;

- irrespective of the relative depths, the vertical extent of the storage system where precipitation of minerals occur, should be limited since the scattering of natural sample composition along isobaric curves is very small;

- considering even the early phase of crystallization in which only olivine is on the liquidus, large part of the cooling (1300-1150°C) occurs at pressure higher than 350 MPa and the last temperature drop ( $\approx 30^\circ\text{C}$ ) takes place only during the final stage of the ascent to the surface.

## 6. Discussion

### 6.1. Ascent dynamics from geophysical and geodetical constraints

#### 6.1.1. Pre-eruptive (July-October 2011)

In the first period of the unrest crisis, until early September, geophysical and geodetical signals indicate that magma was emplacing within the lower crust or close to the Moho discontinuity that for Canary Islands is estimated to be at 13-16 km of depth [Carracedo 1994, Ranero et al. 1995, Lodge et al. 2012, López et al. 2012]. The distribution and the low-magnitude of seismic events, as well as ground deformation pattern, suggest that small-volume intrusions of magma took place at 8-12 km of depth in the center, center-south sectors of the island. The geometry of the intrusions was pos-

sibly controlled by preexisting intrusive complexes and zones of structural weakness as those revealed by recent magnetic, gravimetric and structural studies [Montesinos et al. 2006, Blanco-Montenegro et al. 2008, García-Yeguas et al. 2012, González et al. 2013, Gorbatiykov et al. 2013, García-Yeguas et al. 2014]. The low-magnitude earthquakes occurred during this phase could be related to the expansion of magma or magmatic fluids within this preexisting fractures system [Hill 1977, Roman et al. 2006]. In addition, the spatial distribution and temporal evolution of the hypocenters, their tight clustering as well as GPS data suggest that magma propagated in different direction possibly as fingers [Pollard et al. 1975, Schofield et al. 2010] characterized by small volume and not capable of generating new fractures inside the volcanic edifice [Gudmundsson and Løtveit 2005].

The drastic change both in the seismicity and ground deformation pattern occurred on early September likely indicates a change in the dynamics of magma movement. Since the volume of magma tapped cannot be accounted by the fracture system that was used in the earlier intrusions, magma started to migrate at depth and southward following zones of structural weakness. Although this migration in depth was interpreted as a “faulty” migration, due to the Moho anomaly [Ibañez et al. 2012], after relocation of seismic events it was clear that it represents a real migration with the hypocenters marking tight clusters. This migration was in the order of 10 km.

Seismic and ground deformation data indicate that ten days before the onset of the eruption, a storage system was emplaced at depth (12-16 km), off the coast of El Julan. This is in agreement with evidence resulting by Interferometric Synthetic Aperture Radar (InSAR) observations of González et al. [2013] and as a whole, with results of analysis of seismic and ground deformation data of García et al. [2014]. The 12 hours of seismic silence occurred between the major  $\text{ML}=4.3$  earthquake and the sudden appearance of seismic multiplets at  $<3$  km of depth close to the future vent was previously interpreted as an extremely rapid ( $0.13 \text{ ms}^{-1}$ ; Martí et al. [2013a]), aseismic magma ascent [Ibañez et al. 2012] whereas the major event was interpreted as the beginning of the ascent [Martí et al. 2013a, 2013b].

We suggest that the seismic silence and seismic activity at shallow depth might occur when the ascending magma found a ductile zone represented by a stagnant magma pocket/s and hydrothermally altered volcanic rocks [Meletlidis et al. 2012, Sigmarsson et al. 2012, Del Moro et al. 2015]. The interaction (heating/pyrometamorphism) between the basanitic magma feeding the eruption, and the rocks/magma of the ductile

tile zone would have initially resulted in an almost aseismic, horizontal expansion of the magma and later in the shallow seismicity. Similar processes have been described in volcanic rift zones of Kilauea [Rubin et al. 1998] and Krafla volcano in Iceland [Einarsson and Brandsdóttir 1980] or for Parícutin volcano [Gardine et al. 2011]. Materials resulting from the interaction of basaltic magma feeding the eruption and preexistent magma pocket/s and hydrothermally altered volcanic rocks were emitted during the first day of the eruption [Meletlidis et al. 2012, Sigmarsson et al. 2012, Del Moro et al. 2015].

### 6.1.2. Syn-eruptive (October 2011-March 2012)

The relatively low magnitude, shallow seismicity at depth of 10-14 km that was registered for about 20

days after the onset of the eruption and again from early January to March 2012, is interpreted here as the readjustment of the stress field nearby the vent and the relaxation of the host rock when finally the eruption ceased, respectively.

Our analysis of seismic data indicates that the deep seismicity in the northern part of the island persisted far longer than previously proposed by Marti et al. [2013a] and consisted in two distinct swarms the first at 20-25 km since October 18 and the second, starting one week later at 15-20 km, respectively. The tendency of these two seismic swarms (a progressive increase in the number and magnitude of the events over a few days culminating in larger seismic events and finally followed by a drop in both the parameters) is almost identical to

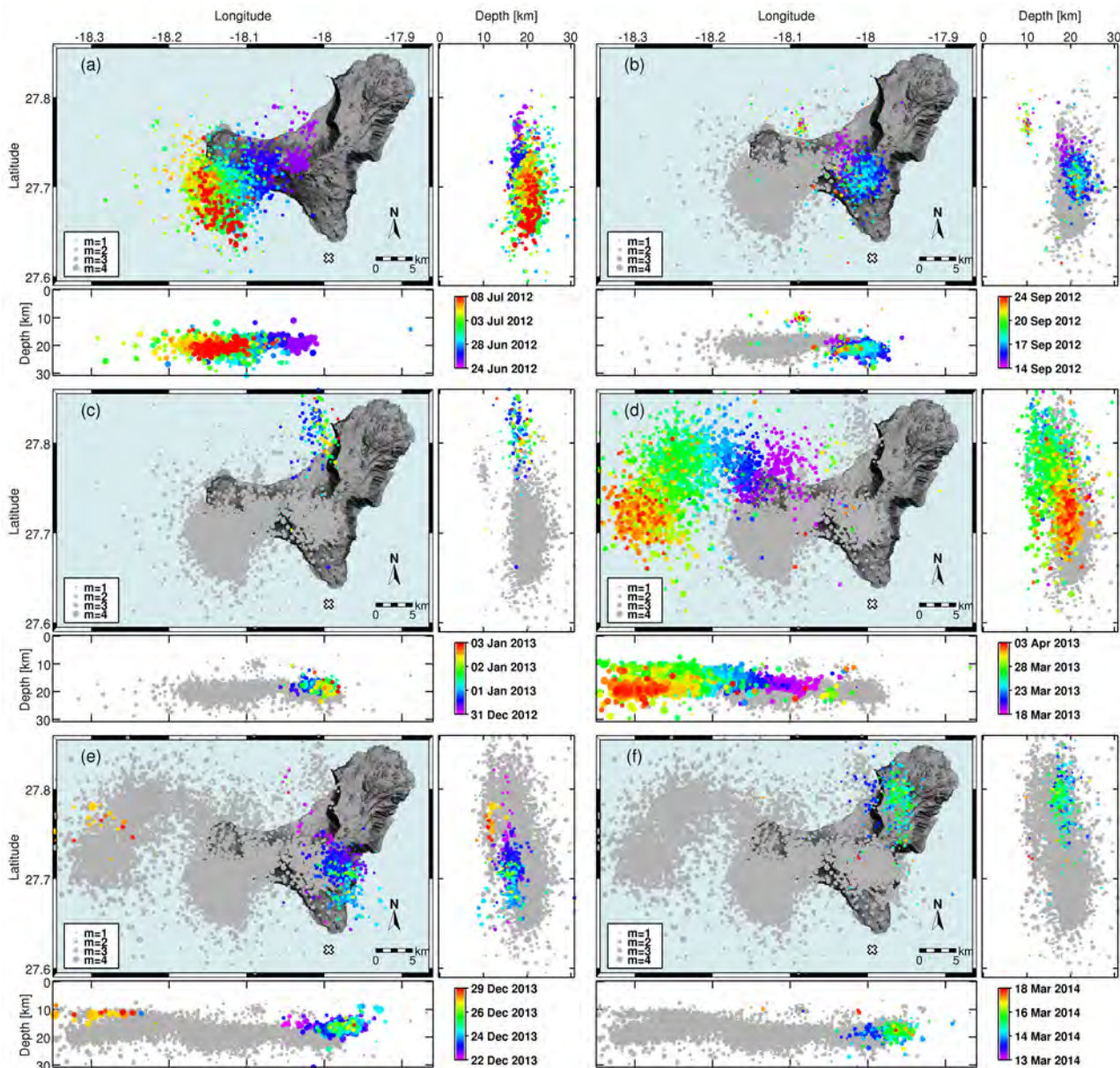


**Figure 12.** Temporal evolution of the latitude, longitude and depth (km) of the earthquakes for the six distinct seismic episodes occurred after the end of 2011-2012 El Hierro eruption (time scale of events is reported in the color bar; in grey are reported earthquakes occurred in the previous seismic episodes).

that of several seismic swarms occurred on the island after the end of the eruption (Figure 12).

Our data show that seismic activity does not correlate with appreciable ground deformation changes. No significant deflation of the whole island was detected as should be expected in case of a deep magma chamber depressurization. In fact, no changes in the horizontal components (northing and easting) of deformation were registered after the onset of the eruption (unless negligible fluctuations) and relative high (2 cm) vertical deflation was registered only by two stations, close the eruptive site (HI09 in La Restinga and HI10 in Tacoron bay) and one (FRON) in El Golfo depression. This, according to Prates et al. [2012], may indicate that the source of deformation was not horizontally distant from the station where deformation was recorded. Thus, the high vertical deformation may be due to a local perturbation of the system e.g. the presence of pressurized magmatic gas close to the deformation site. We propose that a possible mechanism for generating the deep seismicity occurred after October 2011 (two swarms during the eruption and seven more after up to the moment of this writing) is the emplacement of magma at depth without significant deflation of the plumbing system. This is in agreement with conclusions presented by García et al. [2014]. A similar event could have occurred in 1793, when a strong seismic crisis did not result in a volcanic eruption at least subaerial [Villasante-Marcos and Pavón-Carrasco 2014].

### 6.2. Ascent dynamics and magma evolution from petrological data

We observed that the bulk rocks compositions varied significantly during the eruption with a progressive and continuous shift towards more mafic term (Figure 10a). Such variation can be accounted by crystals fractionation and crystals cumulus of mafic phases, which increase from 5 wt. % in the first day of the eruption up to ca. 20 wt. % in January (Figure 10g).

Although thermodynamic modeling cannot discriminate if this process occurs in the mantle reservoir at  $P = 700$  MPa under reduced  $fO_2$  (QFM) or at crustal levels at  $P = 350$  MPa under more oxidized conditions ( $fO_2 = NNO+1$ ), the observed compositional variations imply the existence of a zoned magma body that is progressively withdrawn during the eruption. The overall constancy of highly incompatible elements ratio (e.g. Rb/Nb, Rb/Th, Rb/Lb and Nb/La) versus time indicates that the process of magma differentiation responsible of such a zoning operated from a single parental magma. This interpretation differs from those previously proposed by Martí et al. [2013a, 2013b] and Long-

pré et al. [2014].

Longpré et al. [2014], on the basis of Cpx-melt geobarometry, point to the occurrence of two distinct storage zones in comparable shallow mantle depths in the same pressure range (500-710 MPa) that we investigated with our thermodynamic modeling. They also propose that magmas supplied from these distinct reservoirs mix and homogenize shortly prior to their ascent into a third storage zone within the lower crust.

Mixing evidences of Longpré et al. [2014] are mainly based on the occurrence of a) differentiated liquids found as melt inclusions (MI) in Fe-Ti oxides and b) slight reversed zoning in olivine with core  $Fo_{78}$  and rims  $Fo_{80}$ . Differentiated liquids as those reported in MI by Longpré et al. [2014] implies a correspondent mineral assemblage (e.g.  $Fo < 78$ ) that is not found in El Hierro 2011-12 samples. Notably slight reversed zoning in olivine can also form as result of migration of crystal between compositionally and thermally distinct regions of a cooling and crystallizing magma body [Kahl et al. 2011]. Differences of this amplitude would correspond to temperature differences of few tens of degrees as shown by Martí et al. [2013b] and are compatible with thermal gradient within a zoned magma chamber.

Thus, while we can agree that limited mixing processes may have occurred within this deep evolving storage due to convective circulation, we think that large-scale mixing process involving two reservoirs is unlikely since it is incompatible with regular compositional variations that we observed during the eruption. In fact, the full re-homogenization before the ascent and emplacement in a third crustal storage (10-15 km) would have been followed by an additional process of segregation and cumulus of mafic phases during the syn-eruptive ascent, in order to account for the regular variation observed in bulk rock composition.

Martí et al. [2013a, 2013b] indicate that magma differentiation occurs mainly in the crustal reservoir and show that a recharge event of the shallow magmatic system occurred on early December, 2011, with fresh magma coming from a deeper reservoir. This was proposed on the basis of an observed drop in crystallinity and a change in bulk rock composition between the sample of November 27 and that of December 5, 2011. According to the authors, the December sample (with crystallinity  $\sim 20$  wt. %,  $SiO_2 = 43.76$  wt. % and  $FeO_{tot} = 12.85$  wt. %) marked the arrival of the second magma batch and the November sample (characterized by a considerably higher crystal content of ca. 50 wt. %,  $SiO_2 = 40.31$  wt. % and  $FeO_{tot} = 17.07$ ) is considered the last product of the first magma batch. However, it should be noted that the sample HB5 of Martí et al. [2013a, 2013b] collected on November 27 shows an

anomalous composition if compared to the products of the same day analyzed in this work and in Longpré et al. [2014]. In particular, the high  $\text{FeO}_{\text{tot}}$  content of ca. 17 wt. % is not consistent with the content of  $\text{MgO}$ , which is instead rather comparable with that of the other samples. This high value of  $\text{FeO}_{\text{tot}}$  is found in the Canary Islands only for plutonic rock (e.g. gabbro, pyroxenite and hornblendite; GEOROC-Geochemistry of Rocks of the Oceans and Continents, <http://georoc.mpch-mainz.gwdg.de>). Thus, we suppose that crystallinity and composition of the sample HB5 of Martí et al. [2013a, 2013b] is not representative of the real magma emitted in that day, possibly for the presence of a xenolith (cumulate rock) or recycled material, and cannot be used for petrological reconstruction and modeling.

## 7. Conclusive remarks

Results of the temporal analysis of seismic events, ground deformation patterns and gravity data as well as of the texture and composition of mineral phases, bulk rock and volcanic glass contribute to give new clues on the 2011-2012 eruption at El Hierro Island.

According to geophysical and geodetical data the eruption was driven by a stepwise migration of a batch of magma between three main magmatic environments,

including a deep reservoir, a crustal magma reservoir and a final shallow conduit and vent zone (Figure 13). Initially, the magma emplaced in an indefinite time in deep magma chamber possibly located in the upper mantle. Later magma ascended aiseismically to the lower crust and on July 2011 reached the depth of 8-12 km. Here magma initially propagated as small-volume fingers or lobes not capable of generating new fractures inside the volcanic edifice. Magma path was initially controlled by preexisting intrusive complex and zones of structural weakness within the edifice resulting in a typical distribution of earthquakes. On September 2011 the magma migrated at depth and southward forming a storage system off the coast of El Julan and causing seismic activity at depth of 12-16 km. Petrological data indicate that the eruption was fed by a single magma whose composition varied trough a dominant process of crystals fractionation and crystals cumulus of mafic phases. However, thermodynamic modeling cannot discriminate if this process occurs in the mantle reservoir or in the crustal storage zone.

After a period of stagnation of about a month, the magma rapidly ascended to the final eruptive site suffering only a minor quenching and crystallization of clinopyroxene, olivine and plagioclase. Final aseismic ascent likely occurred trough relatively weak paths. The

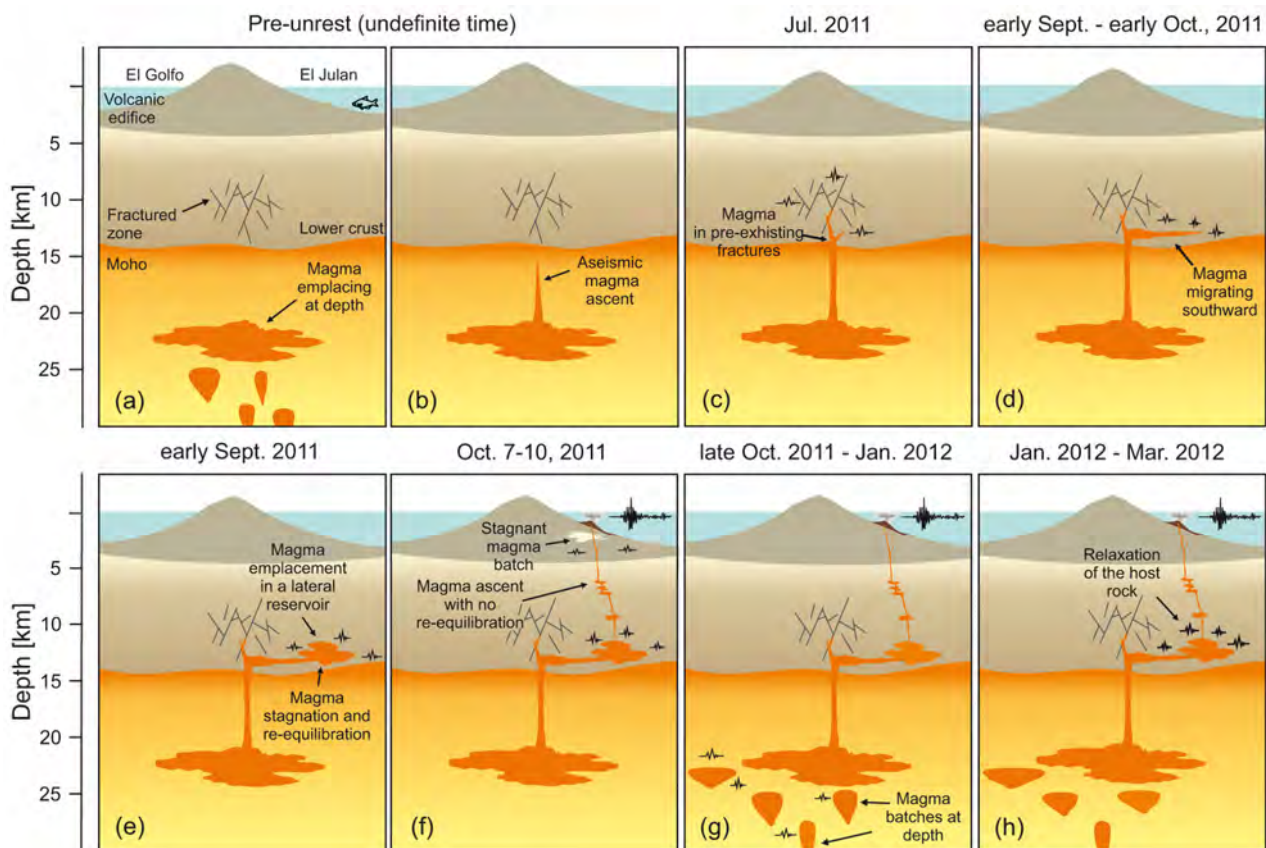


**Figure 13.** Cartoon interpretation (not to scale) of the volcanic system activated in El Hierro Island during the 2011-2012 unrest and eruption (along a north-south cross section). Panels (a-h) show in brief the main events that led to the eruption that were discussed in the text.

stepwise ascent of magma of relatively small volume magma pockets (likely in the form of interconnected dyke and sills) is in agreement with that proposed by Stroncik et al. [2009] for El Hierro and other intraplate volcanoes, which includes multistage magma ascent with major crystal fractionation in the uppermost mantle and short-term stagnation at shallower levels.

**Acknowledgements.** We would like to thank the Volcano Monitoring Group (IGN) for the deployment and maintenance of the seismic and GPS networks along with the gravimetric station on El Hierro. Special thanks are due to the Sociedad de Salvamento y Seguridad Marítima (SASEMAR) for the efforts in sampling (without the personnel and its infrastructure sampling wouldn't have been possible) and the Municipality of El Pinar (especially to Mr. Jesus Pérez Quintero) for their help on logistics. This work was funded by the National Geographical Institute of the Spanish Ministerio de Fomento. We also would like to thank GRAFCAN for the open and free access to the GPS station of FRON and to UCA-CSIC for the data of the HI00 station that was used in the framework of the CSIC-IGN scientific collaboration and advice agreement (2006-2012). ADR was supported by DPC-INGV V1 agreement. The data for this paper are property of Instituto Geográfico Nacional, Spain and can be explored and downloaded on request at [www.ign.es](http://www.ign.es). Two anonymous reviewers and Editor F. Bianco are kindly acknowledged for their constructive revision of the manuscript.

## References

- Acosta, J., E. Uchupi, D. Smith, A. Muñoz, P. Herranz, C. Palomo, P. Llanes, M. Ballesteros and ZEE Working Group (2003). Comparison of volcanic rifts on La Palma and El Hierro, Canary Islands and the Island of Hawaii, *Mar. Geophys. Res.*, 24, 59-90; doi:10.1007/s11001-004-1162-6.
- Blanco-Montenegro, I., I. Nicolosi, A. Pignatelli and M. Chiappini (2008). Magnetic imaging of the feeding system of oceanic volcanic islands: El Hierro (Canary Islands), *Geophys. J. Int.*, 173, 339-350; doi:10.1111/j.1365-246X.2008.03723.x.
- Carracedo, J.C. (1994). The Canary Islands: an example of structural control on the growth of large oceanic island volcanoes, *J. Volcanol. Geoth. Res.*, 60, 225-241; doi:10.1016/0377-0273(94)90053-1.
- Carracedo, J.C., E.R. Badiola, H. Guillou, L. De La Nuez and F.J. Perez Torrado (2001). Geology and volcanology of La Palma and El Hierro, western Canaries, *Est. Geol.*, 57, 175-273.
- Collier, J.S., and A.B. Watts (2001). Lithospheric response to volcanic loading by the Canary Islands: constraints from seismic reflection data in their flexural moat, *Geophys. J. Int.*, 147, 660-676; doi:10.1046/j.0956-540x.2001.01506.x.
- Del Moro, S., A. Di Roberto, S. Meletlidis, M. Pompilio, A. Bertagnini, S. Agostini, F. Ridolfi and A. Renzulli (2015). Xenopumice erupted on 15 October 2011 offshore of El Hierro (Canary Islands): a subvolcanic snapshot of magmatic, hydrothermal and pyrometamorphic processes, *B. Vulcanol.*, 77 (6), 53; doi:10.1007/s00445-015-0940-0.
- Domínguez Cerdeña, I., C. del Fresno and A. Gomis Moreno (2014). Seismicity patterns prior to the 2011 El Hierro Eruption, *B. Seismol. Soc. Am.*, 104 (1), 567-575; doi:10.1785/0120130200.
- Einarsson, P., and B. Brandsdóttir (1980). Seismological evidence for lateral magma intrusion during the July 1978 deflation of the Krafla volcano in NE-Iceland, *J. Geophys.*, 47, 160-165; doi:10.2172/890964.
- García, A., A. Fernandez-Ros, M. Berrocoso, J.M. Marrero, G. Prates, S. De la Cruz-Reyna and R. Ortiz (2014). Magma displacements under insular volcanic fields, applications to eruption forecasting: El Hierro, Canary Islands, 2011-2013, *Geophys. J. Int.*; doi:10.1093/gji/ggt505.
- García-Yeguas, A., I. Koulakov, J.M. Ibáñez and A. Rietbrock (2012). High resolution 3D P-wave velocity structure beneath Tenerife Island (Canary Islands, Spain) based on tomographic inversion of active-source data, *J. Geophys. Res.*, 117; doi:10.1029/2011JB008970.
- García-Yeguas, A., J.M. Ibáñez, I. Koulakov, A. Jakolev, M.C. Romero-Ruiz and J. Prudencio (2014). Seismic tomography model reveals mantle magma sources of recent volcanic activity at El Hierro Island (Canary Islands, Spain), *Geophys. J. Int.*, 199, 1739-1750; doi:10.1093/gji/ggu339.
- Gardine, M., M.E. West and T. Cox (2011). Dike emplacement near Parícutin volcano, Mexico in 2006, *B. Vulcanol.*, 73, 123-132; doi:10.1007/s00445-010-0437-9.
- Ghiorso, M.S., and R.O. Sack (1995). Chemical Mass-Transfer in Magmatic Processes IV. A Revised and Internally Consistent Thermodynamic Model for the Interpolation and Extrapolation of Liquid-Solid Equilibria in Magmatic Systems at Elevated-Temperatures and Pressures, *Contrib. Min.Pet.*, 119 (2-3), 197-212; doi:10.1007/BF00307281.
- González, P.J., S.V. Samsonov, S. Pepe, S.F. Tiampo, P. Tizzani, F. Casu, J. Fernández, A.G. Camacho and E. Sansosti (2013). Magma storage and migration associated with the 2011-2012 El Hierro eruption: Implications for crustal magmatic systems at oceanic island volcanoes, *J. Geophys. Res. Solid Earth*, 118, 1-17; doi:10.1002/jgrb.50289.
- Gorbatikov, A.V., F.G. Montesinos, J. Arnosó, M.Y. Stepanova, M. Benavent and A.A. Tsukanov (2013). New Features in the Subsurface Structure Model of El Hierro Island (Canaries) from Low-Frequency Microseismic Sounding: An Insight into the 2011 Seismo-Volcanic Crisis, *Surv. Geophys.*, 34, 463-489; doi:10.1007/s10712-013-9240-4.

- Gudmundsson, A., and I.F. Løtveit (2005). Dyke emplacement in a layered and faulted rift zone, *J. Volcanol. Geotherm. Res.*, 144 (1), 311-328; doi:10.1016/j.jvolgeores.2004.11.027.
- Guillou, H., J.C. Carracedo, F. Pérez Torrado and E. Rodríguez Badiola (1996). K-Ar ages and magnetic stratigraphy of a hotspot-induced, fast grown oceanic island: El Hierro, Canary Islands, *J. Volcanol. Geoth. Res.*, 73, 141-155; doi:10.1016/0377-0273(96)00021-2.
- Gutenberg, B., and C. Richter (1954). *Seismicity of the Earth and Associated Phenomena* (Princeton University Press, Princeton, New Jersey), 2nd ed., 310 p.
- Hill, D.P. (1977). A model for earthquake swarms, *J. Geophys. Res.*, 82, 1347-1352; doi:10.1029/JB082i008p01347.
- Ibáñez, J.M., S. De Angelis, A. Díaz-Moreno, P. Hernández, G. Alguacil, A. Posadas and N. Pérez (2012). Insights into the 2011-2012 submarine eruption off the coast of El Hierro (Canary Islands, Spain) from statistical analyses of earthquake activity, *Geophys. J. Int.*, 191, 659-670; doi:10.1111/j.1365-246X.2012.05629.x.
- Kahl, M., S. Chakraborty, F. Costa and M. Pompilio (2011). Dynamic plumbing system beneath volcanoes revealed by kinetic modeling, and the connection to monitoring data: An example from Mt. Etna, *Earth Plan. Sci. Lett.*, 308, 11-22; doi:10.1016/j.epsl.2011.05.008.
- Lodge, A., S.E.J. Nippres, A. Rietbrock, A. García-Yeguas and J.M. Ibáñez (2012). Evidence for magmatic underplating and partial melt beneath the Canary Islands derived using teleseismic receiver functions, *Phys. Earth Plan. Int.*, 212, 44-54; doi:10.1016/j.pepi.2012.09.004.
- Longpré, M.A., A. Klügel, A. Diehl and J. Stix (2014). Mixing in mantle magma reservoirs prior to and during the 2011-2012 eruption at El Hierro, Canary Islands, *Geology*; doi:10.1130/G35165.1.
- López, C., M.J. Blanco, R. Abella, B. Brenes, V.M. Cabrera Rodríguez, B. Casas, I. Domínguez Cerdeña, A. Felpeto, M. Fernández de Villalta, C. del Fresno, O. García, M.J. García-Arias, L. García-Cañada, L. Gomis Moreno, E. González-Alonso, J. Guzmán Pérez, I. Iribarren, R. López-Díaz, N. Luengo-Oroz, S. Meletlidis, M. Moreno, D. Moure, J. Pereda de Pablo, J. Rodero, E. Romero, S. Sainz-Maza, S.A. Sentre Domingo, P.A., Torres, P. Trigo and V. Vilasante-Marcos (2012). Monitoring the volcanic unrest of El Hierro (Canary Islands) before the onset of the 2011-2012 submarine eruption, *Geophys. Res. Lett.*, 39, L13303; doi:10.1029/2012GL051846.
- Martí, J., V. Pinel, C. López, A. Geyer, R. Abella, M. Tárrega, M.J. Blanco, A. Castro and C. Rodríguez (2013a). Causes and mechanisms of the 2011-2012 El Hierro (Canary Islands) submarine eruption, *J. Geophys. Res. Solid Earth*, 118, 823-839; doi:10.1002/jgrb.50087.
- Martí, J., A. Castro, C. Rodríguez, F. Costa, S. Carrasquilla, R. Pedreira and X. Bolos (2013b). Correlation of Magma Evolution and Geophysical Monitoring during the 2011-2012 El Hierro (Canary Islands) Submarine Eruption, *J. Pet.*, 54 (7), 1349-1373; doi:10.1093/petrology/egt014.
- Meletlidis, S., A. Di Roberto, M. Pompilio, A. Bertagnini, I. Iribarren, A. Felpeto, P.A. Torres and C. D'Oriano (2012). Xenopumices from the 2011-2012 submarine eruption of El Hierro (Canary Islands, Spain): Constraints on the plumbing system and magma ascent, *Geophys. Res. Lett.*, 39, L17302; doi:10.1029/2012GL052675.
- Mogi, K. (1958). Relations between the eruptions of various volcanoes and the deformations of the ground surface around them, *Bull. Earthquake Res. Inst.*, University of Tokyo, 36, 11-123.
- Montesinos, F.G., J. Arnos, M. Benavent and R. Vieira (2006). The crustal structure of El Hierro (Canary Islands) from 3-d gravity inversion, *J. Volcanol. Geoth. Res.*, 150, 283-299; doi:10.1016/j.jvolgeores.2005.07.018.
- Münn, S., and A. Klügel (2006). Gravitational spreading controls rift zones and flank instability on El Hierro, Canary Islands, *Geol. Mag.*, 143, 257-268; doi:10.1017/S0016756806002019.
- Pérez, N.M., G.D. Padilla, E. Padrón, P.A. Hernández, G.V. Melián, J. Barrancos, S. Dionis, D. Nolasco, F. Rodríguez, D. Calvo and I. Hernández (2012). Precursory diffuse CO<sub>2</sub> and H<sub>2</sub>S emission signatures of the 2011-2012 El Hierro submarine eruption: Canary Islands, *Geophys. Res. Lett.*, 39; doi:10.1029/2012GL052410.
- Pollard, D.D., O.H. Muller and D.R. Dockstader (1975). Form and growth of fingered sheet intrusions, *Geol. Soc. Am. Bull.*, 86, 351-363; doi:10.1130/0016-7606(1975)86<351:TFAGOF>2.0.CO;2.
- Prates, G., A. Garcia, A. Fernández-Ros, J.M. Marrero, R. Ortiz and M. Berrocoso (2012). Enhancement of sub-daily positioning solutions for surface deformation surveillance at El Hierro volcano (Canary Islands, Spain), *B. Volcanol.*, 75, 724; doi:10.1007/s00445-013-0724-3.
- Ranero, C.R., M. Torne and E. Banda (1995). Gravity and multichannel the seismic reflection constraints on lithospheric structure of the Canary Swell, *Mar. Geophys. Res.*, 17, 519-534; doi:10.1007/BF01204342.
- Rivera, J., G. Lastras, M. Canals, J. Acosta, B. Arrese, N.

- Hermida, A. Micallef, O. Tello and D. Amblas (2013). Construction of an oceanic island: Insights from the El Hierro (Canary Islands) 2011-2012 submarine volcanic eruption, *Geology*, 41 (3), 355-358; doi:10.1130/G33863.1.
- Roman, D.C., J. Neuberg and R.R. Lockett (2006). Assessing the likelihood of volcanic eruption through analysis of volcanotectonic earthquake fault-plane solutions, *Earth Plan. Sci. Lett.*, 248, 244-252; doi:10.1016/j.epsl.2006.05.029.
- Rubin, A.M., D. Gillard and J.-L. Got (1998). A reinterpretation of seismicity associated with the 1983 dike intrusion at Kilauea Volcano, Hawaii, *J. Geophys. Res.*, 103, 10003-10015; doi:10.1029/97JB03513.
- Santana-Casiano, J.M., M. González-Dávila, E. Fraile-Nuez, D. de Armas, A.G. González, I. Domínguez Cerdeña and J.F. Escánez (2013). The natural ocean acidification and fertilization event caused by the submarine eruption of El Hierro, *Sci. Rep.*, 3; doi:10.1038/srep01140.
- Schofield, N., C. Stevenson and T. Reston (2010). Magma fingers and host rock fluidization in the emplacement of sills, *Geology*, 38 (1), 63-66; doi:10.1130/G30142.1.
- Sigmarsson, O., D. Laporte, B. Devouard, J. Martí, J.L. Devidal and M. Carpentier (2012). Formation of U-depleted rhyolite from a basanite at El Hierro, Canary Islands, *Contrib. Min. Pet.*, 165, 601-622; doi:10.1007/s00410-012-0826-5.
- Smith, P.M., and P.D. Asimow (2005). *Adiabat\_1ph*: A new public front-end to the MELTS, pMELTS, and pHMELTS models, *Geochem. Geophys. Geosys.*, 6 (1); doi:10.1029/2004GC000816.
- Stroncik, N.A., A. Klügel and T.H. Hansteen (2009). The magmatic plumbing system beneath El Hierro (Canary Islands): constraints from phenocrysts and naturally quenched basaltic glasses in submarine rocks, *Contrib. Min. Pet.*, 157, 593-607; doi:10.1007/s00410-008-0354-5.
- Troll, V.R., A. Klügel, M.-A. Longpré, S. Burchardt, S. F.M. Deegan, J.C. Carracedo, S. Wiesmaier, U. Kueppers, B. Dahren, L.S. Blythe, T. Hansteen, C. Freda, D.A. Budd, E.M. Jolis, E. Jonsson, F. Meade, S. Berg, L. Mancini and M. Polacci (2011). Floating sandstones off El Hierro (Canary Islands, Spain): The peculiar case of the October 2011 eruption, *Solid Earth Discussion*, 3, 975-999; doi:10.5194/sed-3-975-2011.
- Villasante-Marcos, V., and F.J. Pavón-Carrasco (2014). Palaeomagnetic constraints on the age of Lomo Negro volcanic eruption (El Hierro, Canary Islands), *Geophys. J. Int.*, 199, 1497-1514; doi:10.1093/gji/ggu346.

---

Corresponding author: Alessio Di Roberto,  
Istituto Nazionale di Geofisica e Vulcanologia, Sezione di Pisa,  
Pisa, Italy; email: alessio.diroberto@ingv.it.

© 2015 by the Istituto Nazionale di Geofisica e Vulcanologia. All rights reserved.

Meletlidis et al., *New insight into the 2011-2012 unrest and eruption of El Hierro Island (Canary Islands) based on integrated geophysical, geodetical and petrological data*

## Supplementary materials

### 1. Methods and materials

#### 1.1. Seismicity

On July 2011, only two seismic stations were present on the island of El Hierro (stations CHIE and CTIG in Figure 1). Seven additional seismic stations with real-time data transmission were deployed on the island within the first days of the seismic unrest (Figure 1). The configuration of the seismic network allowed localization of hypocentral positions with uncertainties in the order of 3 km in horizontal direction and of 5 km in depth (IGN seismic catalogue at [www.ign.es](http://www.ign.es)). These high uncertainties are typical of volcanic islands and arise because of the geometric limitations of the seismic network and for the big lateral non-homogeneities of the velocity models. We partially overcame this issue using hypocentral relocations of Domínguez Cerdeña et al. [2014] obtained by means of hypoDD algorithm [Waldhauser and Ellsworth 2000] on earthquakes characterized by magnitude  $>1.5$  (ca. 3600). This method allowed more high-resolution hypocentral relocation and ensured a higher quality of the results respect to previous published researches. The velocity model used for these new locations was a four-layer model based on Dañoibeitia [1980] and was the same used to obtain catalogue hypocenters.

The dataset used in this work includes the 3600 pre-eruptive events with magnitude larger than 1,5 relocated by Domínguez Cerdeña et al. [2014], the 2400 syn-eruptive events and the 5600 post eruptive earthquakes located during the 6 reactivations from June 2012 to March 2014. The last two sets were obtained from the public IGN seismic catalogue at [www.ign.es](http://www.ign.es).

The problem to obtain the focal mechanism of the whole dataset is difficult due to the low number of seismic stations and also most of them are short period.

#### 1.2. Deformation

Within the first weeks of the seismic unrest, 14 GPS stations were deployed all over the El Hierro Island (Figure 1) to complement the pre-existing station (FRON) run by the Canary Islands Government. One of them (HI00 - Valverde) was run by the CSIC-UCA scientific group and three of the receivers were installed in a periodical basis (every 2 days once the eruption started) along the West Rift. GPS data used in this study

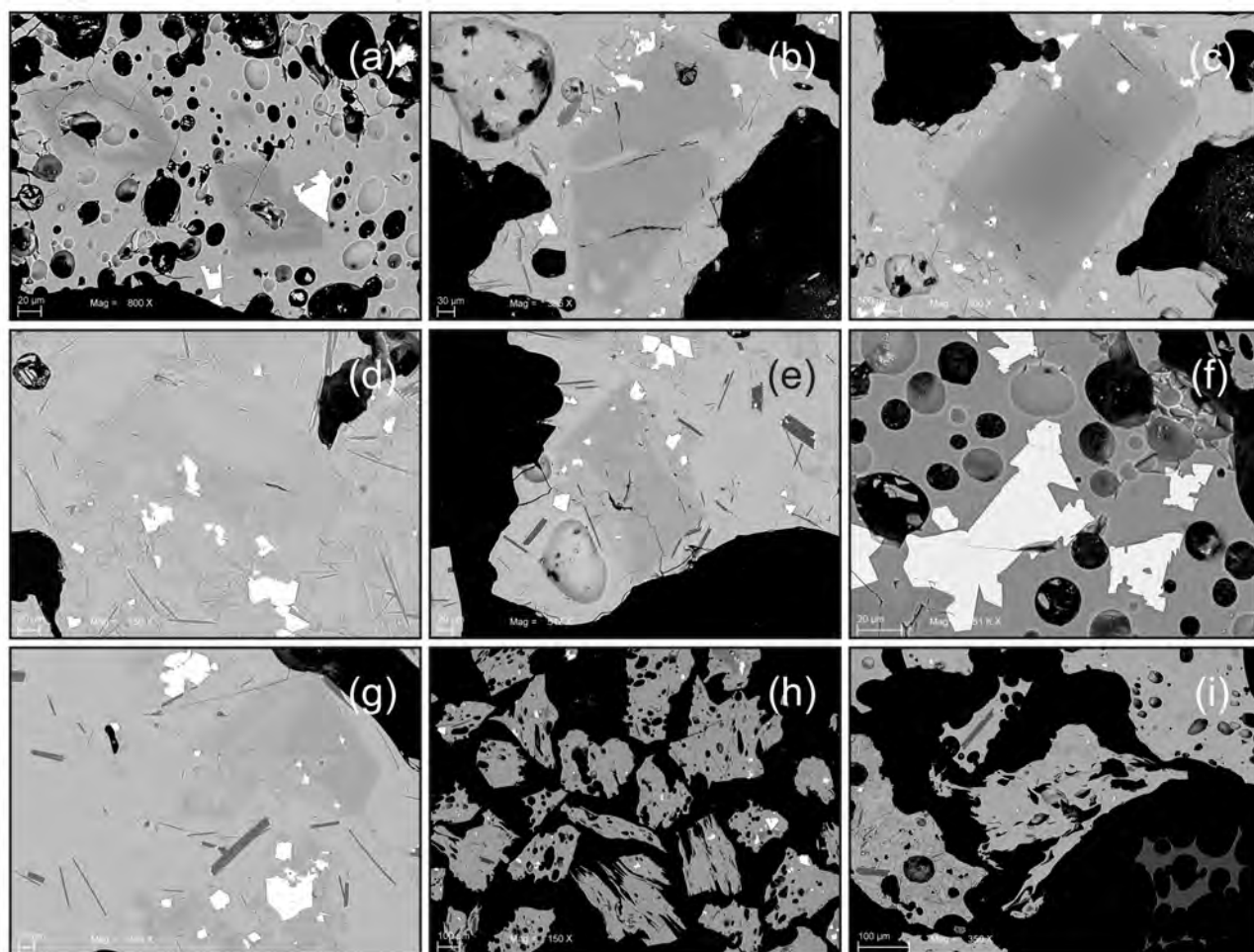
have a 30 s sampling rate and were processed using Bernese software version 5.0 [Dach et al. 2007] to obtain daily coordinates solutions. The data were analyzed in the framework of a GPS network consisting of more than 30 GPS stations located in the Canary Islands, Azores, south of Spain and north of Africa. Reference frame ITRF2008 was determined using minimum constrains to an IGS core site group of five stations. The ocean-loading model FES2004 was applied and the IGS absolute antenna phase center model was applied for satellite and stations antennas. Precise satellite orbits from the IGS were also used [Kouba 2009]. North, east and vertical deformation components (n,e,u) were calculated daily from the coordinates obtained in the process.

Then, deformation data were calculated for each pre-eruptive phase based on the GPS time series and was inverted using the dMODELS software package [Battaglia et al. 2013a, 2013b], which uses a nonlinear inversion algorithm to determine the best fit parameters for the deformation source (i.e., location, depth, pressure/volume).

Due to the radial pattern of ground deformation seen on the island and the short-time scale of the unrest episode, we present here the results for each pre-eruptive phase of a spherical point source of varying pressure within an elastic, isotropic and homogeneous half-space [Mogi 1958] (Poisson's ratio equal to 0.25) (Table 1). This model has been proved to be a good approximation in El Hierro 2011-2012 eruption based on InSAR data [González et al. 2013]. Although more models need to be addressed, and noting that heterogeneities of the media or the topography of the island are not considered and might bias the results [Masterlark 2007], this simple model should be considered as a first approximation of the deformation source [Lisowski 2006], useful to track and evaluate the evolution of magma with time.

#### 1.3. Gravimetry

A Micro-g Lacoste gphone was deployed on the island since August 2011 [Sainz-Maza Aparicio et al. 2014]. At the beginning of the crisis it was installed in El Golfo area, but due to the seismicity migration it was moved in the center of the island some days before the onset of the eruption (Gh02; Figure 1). Gravity data were originally recorded at 1 Hz sampling rate. Unfortunately, at this sampling rate, the noise due to the continuous seismicity over the gravity sensor covered any variation in the gravity signal. To overcome this issue the data have been decimated and filtered at 1 min. Sampling of gravimeter levels (tiltmeters value), was performed at 1 s.



**Supplementary Figure 1.** Scanning electron microscope backscattered (SEM-BSE) images representative of textures and main mineral assemblage identified in products erupted during the 2011-2012 eruption of El Hierro. (a) Skeletal olivine micro-phenocrysts in basanite crust from coconut-like bombs erupted on October 15, 2011; (b) Olivine phenocrysts with embayed boundaries from floating lava balloon emitted on January 1, 2012; (c) Normally zoned ( $Fo_{87-82}$ ) olivine phenocrysts from floating lava balloon emitted on December 6, 2011; (d) Phenocrysts (patchy, hourglass and oscillating zoned), micro-phenocrysts (hourglass zoned) and microlites of clinopyroxene in glassy matrix from lava balloon emitted on December 6, 2011. All crystals exhibit texture typical of fast growth. (e) Clinopyroxene phenocrysts (hourglass and oscillating zoned) in glassy matrix with spinels and plagioclase microcrystals from January 4, 2012, products. (f) Typical fast grow texture on spinel crystals from basanitic crust of bombs erupted on October 15, 2011; (g) Acicular to elongated crystals of plagioclase in glassy groundmass from January 19, 2012, floating lava balloons. (h-i) Poorly to moderately vesicular ash sampled in water column on November 5, 2011. To notice in (i) the high-vesicular, dark fragment of xenopumice with rhyolitic composition that was probably carried from the seafloor during the intense gas and ash emission.

#### 1.4. Sampling and study of erupted products

Detailed textural, petrographic and geochemical (bulk rock, groundmass glass and mineral phases composition) analysis were completed on 15 samples. Samples were collected during almost the entire duration of the eruption between October 15, 2011, and February 12, 2012 (Table 2). The sampling was not always possible because of adverse sea conditions and the extreme danger of sampling operations. Samples consist of three floating scoriaceous fragments, nine lava balloons and three samples of ash and lapilli. Two samples of ash and fine lapilli (November 5 and 6, 2011) were sampled in the water column during a survey of R/V Ramón Margalef (Spanish Institute of Oceanography - IEO) by means of WP2 closing net. They were recovered during the periods of extremely intense degassing when

episodes of strong bubbling took place (November 5 and 6, 2011). A third ash sample was recovered on February 12, 2012, during the final stages of the eruption in a period of low degassing.

For each sample (except for ash and fine lapilli) at least three polished thin sections were prepared being representative of the entire thickness of the sample, from the external and quenched rim which was originally in contact with the seawater, to the inner portion. Ash and lapilli samples were embedded in epoxy resin and prepared as standard thin section.

Samples textures were studied using an optical microscope and a Zeiss EVO-MA-10 scanning electron microscope (SEM) at the Istituto Nazionale di Geofisica e Vulcanologia (INGV-Sezione di Pisa).

Chemical major element composition of glass was

analyzed at the Laboratorio Microsonda Elettronica C.N.R.-I.G.G. of Florence using a JEOL JXA-8600 microprobe (EMP) equipped with 4 wavelength dispersive spectrometers (operating conditions 15 kV accelerating voltage, 10 nA beam current, 10  $\mu$ m probe diameter and 20 s (10 s for Na and 40 s for Cl and F) and 20 s acquisition time for peak and background (40 s for Cl and F, respectively). Glass analysis was performed by EMP with defocused beam (10  $\mu$ m) on selected microlite-free glass chips representing the quenched external portion of the samples. This ensures that glass compositions are not affected by post-eruptive crystallization. The composition of mineral phases was analyzed at the INGV-Sezione di Pisa, with SEM equipped with Isis EDS microanalysis system (operating conditions 15 kV, 400-500 pA, 1-2  $\mu$ m of probe diameter, 100 seconds of acquisition time, ZAF and natural mineral as calibration standards).

The chemical composition of bulk rocks was determined by ALS Minerals, (Sevilla, Spain) using lithium metaborate/lithium tetraborate fusion followed by ICP-AES for whole rock analyses (ALS package ME-ICP06) and ICP-MS for trace elements (ALS package ME-MS81).

## References

- Battaglia, M., P.F. Cervelli and J.R. Murray (2013a). dMODELS: A MATLAB software package for modeling crustal deformation near active faults and volcanic centers, *J. Volcanol. Geoth. Res.*, 254, 1-4.
- Battaglia, M., P.F. Cervelli and J.R. Murray-Muraleda (2013b). Modeling crustal deformation - A catalog of deformation models and modeling approaches, *U.S. Geological Survey Techniques and Methods*, vol. 13, chap. B1, 96 p.
- Dach, R., U. Hugentobler, P. Fridez and M. Meindl (2007). Bernese GPS Software Version 5.0, Astronomical Institute, University of Bern, Report.
- Dañobeitia, J.J. (1980). Interpretación de la estructura de la corteza en el Archipiélago Canario a partir de perfiles sísmicos profundos de refracción (Ph.D. thesis), Madrid, Universidad Complutense de Madrid, Spain, 91 p.
- Domínguez Cerdeña, I., C. del Fresno and A. Gomis Moreno (2014). Seismicity patterns prior to the 2011 El Hierro Eruption, *B. Seismol. Soc. Am.*, 104 (1), 567-575; doi:10.1785/0120130200.
- González, P.J., S.V. Samsonov, S. Pepe, S.F. Tiampo, P. Tizzani, F. Casu, J. Fernández, A.G. Camacho and E. Sansosti (2013). Magma storage and migration associated with the 2011-2012 El Hierro eruption: Implications for crustal magmatic systems at oceanic island volcanoes, *J. Geophys. Res., Solid Earth*, 118, 1-17; doi:10.1002/jgrb.50289.
- Kouba, J. (2009). A guide to using International GNSS Service (IGS) products: IGS products; <http://igsb.jpl.nasa.gov/components/usage.html>.
- Lisowski, M. (2006). Analytical volcano deformation source models, In: Dzurisin (ed.), *Volcano Deformation*, Springer, Berlin-Heidelberg, 279-304.
- Masterlark, T. (2007). Magma intrusion and deformation predictions: Sensitivities to the Mogi assumptions, *J. Geophys. Res.*, 112, B06419; doi:10.1029/2006JB004860.
- Mogi, K. (1958). Relations between the eruptions of various volcanoes and the deformations of the ground surface around them, *Bull. Earthquake Res. Inst., University of Tokyo*, 36, 11-123.
- Sainz-Maza Aparicio, S., J. Arnosó Sampedro, F. González Montesinos and J. Martí Molist (2014). Volcanic signatures in time gravity variations during the volcanic unrest on El Hierro (Canary Islands), *J. Geophys. Res. Solid Earth*, 119; doi:10.1002/2013JB010795.
- Waldhauser, F., and W.L. Ellsworth (2000). A double-difference earthquake location algorithm: Method and application to the northern Hayward fault, *B. Seismol. Soc. Am.*, 90, 1353-1368; doi:10.1785/0120000006.

---

Corresponding author: Alessio Di Roberto,  
Istituto Nazionale di Geofisica e Vulcanologia, Sezione di Pisa,  
Pisa, Italy; email: [alessio.diroberto@ingv.it](mailto:alessio.diroberto@ingv.it).

© 2015 by the Istituto Nazionale di Geofisica e Vulcanologia. All rights reserved.

*Annex 6.5*

*The 1909 Chinyero eruption on Tenerife (Canary Islands): insights from historical accounts, and tephrostratigraphic and geochemical data.*

*Di Roberto, A., Bertagnini, A., Del Carlo, P., Meletlidis, S., Pompilio, M.*

# The 1909 Chinyero eruption on Tenerife (Canary Islands): insights from historical accounts, and tephrostratigraphic and geochemical data

A. Di Roberto<sup>1</sup> · A. Bertagnini<sup>1</sup> · P. Del Carlo<sup>1</sup> · S. Meletlidis<sup>2</sup> · M. Pompilio<sup>1</sup>

Received: 12 July 2016 / Accepted: 12 November 2016  
© Springer-Verlag Berlin Heidelberg 2016

**Abstract** The last eruption on Tenerife (Canary Islands, Spain) started on 18 November 1909 from the El Chinyero vent on the northwestern Santiago rift. This fissural eruption was well documented by scientists and eyewitnesses, but there is a lack of data on the high-energy phase that produced the most significant emissions of ash and lapilli at the onset of the eruption. Here, we review historical documents (e.g. newspapers, dispatches, telegrams); eyewitness accounts and scientific reports were reviewed from a volcanological perspective and integrated with data from the analysis of deposit features, allowing an accurate reconstruction of the eruption and its dynamics. The 1909 eruption of Chinyero was fed by a compositionally discrete magma batch that ascended rapidly within the crust, producing rather violent pulsating Strombolian explosive activity in the early phases of the eruption. This activity produced a ca. 80 m high scoria cone and heavy fall-out of lapilli and ash over the entire northern sector of the island of Tenerife. The energy of explosive activity waned after 3 days, giving way to the weak Strombolian explosive activity that contributed to a lesser extent to the buildup of the pyroclastic pile. Eruptions such as those from the Chinyero vent in 1909 are representative of rift activity on Tenerife and constitute a volcanic hazard for present-day inhabitants.

**Keywords** Chinyero · Tenerife · Violent strombolian · Volcanic hazard

## Introduction

Thirteen eruptions have been identified in the last 2000 years of activity at the Teide Volcanic Complex (Tenerife, Canary Islands; Carracedo 2013). This volcanic activity includes felsic eruptions from the central Pico Viejo–Teide volcanic complex (summit activity and peripheral domes) and basaltic eruptions along the rift systems. In historical times, six basaltic eruptions (1492, 1704, 1705, 1706, 1798 and 1909) produced scoria cones and lava flows. Some of these (e.g. the 1706 eruption of Garachico Volcano and the 1909 eruption) caused extensive damage and threatened the population, while during other eruption (e.g. 1704–1705), casualties were caused by earthquakes associated with volcanic activity (Romero 1991).

A major effort has been made to assess volcanic hazards in the area, mainly in relation to a possible felsic-intermediate eruption from the Pico Viejo–Teide volcanic complex (Marti et al. 2008). In contrast, little attention has been given to basaltic flank eruptions. Although these eruptions are considerably less dangerous than the corresponding felsic ones (as a whole less explosive and intense), they are more frequent and may occur much closer to inhabited areas, thereby representing a great threat to the population, infrastructure and economy of the Canary Islands. In particular, ash produced during explosive phases might affect wide areas downwind of the vent and cause damage to agriculture, tourism, human health, transportation and utility systems (air transportation, power and water supply and waste water systems) on Tenerife and its neighbouring islands.

This paper reports on the 1909 basaltic eruption of Chinyero, the most recent eruption on Tenerife. We review collected historical sources, reconstruct the distribution and

---

Editorial responsibility: P. Wallace

✉ A. Di Roberto  
alesio.diroberto@ingv.it

<sup>1</sup> Istituto Nazionale di Geofisica e Vulcanologia, Sezione di Pisa, Via della Faggiola 32, 56126 Pisa, Italy

<sup>2</sup> Centro Geofísico de Canarias, Instituto Geográfico Nacional, c/La Marina, 20, 38001 Santa Cruz de Tenerife, Spain

volume of deposits and describe the nature, texture and chemical compositions of the erupted products, focusing mainly on the pyroclastic products. In addition, simple petrological modelling has yielded information on the dynamics of magma ascent during the eruption. The results of this study provide new insights into the size, intensity and dynamics of the eruption and into the nature and dispersal of products from the last, but still poorly known, eruption of Tenerife. This information is crucial in assessing volcanic hazards posed by small-scale basaltic eruptions in the Canary Islands.

## Geological background

Tenerife is the largest volcanic island in the Canary archipelago (Fig. 1). The subaerial portion of the island consists of a composite volcanic complex formed by alternating eruptive and destructive phases in the last 12 Ma (Ancochea

et al. 1990; Martí et al. 1994). The backbone of the volcano developed during a shield-building phase, today represented by the Anaga (6.5–3.6 Ma), Teno (6.7–4.5 Ma) and Roque del Conde massifs (11.6–3.5 Ma) cropping out as eroded remnants on the three corners of the island. Between ca. 3.3 and 1.9 Ma, the edifice underwent a phase of volcanic quiescence and erosion. Activity resumed approximately at 1.9 Ma and continued until 0.2 Ma, resulting in the construction of the central Las Cañadas composite volcano (Ancochea et al. 1990; Martí et al. 1994). In the same period, predominantly basaltic activity occurred along two well-developed rift systems, one oriented in a NE (the Dorsal rift) direction and the other in a NW direction (Santiago rift), and more diffusely in the southern part of the island (southern volcanic zone). More recently, since ca. 175 ka, volcanic activity within the Las Cañadas caldera formed the central Teide–Pico Viejo edifice and was accompanied by the development of many small monogenetic cones through eruptions occurring outside the

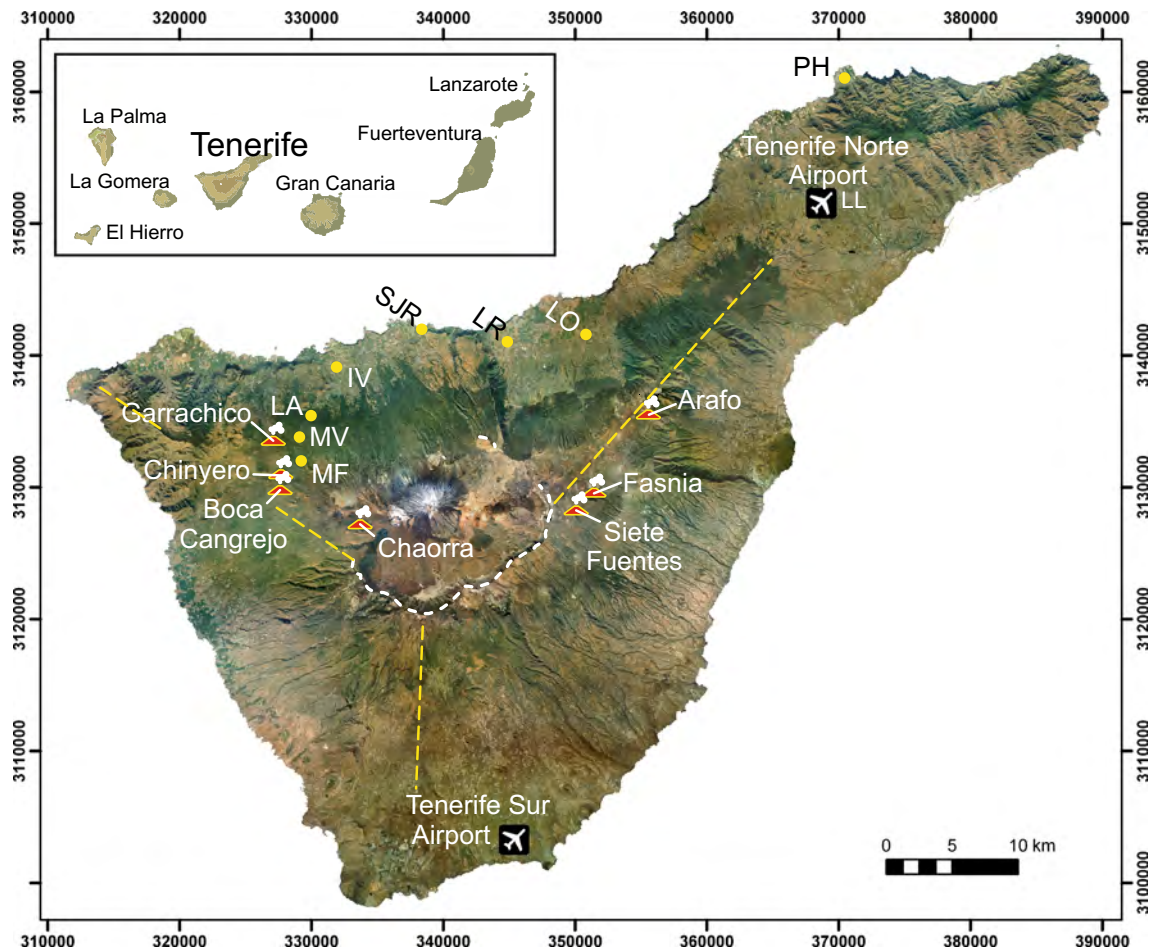


**Fig. 1** Satellite image of Tenerife island with highlighted main geographic features described in the text. Red volcanoes indicate vents of historical flank eruptions of Boca Cangrejo (1492), Siete Fuentes (1704), Fasnía (1705), Arafo (1705), Garrachico (1706), Chaorra (1798) and Chinyero (1909). Yellow dots indicate the main localities mentioned in the paper: IV Icod de los Vinos, LA Las Abiertas, LL La

Laguna, LO La Orotava, LR Los Realejos, MF Montaña de la Flores, MV Montaña de Vancheque, PV Pico Viejo, T Teide, SJR San Juan de la Rambla. White dashed line indicates the rim of Las Cañadas caldera, whereas the yellow line highlights the direction of the three rift zones. Inset: Map of the Canary Islands. Reference system UTM Zone 28N, Datum WGS84

caldera. In historical times, five mainly basanite eruptions have occurred outside the Las Cañadas caldera: in 1492 (Boca Cangrejo), 1704–1705 (Arafo-Fasnia-Siete Fuentes), 1706 (Garrachico) and 1909 (Chinyero; Carracedo 2013). In addition, magma with intermediate composition (tephriphonolite) erupted on 1798 during the Chaorra eruption on the southwest flank of Pico Viejo (Carracedo 2013; Fig. 1).

## Methods

Grain size and component analyses were carried out on tephra samples in the laboratory. Samples were washed in an ultrasonic bath for 5 min and subsequently sieved at one  $\phi$  ( $\phi$  = negative log base 2 of the grain diameter) for the  $-4 \phi$  (16 mm) to  $+5 \phi$  (0.032 mm) grain size range. The  $Md\phi$  (median) and  $\sigma\phi$  (sorting) were calculated from the grain size distribution (Inman 1952). The total grain size distribution of pyroclastic deposits cropping out in proximal areas was estimated using field data and the TOTGS (Biass and Bonadonna 2014) Matlab® graphical user interface for the code published by Bonadonna and Houghton (2005).

Three samples representative of the whole pyroclastic fall-out sequence were selected for detailed textural, mineralogical and geochemical analyses: samples 11A, B and C (Fig. 2) represent the base, the intermediate portion and the upper portion of the eruptive sequence, respectively. These were sampled in a stratigraphic trench (130 cm) dug ca. 250 m NE of the main vent and 50 m from the base of the cone (Fig. 2), where the pyroclastic fallout deposit is thickest.

Textural observations and major element analysis of mineral phases and matrix glasses were carried out using a Zeiss EVO MA 10 scanning electron microscope equipped with an Oxford Si(Li) energy-dispersive X-Ray detector at Istituto Nazionale di Geofisica e Vulcanologia (INGV), Sezione di Pisa. Analytical conditions were as follows: 15 kV accelerating voltage, 400–500 pA beam current, 1–2  $\mu$ m beam diameter, 100 s acquisition time, ZAF and natural minerals as calibration standards. Analytical errors were estimated from mineral and natural glass standards and are <1% for concentrations greater than 15 wt.%, 2% for concentrations of 5–15 wt.%, 10% for concentrations of 1–5 wt.% and 30% for concentrations <1 wt.%. ALS Minerals (Sevilla, Spain) determined the chemical composition of bulk rocks using lithium metaborate/lithium tetraborate fusion followed by ICP-AES for major element analysis (ALS package ME-ICP06) and ICP-MS for trace element analysis (ALS package ME-MS81).

## Results

### Historical reports and eyewitness accounts

We collected available historical sources on the 1909 Chinyero eruption and reviewed them from a volcanological perspective. Most data were gathered from the exhaustive descriptions of the eruption made by Ponte and Cologan (1911) and Fernández Navarro (1911). The former provide a personal eyewitness account of the eruption starting the early morning of 19 November (second day of the eruption) until 26

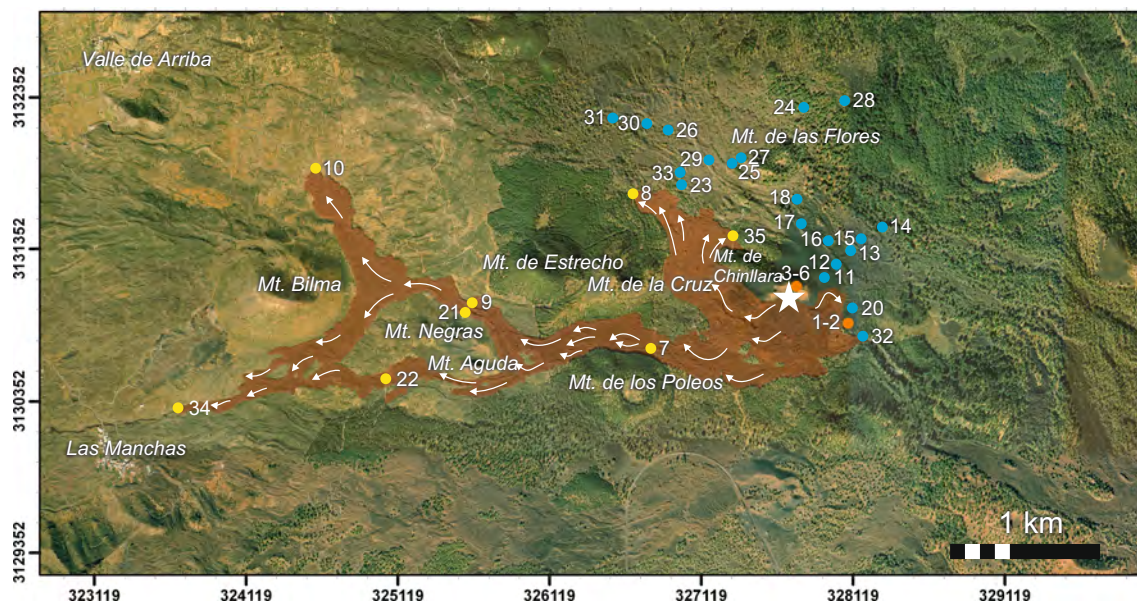


**Fig. 2** Satellite view of the area involved in the 1909 eruption of Chinyero, Tenerife, with highlighted main geographic features described in the text. White star indicates the main vent of Chinyero. Coloured dots represent stratigraphic sections identified, measured and

described around the cone of Chinyero and yielding samples of pyroclastic fall deposit (blue dots), lava (yellow dots) and spatter (orange dots). Reference system UTM Zone 28N, Datum WGS84

November 1909, including a description of the eruptive phenomena and data on the nature, volume and impact of erupted products, as well as an accurate description of the evolution of the lava flow field. The latter combines numerous eyewitness accounts to draw a very clear picture of the eruption and also describes the dispersal of pyroclastic products in medial and distal sites. Additional information derives from the paper by Perret (1914), who visited the site of the eruption in December 1909. Lastly, much crucial information was derived from dispatches and telegrams sent by/to the local authorities, as well as from reports in newspapers of the time, most of which were collected by Tous Meliá (2011).

### *The eruption chronology*

The eruption of Chinyero was preceded by intense seismic activity. From March 1908 until October 1909, a number of low- to high-intensity tremors were perceived in different areas of the island (Albert et al. 2016). Some tremors were also felt on the island of Gran Canaria, ca. 100 km from Tenerife (inset in Fig. 1; Perret 1914; Albert et al. 2016). The earthquakes became more frequent in November 1909; at La Orotava village (LO in Fig. 1), located ca. 25 km NE of the future vent, witnesses report that the branches of Araucaria trees shook continuously due to seismic activity (Perret 1914). On April 1909, a strong fumarole emission began from the central Teide Volcano crater, as revealed by the deposition of sulphur; this was accompanied by a general increase in ground temperature throughout the cone which melted the snowcap (Fernández Navarro 1911). Fumarole activity in the following months was so intense that on 22 June 1909, the Barcelona newspaper *La Vanguardia* reported that a new volcano had opened at the base of Pico del Teide, where large plumes of steam were issued from the foot of the cone. No information on other possible precursors such as ground deformation or degassing was reported, not even in other areas of the island.

The eruption began at 2:30 p.m. on 18 November 1909 and ended on 28 November 1909. It took place on a gently WNW-sloping surface and on the flanks of Montaña de Chinllara (Fig. 2), a ca. 40 m-high horseshoe-shaped cone resulting from an older eruption. José Hernández Lorenzo and his son Miguel Hernández Grillo, who were working 300 m from the future Chinyero vent (Fernández Navarro 1911), witnessed the onset of the eruption. They reported that the initial phase of the eruption consisted in an energetic explosion, during which gorse bushes, earths and blocks of rock were thrown about 150 m into the air; it was accompanied by the emission of dark, hot “sand” (Fernández Navarro 1911).

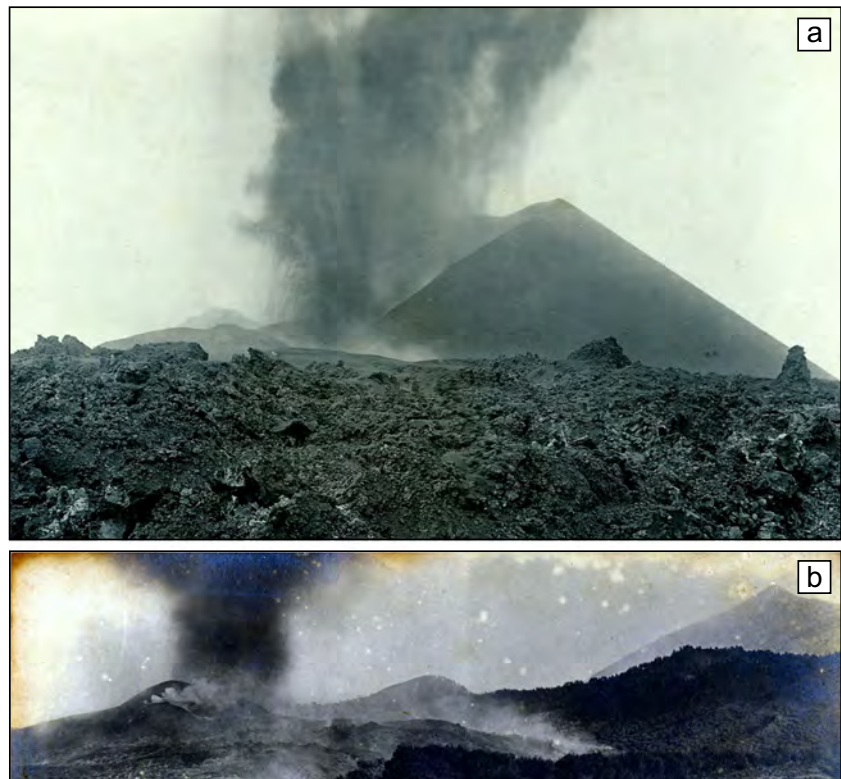
No detailed information on the style or intensity of the eruption is available for the subsequent 17 h. The first detailed description of eruptive phenomena refers to 19 November, the second day of eruption, when at 7:30 a.m. Antonio de Ponte and Cologan reached the site of the eruption. However, in the afternoon and during the night of 18 November, the eruption must have been

relatively violent and intense. This is consistent with the details reported in a telegram sent by the Mayor of Icod (9 km from the Chinyero vent) to the governor during the night of 18 November in which he describes: “...*Very great detonations, a glowing red column of smoke* and with the description of Fernández Navarro (1911) of a “*light [that] was strong enough so that the phenomenon [the eruptive column] was clearly visible from La Laguna, and even from the islands of Gomera and Gran Canaria, even in points from which the volcano is not directly visible*”. Note that Chinyero is ca. 48 km from the city of La Laguna, from which it is hidden by the ca. 1100 m-high margin of the NE rift. Similarly, Gran Canaria is located about 100 km from the Chinyero vent. Moreover, the Chinyero vent is not directly visible from any city in Gran Canaria because it is hidden by the volcanic edifices of Teide and Pico Viejo and by the margin of Las Cañadas caldera, which reaches a height of 2700 m.

On the early morning of 19 November, an undefined number of eruptive vents (up to nine are reported) aligned along a ca. 500 m-long SE–NW fracture were simultaneously active. Volcanic activity through multiple vents was also caught in photographs (Fig. 3; Tous Meliá 2011). However, eyewitnesses agree that activity was soon limited to a few (possibly 3–4) very closely spaced vents near the present cone and that these vents remained active until the end of the eruption on 28 November 1909. On the morning of 19 November, only 17 h after the beginning of the eruption, a cone as high as ca. 80 m had already developed (Fig. 3). During the first 3 days, the eruption consisted of persistent, energetic explosions closely spaced in time that produced a shower of highly fragmented, incandescent pyroclastic material, alternating with phases during which almost continuous fire fountaining fed the lava flows (Fernández Navarro 1911; Ponte and Cologan 1911). During this period, the eruption intensity increased progressively. From 22 November 1909 (day four of the eruption) to the end of the eruption, the intensity decreased progressively: explosive activity consisting of rhythmic, low energy Strombolian explosions was accompanied by weak, thin and whitish vapour plumes (Fig. 3; Fernández Navarro 1911). A final flare-up of the eruption occurred on the ninth day, during which Vulcanian explosions (Fernández Navarro 1911; Ponte and Cologan 1911) emitted dark ash-laden clouds, blocks and bombs.

The emission of lava was simultaneous with the onset of explosive activity and on the morning of 19 November a lava flow of ca. 200 m and with a thickness of about 2 m had already emplaced (Ponte and Cologan 1911). The emission took place initially from numerous vents aligned along the eruptive fissure but soon it concentrated in two or three vents located close to the crater that remained active until the end of the eruption. Fernández Navarro (1911) reports that the lava was extremely fluid, hot and able to flow at a considerable average speed of 21 m/h (ca. 4 km in 8 days). The shape of the lava flow field was strongly controlled by ground morphology, and flows developed as a braided system around previous

**Fig. 3** Photographs of the 1909 eruption of Chinyero volcano (National Heritage of Spain). Eruption seen from **a** el Pino de Chasna and **b** Montana Poleos, respectively



topographic obstacles (Fig. 2). One main lava flow extended 4.6 km westward along the Santiago Valley (barranco los Ovejeros). This flow initially ran between the old volcanic edifices of Mt. de la Cruz and El Estrecho (to the North) and of Mt. de los Poleos (to the South). About 2 km from the vent, the principal flow reached a series of old conelets (Mt. Negras, Mt. Aguda, Las Piedras), where it branched into two flows. The first continued for ca. 1.3 km in a NW direction before dividing near Mt. de Bilma into two more branches directed NW (ca. 800 m) and SW (ca. 1 km). The second branch ran ca. 2.2 km in a westward direction, stopping 500 m short of the village of Las Manchas and attaining the greatest distance from the cone of ca. 4.6 km. A secondary, relatively shorter lava flow extended for less than 1.3 km N–NW, bordering Mt. de la Cruz and forming a lava pond. Topographic obstacles stopped minor eastward flows. The lava field is reported to have a total volume of  $11\text{--}15 \times 10^6 \text{ m}^3$  (Fernández Navarro 1924; Carracedo 2013) and a surface area of  $1.73 \text{ km}^2$  (Solana 2012). There were no casualties or damage to villages, but lava flow invasion and lapilli/ash fallout inflicted great damage to agriculture. The eruption had a very negative social impact on the island population and on foreign tourism (Barrera 2009).

#### *Eruption deposits*

According to eyewitness descriptions, pyroclastic products in very proximal sites consisted of juvenile vesicular black lapilli

and dense bombs (up to  $1 \text{ m}^3$  in volume), which, to the east, formed a crescent-shaped scoria cone 80 m high and 300 m wide (Fernández Navarro 1911). Fernández Navarro (1911) reported more than 3-m thick accumulations of pyroclastic products close to the cone (Table 1). The same author reports that the thickness of the deposit (consisting mainly of lapilli) 1 km from the vent was sufficient to uniformly mantle the pre-existing topography and completely cover the unevenness of the ground (e.g. small drains and pits); it was therefore of the order of several tens of centimetres. At this distance, Collet and Montagner (1910) estimate a minimum deposit thickness of 10–20 cm, whereas close to Mt. de las Flores (Figs. 1 and 2), Ponte and Cologan (1911) report the fallout of egg-sized scoria on the early morning of 19 November (Table 1).

In medial to distal areas, several authors report the heavy fallout of lapilli and ash that was dispersed in a NE direction by the prevailing southerly winds. The fallout of black lapilli “with size comparable to that of a pea” occurred at Las Abiertas (LA in Fig. 1, Table 1) located ca. 5 km from the vent (Fernández Navarro, (1911)). At approximately the same distance, close to Mt. de Vancheque (MV in Fig. 1), “the walk toward the Chinyero was [as] difficult as walking on a sand beach” (Fernández Navarro 1911), implying that the thickness of the lapilli was likely of the order of tens of centimetres.

On 20 November 1909, the La Orotava newspaper “Arautápala” reported that: “at a distance of two leagues [ca. 11 km] small volcanic scoriae with the size of an hazelnut [i.e. ca. 15 mm] were driven by light atmospheric currents;

**Table 1** Approximate size of particles from the fallout and thickness of deposits reported by scientists and witnesses at various distances from the vent during the 1909 Chinyero eruption

Site	Distance (km-vent)	Approximate size of particles (mm)	Thickness	Reference
–	0	–	>300 cm	Fernández Navarro (1911)
Mt. de las Flores	1	50–70	–	Ponte y Cologan (1911)
–	1	<64	Tens of cm	Fernández Navarro (1911)
Las Abiertas	5	10	–	Fernández Navarro (1911)
close Mt. de Vancheque	5	–	Tens of cm	Fernández Navarro (1911)
Icod	9	9–15	Several cm	Newspaper “Arautápala” 20 November 1909
Icod	9	1–1.8	Several cm	Fernández Navarro (1911)
–	11	9–15	–	Newspaper “Arautápala” 20 November 1909
La Rambla	15	–	A few mm	Cabrera Diaz (1911)
Los Realejos	19	9–15	–	Newspaper “Arautápala” 20 November 1909
La Orotava	25	–	A few mm	Fernández Navarro (1924)
Punta del Hidalgo	52	–	A few mm	Fernández Navarro (1924)
Las Palmas (Gran Canaria)	130	–	–	newspaper “ABC Martes” 23 November 1909

similarly, products of comparable size were transported to the jurisdiction of Los Realejos [LR in Fig. 1, located 19 km from the vent]”; similar pyroclastic products fall “in considerable amount, almost with the intensity of a regular rain, completely covering up the streets of the town of Icod [IV in Fig. 1, located 9 km NNE of Chinyero]”. Similarly, Fernández Navarro (1911), reported that in Icod, “a black cap of ash covered the ground evenly, giving it a weird aspect”. Here, volumes of “2–3 fanegas”, i.e. a traditional volume or capacity unit of measurement equivalent to 55.5 l (ca. 111 to 166.5 l) of ash with the grain size of gunpowder (coarse ash to fine lapilli) were recovered from the rooftops of some houses. Significant fall-out of ash and lapilli also occurred in the village of La Rambla (LR in Fig. 1; Table 1) located ca. 15 km NE of the vent (Cabrera Diaz 1911).

A thin layer of fine ash was deposited on the village of La Orotava, located about 25 km from the vent (Burchard 1909; Fig. 1). On Tenerife, the most distal site where very fine ash fell is Punta del Hidalgo (PH in Fig. 1), some 52 km NE of the Chinyero Vent (Fernández Navarro 1924). Lastly, on 21 November, some ashes reportedly fell out in Las Palmas (Table 1), in the northern portion of the neighbouring island of Gran Canaria, located some 130 km from the vent (inlet in Fig. 1).

There are no clear reports of the maximum height attained by the eruptive column, especially in the early stages of the eruption. However, there are many reports by scientists and eyewitnesses on the maximum height reached by glowing pyroclastic products, especially in the first 3 days of the eruption (Table 2); this ranges from ca. 200 m during the opening

phases (Fernández Navarro 1911) to over 1000 m (Burchard 1909), with values of around 500–700 m reported several times (ABC Martes 1909; El Dia De Madrid 1909; Ponte and Cologan 1911; Tous Meliá 2011; Table 2).

### Field survey and deposit analysis

During fieldwork, we identified, measured and described Chinyero deposits in 35 stratigraphic sections (Fig. 2); these were made in natural exposures, road cuts and trenches dug around the Chinyero scoria cone, yielding 17 samples of pyroclastic fall deposits (blue dots), 10 lava samples (yellow dots) and 6 lava spatter samples (orange dots).

### Pyroclastic fallout proximal stratigraphy, texture and volume

Pyroclastic deposits comprise the Chinyero scoria cone and a tephra fallout sheet. The cone is presently ca. 80 m high. It is highly breached, asymmetric and slightly elongated in a WNW–ESE direction. Some information on its internal structure can be obtained by observing the deposits exposed on the breached wall (Fig. 4b), and the large rafted blocks of scoria cone carried atop the lava tongues (Fig. 4c) up to distances of 1 km from the vent (Brown et al. 2015). The cone deposits (Fig. 4b) mainly consist of ash, medium to coarse scoriaceous lapilli and bombs (occasionally fluidal or flattened) and rare dense blocks, organized in massive to faint planar parallel, decimetre to metre-thick beds. Cone deposits are mostly non-welded to slightly agglutinated. The topmost part of the

**Table 2** Reports by scientists and eyewitnesses on the maximum height reached by glowing pyroclastic products

Day	Column height (m)	Citation	Translation	Reference
18 November 1909 (opening phase)	ca. 250	“Los escobones ( <i>Cytisus proliferus</i> ), dando vuelta, subían como tres pinos de los mas altos [...]”	Brooms, spinning in the air, rose up as high as three of the tallest pine trees [...]	Fernández Navarro, (1911)
19 November 1909	–	“[...] una gruesa columna de humo, cuya negra masa se inflamaba á trechos, subía ligera perdiéndose en el cielo”.	A large column of smoke, whose black mass was inflamed at intervals, rose up light and getting lost in the sky.	Ponte and Cologan (1911)
19 November 1909	500	“[...] los materiales ligeros y las cenizas enrojecidas continuaban hasta unos quinientos metros, en medio de una columna de humo rojo”.	The light materials and the glowing ash continued for other [+50 m] 500 m within a column of red smoke.	Ponte and Cologan (1911)
21 November 1909	500–600	“Visitado el volcán en la mañana de hoy, se ve arroja lava á mas de 500 ó600 metrós de altura por cuatro bocas”.	Visiting the volcano this morning, I saw red lava at more than 500 or 600 m of height from four vents.	Headmaster of local Red Cross—newspaper “ABC Martes” 23 November 1909
22 November 1909	1000	“Am 22. November sind von einem Beobachter aus Garrachico Feuergarthen bis zu 700 m beobachtet, eine Angabe, deren Richtigkeit mir durchaus wahrscheinlich ist, denn an dem klaren Abende jenes Tages sah ich von Orotava aus eine rot beleuchtete rauchende Säule, deren Kuppe, unter Vergleich mit dem Gipfel des viel näheren Pico de Teyde, wohl 2500 m oder mehr Höhe über dem Meeresspiegel besaß”.	On 22 November an observer from Garrachico saw a fire fountain of 700 m that is reasonable because during the clear evening of that day I saw from Orotava a glowing red column of smoke whose height, in comparison with the top of the nearest Pico del Teide, should have an height of 2500 m or more on the sea level.	Burchard (1909)
–	>>500–600	“He visto, reloj en mano, ascender durante treinta y siete segundos, bloques enormes de más de tres ó cuatro metros cúbicos, rectos hacia el cielo [...]” “[...] Cálculo, y no exagero que esos bloques, han alcanzado alturas de 500 a 600 metros, mientras quelas escorias, semejantes á piedra pómez negra, flotaban a muchissima mayor altura”.	I have seen, watch in my hand, huge blocks of more than three or four cubic meters, rise straight into the sky, for 37 s. I calculate, and not exaggerating, that these blocks have reached heights of 500 m or more, whereas those scoria, resembling black pumice, floated to a much greater height.	El Dia De Madrid (1909)

cone consists of an almost continuous, decimetre-thick bed of agglutinated spatters.

Rafted blocks of scoria cone are formed by oxidized scoria clasts (up to some decimetres) that are usually weakly stuck together and poorly deformed (single clasts maintain almost unaltered their external shape) to weakly agglutinated and slightly deformed, especially at the contact with the underlying lava flow (Fig. 4b).

Pyroclastic fallout deposits are well preserved only in very proximal locations  $\leq 1$  km from the vent and mostly E–ENE of the scoria cone (Fig. 4a). The maximum thickness of the pyroclastic fallout deposit (ca. 130 cm) was measured in a stratigraphic trench dug about 250 m NE of the main vent and 50 m from the base of the cone (Fig. 2). Near the scoria cone, to the north and the east, the fallout deposit lies on reddish, scoriaceous surfaces of older lava flows and pyroclastic rocks from Montaña Chío (Carracedo et al. 2007) and Montaña Reventada (Araña et al. 1994), whereas in vegetated areas, it covers a dark soil. Occasionally, burnt plants and partially carbonized stems of Canary Island pine trees (*Pinus canariensis*) were

found buried under the pyroclastic fallout deposits. On the top of the pyroclastic sequence around the cone, numerous ribbon- and spindle-shaped, poorly vesicular bombs and blocks as large as  $60 \times 40$  cm lie above the fallout deposit (Fig. 4e). Moving away from the vent area, the deposit thins rapidly, becoming progressively less distinct, and overlaps fallout deposits (ash and lapilli) produced during the 1706 eruption of the Garachico Volcano, from which they are occasionally separated by a <1-cm thick yellowish soil or by a faint, brownish oxidation surface (Fig. 4c). At distances greater than 1 km from the vent the deposit consists only of sparse lapilli and coarse ash virtually indistinguishable from the underlying deposits of the 1706 eruption of Garachico Volcano. The original stratigraphy and structure of the pyroclastic deposit are difficult to reconstruct S–SE of the Chinyero scoria cone. The pyroclastic blanket is highly disrupted and reworked and alternates with the lava flow tongues (Fig. 4d). The lava flow field is only occasionally partially to completely covered by almost undeformed ash and lapilli deposits derived from the eruption, as also pointed out by Brown et al. (2015).

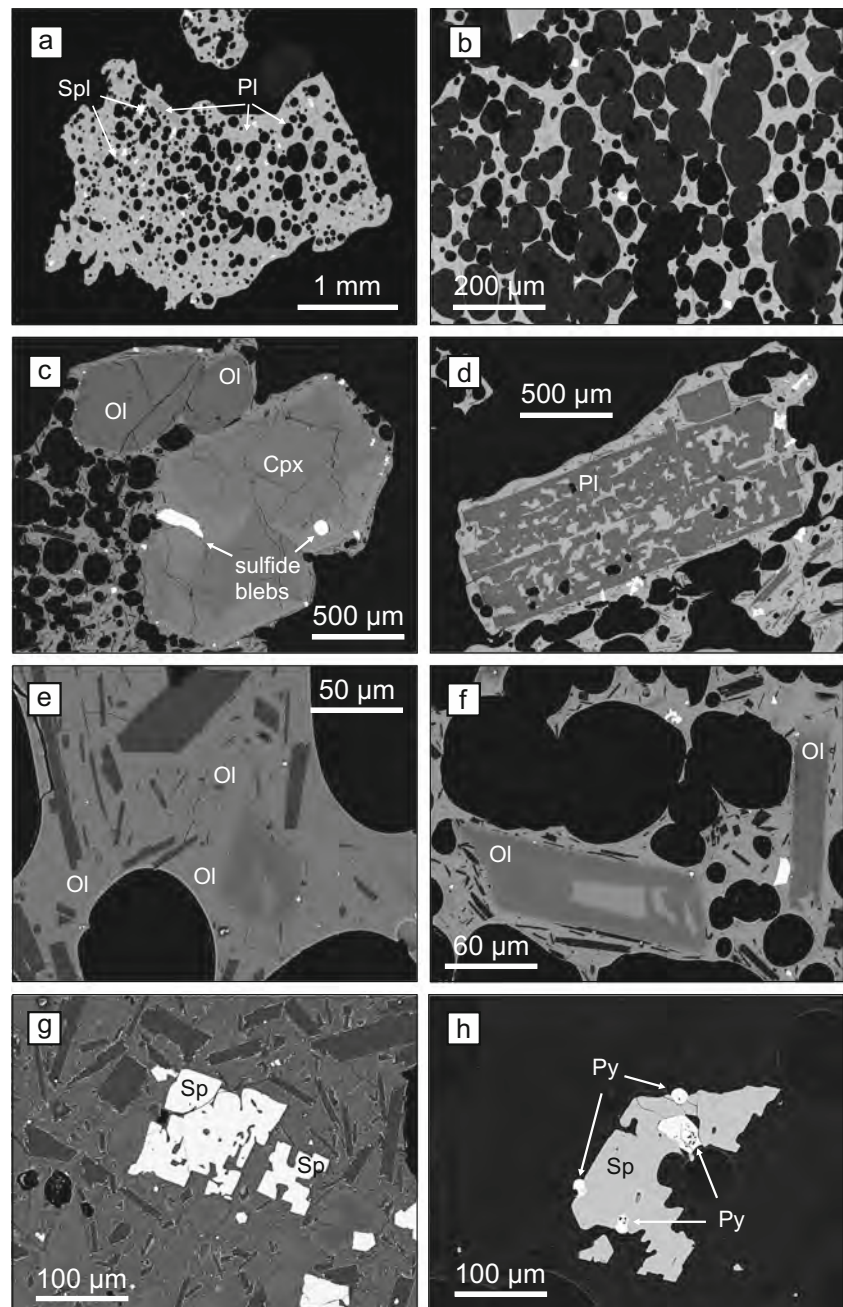
**Fig. 4** Scoria cone and pyroclastic deposits of the 1909 eruption of Chinyero, Tenerife. **a** Panoramic view (from NE) of the Chinyero scoria and pyroclastic deposits emplaced over scoriaceous lava flows from a previous eruption. **b** Panoramic view of the breached wall of Chinyero scoria cone showing the internal structure and deposits; **c** Two rafted blocks deriving from the scoria cone. Blocks are made of single centimetre–diameter scoria clasts, undeformed and weakly stuck together. At the base of the block, a 10–20-cm thick bed is present where scoria clasts are incipiently welded to slightly deformed. **d** Small stratigraphic trench dug approximately 600 m from the main vents of Chinyero (point 15 in Fig. 2) showing the pyroclastic fall deposits of Chinyero overlying pyroclastic deposits from a previous eruption (likely the 1706 eruption of Garrachico) and separated only by a thin reddish pedogenized horizon. **e** SSE view of tephra fall deposits (disrupted and tilted) emplaced on the lava flow of the 1909 eruption of Chinyero. **f** A broken, spindle-shaped volcanic bomb laying on the top of the Chinyero eruptive sequence (approximately size  $60 \times 40$  cm)



In vertical section, the deposit is massive, with vague normal grading, and consists of dark, lustrous glassy particles of angular to ragged shape. Particles range from moderately vesicular to highly vesicular (according to the classification of Houghton and Wilson 1989); the former has abundant isolated spherical, elliptical to slightly deformed, occasionally

coalesced vesicles surrounded by thick glass septa, whereas the latter are microvesicular or have abundant spherical coalescing vesicles separated by thin glass walls (Fig. 5a, b). Coalesced vesicles often give rise to connected fluid flow paths several millimetres in length (Fig. 5b). Lithic fragments represent less than 1% of the deposit and consist of dense,

**Fig. 5** Scanning electron microscope backscattered (SEM-BSE) images representative of textures and main mineral assemblage identified in pyroclastic fall deposits and lavas from 1909 eruption of Chinyero, Tenerife. Mineral abbreviations after Whitney and Evans (2010). **a** Moderately vesicular lapilli bearing microlites of plagioclase (*Pl*) and spinel (*Sp*). **b** Highly vesicular lapilli with coalesced vesicles that lead to connected fluid flow paths. **c** Phenocrysts of clinopyroxene (*Cpx*) and olivine (*Oi*) within a moderately vesicular lapillus with groundmass rich in microlites of *Pl*. **d** Sieve textured zoned phenocrysts of plagioclase. **e, f** Skeletal to hopper microlites of olivine set in a plagioclase microlite-rich groundmass. **g** Skeletal, relatively un-zoned spinels in glassy groundmass with plagioclase, clinopyroxene and rare olivine microlites. **h** Pyrite (*Py*) blebs enclosed in embayed boundary of skeletal spinel and olivine microphenocrysts



highly crystallized lava fragments and minor oxidized scoriaeous lapilli with a greyish–reddish colour. The relative proportion of juvenile and lithic components remains the same throughout the sequence.

The complete characterization of grain size distributions was not possible due to a lack of data across the entire dispersal area, especially in medial and distal sites where the deposits are eroded and strongly reworked. However, analytical results indicate that all samples consist of unimodal, well sorted to very well sorted ( $\sigma\phi = 1.85$  to  $0.85$ ), fine to medium lapilli ( $Md\phi = -1.04$  to  $-2.63$ ). TOTGS distribution results also reveal the coarse nature of the Chinyero pyroclastic

fallout deposits, with particles  $>1$  mm in diameter accounting for ca. 85 wt.% of the total tephra fall deposit (Fig. 6).

The estimated volume of pyroclastic deposits still traceable around the cone is of the order of  $5 \times 10^5 \text{ m}^3$  ( $5.10 \times 10^{-4} \text{ km}^3$ ) and was calculated from isopach maps using the method described by Pyle (1989). Even for this very limited area, the volume calculation is affected by intense reworking and erosion processes that considerably reduced the thickness of the deposit, in some cases, by half with respect to that indicated in historical accounts; the calculated volume is therefore only a fraction of the true volume. For this reason, the order of magnitude of the volume of pyroclastic deposits was estimated by

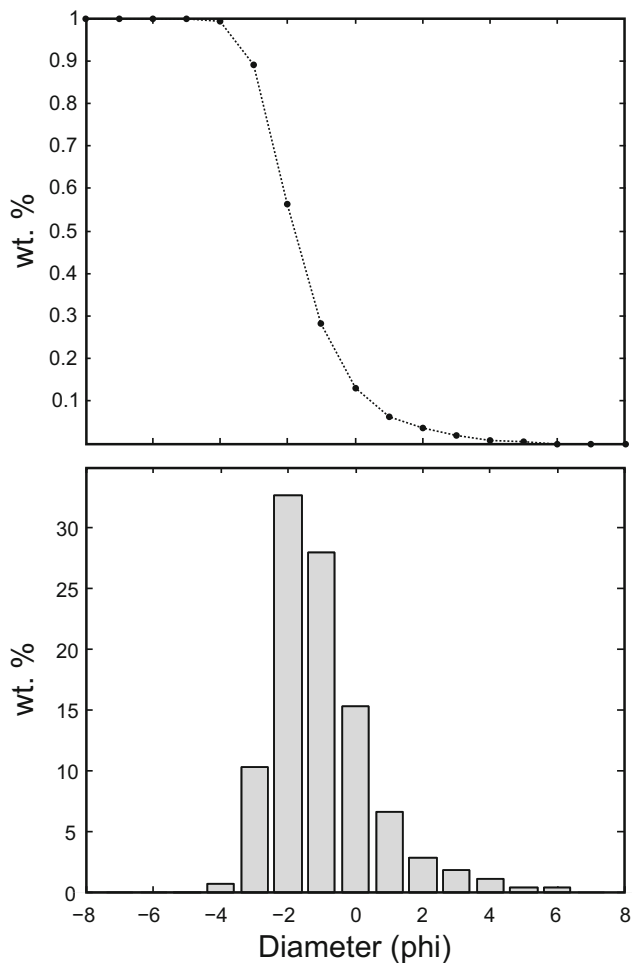


**Fig. 6** Grain size distributions for the Chinyero pyroclastic deposits calculated using the Matlab script TOTGS of Biass and Bonadonna (2014)

tracing two large isopachs (5 and 0.5 cm) corresponding to the thickness of deposits reported in historical accounts for medial to distal sites (Fig. 7). The resulting estimated volume is approximately  $1.24 \times 10^7 \text{ m}^3$  ( $1.24 \times 10^{-2} \text{ km}^3$ ). The volume of the pyroclastic cone was also estimated approximating the volcanic edifice to a cone with a radius of ca. 190 m and height of 80 m; the resulting volume is of the order of  $2 \times 10^6 \text{ m}^3$ . The minimum volume of pyroclastic deposits emitted during the Chinyero eruption is thus of the order of  $1.5 \times 10^7 \text{ m}^3$  ( $1.5 \times 10^{-2} \text{ km}^3$ ).

By using measured deposit densities between 700 and  $1000 \text{ kg/m}^3$ , we calculated a fallout mass of  $0.87 \times 10^{10}$  to  $1.24 \times 10^{10} \text{ kg}$ . Concerning the scoria cone, we used as reference value the  $1800 \text{ kg/m}^3$  of Pioli et al. (2008) given for the scoria cone built during the Violent Strombolian eruption of Paricutin, thus resulting in a mass of  $0.36 \times 10^{10} \text{ kg}$ . Accordingly, the dense rock equivalent (DRE) volume (calculated assuming an average magma density of  $2700 \text{ kg/m}^3$ ; Lange et al. 1990) of pyroclastic deposits varies between 4.5 and  $5.9 \times 10^6 \text{ m}^3$ .

### Lava flow, texture and volume

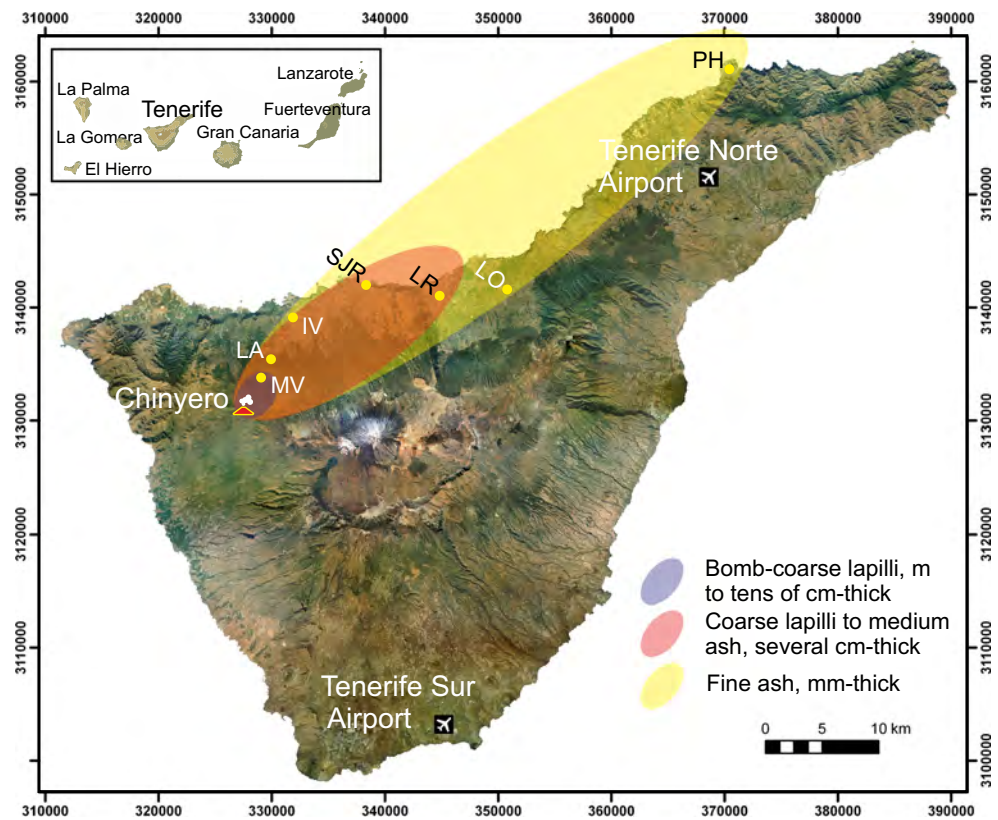
The lava flow field extends westward for 4.6 km from the vent and covers an area of  $\sim 2.7 \text{ km}^2$  (Carracedo 2013) being strongly conditioned by the pre-existent morphology (Fig. 2). As mentioned above, the lava field is reported to have a total volume of ca.  $1.1\text{--}1.5 \times 10^7 \text{ m}^3$  (Fernández Navarro 1914; Carracedo 2013) that is comparable to the volume of pyroclastic deposits. On the basis of historical accounts, we know that lava emission started at the beginning of the eruption from some vents aligned along the eruptive fissure and after it concentrated in two to three vents located close to the crater that remained active until the end of the eruption (Fernández Navarro 1911). The effusive activity formed a compound lava flow field made of blocky aa lava and characterized in some external parts by toothpaste lava spilled from some ephemeral vents. Along the main stream flow, some hornitos occur which are typical features of basaltic eruptions. In few areas close to the base of the scoria cone where lava ponded, the surfaces of lava flows are shelly or ropy. No evidence for clastogenic or rheomorphic flows has been found around the cone or within the whole lava flow field. The emitted mass results in  $2.6\text{--}3.6 \times 10^{10} \text{ kg}$  by using as reference value the  $2380 \text{ kg/m}^3$  of Pioli et al. (2008) given for the lavas of Paricutin. The calculated DRE volume is  $9.6\text{--}13.3 \times 10^6 \text{ m}^3$ .

### Bulk rock and glass compositions

Bulk rock compositions were determined on ten samples of lava flows (yellow dots in Fig. 2) and on two spatter bombs, one close to the first vent opened and the other on top of the pyroclastic cone (orange dots in Fig. 2). Five lava samples were collected at the front of the main lava tongues descending from the Chinyero cone, four from road cuts through the main flow units, and one sample was collected from a lava pond NE of the cone (Fig. 2).

The bulk rock major element composition is basaltic (normative Ol.  $>10\%$ ) and homogeneous (Fig. 8a; Table 3). Lava and pyroclast compositions are indistinguishable; their variability falls within analytical error. In the total alkali silica (TAS; Le Bas et al. 1986) classification diagram, bulk rock major element compositions plot close to the lowermost end of the basaltic–phonolite series of the Teide–Pico Viejo Volcanic Complex (Ablay et al. 1998) and overlap with the only compositional data on this eruption available in the literature (yellow square in Fig. 8b). Glass compositions are slightly more variable than bulk rock compositions, showing higher  $\text{FeO}_{\text{tot}}/\text{MgO}$  values and comparable  $\text{CaO}/\text{Al}_2\text{O}_3$  ratios (Fig. 8b). This trend is compatible with limited fractional crystallization dominated by olivine.

**Fig. 7** Map of Tenerife island showing distribution of pyroclastic fall deposits reconstructed on the basis of historical reports and used to the approximate calculation of tephra volume. Reference system UTM Zone 28N, Datum WGS84



### Texture and compositions of mineral phases

All studied samples, including pyroclastic fallout deposits and lavas, are porphyritic rocks with <1 to 5 vol.% phenocrysts (up to 2.5 mm in size) of clinopyroxene, spinel, rare olivine and plagioclase. Variable amounts of microphenocrysts and microlites of the same phases always occur.

The groundmass in pyroclasts is hyalopilitic and composed mostly of plagioclase laths + Fe–Ti oxides + clinopyroxene + olivine (Fig. 5a–c). Lavas show a fine-grained pilotaxitic groundmass consisting of plagioclase laths, clinopyroxene, spinel and olivine. Potassium feldspar formed during the late stages of crystallization, filling the interstices left by previous phases. Most phenocrysts in pyroclastic products and lavas are rounded to subrounded or embayed (olivine and spinel) and show sieve textures (plagioclase) or complex patchy and oscillatory zoning (clinopyroxene), whereas groundmass microphenocrysts commonly exhibit much more euhedral habits.

Clinopyroxene is the most abundant phase and occurs both as <2.5 mm subequant euhedral to subhedral phenocrysts, microphenocrysts and microlites (Fig. 5). Clinopyroxene phenocrysts and microphenocrysts in both lavas and tephra plot mostly in the field of diopside, with few compositions in the fassaite field (both cores and rims have been analysed for zoned crystals). Mg# ( $Mg\# = (Mg / (Mg + Fe))$  as cation) varies from 0.79 to 0.67 with substantial overlap between

microlites and phenocrysts in both lavas and pyroclasts. Figure 9a shows that phenocrysts and microlites with Mg# between 0.71 and 0.79 could be in equilibrium with the matrix glass, assuming a  $K_d$  cpx-liq value of 0.27 (Putirka 2008). Phenocrysts commonly show complex patchy and oscillatory zoning, whereas hourglass zoning is common in microphenocrysts. Compositional zoning reflects changes in Mg# and in  $TiO_2$ ,  $Al_2O_3$  and  $SiO_2$  contents. Cu–Fe sulphide and Fe sulphide blebs and globules are commonly enclosed in clinopyroxene crystals. A detailed description of sulphide inclusions is given below.

Olivine occurs as subhedral, rounded and embayed phenocrysts up to 1 mm in size, microphenocrysts <300  $\mu m$  (Fig. 5c) and microlites (Fig. 5e, f). Micrometre-thick rims of clinopyroxene often grow on the rims of olivine phenocrysts. Olivine occasionally forms glomeroporphyritic aggregates with interstitial clinopyroxene, plagioclase and spinel. Microphenocryst and microlite crystal habits commonly show embayed boundaries and skeletal, hopper and dendritic shapes (Faure and Schiano 2004, 2005; Fig. 5e). The composition of olivine varies from  $Fo_{85}$  to  $Fo_{69}$ , with Fo-rich compositions (>80) in pyroclasts and Fo-poor (<74) compositions in lava microlites. Figure 9b shows that microlite from lavas and pyroclasts could be in equilibrium with matrix glass and the bulk rock compositions, whereas phenocryst compositions ( $Fo > 80$ ) record precipitation from melts with higher Mg# (based on a  $K_d$  ol-liq value = 0.30; Roeder and Emslie 1970).

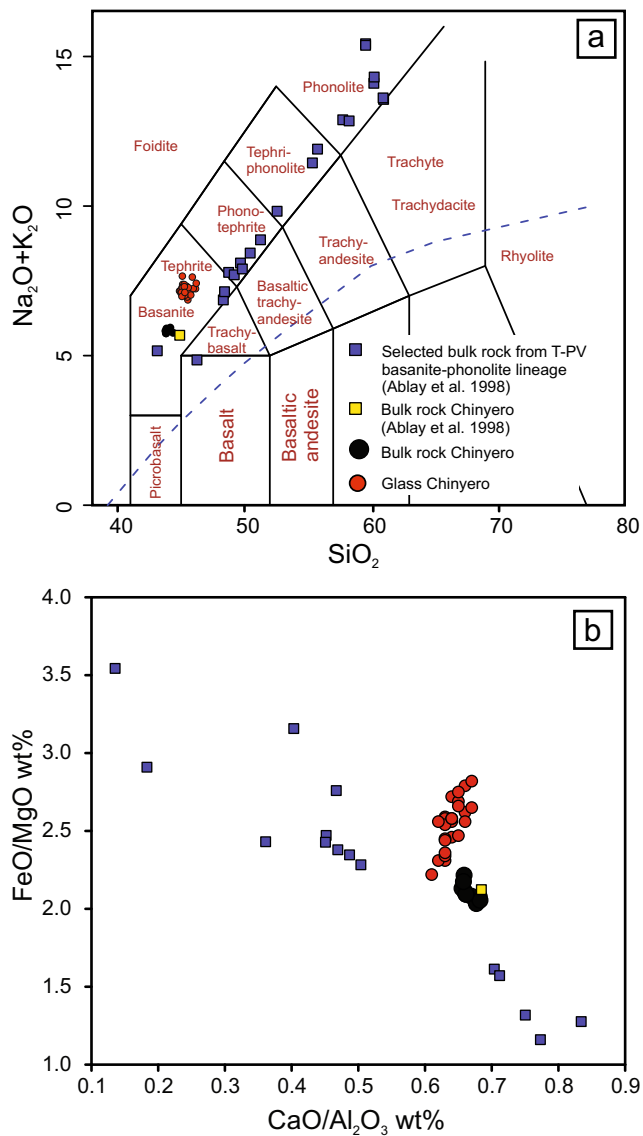


**Fig. 8** **a** Total alkali silica (TAS; LeBas et al. 1986) and **b**  $\text{Fe}/\text{MgO}$  versus  $\text{CaO}/\text{Al}_2\text{O}_3$  diagram showing composition of bulk rock (black dots) and glass (red dots) of Chinyero samples in comparison with bulk rock composition from the basanite–phonolite series of Teide–Pico Viejo Volcanic Complex, Tenerife (Ablay et al. 1998)

Spinel occurs both in pyroclastic products and lavas as <math>500\text{-}\mu\text{m}</math> phenocrysts, microphenocrysts and microlites and comprise minerals of the titanomagnetite series (Fig. 5a–g). Crystals have very variable morphologies. Spinel phenocrysts are usually subequant subhedral, anhedral to polyhedral, often with rounded shapes, although amoeboid crystals are also common. Microphenocrysts and microlites are variable in shape, ranging from euhedral, subhedral or polyhedral to skeletal and dendritic. Cu–Fe sulphide and Fe sulphide blebs and globules are commonly enclosed in spinel phenocrysts and microphenocrysts (Fig. 5h).

Pyroclastic products and lavas contain scarce phenocrysts of plagioclase <math><2\text{ mm}</math> and abundant microphenocrysts

<math><250\text{ }\mu\text{m}</math>. These crystals have euhedral to subhedral shapes and commonly show sieve textures (Fig. 5d). Euhedral to subhedral plagioclase laths also form the main part of the groundmass in lavas and in some crystallized portions of pyroclasts (Fig. 5e–g). Compositions range from  $\text{An}_{87}$  to  $\text{An}_{58}$  with a peak around  $\text{An}_{72}$ . Phenocrysts occasionally exhibit zoning with  $\text{An}_{82-87}$  cores and  $\text{An}_{67-72}$  rims. Microphenocrysts show a homogeneous  $\text{An}_{70-72}$  composition comparable to that of phenocryst rims. Microlites contain less than 67  $\text{An}\%$ .

As mentioned above, spherical to amoeboid  $\text{Fe}(\pm\text{Cu})$ -sulphide blebs and globules are common in clinopyroxene and spinel crystals, in silicate melt inclusions within clinopyroxene and spinel crystals or in glass embayments along clinopyroxene and spinel crystal borders. They also rarely occur in pyroclasts as dispersed globules within the glassy groundmass. The size of sulphide inclusions ranges from  $250\text{ }\mu\text{m}$  to a few micrometres, and peaks between 15 and  $35\text{ }\mu\text{m}$ . Most of the inclusions have a rounded, oval or amoeboid shape (Fig. 5h). In the Cu–Fe–S system, sulphide compositions plot close to the pyrite end-member.

## Discussion

The 1909 eruption of Chinyero was previously considered to be low intensity explosive Strombolian activity that did not represent a serious threat to the population or production facilities of the time. This assumption mainly derives from the little photographic evidence of volcanic activity and from incomplete and fragmentary descriptions of the eruptive phenomena by eyewitnesses and scientists who observed the eruption only several hours after its onset or even weeks after it ended. However, data derived from the comprehensive review of historical sources and from early scientific reports, combined with field and laboratory data on deposits, reveal a very different scenario and clarify some crucial aspects regarding volcanic hazards in the modern Canary Islands.

## Eruption style and dynamics

The eruption of Chinyero started on 18 November 1909 with the opening of several vents along a fracture system. No traces of this very early phase are preserved in the stratigraphic record. The initial opening phase was rapidly followed by energetic Strombolian activity that probably lasted less than 17 h, the time interval between the onset of the eruption and the first observations by Ponte and Cologan in the early morning of 19 November. In this period, the monotonous sequence of well sorted, moderately to highly vesicular scoriaceous lapilli and ash was emplaced in the areas surrounding the volcano and up to several kilometres from the vent; the Chinyero scoria cone was also built and the first lava flow with a length of ca. 200 m

**Table 3** Major, minor and trace element composition of pyroclasts and lavas from the 1909 eruption of Chinyero, Tenerife

Sample no. Rock type	Lapilli and ash (glass)		CHIN1 Spatter	CHIN3 Spatter	CHIN7 Lava	CHIN8 Lava	CHIN9 Lava	CHIN10 Lava	CHIN21 Lava	CHIN22 Lava	CHIN-LL Lava	CHIN-LF Lava
Method	EPMA <i>n</i> = 30	s.d.	ICP	ICP	ICP	ICP	ICP	ICP	ICP	ICP	ICP	ICP
SiO <sub>2</sub>	45.3	0.87	44	43.9	43.5	43.7	44.4	43.3	44	43.9	44.1	45.1
TiO <sub>2</sub>	4.27	0.30	3.8	3.82	3.83	3.83	3.83	3.8	3.77	3.78	3.86	3.85
Al <sub>2</sub> O <sub>3</sub>	15.58	0.37	16.3	16.4	16	16.2	16.25	15.9	16.25	16.1	16.4	16.5
FeO	11.24	0.74										
Fe <sub>2</sub> O <sub>3</sub>			12.6	12.65	12.75	12.65	12.75	12.7	12.5	12.4	13.25	13.15
CaO	9.59	0.99	10.75	10.75	10.9	10.85	11	10.85	10.75	10.65	10.8	10.85
MgO	4.35	0.46	5.37	5.34	5.52	5.47	5.64	5.56	5.37	5.33	5.38	5.44
MnO	0.21	0.11	0.18	0.18	0.18	0.18	0.18	0.17	0.18	0.18	0.19	0.19
K <sub>2</sub> O	2.40	0.40	1.63	1.64	1.57	1.61	1.61	1.57	1.63	1.59	1.61	1.63
Na <sub>2</sub> O	5.05	0.38	4.23	4.22	4.13	4.17	4.26	4.11	4.28	4.11	4.18	4.25
P <sub>2</sub> O <sub>5</sub>	1.18	0.16	0.92	0.94	0.89	0.91	0.93	0.89	0.94	0.92	0.88	0.9
S	0.19	0.09										
Cl	0	0										
L.O.I.			-0.63	-0.49	-0.46	-0.58	-0.71	-0.7	-0.72	-0.55	-0.58	-0.42
Total	99.30	1.13	99.33	99.54	98.99	99.18	100.33	98.34	99.14	98.6	100.27	101.65
Ag			<0.5	<0.5	<0.5	<0.5	<0.5	<0.5	<0.5	<0.5	<0.5	<0.5
As			<5	<5	<5	<5	<5	<5	<5	<5	<5	<5
Ba			612	603	589	633	633	549	570	549	524	504
Cd			<0.5	<0.5	<0.5	<0.5	<0.5	<0.5	<0.5	<0.5	1	0.7
Ce			127	126	124	131	135	112	128	120	120	116
Co			38	39	40	38	39	41	39	38	38	40
Cr			<10	<10	10	10	30	30	10	<10	20	30
Cs			0.4	0.4	0.5	0.6	0.4	2.0	0.4	0.3	0.4	0.4
Cu			24	22	28	26	28	29	23	24	29	30
Dy			7.3	7.2	7.23	7.29	7.76	6.58	7.45	6.89	6.74	6.51
Er			3.29	3.05	3.28	3.47	3.1	2.82	3.0	2.89	2.91	2.73
Eu			3.83	3.7	3.77	3.76	3.94	3.43	3.92	3.6	3.57	3.56
Ga			27	25.9	28	29.1	30.4	22.8	25.7	24.1	24.2	23.9
Gd			10.05	9.87	11.1	10.9	11.3	8.88	10.2	9.53	8.95	9.28
Hf			8.4	8.3	8.2	8.2	8.3	7.1	7.1	6.9	6.6	6.3
Ho			1.28	1.26	1.29	1.29	1.34	1.09	1.24	1.21	1.15	1.13
La			64.5	62.6	62.7	66.4	66.1	58.6	60.3	57.0	58.8	57.4
Li			10	10	10	10	10	10	10	10	10	10
Lu			0.33	0.34	0.34	0.36	0.36	0.31	0.32	0.26	0.28	0.3
Mo			<1	<1	<1	<1	<1	<1	<1	<1	2.0	2.0
Nb			92.9	92.3	93.0	96.6	99.8	80.1	83.5	79.2	78.6	75.1
Nd			65.8	63.8	65.5	66.4	68.9	53.9	62.7	60.6	57.4	54.1
Ni			7	7	14	12	14	17	8	7	16	17
Pb			2	<2	2	<2	<2	<2	4	<2	<2	<2
Pr			15.95	15.9	15.7	16.3	16.45	13.8	14.95	14	13.55	12.8
Rb			34.4	35.4	34.8	37.4	37	32.6	35.6	35.2	35.8	33.8
Sc			17	16	17	17	17	18	16	17	17	17
Sm			12.7	11.65	12.15	12.9	13.1	11.4	11.85	11.45	11	11.5
Sn			2	2	3	3	2	1	2	2	3	2
Sr			1255	1255	1210	1280	1305	1140	1235	1170	1135	1120
Ta			4.1	4.1	3.6	4.2	3.8	2.6	3.9	3.6	3.4	4.2
Tb			1.5	1.44	1.34	1.55	1.43	1.19	1.38	1.24	1.31	1.27
Th			5.6	5.54	5.38	5.63	5.83	4.86	5.48	5.18	5.26	4.97
Tl			<10	<10	10	<10	<10	<10	<10	<10	<10	10
Tm			0.34	0.34	0.4	0.38	0.42	0.33	0.43	0.4	0.37	0.36
U			1.33	1.35	1.37	1.34	1.38	1.16	1.26	1.2	1.2	1.2
V			353	344	368	376	380	327	338	325	312	296
W			1	1	1	1	2	1	1	1	2	1
Y			34.3	33.6	32.5	35.3	35.9	31	32.4	30.8	30.1	29
Yb			2.65	2.45	2.5	2.18	2.54	2.03	2.16	2.22	2.12	2.04
Zn			123	121	121	120	119	121	122	123	119	120
Zr			349	343	341	361	361	298	310	295	300	285

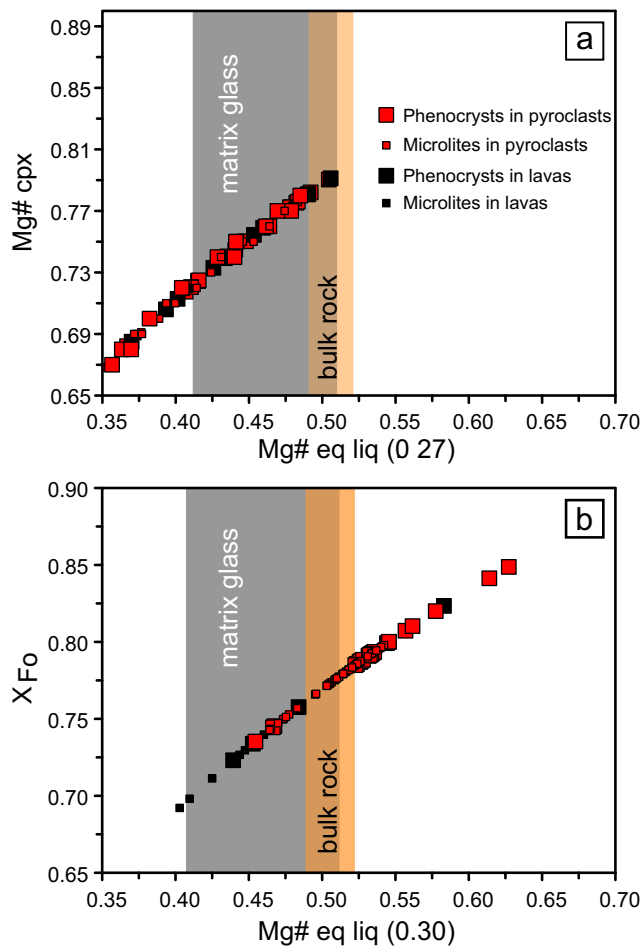


**Fig. 9** Fe–Mg distribution between clinopyroxene, olivine and melt in pyroclasts and lavas. **a**  $X_{\text{Fo}}$  in olivine and **b** Mg# cpx plotted as a function of Mg# of equilibrium melts (Mg# eq liq). **a** Calculations performed with a clinopyroxene–melt Fe–Mg partition coefficient ( $K_d$  cpx-liq) of 0.27 according to Putirka et al. (2008); **b** Calculations performed with an olivine–melt Fe–Mg partition coefficient ( $K_d$  ol-liq) of 0.30 according to Roeder and Emslie (1970). Mg# values for equilibrium melts, natural glasses and bulk rocks are calculated with a  $\text{Fe}_2\text{O}_3/\text{FeO}$  ratio of 0.35 (glass) or 0.27 (bulk rock) based on an assumed  $f\text{O}_2$  corresponding to the NNO buffer. Compositions of natural glasses and bulk rocks are shown for comparison

was emplaced. Eruption intensity likely peaked during this initial phase.

The rate of growth of the Chinyero cone (assuming a maximum duration of 17 h) was comparable or even higher than those of scoria cones built during the violent Strombolian eruptions of Parícutín Volcano in México (30–50 m on the first day and 60 m after 3 days; Foshag and Gonzalez 1956), during the violent Strombolian eruption of Irazú Volcano in AD 1723 (Alvarado and Schmincke 2013) or during the 2001 eruption of Mt. Etna (50–100 m in a couple of days to a week; Behncke and Neri 2003; Calvari and Pinkerton 2004). The mass discharge rate (MDR) calculated assuming a deposit density of ca.  $1000 \text{ kg/m}^3$  is of the order of  $2\text{--}2.6 \times 10^5 \text{ kg/s}$  and comparable to those calculated for other mid-intensity,

violent Strombolian eruptions at Vesuvius and Etna volcanoes (Cioni et al. 2008, 2010).

Similarly, the characteristics of the cone facies (e.g. well fragmented and mostly non-welded), the thickness and architecture of the pyroclastic sequence, the nature of particles and the dispersal of products are akin to those of violent Strombolian eruptions, during which rapidly pulsating or steady eruption columns produce the fallout of well-fragmented pyroclasts and very minor ballistic bombs (e.g. Valentine 1998; Arrighi et al. 1999; Valentine et al. 2005; Valentine and Gregg 2008; Cioni et al. 2010; Barsotti et al. 2015). The violent Strombolian phase probably continued for the first 3 days of eruption, with pulsating eruptions until 21 November. A recent work by Brown et al. (2015) based on field relationships between pyroclastic products and lava flows suggest that the emission of ash and lapilli fallout from quasi-steady eruption plumes alternated with the effusion of lavas. After the Violent Strombolian phase, the eruption rapidly waned, giving way to a low-energy phase of Strombolian activity that continued until the eruption ceased along with the emission of lavas from the crater located at the base of the cone; this phase did not effectively contribute to the buildup of the pyroclastic pile, except in areas very proximal to the scoria cone and atop the lava flows (Brown et al. 2015). The eruption ended with a Vulcanian-style flare-up during which abundant bombs and dense blocks were emitted. A minimum estimated DRE volume of the eruption ranges between  $14.1$  and  $19.1 \times 10^6 \text{ m}^3$ . The DRE of effusive activity is approximately double that of explosive activity. However, this is definitely a minimum estimate because of the intense reworking and erosion processes that affected the fallout deposit.

### Feeding the eruption

The Chinyero eruption was preceded by intense seismic activity, which began in July 1908, more than 1 year before the eruption, and by several other precursors such as fumaroles over the central crater of Teide Volcano and a general increase in ground temperature throughout the cone. Except for the 1798 Eruption of Cahorra Volcano, which was preceded by 3 years of seismic activity (Cologan Fallow 1798), the seismic precursors of the other historical flank eruptions of Tenerife were considerably shorter, lasting just a few days to a week. Only a week of strong seismicity occurred prior to the 1704–1705 eruption of Arafo–Fasnia–Siete Fuentes (Viera and Clavijo 1776; Carracedo 2013); this continued until the 1706 Eruption of Garachico Volcano. The seismic crisis that preceded the eruption of Chinyero was possibly associated with the intrusion and movement of an undefined volume of magma through the ocean crust and under the Tenerife volcanic complex, similarly to the 2011–2012 eruption of El Hierro, Canary Islands (Martí et al. 2013a, b; Meletlidis et al. 2015 and references therein). The contemporaneous formation of

strong fumarole activity at the base of the Pico Viejo cone could likewise be the result of the deep injection of a new magma intrusion, with the release of fluid and heat to the hydrothermal system.

Analytical data on erupted products reveal no time-related trends in crystal contents or in bulk rock, glass and minerals compositions. This indicates that the whole eruption was fed by a single, relatively small, very homogeneous batch of magma. The low phenocryst content in both fallout pyroclastic deposits and lavas suggests that the magma rapidly rose to the surface without stalling significantly along the route. In particular, the substantial equilibrium between the melt and clinopyroxene phenocrysts, as well as melt and olivine microlite, points to crystallization during ascent, whereas high-Fo olivine phenocrysts record early crystallization and equilibrium with more Mg-rich liquids.

Sulphides such as those identified in Chinyero products are very useful in understanding physical and chemical conditions (P, T, volatiles and  $fO_2$ ) in the magmatic systems during pre-eruptive stalling and ascent, as well as in identifying processes of contamination and assimilation of country rocks (Holwell et al. 2011). However, the detailed analysis and interpretation of sulphides are beyond the scope of this paper and will be addressed in future studies.

### Eruption impact and hazard implications

This study reveals that the intensity and magnitude of the 1909 Chinyero eruption were much greater than previously reported and resulted in the distribution of pyroclastic products very far from the source. Contrary to previous assumptions, at least during the first 3 days, the eruption was not a low-intensity Strombolian eruption but a violent Strombolian eruption that caused the significant fallout of lapilli up to 20 km from the vent and of ash 130 km from the vent.

Should an eruption of comparable size/intensity occur in the future, ash and lapilli would likely be dispersed over a large part of the island of Tenerife, possibly reaching other islands in the archipelago and causing problems to inhabitants, tourists and infrastructures. For example the municipalities that were affected by ash and lapilli falls during the 1909 Chinyero eruption now count more than 215,000 inhabitants (2013 census). These contain structures such as critical ground transportation systems (highways), hospitals, tourist facilities and areas dedicated to the production of valuable agricultural products (wine) that would all be exposed to volcanic ash. In addition, Tenerife North airport (San Cristóbal de La Laguna, Santa Cruz de Tenerife) is located ca. 47 km NW of the Chinyero Vent, in the direction in which the fine ash drifted during the 1909 eruption. Tenerife South Airport (Granadilla, Santa Cruz de Tenerife) is located ca. 35 km SW of the vent. Both airports are in the range of ash dispersed during the 1909 Chinyero eruption and, in general, of ash dispersal from this

type of basaltic eruption. Should such an eruption occur, air transport from/to Tenerife would likely be interrupted, causing substantial direct, indirect and induced impacts on industries dependent on air transport (e.g. travel and tourism, global exchange of goods, manufacturing supply chains). Note that the Chinyero eruption caused problems for tourism already in 1909, in an economic and social context completely different from the present one. Tourism is presently the economic driving force in the Canary Islands, with Tenerife alone receiving more than 5 million visitors per year.

### Concluding remarks

The 1909 Chinyero eruption was fed by a compositionally homogeneous batch of magma that ascended rapidly from depth without significant stalling. At least in the early phases, the ascending magma produced a rather violent eruption. During the first 17 h and, in general, during the first 3 days of the eruption, the growth rate of the Chinyero scoria cone, the rate of emission of pyroclastic materials, the nature and architecture of the pyroclastic sequence, as well as the dispersal of products, were akin to those of violent Strombolian eruptions: rapidly pulsating or quasi-steady eruption columns produced the fallout of well-fragmented pyroclasts and scarce ballistic bombs. This type of activity produced the heavy fallout of lapilli and ash over the entire NE flank of the island of Tenerife, with fine ash reaching the island of Gran Canaria situated more than 100 km from the vent. The gentle Strombolian explosive activity captured in photographs and described by eyewitnesses and scientists of the time is not representative of the eruption but only of the lower intensity phases that contributed to a lesser extent to the buildup of tephra blanket. In order to correctly assess hazard and plan risk reduction strategies for the island of Tenerife and for the archipelago in general, the scientific community must make an extra effort to evaluate the real intensity and magnitude of past basaltic eruptions along the Tenerife rift zones.

**Acknowledgements** This work was financially supported by INGV-Pisa. We thank the reviewer G. Valentine and the editor P. J. Wallace for their constructive comments and suggestions that improved the quality of the manuscript.

### References

- ABC MARTES (1909) La Erupcion del Teide. ABC Hemeroteca. Available via DIALOG. <http://hemeroteca.abc.es/nav/Navigate.exe/hemeroteca/madrid/abc/1909/11/23/012.html>
- Ablay GJ, Carroll MR, Palmer MR, Marti J, Sparks SJ (1998) Basanite-phonolite lineages of the Teide-Pico Viejo volcanic complex, Tenerife, Canary Islands. *J Pet* 39(5):905–936. doi:10.1093/ptroj/39.5.905

- Albert H, Costa F, Martí J (2016) Years to weeks of seismic unrest and magmatic intrusions precede monogenetic eruptions. *Geology*. doi:10.1130/G37239.1
- Alvarado GE, Schmincke H-U (2013) The 1723 A.D. violent strombolian and phreatomagmatic eruption at Irazú volcano, Costa Rica. *Rev Geol Am Central* 48:41–61
- Ancochea E, Fuster JM, Ibarrola E, Cendrero A, Coello J, Hernan F, Cantagrel JM, Jamond C (1990) Volcanic evolution of the island of Tenerife (Canary Islands) in the light of new K-Ar data. *J Volcanol Geot Res* 44(3–4):231–249. doi:10.1016/0377-0273(90)90019-C
- Araña V, Martí J, Aparicio A, García-Cacho L, García-García R (1994) Magma mixing in alkaline magmas: an example from Tenerife, Canary Islands. *Lithos* 31(1–2):1–19
- Arrighi S, Principe C, Rosi M (1999) Violent strombolian and subplinian eruptions at Vesuvius during post-1631 activity. *Bull Volcanol* 63: 126–150. doi:10.1007/s004450100130
- Barrera JL (2009) El centenario de la erupción del volcán Chinyero, en Tenerife. *Tierra y Tecnología* 35:3–23
- Barsotti S, Neri A, Bertagnini A, Cioni R, Mulas M, Mundula F (2015) Dynamics and tephra dispersal of violent strombolian eruptions at Vesuvius: insights from field data, wind reconstruction and numerical simulation of the 1906 event. *Bull Volcanol* 77:58. doi:10.1007/s00445-015-0939-6
- Behncke B, Neri M (2003) The July–August 2001 eruption of Mt. Etna (Sicily). *Bull Volcanol* 65:461–476. doi:10.1007/s00445-003-0274-1
- Biasi S, Bonadonna C (2014) TOTGS: total grainsize distribution of tephra fallout, <https://vhub.org/resources/3297>.
- Bonadonna C, Houghton BF (2005) Total grain-size distribution and volume of tephra-fall deposits. *Bull Volcanol* 67:441–456. doi:10.1007/s00445-004-0386-2
- Brown RJ, Thordarson T, Self S, Blake S (2015) Disruption of tephra fall deposits caused by lava flows during basaltic eruptions. *Bull Volcanol* 77:90. doi:10.1007/s00445-015-0974-3
- Burchard O (1909) Ein neuer vulkanischer Ausbruch auf Teneriffa. *Globus: illustrierte Zeitschrift für Länder und Völkerkunde* 97:21–25
- Cabrera Diaz A (1911) Memoria del curso de 1909 a 1910 del Instituto General y Tecnico de Canarias. Santa Cruz de Tenerife, 109 pp.
- Calvari S, Pinkerton H (2004) Birth, growth and morphologic evolution of the ‘Laghetto’ cinder cone during the 2001 Etna eruption. *J Volcanol Geotherm Res* 132:225–239. doi:10.1016/S0377-0273(03)00347-0
- Carracedo JC, Rodríguez Badiola E, Guillou H, Paterne M, Scaillet S, Pérez Torrado FJ, Paris R, Fra-Paleo U, Hansen A (2007) Eruptive and structural history of Teide Volcano and rift zones of Tenerife, Canary Islands. *Geol Soc Am Bull* 119(9):1027–1051
- Carracedo JC (2013) The last 2 ky of eruptive activity of the Teide volcanic complex: features and trends. In: Troll VR, Carracedo JC (eds) *Teide volcano*. Springer, Berlin, pp. 129–153
- Cioni R, Bertagnini A, Santacroce R, Andronico D (2008) Explosive activity and eruption scenarios at Somma-Vesuvius (Italy): towards a new classification scheme. *J Volcanol Geotherm Res* 178:331–346. doi:10.1016/j.jvolgeores.2008.04.024
- Cioni R, Bertagnini A, D’Orlando C, Pompilio M (2010) Past and present mid-intensity explosive eruptions of Italian volcanoes and their impact on human activity. *J Virt Expl*. doi:10.3809/jvirtex.2009.00229
- Collet LW, Montagnier HF (1910) Sur la récente éruption du Chinyero à Tenérif. *Archives des Sciences Physiques et Naturelles de Genève* 29:422–424
- Cologan Follow B (1798) La erupción del 9 de junio de 1798 de las Narices del Teide.
- El Día de Madrid (1909) La Erupción del Teide. Biblioteca Nacional de España. Available via DIALOG. <http://hemerotecadigital.bne.es/issue.vm?id=0003478909&search=&lang=es>
- Faure F, Schiano P (2004) Crystal morphologies in pillow basalts: implications for mid-ocean ridge processes. *Earth Plan Sci Lett* 220:331–344. doi:10.1016/S0012-821X(04)00057-3
- Faure F, Schiano P (2005) Experimental investigation of equilibrium conditions during forsterite growth and melt inclusion formation. *Earth Plan Sci Lett* 236:882–898. doi:10.1016/j.epsl.2005.04.050
- Fernández Navarro, L (1911) Erupción volcánica del Chinyero (Tenerife) en noviembre de 1909. *Anales de la Junta para Ampliación de Estudios e Investigaciones Científicas, V, Mem. 1*, 99 pp.
- Fernández Navarro L (1924) Datos sobre el volcanismo canario. *Bull Volcanol* 2:129–155
- Foshag WF, Gonzalez R (1956) Birth and development of Parícutin volcano Mexico. *Geological Survey Bulletin* 965-d
- Holwell DA, McDonald I, Butler IB (2011) Precious metal enrichment in the Platreef, Bushveld Complex, South Africa: evidence from homogenized magmatic sulfide melt inclusions. *Contrib Min Pet* 161(6):1011–1026. doi:10.1007/s00410-010-0577-0
- Houghton BF, Wilson CJN (1989) A vesicularity index for pyroclastic deposits. *Bull Volcanol* 51:451–462
- Inman DL (1952) Measures for describing the size distribution of sediments. *J Sed Res* 22(3):125–145. doi:10.1306/D42694DB-2B26-11D7-8648000102C1865D
- Lange RL, Carmichael ISE (1990) Thermodynamic properties of silicate liquids with emphasis on density, thermal expansion and compressibility. In: Nicholls J, Russell JK (eds) *Modern methods of igneous petrology: understanding magmatic processes*. Reviews in mineralogy 24, Mineral Soc AM, Washington, DC, pp 25–64
- Le Bas MJ, Le Maitre RW, Streckeisen A, Zanettin B (1986) A chemical classification of volcanic rocks based on the total alkali-silica diagram. *J Pet* 27:745–750. doi:10.1093/petrology/27.3.745
- Martí J, Spence R, Calogero E, Ordoñez A, Felpeto A, Baxter P (2008) Estimating building exposure and impact to volcanic hazards in Icod de los Vinos, Tenerife (Canary Islands). *J Volcanol Geotherm Res* 178:553–561. doi:10.1016/j.jvolgeores.2008.07.010
- Martí J, Pinel V, López C, Geyer A, Abella R, Tárraga M, Blanco MJ, Castro A, Rodríguez C (2013a) Causes and mechanisms of the 2011–2012 El Hierro (Canary Islands) submarine eruption. *J Geophys Res Solid Earth* 118:823–839. doi:10.1002/jgrb.50087
- Martí J, Castro A, Rodríguez C, Costa F, Carrasquilla S, Pedreira R, Bolos C (2013b) Correlation of magma evolution and geophysical monitoring during the 2011–2012 El Hierro (Canary Islands) submarine eruption. *J Pet* 54(7):1349–1373. doi:10.1093/petrology/egt014
- Meletlidis S, Di Roberto A, Dominguez Cerdana I, Pompilio M, García-Canada L, Bertagnini A, Benito-Saz MA, Del Carlo P, Sainz-Maza Aparicio S (2015) New insight into the 2011–2012 unrest and eruption of El Hierro Island (Canary Islands) based on integrated geophysical, geodetical and petrological data. *An Geophys*. doi:10.4401/ag-6754
- Perret FA (1914) The volcanic eruption of Tenerife in the autumn of 1909. *Zeitschrift für Vulkanologie* 1:20–31
- Pioli L, Erlund E, Johnson E, Cashman KV, Wallace P, Rosi M, Delgado Granados H (2008) Explosive dynamics of violent Strombolian eruptions: the eruption of Parícutin Volcano 1943–1952 (Mexico). *Earth Planet Sci Lett* 271:359–368. doi:10.1016/j.epsl.2008.04.026
- Pyle DM (1989) The thickness, volume and grainsize of tephra fall deposits. *Bull Volcanol* 51:1–15. doi: 10.1007/BF0108675
- Ponte and Cologán, A (1911) Volcán del Chinyero. Memoria histórico-descriptiva de esta erupción volcánica caecida en 18 de noviembre de 1909. *Tipolit, Tenerife*, 61 pp
- Putirka KD (2008) Thermometers and barometers for volcanic systems. In: Putirka KD, Tepley F (eds) *Minerals, Inclusions, and*

- Volcanic Processes: Reviews in Mineralogy and Geochemistry, 69, pp. 61–120.
- Roeder PL, Emslie RF (1970) Olivine-liquid equilibrium. *Contrib Min Pet* 29:275–289
- Romero C (1991) Las manifestaciones volcánicas históricas del Archipiélago Canario. Santa Cruz de Tenerife, Consejería de Política territorial Gobierno de Canarias, 1463 p
- Solana C (2012) Development of unconfined historic lava from fields in Tenerife: implications for the mitigation of risk from a future eruption. *Bull Volcanol*. doi:[10.1007/s00445-012-0670-5](https://doi.org/10.1007/s00445-012-0670-5)
- Tous Meliá J (2011) La erupción del Chinyero a través de la cartografía, la fotografía y los documentos oficiales: (del 18 al 27 de noviembre de 1909). Tous Meliá J (ed), San Cristóbal de La Laguna, 335 pp.
- Valentine GA (1998) Eruption column physics. In: Freundt A, Rosi M (eds) *From magma to tephra*. Elsevier, Amsterdam, pp. 91–138
- Valentine GA, Krier D, Perry FV, Heiken G (2005) Scoria cone construction mechanisms, Lathrop wells volcano, southern Nevada, USA. *Geology* 33:629–632. doi:[10.1130/G21459AR.1](https://doi.org/10.1130/G21459AR.1)
- Valentine GA, Gregg TKP (2008) Continental basaltic volcanoes—processes and problems. *J Volcanol Geotherm Res* 177:857–873. doi:[10.1016/j.jvolgeores.2008.01.050](https://doi.org/10.1016/j.jvolgeores.2008.01.050)
- Viera and Clavijo J (1776) *Noticias de la Historia General de las Islas Canarias: Tenerife*. Goya (ed), Sta. Cruz de Tenerife
- Whitney D, Evans BW (2010) Abbreviations for names of rock-forming minerals. *Am Mineral* 95:185–187. doi:[10.2138/am.2010.3371](https://doi.org/10.2138/am.2010.3371)